Finite Element Modelling (Including Material Grain Refinement Prediction) when Turning Advanced Aerospace Alloys

by

Raul E. Munoz

A thesis submitted to
The University of Birmingham
for the degree of
DOCTOR OF PHILOSOPHY

School of Mechanical Engineering
College of Engineering and Physical Sciences
The University of Birmingham
September 2014

ABSTRACT

Following a comprehensive literature survey covering theoretical and experimental characteristics as well as finite element (FE) modelling of the metal cutting process, 2D and 3D fully-coupled thermo-mechanical FE models were developed to simulate the orthogonal turning of advanced aerospace alloys including Ti-6Al-4V and Inconel 718 superalloy. In addition to evaluating the influence of operating conditions on response measures such as cutting forces, workpiece/cutting tool/tool-chip interface temperatures and chip morphology, the FE models were extended to enable the prediction of grain size distribution due to dynamic recrystallisation (DRX) of the workpiece microstructure following machining.

Only a small number of publications have focused on modelling surface integrity parameters, which have largely been confined to the prediction of residual stresses with some recent work addressing workpiece material grain size distribution. This was partly attributed to the limitations of the material models used, such as that proposed by G.R. Johnson and W.H. Cook (JC) in 1983, which is derived empirically (the model constants are determined through curve fitting of experimental data).

Initial 2D and 3D FE models when orthogonally machining Ti-6Al-4V with K20 inserts at a cutting speed of 60, 90 and 120m/min and a feed rate of 0.125mm/rev, were developed using the commercial software ABAQUS 6.10-1, which incorporated the JC constitutive model with material constants sourced from the literature. This allowed the assessment of the JC model for characterising the constitutive response of the alloy and as a precursor to mainstream work on Inconel 718. The 2D FE model was formulated utilising the Arbitrary Lagrangian Eulerian method with adaptive remeshing, while a pure Lagrangian description was used in the 3D simulations. In both cases, the FE models were coupled with flow softening/damage models to predict chip formation/morphology. The energy-based fracture model proposed by M.G. Cockcroft and D.J. Latham (CL) in 1968 and the more recent Rittel-Wang-Merzer (RWM) flow softening/damage relationship, were evaluated in the 3D FE model, however the latter was employed in the 2D FE model only. Both damage criteria were implemented in the FE models through the development of a user customised VUMAT subroutine, which also included the mathematical formulation of the JC material model. At 120m/min, the 2D FE model overestimated the tangential and feed forces when compared against experimental results, with corresponding deviations of 22.8% and 37.9%. Higher discrepancies were observed in the 3D simulations, although the RWM damage criterion showed lower errors in tangential and feed forces (52% and 138%) when compared to the CL formulation (166% and 350%).

The Mechanical Threshold Stress (MTS) model was developed to better represent the viscoplastic behaviour of Inconel 718, which couples strain rate and temperature effects with regard to flow stress and plastic strain. The low and elevated strain rate/temperature flow stress data required to define the material model were obtained from compression tests using a Gleeble and Split Hopkinson Pressure Bar apparatuses respectively. New constants for the JC relationship were calculated to evaluate both material models, however the MTS model was only used to predict DRX due to its more robust background.

FE simulations (2D/3D) following orthogonal turning of Inconel 718 with PCBN tools at cutting speeds of 200, 250 and 300m/min and feeds of 0.08 and 0.2mm/rev, were carried out using the JC and MTS material models with the RWM damage criterion. The 3D simulations based on the MTS model showed superior accuracy over the JC relationship when predicting tangential forces (average error of ~6.8% and ~23% compared to ~18.2% and ~34% when machining at feed rates of 0.2 and 0.08mm/rev respectively), although the modelled chip morphology and workpiece/tool temperature were similar in both cases.

Grain refinement and consequently flow stress softening of Inconel 718 workpiece material following machining was modelled by developing a novel mathematical expression for describing the evolution law within the context of the MTS framework. As with the MTS constitutive model and RWM/CL damage criteria, the DRX module was incorporated into the 3D orthogonal turning FE simulation via a more elaborated VUMAT subroutine, however in conjunction with the RWM model only. While the estimated average minimum grain size was 1.18μm when operating at 0.08mm/rev, the white layer thickness was 2-5 times higher than the experimentally measured value (~10μm in average). Although the predicted minimum grain size when cutting at 0.2mm/rev was relatively similar to that obtained before (average of 1.08μm), the white layer thickness (mean value of 9.2μm) exhibited an augmented accuracy when compared to the average value encountered experimentally, which was ~4μm. Chip morphology together with tangential/feed forces were in general well predicted, with mean errors of 7.1/13.2% and 25/10% for feed rates of 0.2 and 0.08mm/rev respectively in the latter case, suggesting that the suppositions made when including/developing the DRX module in the formulation of the constitutive and damage models were reasonable.

ACKNOWLEDGEMENTS

The author would like to express his sincere gratitude to the following people and organisations for their cooperation and support throughout the duration of this research project:

Dr. Sein L. Soo (Head of the Machining Research Group) and Prof. David K. Aspinwall, both in the School of Mechanical Engineering, University of Birmingham for their academic supervision, guidance and constructive advice.

Prof. Daniel Rittel from the Dynamic Fracture Laboratory, Faculty of Mechanical Engineering, Technion – Israel Institute of Technology and his team, for their kind collaboration in providing use of the their Split Hopkinson Pressure Bar (SHPB) apparatus to generate elevated strain rate/temperature flow stress data for Inconel 718. Dr. Avraham Dorogoy in the Faculty of Mechanical Engineering, Technion – Israel Institute of Technology is also acknowledged for the helpful discussions regarding damage models/damage evolution criteria and their subsequent application into finite element models.

Dr. Santiago A. Serebrinsky in the Centre for Industrial Research – TenarisSiderca, Campana, Buenos Aires, Argentina; his help in initiating contact with Prof. Rittel is greatly appreciated.

Mr. Richard Fasham (retired) and Mr. Andrew Loat, research technicians within the Machining Research Group, School of Mechanical Engineering, University of Birmingham for their invaluable assistance with the initial component manufacture and mechanical assembly of the SHPB rig designed at Birmingham. Additional thanks are due to Mr. Loat for his help with the workpiece material and test specimen preparation for the orthogonal cutting experiments and SHPB trials respectively.

Former and current members of the Machining Research Group for the productive exchange of ideas and countless discussions in conjunction with the unforgettable amusing moments shared throughout the course of study.

The Roberto Rocca Education Program (named after the late General Manager and CEO of the Techint Group, Dr. Roberto Rocca) together with its world leading sponsoring companies Tenaris, Ternium and Techint, as well as the School of Mechanical Engineering, University of Birmingham for providing scholarships to support the work.

Finally but most importantly, I am extremely indebted to my beloved parents Jorge and Delia, younger sister Carolina as well as her husband Juan and my goddaughter Julia Myriam for being the measureless emotional pillar that has helped me overcome the many difficulties and challenges faced throughout my time at the University.

TABLE OF CONTENTS

LIST OF FIGURES

LIST OF TABLES

NOMENCLATURE AND LIST OF SYMBOLS

γ'	Gamma prime (Inconel 718 main strengthening phase).
γ''	Gamma double prime (Inconel 718 secondary strengthening phase).
fcc, bcc, hcp	Face-centred cubic, Body-centred cubic, Hexagonal closed-packed.
F_c	Cutting force in machining (N).
F_t	Feed force in machining (N).
F_p	Thrust (or radial) force in machining (N).
φ	Shear angle (º).
β	Mean friction angle (º).
α	Tool rake angle (º).
S_A	Shear stress acting on the shear plane (MPa).
S_n	Normal stress acting on the shear plane (MPa).
S_0, k_s	Shear plane model constants.
C_s	Machining constant according to the shear plane model.
Seco, Sandvik	Tools and tooling systems engineering group/supplier.
AISI	American Iron and Steel Institute.
SAE	Society of American Engineers.
SHPB	Split Hopkinson Pressure Bar.
USA	United States of America.
N	Nitrogen.
FEM	Finite Element Modelling.
FE	Finite Element.
$\bar{\sigma}$	Flow stress in tension/compression (MPa).
σ_1, n_1	Power-law model constants.
AISI H13	Chromium martensitic hot-work tool steel.
HY-100	Seawolf-class type submarine steel.
2D, 3D	Two dimensional, Three dimensional.
$\bar{\tau}$	Stress due to friction between tool and workpiece (MPa).
$\bar{\tau}_f$	Stress due to friction in the sticking zone (MPa).
$\dot{\varepsilon}_{ij}^{p}$	Plastic strain rate tensor generic component.
σ_{ij}	Stress tensor generic component.
β_1	Flow law internal variable.
T	Temperature (ºC), (K).
∂	Partial derivative operator.
$g_{ij}(\sigma_{ij}, T, \beta_1)$	Flow law generic tensor component.
$g(\sigma_{ij}, T, \beta_1)$	Flow potential (scalar function).
$\phi(\sigma_{ij}, T, \beta_1)$	Positive scalar function.
J_1, J_2	First and second stress deviator invariants.
S_{ij}	Deviatoric stress tensor generic component.
δ_{ij}	Kronecker delta.
Ω	General flow potential.
c_i	Scalar.
f	Yield function/criterion that defines the yield surface's boundary.
$\dot{\bar{\varepsilon}}^{p}$	Equivalent (or effective) plastic strain rate.
f_i	Field variable.
$\bar{\sigma}_0(\bar{\varepsilon}^{p}, T, f_i)$	Static [effective plastic strain/temperature/field variable dependent] yield stress (MPa) in tension/compression.

$D_a(T, f_i)$	Generic [temperature/field variable dependent] function.
$m_1(T, f_i)$	Generic [temperature/field variable dependent] parameter.
$\dot{\varepsilon}_{ij}^{e}$	Elastic strain rate tensor generic component.
$\dot{\varepsilon}_{ij}$	Strain rate tensor generic component.
S_{ijkl}	Elastic compliance tensor generic component.
ΔT	Temperature increment (K).
α_2	Thermal Expansion Coefficient (10^{-6}/K).
ν	Poisson's ratio (-).
E	Young's modulus (MPa).
$\bar{k}$	Flow stress in shear (MPa).
$\bar{\sigma}_q, \sigma_t$	Generic effective stress in tension/compression (MPa).
$\bar{k}_0(\bar{\varepsilon}^p, T, f_i)$	Static [effective plastic strain/temperature/field variable dependent] yield stress in shear (MPa).
$\bar{k}_q$	Generic effective stress in shear (MPa).
$\bar{\varepsilon}_y$	Generic effective plastic strain in tension/compression (-).
$\bar{\gamma}_y$	Generic effective plastic strain in shear (-).
n_2	Hardening law constant.
dt	Time differential for integration purposes (s).
JC	Johnson-Cook.
OFHC	Oxygen-free high thermal conductivity copper.
A, B, C, n, m	Johnson-Cook viscoplastic model constants.
$\dot{\bar{\varepsilon}}_0$	Reference strain rate in tension/compression (s^{-1}).
$\dot{\bar{\gamma}}_0$	Reference strain rate in shear (s^{-1}).
T_r	Reference (ambient) temperature (293K).
T_m	Melting temperature (ºC), (K).
MTS	Mechanical Threshold Stress.
$\hat{\sigma}$	Flow stress at $T = 0K$ (known as the Mechanical Threshold Stress).
$\hat{\sigma}_a \equiv \sigma_a$	Temperature independent stress component (MPa).
$\hat{\sigma}_i$	Structure parameter (MPa).
$\hat{\sigma}_e$	Term that characterises rate dependent processes (MPa).
s, s_i, s_e	Fitting parameters (also known as scaling factors).
$g_0, g_{0i}, g_{0e}, g_{es0}$	Normalised activation energies.
μ	Shear modulus (MPa).
b	Magnitude of the Burgers vector (m).
k	Boltzman's constant (J/K).
p, q, p_i, q_i, p_e, q_e	Mechanical Threshold Stress model constants.
μ_0	Shear modulus at $T = 0K$ (MPa).
n_3	Constant value to account for a more complex expression of the flow stress in the MTS constitutive model.
θ	Structure evolution (internal hardening rate).
θ_h	Strain hardening (due dislocation accumulation) term.
θ_r	Dynamic recovery (due to dislocation annihilation) term.
α_i	Fitting constant.
θ_0	Experimental strain hardening rate parameter.
$\hat{\sigma}_{es}$	Saturation stress (MPa).
$\hat{\sigma}_{es0}$	Constant stress value in the MTS constitutive model (MPa).
$\dot{\varepsilon}_{es0}, \dot{\bar{\varepsilon}}_{0i}, \dot{\bar{\varepsilon}}_{0e}$	Constant strain rate values in the MTS constitutive model (s^{-1}).
UMAT	User defined material subroutine for ABAQUS/Standard analyses.

VUMAT	User defined material subroutine for ABAQUS/Explicit analyses.
DEPVAR	Internal state variable/s to be defined (VUMAT).
stressNew	Stress tensor component to be updated (VUMAT).
stateNew	State variable to be updated (VUMAT).
nprops	Quantity of state variables associated with a material (VUMAT).
nblock	Number of material points to be processed (VUMAT).
ndir	Number of direct components in the stress tensor (VUMAT).
nshr	Number of indirect components in the stress tensor (VUMAT).
nstatev	Number of user defined state variables (VUMAT).
enerInternNew	Internal specific energy at each material point to be updated (VUMAT).
enerInelasNew	Dissipated specific energy at each material point to be updated (VUMAT).
SDV	State-dependent variable (VUMAT).
x, y, z	Spatial coordinates.
XC,YC,ZC	Generic coordinates in three-dimensional space.
t	Temporal coordinate, time (s).
ALE	Arbitrary Lagrangian Eulerian.
AR	Adaptive Remeshing.
lc	Sliding region theoretical length (mm).
lp	Sticking region theoretical length (mm).
k_{chip}	Average value of the shear flow stress (MPa).
μ_p	Coefficient of friction (-).
$\bar{\sigma}_n$	Normal stress (MPa).
AISI P20	Low carbon mould steel.
HRc	Rockwell C Hardness.
TCC	Thermal Contact Conductance (kW/m^{2}K).
$\varepsilon_1^p, \varepsilon_2^p, \varepsilon_3^p$	Principal plastic strain tensor components.
$\bar{\varepsilon}_{max}^p$	Maximum effective plastic strain (-).
SAE 4340	High tensile alloy steel.
D	Level of damage in a finite element (it varies from 0 to 1).
$\Delta\bar{\varepsilon}^p$	Effective plastic strain increment (-).
$\overline{\varepsilon}_{max}^p$	Effective plastic strain corresponding to onset of damage (-).
d_1, d_2, d_3, d_4, d_5	Johnson-Cook damage model constants.
σ_{hyd}	Hydrostatic (volumetric) stress (MPa).
CL	Cockcroft-Latham.
C_1	Accumulated specific energy constant (J/m^3).
$d\bar{\varepsilon}^p$	Effective plastic strain differential for integration purposes (-).
σ_1	Maximum principal stress (MPa).
RWM	Rittel-Wang-Merzer
W	Accumulated [elastic and plastic] specific energy (J/m^3).
W_{crit}	Critical [elastic and plastic] specific energy (J/m^3).
$d\varepsilon_{ij}$	Strain differential for integration purposes.
$\bar{\sigma}'$	Deteriorated flow stress due to damage (MPa).
a	Constant used in the RWM model for softening/damage purposes.
W_{frac}	Fracture specific energy (J/m^3).
SI	Surface Integrity.
AISI 52100	High chromium, high carbon bearing steel.
CBN, PCBN	Cubic Boron Nitride, Polycrystalline Cubic Boron Nitride.
MC	Mixed Ceramic.
AISI D2	Air hardening, high carbon, high chromium tool steel.

SEM, EBSD	Scanning Electron Microscopy, Electron Backscatter Diffraction.
DRX	Dynamic Recrystallisation.
ASB	Adiabatic Shear Bands/Banding.
HF	Hydrofluoric acid.
Ni	Nickel.
H	Hydrogen.
O	Oxygen.
Cr	Chromium.
Fe	Iron.
Nb	Niobium.
Mo	Molybdenum.
Ti	Titanium.
Al	Aluminium.
C	Carbon.
V	Vanadium.
Co	Cobalt.
SiC	Silicon Carbide.
HCl	Hydrochloric acid.
$CuCl_2$	Copper Chloride.
BDMS	Bright Drawn Mild Steel.
PN	Part Number.
BOM	Bill Of Materials.
Le	Length (mm).
Di, di, Ø	Diameter (mm).
WEDM	Wire Electrical Discharge Machining.
k_1	Value used to calculate the constants of the JC material model.
Ω_{L-B}	General flow potential proposed by Lubarda and Benson (2002).
Ω_{A-L}	General flow potential proposed by Asaro and Lubarda (2006).
K	Bulk modulus (MPa).
λ	Lame's constant.
p_{ij}	Volumetric stress tensor generic component.
$\Delta\varepsilon_{ij}^{p}$	Incremental plastic strain rate tensor generic component (-).
ΔS_{ij}	Incremental deviatoric stress tensor generic component.
$\Delta\varepsilon_{ij}^{e}$	Incremental elastic strain tensor generic component.
Δt	Incremental time (s).
S_{ij}^{0}	Deviatoric stress tensor generic component at a time t.
$\varepsilon_{ij}^{e}\big\vert_{t}$	Elastic stress tensor generic component at a time t.
H	Hardening parameter.
f_a, f'_a	Generic function and its first ordinary derivative.
c_p	Generic term defined for simplification purposes in the Newton's method.
$\overline{\sigma}_C$	Von Mises stress calculated at the current time step.
$\Delta\overline{\varepsilon}_0^{p}$	Initial effective plastic increment for iteration purposes (-).
c_p	Parameter used to update the current plastic strain increment.
$\left[S_{ij}\right]_{new}$	Deviatoric stress tensor component at the end of the increment.
$\overline{\sigma}_{new}$	Flow stress at the end of the increment.
$\left[S_{ij}\right]_{old}$	Deviatoric stress tensor component at the beginning of the increment.
$\left[\sigma_{ij}\right]_{new}$	Stress tensor component at the end of the increment.

$[\sigma_{ij}]_{old}$	Stress tensor component at the beginning of the increment.
$[p_{ij}]_{new}$	Volumetric stress tensor component at the end of the increment.
B_1	Independent term for fitting purposes.
U	Internal specific energy (J/m^3).
ρ_o	Density (kg/m^3).
U_{new}	Specific internal energy at the end of the increment (J/m^3).
U_{old}	Specific internal specific energy at the beginning of the increment (J/m^3).
U^p_{new}	Specific dissipated plastic energy at the end of the increment (J/m^3).
U^p_{old}	Specific dissipated plastic energy at the beginning of the increment (J/m^3).
Z	Zener-Hollomon parameter.
Q	Activation energy per mole (J/mol).
R	Universal gas constant (K^{-1}).
ΔG	Activation energy (J).
W_R	Specific energy corresponding to onset of recrystallisation (J/m^3).
k_W	Value adopted to trigger dynamic recrystallisation ($0 < k_W < 1$).
ρ	Average dislocation density (m^{-2}).
σ_0	Effective stress value to relate dislocation density to flow stress (MPa).
α_1	Constant value to relate dislocation density to flow stress.
K_d, K_z	Positive constants to calculate grain size according to Park et al. (2001).
K_a, K_b	Fitting constants used to relate the dislocation density to the plastic strain.
$h(\bar{\varepsilon}^p, \rho)$	Proposed law representing softening due to dynamic recrystallisation.
k_a, k_b, k_c, k_d	Constants added to the 'new' evolution law $d\hat{\sigma}_e(\bar{\varepsilon}^p)/d\bar{\varepsilon}^p$.
K_g	General constant used in the term $h(\bar{\varepsilon}^p, \rho)$.
K_1, K_2, K_3, K_4, K_5	Constants to compute for the 'new' evolution law of the MTS model.
d	Average grain size (mm).
d_{ini}	Initial grain size (mm).
h_1, h_2	Fitting constants to calculate grain size due to machining.
$\bar{\sigma}_{max}$	Flow stress corresponding to onset of damage (MPa).
$\bar{\varepsilon}^p_{ecrit}$	Effective plastic strain corresponding to onset of recrystallisation (-).
k_E	Parameter that relates the energy calculated in tensor fashion from the RWM model and that under the plastic stress-strain curve.
U^p_1, U^p_2, U^p_3	Specific dissipated plastic energies calculated in specific regions of the plastic stress-strain curve (J/m^3).

CHAPTER 1

INTRODUCTION

1.1 Background to the project and research motivation

In general, investigations pertaining to material removal processes and in particular those related to conventional machining have largely been experimentally-based. Although relatively straightforward to implement and able to provide quantitative as well as empirical results, experimental machining research is expensive and time-consuming, especially when involving advanced aerospace workpiece materials such as Ti-6Al-4V and Inconel 718. These alloys are generally utilised in jet engines and due to their favourable mechanical attributes have brought the aerospace industry to a safer and more reliable level of confidence than in the past. Therefore their relevance as materials competent enough to satisfy mechanical and thermal requirements in the most extreme in-service conditions cannot be neglected and as such, have been a matter of intense examination.

From an industrial point of view, research is of tremendous importance as the manufacturing, in particular machining, of aerospace components plays a critical role in their subsequent reliability to operate under the aforementioned demanding conditions. However conducting extensive cutting experiments in industry is also a path that brings along not only excessive costs and elevated analysis time, but also restrictions when trying to investigate critical tool and workpiece areas as well as mechanisms that affect the performance of the manufactured components.

In consequence, the search for an alternative less resource intensive and costly to study metal cutting operations has directed the scientific/industrial community to the employment of numerical approaches, which have also had the advantage of being able to shed light on important issues as never before. In this regard, the finite element (FE) method has been the preferred choice utilised by researchers (since the 1970's) in a computational

framework, due to its powerful mathematical and physical formulation to provide trustable results in countless situations. Taking into account these benefits over purely experimental work, it was decided to continue this line of thought and investigate with more detail the cutting process by utilising the FE method.

Despite extensive work and development over the past 40 years, a definitive constitutive model able to characterise workpiece material viscoplastic response as well as an appropriate criterion to simulate chip formation/morphology under machining conditions, remains elusive. Although frictional effects between the workpiece and tool are of vital importance and yet to be fully understood, a proper constitutive model is mandatory as it commands exclusively all subsequent FE outputs (e.g. stresses), including those due to friction. With this in mind therefore, attention was initially paid to constitutive modelling while friction was left as an issue to investigate later. Nevertheless, many FE models have been developed over the past decade relating to the cutting of aerospace alloys such as Ti-6Al-4V and Inconel 718 which provide reasonable predictions of cutting force and workpiece/tool temperature.

The lack of appropriate material flow data (e.g. at low/high strain rates and temperatures) and insufficient consideration of variables in current constitutive relationships have made the simulation of workpiece surface integrity parameters such as microstructural alterations, microhardness variations and ultimately fatigue performance following machining less successful. This problem, together with the concern of working with a robust constitutive model, has in consequence formed the basis for the present work, whose goals are described in the following section.

1.2 Aims and objectives of the work

In order to address the relevant issues mentioned above, the overall aim of the research work was to improve the capability of finite element simulations in order to predict workpiece surface integrity following the orthogonal machining of advanced aerospace materials. Specific objectives were:

– Initial assessment of different 2D/3D modelling strategies incorporating workpiece/tool thermal properties when orthogonally turning Ti-6Al-4V together with identification of suitable constitutive/damage models.

– Design and manufacture of a Split Hopkinson Pressure Bar testing apparatus to generate elevated strain rate/temperature flow stress data for Inconel 718 as input to determine material variables for the physical-based Mechanical Threshold Stress model as an alternative to the empirical Johnson-Cook relationship.

– The formulation of 2D and 3D fully coupled thermo-mechanical FE models to simulate the orthogonal turning of Inconel 718 characterised by physical-based and empirical constitutive models as well as an energy-based criterion (as opposed to those relying on simple fracture criteria), for the prediction of chip formation/morphology.

– The development of a bespoke mathematical model to predict dynamic recrystallisation of workpiece microstructure when orthogonally turning Inconel 718.

– Experimental validation of both 2D and 3D thermo-mechanical FE models when machining Ti-6Al-4V and Inconel 718 in terms of cutting forces and chip dimensions/size, in addition to cutting temperatures, white layer thickness and grain size distribution for the latter.

1.3 Thesis structure

Chapter 2 initially outlines the metallurgical/mechanical/thermal properties of Ti-6Al-4V and Inconel 718 alloys and their machinability aspects. A thorough revision of the analytical/mechanistic and temperature models intended to portray orthogonal cutting is provided, followed by highlighting the key features of high strain rate/temperature testing by means of the Split Hopkinson Pressure Bar machine and advances made/techniques employed since the 1970's when using the FE method to simulate the process. Finally, surface integrity and (dynamic) recrystallisation principal concepts are presented to enable a concluding constructive discussion based on previous findings of the literature review.

Chapter 3 describes the cutting trials performed on Ti-6Al-4V and Inconel 718 for validation purposes and the procedures carried out for metallurgical/surface integrity analysis. The experimental generation of high strain rate/temperature flow stress data for Inconel 718 with the Split Hopkinson Pressure Bar apparatus is delineated and guidelines/best practices when designing the testing machine are provided.

Chapter 4 deals with the development of 2D/3D FE models to simulate orthogonal machining of Ti-6Al-4V and Inconel 718, including a variety of situations which make use of

the Johnson-Cook/Mechanical Threshold Stress material models in conjunction with damage criteria such as Cockcroft-Latham and Rittel-Wang-Merzer. Damage values as well as the method to calculate the constants corresponding to both constitutive models (based on previous low and high strain rate/temperature flow stress data) for Inconel 718 are presented. Predicted plastic stress-strain curves are compared to those obtained experimentally. The subsequent development of a user subroutine VUMAT to characterise material and damage behaviours is shown by deriving the explicit rate equations. Last but certainly not least, a bespoke mathematical model to predict workpiece material grain refinement (due to dynamic recrystallisation) linked to the Mechanical Threshold Stress and Rittel-Wang-Merzer models is outlined and discussed.

Chapter 5 details numerical predictions in terms of cutting forces, workpiece/tool temperature, chip morphology (including a detailed comparison between chip peak, valley and pitch estimations and their experimental counterparts) when machining Ti-6Al-4V and Inconel 718 at various cutting speeds and feeds. A critical assessment of all the initial FE simulations as well as those incorporating the module to predict workpiece grain refinement of Inconel 718 against exhaustive experimental evidence is made and results are critically discussed. The energy-based Rittel-Wang-Merzer damage model is finally analysed as a plausible criterion to trigger adiabatic shear banding to produce chip serration without the need for making use of arbitrary techniques/assumptions.

Chapter 6 provides relevant conclusions derived from the research activity by summarising the experimental and FE modelling findings while Chapter 7 concludes the investigation by making suggestions for future work. Chapter 8 contains the literature review references and the Appendices are intended to show additional information related to the work (e.g Split Hopkinson Pressure Bar design guidelines and drawings, numerical validation of VUMAT subroutines, etc.).

CHAPTER 2

LITERATURE REVIEW

2.1 Aerospace alloys

2.1.1 Introduction

Materials employed in high-performance applications such as those encountered in the aerospace industry are typically required to withstand severe operating conditions, usually over extended periods of time under fluctuating loading.

Titanium-based alloys are among some of the most widely used in aeroengine parts due to their favourable attributes including corrosion resistance, high strength to weight ratio (density of 4,430kg/m^3) and good mechanical toughness. The majority of titanium alloys (with the exception of gamma titanium aluminide intermetallics) however are generally limited to operating in moderate service temperatures (~<350ºC). This in consequence precludes their utilisation in the hotter sections of gas turbine engines where temperatures approach 1,100ºC. Here, superalloys (term used to represent those materials capable of maintaining their strength at elevated temperatures) are used due to their ability to operate at elevated temperatures and pressures. Other key properties include outstanding hot corrosion and oxidation resistance together with good fatigue and creep characteristics.

The developments in superalloys have been extensive, with over 100 different compositions listed by Reed (2006), which are categorised into three main groups based on the major constituent namely iron, chromium or nickel. The great majority of aeroengine components are made from nickel-based superalloys.

2.1.2 Titanium based alloy - Ti-6Al-4V

2.1.2.1 Metallurgical and mechanical properties

Generally utilised in wrought form (rather than cast) in the aerospace industry, annealed Ti-6Al-4V alloy (1hr at ~700ºC then furnace cooling) typically consists of two coexisting equiaxed-like alpha and beta phases. The former is relatively soft and comparable to that in commercially pure titanium, however the addition of stabilising compounds such as aluminium serves to increase its strength. The beta phase provides the high temperature properties of the alloy, with stabilisation at ambient temperature accomplished by the addition of adequate quantities of vanadium (>15wt.%), molybdenum and iron. When further strengthening of the alloy is required, an appropriate solution treatment (1hr at ~960ºC) followed by a quenching procedure can be performed, which produces a mixed alpha′-martensite, alpha-alpha′or alpha-alpha″ microstructure, depending on the temperature used (Welsch et al., 2003). Subsequent ageing is then usually conducted in order to relieve the residual stresses produced by the previous quenching operation, and thus increase the maximum strength level (MIL-HDBK-5J, 2003). The toughness of Ti-6Al-4V in its annealed condition can be maintained at temperatures as low as -200ºC whereas it can withstand temperatures up to ~400ºC without any significant loss of ductility (Welsch et al., 2003). Moreover, the alpha and beta phases provide the alloy with good corrosion/creep/crack growth resistance in conjunction with a fracture toughness of 510MPa/$\sqrt{\text{in}}$ (Salem et al., 2008). The typical chemical composition of the Ti-6Al-4V according to Boivineau et al. (2006) is given in Table 1:

Element	Al	C	Fe	H	N	O	V	Ti
Composition (mass%)	6	0.1	0.4	0.015	0.05	0.2	3.5–4.5	Balance

Table 1. Conventional chemical composition of annealed Ti-6Al-4V alloy.

2.1.2.2 Machinability aspects

With a yield strength varying from 760 to 895MPa in its annealed state at ambient temperature, Ti-6Al-4V generally has favourable formability characteristics, either at ambient or elevated temperatures. However the turning/orthogonal machining of Ti-6Al-4V alloy is somewhat more challenging due to its low diffusivity and thermal conductivity (~7.2W/mK)

which can lead, depending on the operating parameters, to cutting temperatures as high as ~1,000ºC (Ozel et al., 2010). This can consequently have a detrimental impact on the mechanical properties of the workpiece material. Furthermore, Ti-6Al-4V has a strong affinity to react chemically at elevated temperatures with almost all cutting tool materials and coatings thereby accelerating wear produced by solution and oxidation mechanisms resulting in a decrease in tool life (Rao et al., 2011). Nevertheless, tungsten carbide (WC/Co) cutting tools remain as the most used when machining Ti-6Al-4V alloy due to their superior performance when compared to others, such as ceramics (Ezugwu and Wang, 1997).

2.1.2.3 General applications

Although the use of Ti-6Al-4V alloy (developed in the 1950's) was initially focused on compressor blades for gas turbine engines, its range of application has been extended to include turbine blades and discs, wheels, casings, etc., as well as airframe components. Moreover, the employment of Ti-6Al-4V can be expanded to the automotive (valves, drive shafts, suspension springs, etc.), chemical, medical (for hip, knee implants) and naval industries (propulsion valves, combat equipment, etc.), due to its versatility combined with enhanced superplastic forming features (Welsch et al., 2003); approximately accounting for 50% (in terms of weight) of all titanium used worldwide.

2.1.3 Nickel-based superalloy - Inconel 718

2.1.3.1 Metallurgical and mechanical properties

In general, most nickel-based superalloys consist of a γ matrix (fcc phase) of nickel which contains solid-solution elements including cobalt, iron, ruthenium, molybdenum, rhenium, tungsten and chromium. Nickel is the main constituent accounting for ~50wt.%, with large amounts of Cr to increase the corrosion resistance of the superalloy (Reed, 2006). The addition of aluminium and titanium provokes the precipitation of the main strengthening phase γ' (fcc structure), due to their affinity with nickel to form compounds like Ni_3Al and Ni_3Ti, that enhance high temperature strength and creep properties (Donachie and Donachie, 2002). A secondary strengthening phase γ'' is also usually present in nickel-based superalloys due to the presence of niobium which forms a Ni_3Nb composition. Both the γ' and γ'' phases augment the strength of the material as they precipitate coherently resulting in a considerable

lattice mismatch. Carbides, borides and topologically close-packed (tcp) phases may also appear when over-ageing the superalloy (an incoherent orthorhombic δ phase is also likely to appear in this condition, but with negligible influence on material strengthening).

Inconel 718, which contains high levels of iron and chromium (~20%), is one of the most widely utilised nickel-based superalloys in aeroengines and is generally supplied in two mechanical/metallurgical conditions: solid-solution (annealed) and precipitation hardened (aged) (Donachie and Donachie, 2002). While low levels of strengthening phases are present in the annealed state, the alloying elements are dissolved in the matrix, which is a necessary condition for proper precipitation during the ageing treatment. The precipitation hardened state (which produces a typical hardness value of ~44HRc) has the highest mechanical properties with both the γ' and γ'' phases coexisting as coherent strengthening precipitates and is capable of maintaining its yield strength (~1,200MPa) up to ~650ºC, as well as its ductility and toughness down to -40ºC (De Mange et al., 2009; Slama and Abdellaoui, 2000). The general composition of Inconel 718 is shown in Table 2:

Nickel (plus Cobalt)	50.00-55.00
Chromium	17.00-21.00
Iron	Balance*
Niobium (plus Tantalum)	4.75-5.50
Molybdenum	2.80-3.30
Titanium	0.65-1.15
Aluminum	0.20-0.80
Cobalt	1.00 max.
Carbon	0.08 max.
Manganese	0.35 max.
Silicon	0.35 max.
Phosphorus	0.015 max.
Sulfur	0.015 max.
Boron	0.006 max.
Copper	0.30 max.

Table 2. Typical chemical composition of Inconel 718 superalloy, which conforms to AMS specifications (Special Metals, 2007). *It can include trace quantities of alternate elements.

The microstructure of Inconel 718 which has been precipitation hardened is primarily characterised by the γ''precipitate (the volume fraction of γ'' to γ' is at a ratio of 4:1 according to Chaturvedi and Han (1983) and Slama and Abdellaoui (2000), which is the principal strengthening mechanism and exhibits a disc-shaped morphology while the γ' is generally spherical, as shown in Figure 1:

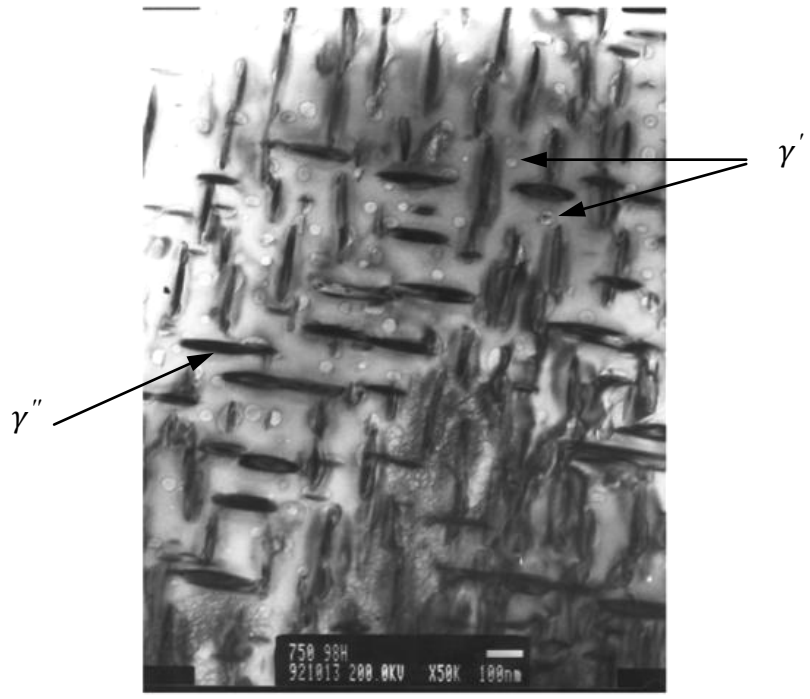

Figure 1. Microstructure of Inconel 718 showing γ' (spherical) and γ'' (disc-shaped) phases following ageing at 750ºC for 100hs, according to Slama and Abdellaoui (2000).

2.1.3.2 Machinability aspects

Inconel 718 superalloy in the solution treated and aged condition is generally regarded as a difficult-to-cut material. Tool life is typically low with wear triggered by mechanisms such as workpiece adhesion and welding. Wear due to abrasion is also likely to occur, which results from the fluctuating contact between hard particles of the workpiece material (such as primary carbides NbC and TiC) and the cutting tool (Kitagawa et al., 1997). Furthermore, the significant amounts of plastic deformation and heat generated (the latter in part due to the material's low thermal conductivity, ~11.4W/mK) during machining can compromise workpiece properties and fatigue performance (Devillez et al., 2007). The relatively poor machinability is characterised by high cutting forces and high temperatures in general (~900ºC when operating at 30m/min and up to 1,300ºC at speeds of ~300m/min as encountered by Sharman et al., 2006), which in consequence necessitates the selection of appropriate tools and cutting parameters. When cutting with carbide tools (even in dry conditions) at relatively low cutting speeds such as 40-60m/min, temperatures might not exceed 650ºC, however rapid tool wear occurs mainly due to abrasion and microchipping (Thakur et al., 2009).

2.1.3.3 General applications

The main application area for Inconel 718 superalloy is in the aerospace industry, particularly for the fabrication of components in gas turbines, rocket engines and heat exchangers (Reed, 2006). In the hot regions of aircraft jet engines such as the combustor and turbine sections, ~50% of their total weight is attributed to the use of Inconel 718 (Pollock and Tin, 2006). Other major applications include power generation systems in the oil and gas business (e.g. sealant rings of perforating guns) together with parts for nuclear reactors and chemical processing plants.

2.2 Theory of the metal cutting process

2.2.1 Introduction

The first machine tools for mechanical metal cutting were developed in the 18th century, and were primarily employed for removing material from a (cylindrical in most of the cases) rotating workpiece. The process widely known as turning involves a cutting tool fed parallel to the longitudinal axis of a bar similar to that shown in Figure 2, although the tool path can vary to generate different features on the part.

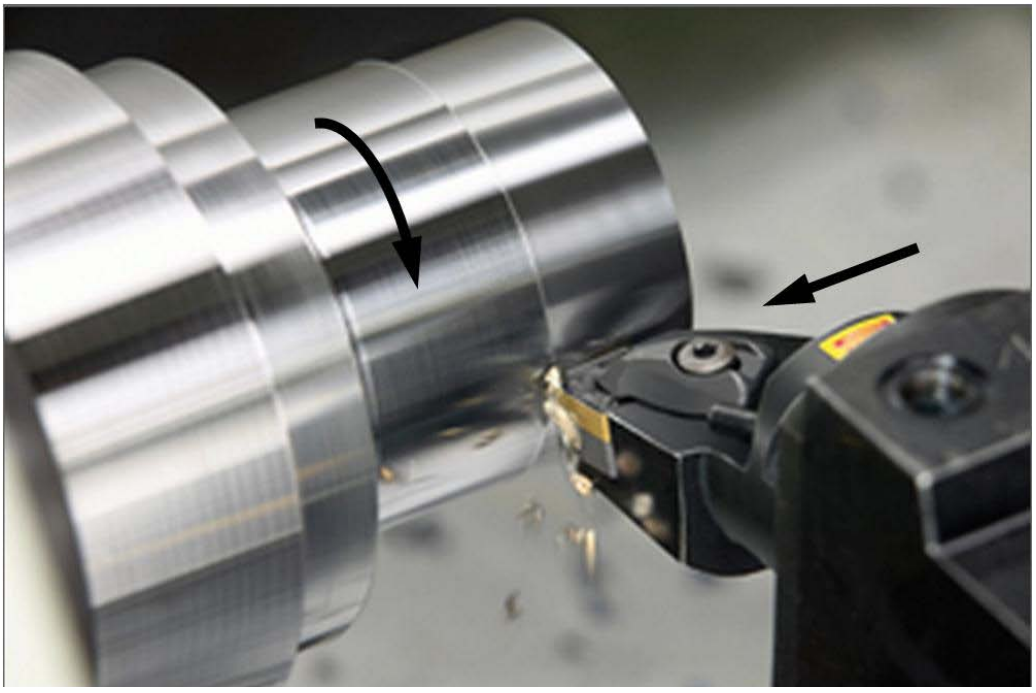

Figure 2. Generalised turning operation (SANDVIK Coromant AB, 2011).

Irrespective of tool geometry and cutting conditions, the forces associated with the process can be resolved into three main components, as shown schematically in Figure 3, which are:

- Cutting force F_c: acts on the tool rake face and perpendicular to its cutting edge, it is generally the largest force component,
- Feed force F_t: this component acts in the direction of tool feed,
- Thrust or radial force F_p: acts in the radial direction of the workpiece. Typically has the lowest magnitude compared to the other forces.

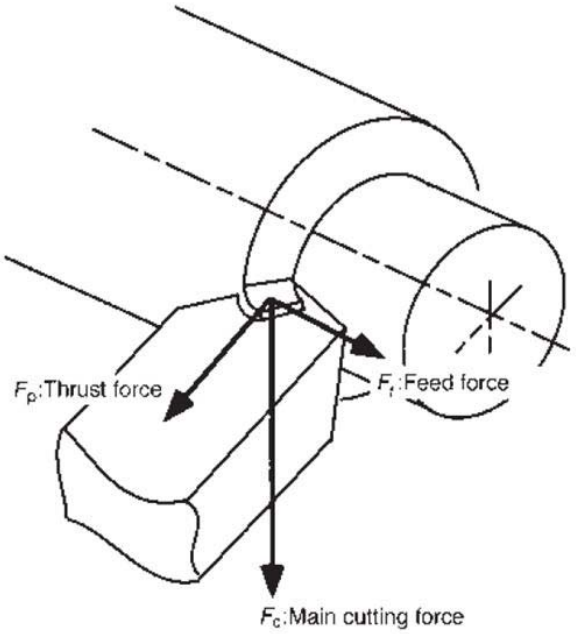

Figure 3. Primary cutting force components in turning (Childs et al., 2000).

When the tool cutting edge is aligned perpendicular to the feed direction, the operation is described as orthogonal turning/cutting. In this situation, the process can be represented as a two-dimensional or plane strain configuration, which has formed the foundation of studies in developing the theory and mechanics of metal cutting. The following section details the literature on analytical and mathematical models for describing the chip formation process and prediction of various response factors.

2.2.2 Analytical/mechanistic models

Early investigations of the cutting process identified that the chip was formed by shearing (Thime, 1870), however the conclusions were derived primarily from experimental

observations but without any mathematical basis to describe the mechanics of the process. The first attempts to analytically study the metal machining operation can be traced back to the 1890's, when Russian scientists proposed the notion of a 'shear plane' to describe chip formation (Zvoryking, 1896; Briks, 1896). However, as their work was little known to researchers in Europe and the USA until the 1930's where a handful began to publish their studies, little improvements on the field had been consummated.

It is generally regarded that the contemporary study of the metal cutting process started with the work of Piispanen (1937). The author focused his analysis on the orthogonal machining operation and developed mathematical expressions to describe continuous chip formation, which was comprised of thin lamellas formed through a shear mechanism (without built-up edge) and is shown schematically in Figure 4:

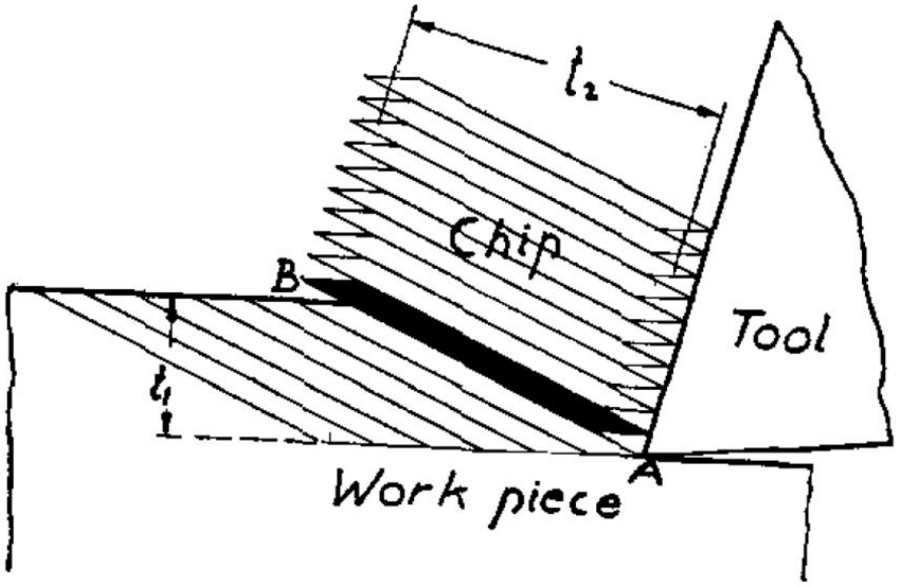

Figure 4. Initial chip formation scheme represented as a series of thin lamellas, according to Piispanen (1937).

The work was immediately followed by Ernst (1938), who presented a qualitative discussion of the process mechanics. A subsequent, more complete investigation involving a mathematical approach which re-introduced the concept of shear plane was undertaken by Ernst and Merchant (1941). By assuming plane strain conditions, the authors postulated that separation of the workpiece material and hence chip formation occurred due to high stresses which acted along the shear plane, see Figure 5:

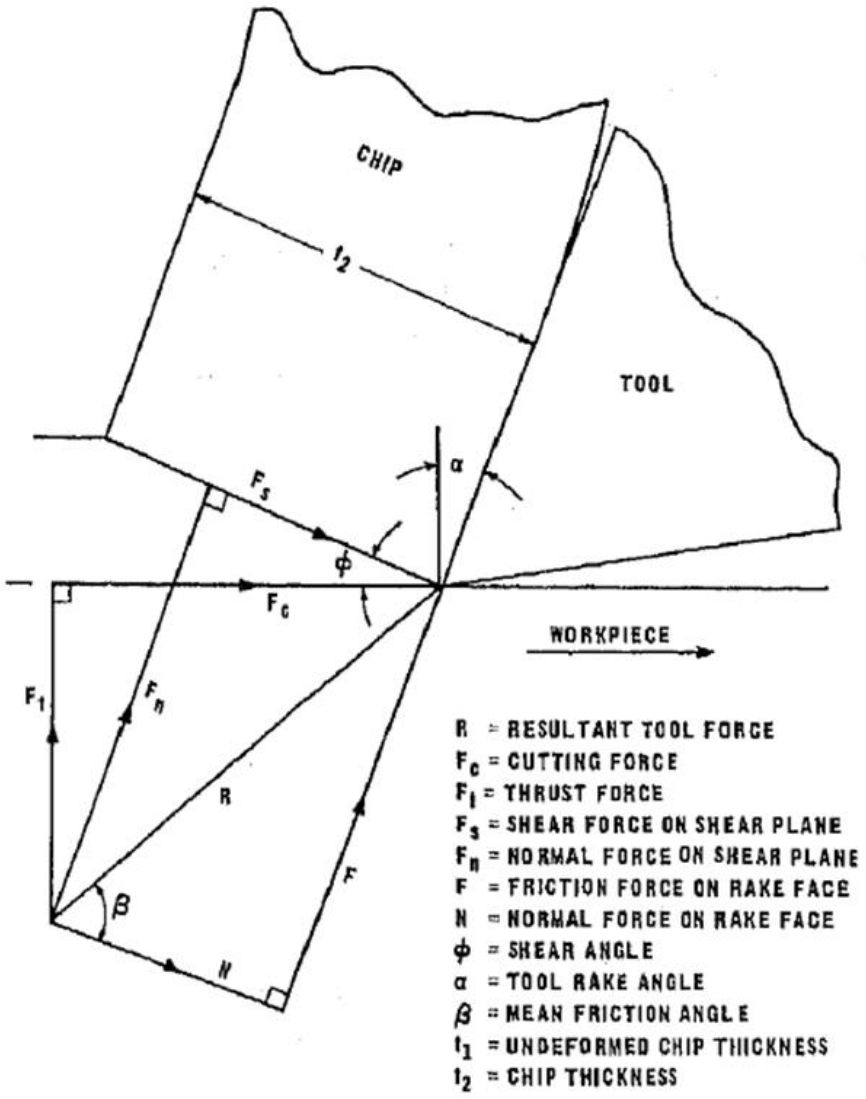

Figure 5. Shear plane model and force diagram developed by Ernst and Merchant (1941).

The study also led to the definition of a force system that could predict the optimum shear angle assuming that the work done was a minimum, which obeyed the following expression:

$$2\varphi + \beta - \alpha = 90° \quad (1)$$

where φ, β and α are the shear, mean friction and tool rake angles respectively. Similarly, Merchant (1944) investigated in detail the basics of the orthogonal and oblique cutting processes by assuming sharp tools in both cases, and found for the former case a similar relationship for the shear angle, with the difference that he minimised the shear strain instead (as opposed to the work done), to obtain the following:

$$2\varphi - \alpha = 90° \quad (2)$$

To improve the shear plane model, Merchant (1945) extended the analysis by assuming that the shear stress S_A acting on the shear plane was influenced by the normal stress S_n, according to Eq. (3):

$$S_A = S_0 + k_s S_n \tag{3}$$

where S_0 and k_s are material constants. This led to a modified form for the shear angle relationship which was:

$$2\varphi + \beta - \alpha = C_s \tag{4}$$

where $C_s = cot^{-1} k_s$ is a machining constant that has different values depending on the cutting conditions. However, the model had several shortcomings, not least that the shear plane model was geometrically-based with no reference to any physical laws. In addition, the effects of plastic strain, shear rate and the resulting temperature rise on the shear plane were not considered.

Later studies aimed at resolving the problems associated with the shear plane model were presented by Lee and Shaffer (1951), who were the first to apply plasticity theory to the orthogonal machining problem, however still assuming plane strain conditions. The authors initially considered the chip as a rigid moving body and proposed slip-line models that accounted for situations where built-up edge was either generated at the tool tip or otherwise, see Figure 6:

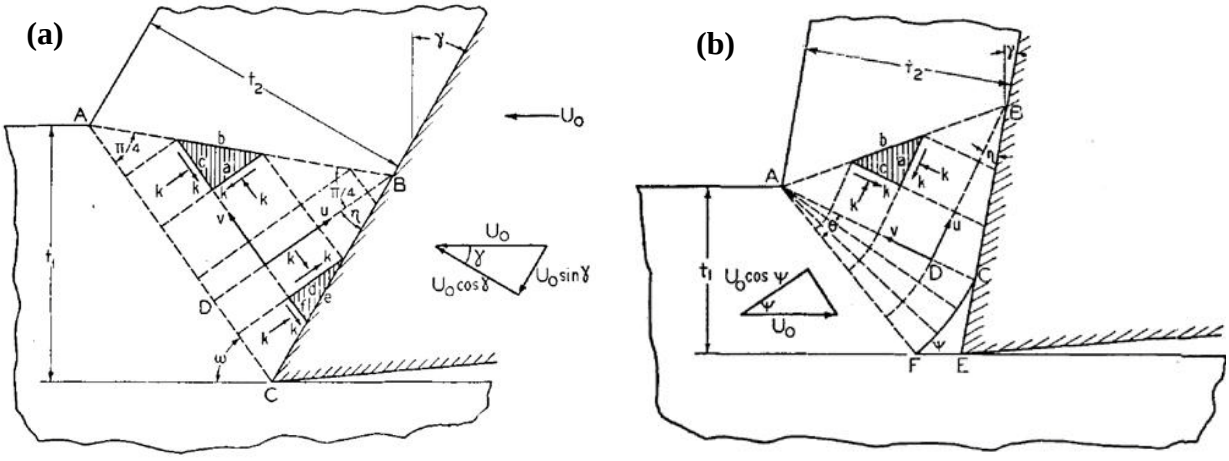

Figure 6. (a) Slip-line model for a blunt tool, (b) Slip-line model for a tool including built-up edge, according to Lee and Shaffer (1951).

For the case without built-up edge, the expression for the shear angle according to the slip-line model was:

$$\varphi + \beta - \alpha = 45° \tag{5}$$

However, the application of the slip-line theory for modelling the cutting process had limited success, due to the difficulties in applying boundary conditions on the free surface of the workpiece and chip.

Shaw et al. (1953) critically debated the assumptions used in the development of the shear plane model together with the associated analytical solutions, by arguing that friction between chip and tool played a significant role in the cutting process and should not be neglected. The authors examined the influence of friction at the tool-chip interface and arrived at the conclusion that the maximum shear stresses were not located along the shear plane, but instead acted at an angle, in contradiction with previous investigations.

From a rigorous mathematical point of view, Hill (1954) highlighted the various deficiencies both the shear plane and slip-line models had, by suggesting that they were focused on determining a single solution (a single shear plane angle) to the orthogonal cutting problem, whereas in reality a range of solutions which depended on the initial conditions given by the tool rake and friction angles should have been considered. By excluding configurations of both angles that overstressed the workpiece material (that produced stress singularities), the author was able to identify such region of variation for the shear plane angle, proving that it could fluctuate instead of remaining immovable like it was assumed in earlier theories.

Further research on the frictional effects in machining was carried out by Takeyama and Usui (1958), who deduced that the coefficient of friction did not follow the usual Coulomb's law, but instead that of Ernst and Merchant (1940). In addition, their results showed that the tool-chip contact area influenced the shear plane angle, further reinforcing the notion that friction must be taken into account when analysing the cutting operation.

Subsequent work performed by Nakayama (1958), who used quick stop devices to examine in greater detail the mechanics of the orthogonal cutting process, proved the existence of a secondary deformation zone at the tool-chip interface, which was found to be roughly triangular in shape with a maximum strain rate value at the tool cutting edge, see Figure 7a:

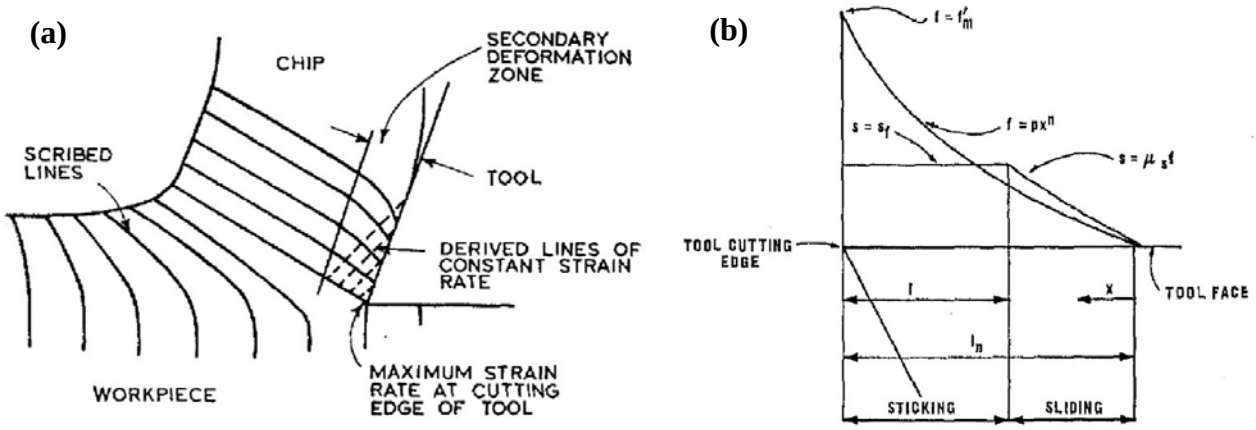

Figure 7. (a) Secondary deformation zone evidenced by Nakayama (1958), (b) Sticking and sliding zones encountered by Zorev (1958).

In parallel, Zorev (1958) identified two different frictional regions acting on the tool's rake face that affected the secondary shear zone, which were termed sticking and sliding friction respectively. Stresses due to friction were found to remain constant in the sticking zone, while in the sliding zone the coefficient of friction did so, see Figure 7b.

Palmer and Oxley (1959) highlighted that the slip-line theory could not account for the flow stress variations observed during machining as workpiece strain hardening was not considered in the theoretical approach. Experimental cutting trials performed on mild steel at low cutting speeds showed that the workpiece plastic deformation at the shear zone occurred over a quasi-triangular region rather than a single line shear plane as assumed in the model by Ernst and Merchant (1941), see Figure 8:

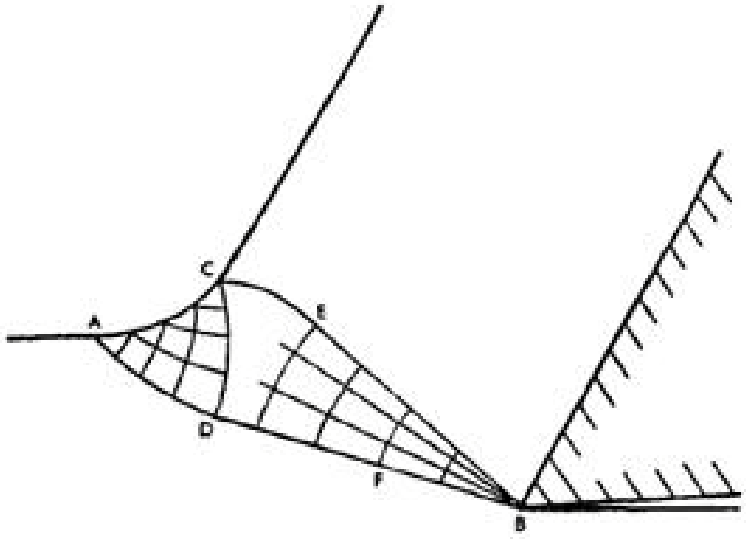

Figure 8. Idealised primary plastic deformation zone outlined by Palmer and Oxley (1959).

The incorporation of a strain hardening parameter in the analysis of the primary deformation zone by Palmer and Oxley (1959) improved the slip-line model and showed that hydrostatic stresses varied from compression at the chip free surface to tension at the adjacent tool cutting edge, however the distribution of stresses deviated from that predicted by conventional plasticity theory.

An alternative to slip-line filed solutions was proposed by Oxley and Welsh (1961), which involved representing the plastic deformation region (see Figure 9a) as a parallel-sided shear zone as shown in Figure 9b, where the edges CD and EF together with the centreline AB correspond to slip-lines for directions of maximum shear stresses. Here, a suitable value for the shear angle φ is selected so that the resultant cutting force direction is in line with that when the mean friction at the tool-chip interface is considered. By calculating φ for a range of cutting conditions, Oxley and Welsh (1961) found that the trends which estimated chip discontinuity at low cutting speeds and those accounting for a reduction in φ as cutting speeds decreased were validated by their experimental results.

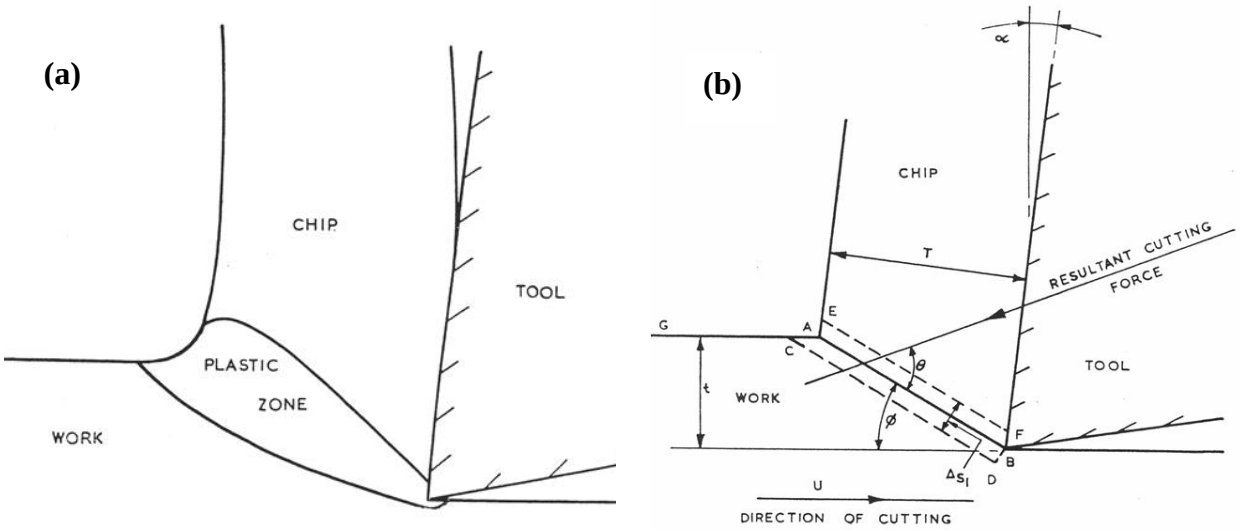

Figure 9. (a) Real deformation zone, (b) Parallel-sided deformation zone proposed by Oxley and Welsh (1961) to represent the real deformation zone.

Oxley and Hatton (1963) further extended the analysis by incorporating experimentally-based stress distributions in both the parallel shear zone and tool-chip interface although for the latter, the study simplified the curvilinear direct and shear stress distributions previously found by Usui and Takeyama (1960) and Zorev (1958) to a linear relationship, as detailed in Figure 10:

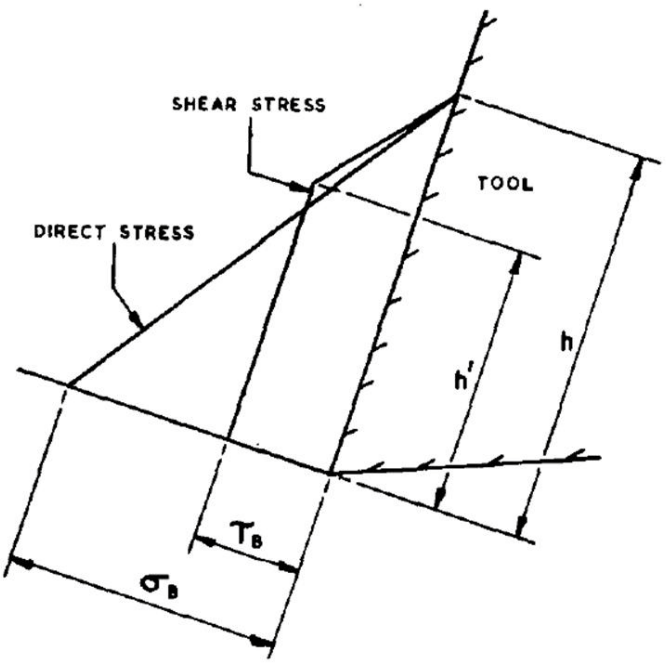

Figure 10. Simplification made by Oxley and Hatton (1963) to represent the sticking and sliding frictional regions in a linear fashion.

It was not until a few years later that Enahoro and Oxley (1966) included the interactions at the secondary deformation zone in their slip-line analysis of the orthogonal cutting process, although the effects of the sticking frictional region were neglected. Despite this, their model of chip flow showed good agreement with corresponding experimental observations. Other notable developments included the evaluation of strain rate effects on the contact interactions between the tool and chip (Fenton and Oxley, 1969) as well as modifications to the shear plane model introduced by Sweeney (1969). Fenton and Oxley (1970) further enhanced the parallel-sided shear model by including the effects the plastic strain, plastic strain rate and temperature, which was validated against orthogonal cutting experiments on SAE 1112 steel. The predicted chip morphology and thickness were found to be within ~5% of the experimental results.

A more exhaustive study was performed by Roth and Oxley (1971), who analysed the cutting process by applying the slip-line approach to analytically represent both the primary and secondary deformation zones together with experimental material input data. The slip-line model was employed for predicting the flow velocity and stresses and showed that the hydrostatic stresses varied from compression to tension along the boundary AB, as shown in Figure 11:

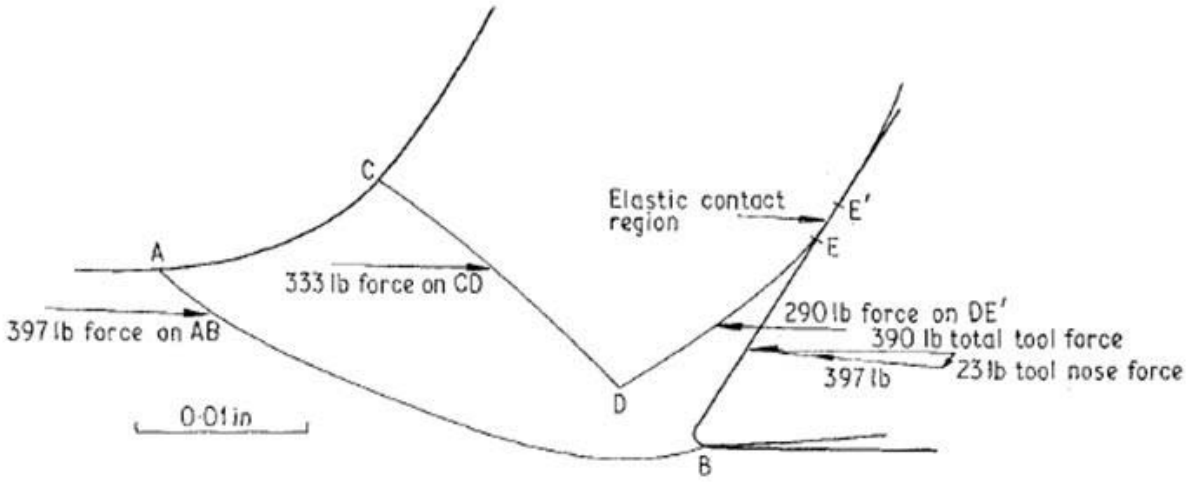

Figure 11. Slip-line model including both the primary and secondary deformation zones developed by Roth and Oxley (1971).

The boundary slip-lines CD and DE allowed the prediction of forces acting at various regions such as the tool-chip interface and tool tip. In the former, normal and hydrostatic forces were found to be compressive, while the force at the tool nose force was significant for depths of cut ~0.0254mm. The model however was only applicable at low cutting velocities implying that effects such as strain rate and temperature, which are usually high when machining, were neglected from the analysis.

Despite the substantial research in analytical modelling of the cutting operation, the complexity and overwhelmingly large number of factors which affect the process are such that it has been impossible to consider all combinations of parameters in a single analytical solution. Nevertheless, efforts have still been dedicated to the analytical modelling of the cutting process, with recent work published by Fang et al. (2001) who presented a universal slip-line model which accounted for chip features following 2D machining with restricted contact tools. It was shown that slip-line models previously developed by other researchers could be considered special cases of the universal one, which was able at the same time of providing a satisfactory explanation for the built-up edge effect. Fang and Jawahir (2002) expanded on this by validating the newly universal slip-line model against experimental evidence (with no recourse of empirical data as input) and achieved a reasonable agreement between them both. A summary of the latest advances in this area of investigation is given by Arrazola et al. (2013), however it has to be stressed that research on developing predictive capability for machining processes over the past three decades has primarily focused on computational based techniques (in particular the finite element method) and will be discussed later in this chapter.

2.2.3 Cutting temperature prediction models

The earliest investigation concerning the prediction of temperatures in machining was undertaken by Hahn (1951). The author theoretically calculated the temperatures in both the shear plane and chip by applying a classical mathematical approach and assumed that the shear plane was a moving oblique heat source through the workpiece. The length of the heat source was considered to be infinite. For high cutting speeds the model provided reliable predictions however at low speeds, the solution was inaccurate as conduction into the surrounding material accounted for the majority of heat being transferred from the source. Furthermore, the model failed to consider the change in direction of the chip after passing through the shear plane.

A later study conducted by Rapier (1954) first calculated the temperatures in the tool, workpiece and chip, which were treated as separate bodies due to the complexity of the cutting process. By utilising analytical and relaxation (iterative) techniques of resolution for each system based on an idealised cutting model as shown in Figure 12, the author provided not only the effect of cutting speed and feed, but also a more complete method to estimate temperature distribution, which was not previously possible with pure analytical approaches.

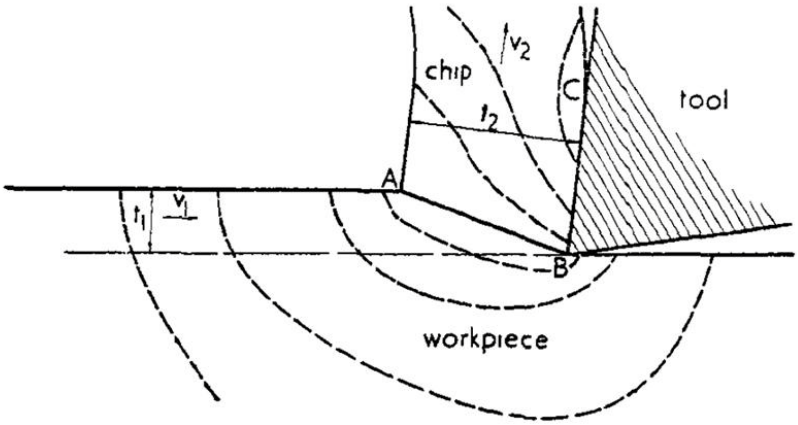

Figure 12. Idealised cutting model proposed by Rapier (1954) to predict the temperature distribution in tool, workpiece and chip.

Leone (1954) as well as Loewen and Shaw (1954) calculated the temperatures in the shear plane by considering the chip as a finite moving entity along the top of the workpiece together with the assumption of uniform velocity, however the analysis did not account for the heat flow into the chip by mass transfer mechanisms. The two studies were similar because the calculation of heat generated (and thus temperatures) between chip and workpiece was made by equating average values of shear plane and chip temperatures,

therefore the solution to the problem was comparable. A subsequent analysis presented by Chao and Trigger (1955) considered not only the workpiece as being semi-infinite (instead of infinite), but also the associated heat flow and obtained a solution similar to that initially found by Hahn (1951).

In an attempt to overcome the problems encountered by previous researchers in the prediction of temperatures due to the simplifications incorporated in the cutting models, Weiner (1955) developed an alternative analytical solution which ignored the heat transfer by conduction between chip and workpiece (zone A) and considered the chip velocity as being perpendicular to the shear plane (zone B), see Figure 13:

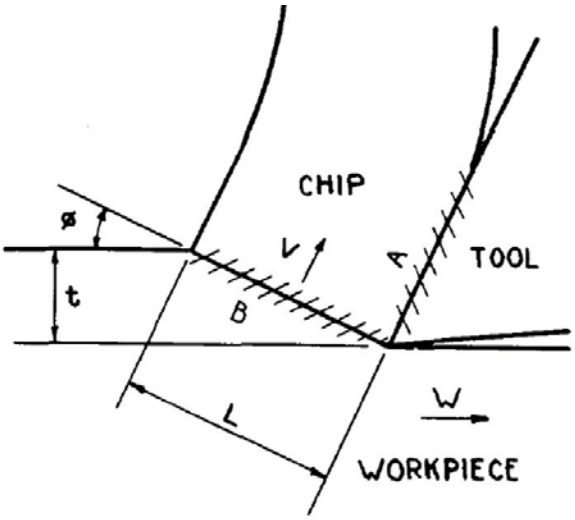

Figure 13. Zones of heat generation considered by Weiner (1955) to improve on previous studies.

In addition to simplifying the mathematical formulation, the two assumptions enabled the influence of operating variables to be quantified when predicting the temperature distribution along the shear plane.

With the objective of improving on their previous results, Chao and Trigger (1958) developed a non-iterative method to calculate the distribution of temperature in the tool-chip and the tool-workpiece regions, as seen in Figure 14. The approach considered three heat sources contributing to the rise in temperature when machining annealed AISI 4142 steel with carbide tools at cutting speeds of 91, 151 and 213m/min. These were along OW (shear zone, where the highest plastic deformation was found), OT (tool-chip interface) and OF (region where frictional rubbing between the tool edge and workpiece was located).

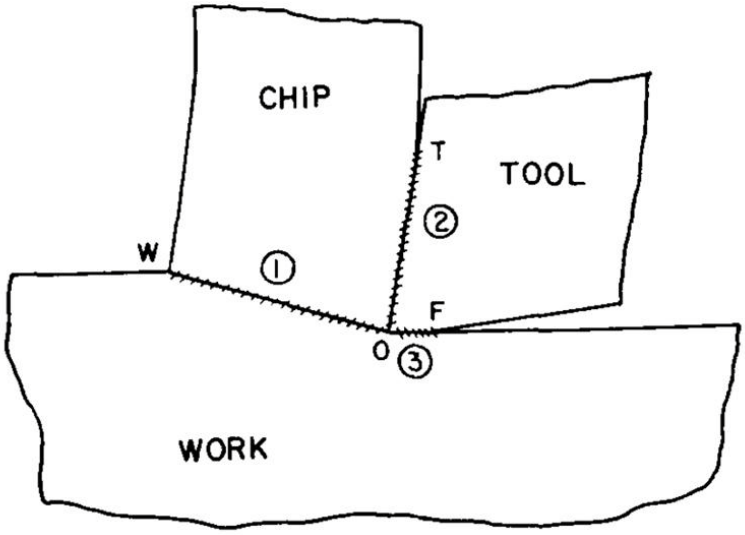

Figure 14. Approach by Chao and Trigger (1958) to account for three different heat sources in cutting.

As expected, the predicted temperature at the tool-work interface was significantly affected by tool wear, unlike that in the tool-chip contact region. It was also confirmed that temperatures increased with cutting speed in both regions, however at a higher rate in the former, which was validated by experimental data.

In order to assess the effect of temperature on the material plastic response when dry machining SAE 1015 steel with carbide tools at various cutting speeds (38, 101, 194 and 227m/min) and feeds (0.1, 0.2 and 0.3mm/rev), Kececioglu (1958) developed relationships to calculate the average shear zone temperature to further study its influence on the mean shear flow stress. Oblique cutting equations were employed together with a new expression that accounted for half the slider length in the shear zone to compute the mean shear zone temperature, which could also be utilised for orthogonal cutting. Although the work showed temperatures in the shear zone had little influence on the shear flow stress, the model did not consider the effect of shear strain/strain rate and compressive stress.

Work published by Boothroyd in the 1960's (Boothroyd, 1961 and Boothroyd, 1963) showed considerable improvement in cutting temperature estimation over the conventional shear plane model. By employing a novel infrared photographic technique to measure the temperature distribution when orthogonally cutting preheated tubular workpieces of brass and mild steel at speeds of 5.5 and 23m/min and feeds of 0.254 and 0.635mm/rev respectively, Boothroyd (1963) identified significant inconsistencies with values at the rake face predicted by previously published theoretical models. To solve the overestimation, the effect of the secondary deformation zone was included in the analysis, which led to a significant improvement in the temperature predictions.

Dutt and Brewer (1965) developed an idealised model of the cutting operation that considered the workpiece, chip and tool, which was solved by making use of the relaxation technique. The work initially achieved a set of general equations for all internal points comprising the workpiece and chip and several of the free surfaces as well as with common boundaries (e.g. the shear plane, chip/tool limits). Subsequent derivation and simultaneous assembly of the equations that best represented the process formed the basis of the numerical iterative method, which produced isothermal lines following convergence that were compared to experimental data from Hollander (1959). Although the arrangement of isothermal lines showed acceptable agreement with the experimental data, the predicted temperatures were much higher than those recorded.

Some contemporary researchers like Komanduri and Hou (2001) have worked on this problem and shown that their proposed analytical method was not only faster, easier and more accurate than numerical formulations, but also that it was giving a deeper understanding of the thermal process in cutting operations. It is highlighted however, that their approach to predict temperature rise distribution (isotherms) in tool, chip and workpiece material was based on those previously developed by Hahn (1951) and Chao and Trigger (1955). In order to solve an inverse heat conduction problem, a non-integer identified model was proposed by Battaglia et al. (2001), which was then applied to the estimation of heat flux in the tool during machining of steel at a cutting speed of 90m/min, feed rate of 0.3mm/rev and depth of cut of 2mm. Even though the model did not necessitate the thermal conductivity or specific heat as inputs, its reliability was based on the identification process, which needed a considerable precision on the laboratory design at that stage. While studying the system workpiece-tool-chip as a whole, Rech et al. (2005) developed an analytical heat transfer model of the machining process which provided a better understanding of the heat flux acting on the tool when this one was composed of coating and substrate respectively. The authors were able to show that in continuous machining, coatings are not capable of insulating the substrate, while the heat flux transmitted to the latter is primarily due to the interactions at the tool-chip interface.

Despite sustained efforts spanning a period of more than 60 years, the complexity of the metal cutting operation is such that the various analytical models proposed to predict temperature achieved a relative success and were generally incapable of accommodating most changes in process conditions (e.g. workpiece material, tool properties, cutting speed, feed rate, etc.), hence providing the opportunity for sophisticated numerical methods to tackle this issue in a more comprehensive fashion.

2.3 Split Hopkinson Pressure Bar testing apparatus

2.3.1 Historical review

When experimentally assessing the transient behaviour of a material under elevated rates of deformation and temperatures (in general for those situations ranging from 100-10,000s^{-1} and 20-1,000ºC respectively), the conventional tensile, pendulum, Charpy or Izod testing methods are ineffective due to the limited range of strain rates achievable. With the increasing interest in the 20th century to evaluate materials for ballistic or impact applications, Hopkinson (1914) developed the eponymously Hopkinson Pressure Bar apparatus, capable of producing high rates of deformation to investigate the material transient response at room temperature. Initially consisting of a cylindrical steel bar held ballistically in which pressure was applied to one end while in the other, a cylindrical pellet (attached to it using a thin layer of grease) was in position to be compressed as shown in Figure 15; the Hopkinson Pressure Bar was simple in its mechanics, but comprised three main limitations.

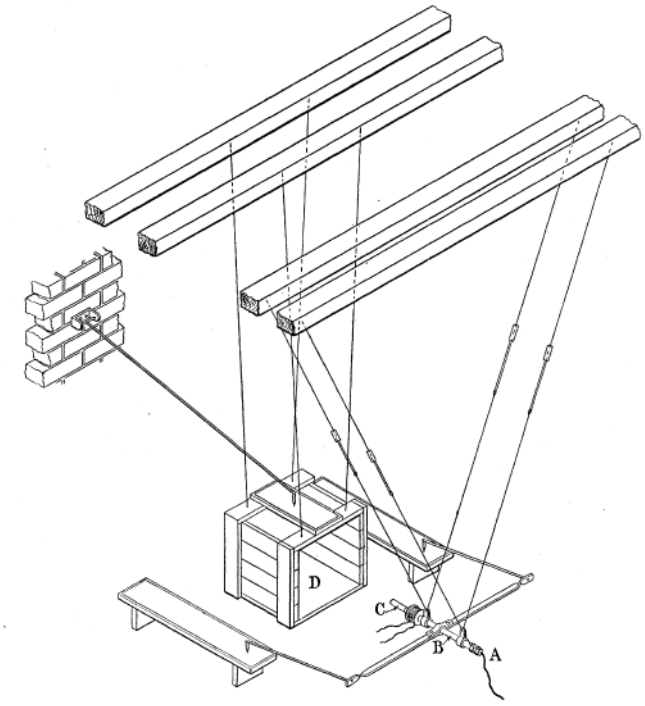

Figure 15. Hopkinson Pressure Bar apparatus experimental setup (Hopkinson, 1914).

Firstly, the resulting pressure-time curve cannot be directly inferred from the test while the force needed to break the grease bond between the bar and pellet, was generally an unknown. The third restriction was the assumption that the pulse form was constant when travelling down through the bar, which was untrue particularly for those pulses that were short (when compared to the diameter of the bar).

In a considerable effort to overcome intrinsic problems of the Hopkinson Pressure Bar associated with inertia effects when measuring stresses and strains, Landon and Quinney (1923) and Davies (1948) developed appropriate recording techniques and further proposed a modification in which measurements were performed using electrical resources respectively. Subsequent work targeted at resolving the mechanical complications concerned with the Hopkinson Pressure Bar was performed by Kolsky (1949), who extended the testing apparatus to involve two steel bars instead of one, which also accommodated the measuring procedure previously developed by Davies (1948) and is schematically represented in Figure 16:

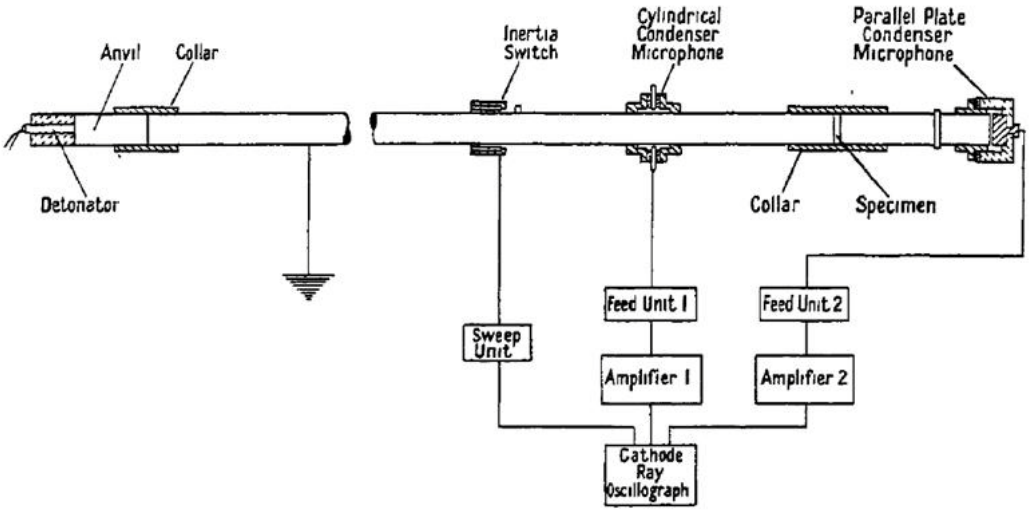

Figure 16. Experimental Hopkinson Pressure Bar disposition developed by Kolsky (1949) that incorporated two bars instead of one.

This experimental arrangement where the main impact bar of the Hopkinson Pressure Bar was 'split/divided' into two became known as the Split Hopkinson Pressure Bar (SHPB), however the term Kolsky Bar was (and is still) used interchangeably to classify the machine. The prevailing notion to differentiate both machines today is that the SHPB is only used for compression tests, while the Kolsky Bar can also be configured for tension/torsion tests.

The test samples (cylindrical with diameters smaller than those of the bars) were located between the ground ends of both bars and lubricated at the interfaces in order to minimise friction effects that could generate erroneous recordings. The arrangement shown in Figure 16 allowed the calculation of pressure and subsequent deformation in the specimen, by measuring the displacement at the free end of bar (primarily produced by a detonator triggered electrically) and the amplitude of the pressure pulse arriving at the sample with condenser-type microphones respectively. Five different materials (lower in strength than the bars) were used for the samples, namely polyethylene, polymethyl methacrylate, copper, lead and rubber, with the first four being slightly greased on their ends, while the latter was

lubricated with glycerol prior to conduct all the tests. Although it was unclear if lateral displacements were occurring and whether friction affected the trials, the updated testing machine achieved an observation time of ~20μs (the higher the better) and provided reliable graphical stress-strain relationships.

While the testing method was successfully utilised by various researchers for over a decade following Kolsky's development (Krafft et al., 1954; Hauser et al., 1961; Davies and Hunter, 1963), a more sophisticated and complete version of the SHPB instrument was presented by Lindholm (1964) while working for the Southwest Research Institute in the USA, with initial work beginning in the early 1960's (ASME, 2006). The experimental technique was extended to simultaneously calculate the stress-strain, stress-time and strain rate-time curves (increasing the observation time up to ~100μs) by modifying the lengths of the incident and transmitter bars, which enhanced the unidirectional nature of the pressure waves. In addition, the author developed a mechanical firing system that used a striker bar of 12.7mm in diameter by 660mm in length instead of using detonators or guns (Krafft et al., 1954). The measurement of the pressure waves travelling through the turned SAE 4340 steel bars comprising a diameter of 12.7mm and a length of 2,400mm was performed using novel strain gauge technology to plot the stress-strain curve, see Figure 17:

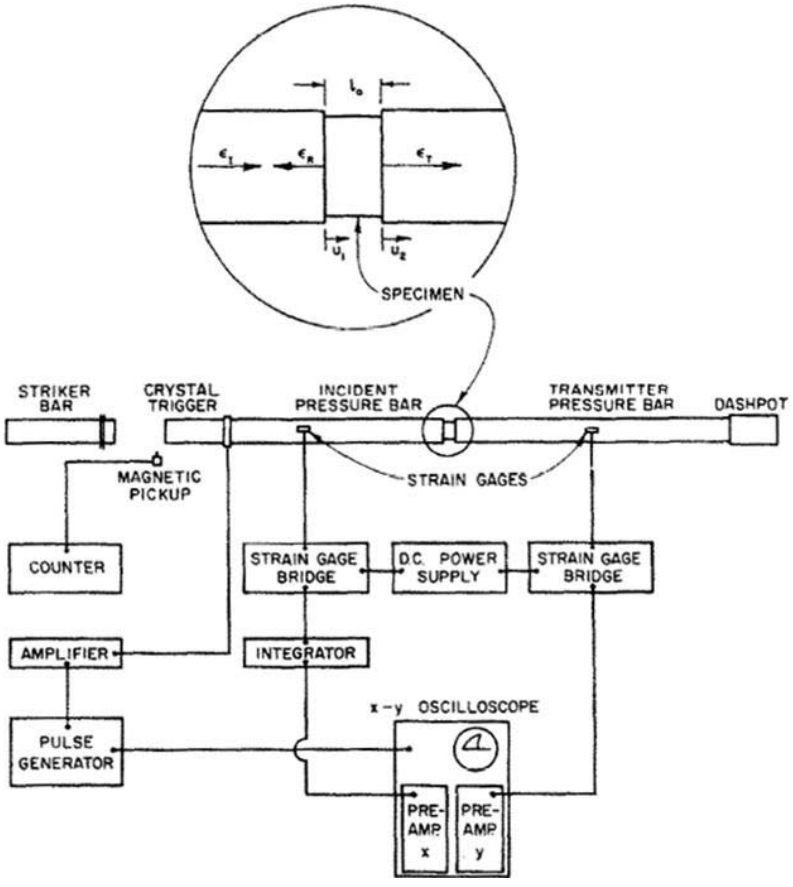

Figure 17. Split Hopkinson Pressure Bar arrangement developed by Lindholm (1964).

By testing lead, aluminium, copper and some non-metallic materials, the efficiency of the newly ameliorated SHPB rig was undoubtedly demonstrated as it was deduced from the data generated.

Incorporation of heating systems were first explored by Lindholm and Yeakley (1968) to conduct SHPB compression and tensile experiments on 1100-0 aluminium at temperatures of 400ºC and strain rates ~1,000s^{-1}. This increased the capability of the SHPB system and made it more suitable to typify the influence low/elevated temperatures had on the dynamic performance of materials. Although the electric oven used to heat the specimens induced a thermal gradient in the incident and transmitter bars (and thus affected the velocity and amplitude of the corresponding pressure waves), the effect was nullified by introducing a correction when analysing the readings. By using the SHPB machine in conjunction with an Instron apparatus to test (in tension and compression) annealed specimens at ambient temperature, the yield strength values obtained were plotted on a stress-strain rate semilog graph to investigate the rate sensitivity of aluminium, which highlighted that increasing (compressive) strain rates acted as hardening mechanisms, as observed in Figure 18:

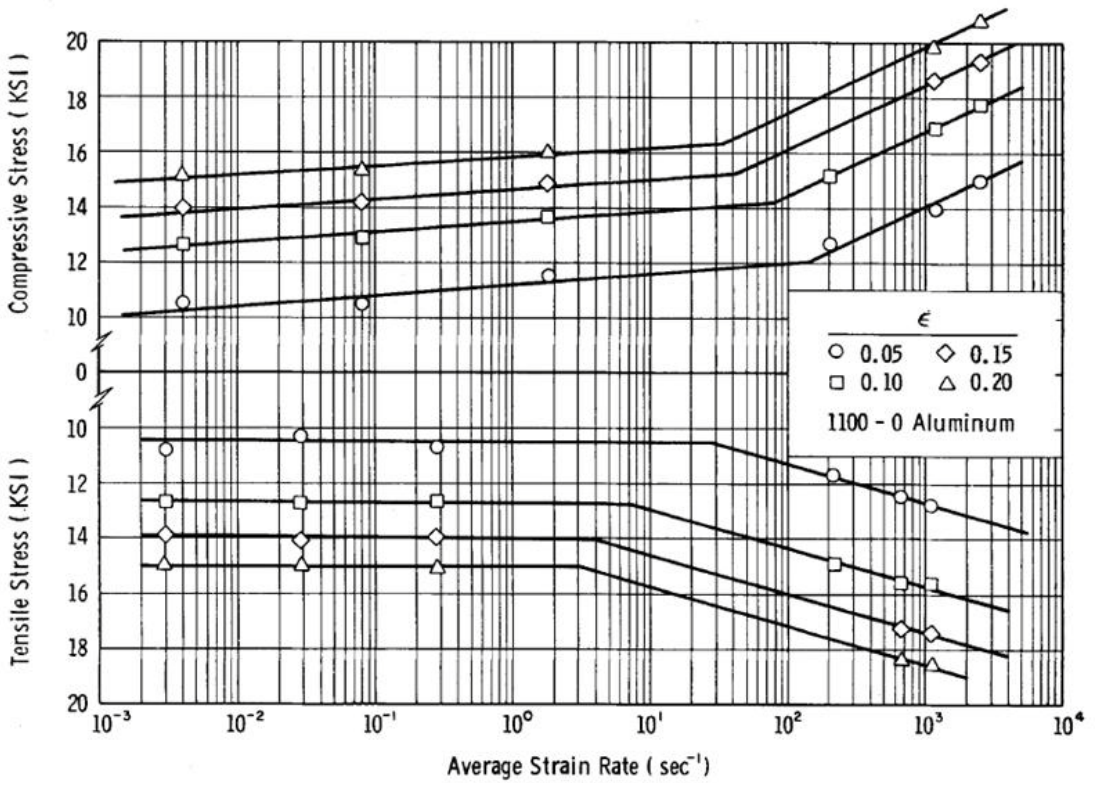

Figure 18. Rate sensitivity plot generated by Lindholm and Yeakley (1968) that clearly shows the strength transition from low to high strain rates.

All SHPB machines currently utilised in universities and research centres still incorporate the original basic features of the system designed by Lindholm (1964). Apart

from minimal differences in the disposition of the strain gauges along the bars, the use of a pneumatic (instead of a mechanical) device to fire the striker bar, the implementation of more complex heating devices (e.g. induction) and the different material/lengths employed for the striker, incident and transmitter bars; the SHPB apparatus remains the most widely used testing method for dynamic characterisation of materials at strain rates and temperatures of up to ~10,000s^{-1} and ~1,000ºC respectively. Fundamental operating principles as well as design best practices relating to the testing machine are summarised in Appendix I.

2.4 Finite element modelling (FEM) following orthogonal machining

2.4.1 Introduction

Tay et al. (1974) were the pioneers in utilising the finite element (FE) method to estimate the temperature distributions in the tool and workpiece following the machining of mild steel at cutting speeds of 29.6, 78 and 155.4m/min, as observed in Figure 19:

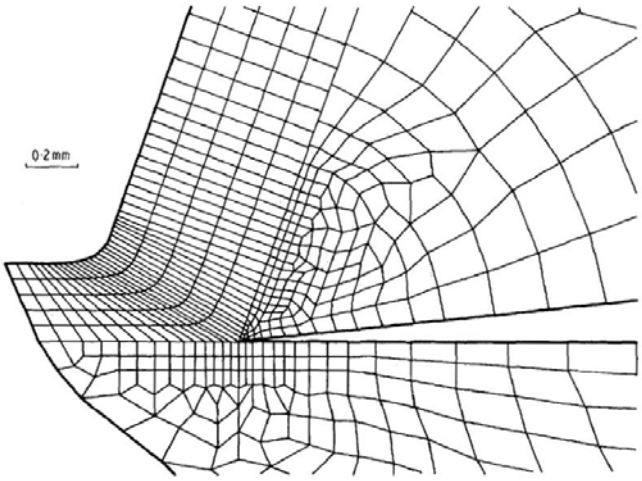

Figure 19. Mesh arrangement for tool and workpiece following Tay et al. (1974).

The relationship the authors used to characterise the material, although in the simple form of $\bar{\sigma} = \sigma_1(\bar{\varepsilon}^p)^{n_1}$, where σ_1 and n_1 are constants, already contemplated variations of its terms with temperature and strain rate, which in addition indicated the path for future research. Although only a preliminary study, the research provided temperatures at regions which were difficult to measure experimentally, with the predictions showing better accuracy compared to previous analytical procedures. Iwata et al. (1984) similarly utilised a material formulation which accounted for the effects of temperature and strain rate, but considered the orthogonal cutting process as being isothermal.

The trend for employing the FE method to investigate the orthogonal cutting operation continued to gain pace in the late 1980's, with multiple characteristics related to the process (e.g. tool and workpiece mechanical, thermal and geometrical properties) being incorporated in the simulations (Carroll and Strenkowski, 1988). Komvopoulos and Erpenbeck (1991) assessed the influence a tool in which a built-up edge was formed would have on either the perfect elastic or elastic-plastic characterisation of the workpiece.

Research in the 1990's extended beyond the prediction of forces and temperatures, with FE models capable of simulating residual stresses on the machined surface (Sasahara et al., 1996), the impact of various tool geometries (Shih, 1996) and different chip morphologies (Ceretti et al., 1999), albeit in 2D configurations. An overview of work on the FE modelling of machining operations undertaken up to the late 1990's was presented by Mackerle (1999). While the vast majority of researchers modelled the machining process from the incipient stage when the tool contacts the workpiece with acceptable precision, others like Dirikolu et al. (2001) proposed an iterative based technique which allowed analysis of the operation to commence in its steady-state condition, with particular interest in evaluating the influence of tool geometries on chip flow. Even though the resolution method showed no convergence difficulties and gave reasonable predictions concerning cutting forces, detailed material flow and frictional data were required of the orthogonal process at the steady-state condition.

Comprehensive work on the modelling of chip morphology was carried out by Ng and Aspinwall (2002) when cutting AISI H13 die steel using PCBN at various cutting speeds. Close agreement between the predicted chip shape/dimensions and experimental results were observed, as shown in Figure 20:

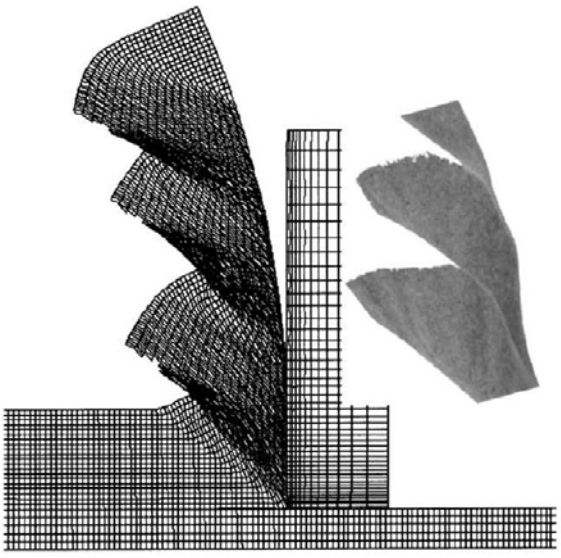

Figure 20. Chip serration predicted by Ng and Aspinwall (2002) when modelling orthogonal cutting of AISI H13 die steel.

By employing a shear strain energy damage criterion together with a remeshing technique to accommodate the large deformation of the finite elements, an accurate simulation of the saw-tooth chip characteristics was achieved. Similarly, Chuzhoy et al. (2003a) attempted to simulate chip serration when orthogonally cutting ductile iron while also including a microstructural-level material model to account for the softening and fracture of the workpiece. A further numerical resolution to the problem implemented by Chuzhoy et al. (2003b) enabled the prediction of chip morphology with respect to different phases of ductile iron, e.g. pearlite and ferrite, thus making the proposed microstructural-level model a reliable tool to investigate the influence of microstructure on the machinability of cast irons.

Concurrently, Shi and Liu (2004) evaluated the performance of four different constitutive material models (derived from the same flow stress data) when predicting temperatures, cutting forces, chip thickness/shear angle and residual stresses following the machining of HY-100 steel. In general, all models showed comparable temperature and force trends, but significantly different estimations of residual stresses. The authors suggested that this could be due to the formulation of the constitutive models, which were largely empirical in nature. Advances in computer technology and FE codes were exploited by researchers including Li and Shih (2005) who developed a full 3D FE model to simulate the machining of commercially pure titanium under cutting speeds of 24.4, 48.8, 97.5 and 195m/min with feeds of 0.254 and 0.381mm/rev at a constant 1.02mm depth of cut, see Figure 21:

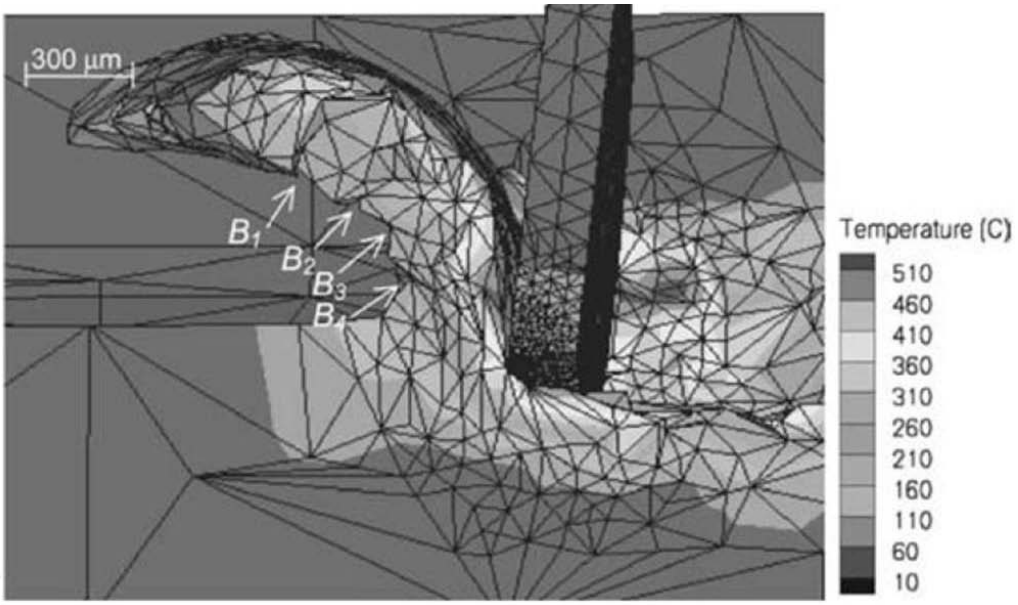

Figure 21. 3D chip formation generated by Li and Shih (2005).

Apart from the prediction of cutting forces combined with satisfactory temperature distributions in tool and workpiece, aspects such as chip curling/flow direction were also

evaluated, which were not possible with 2D models. Such findings demonstrated the feasibility of 3D FE formulations to capture with greater detail the complex mechanisms inherent of the cutting process.

More recent research on the FE modelling of metal cutting has expanded to include aspects such as the development of material models to account for a higher degree of flow softening and succeeding damage (Uhlmann et al., 2007), the influence of tool edge roundness on temperature and/or stress distributions (Ozel and Zeren, 2007), critical assessment of frictional conditions on response measures (Arrazola et al., 2008) as well as predicting metallurgical alterations on the machined surface, which generally act as sources of subsequent damage (Ranganath et al., 2009; Umbrello and Jawahir, 2009).

Sima and Ozel (2010) formulated a FE model which incorporated a cutting tool contacting when cutting Ti-6Al-4V alloy, together with adjustments on the workpiece material law that accounted for flow stress variations with respect to strain, strain rate and temperature. The influence of tool geometry/tool coating coupled with material softening behaviour showed that serrated chip formation typically occurred when temperature at the shear zone was ≥400ºC, see Figure 22:

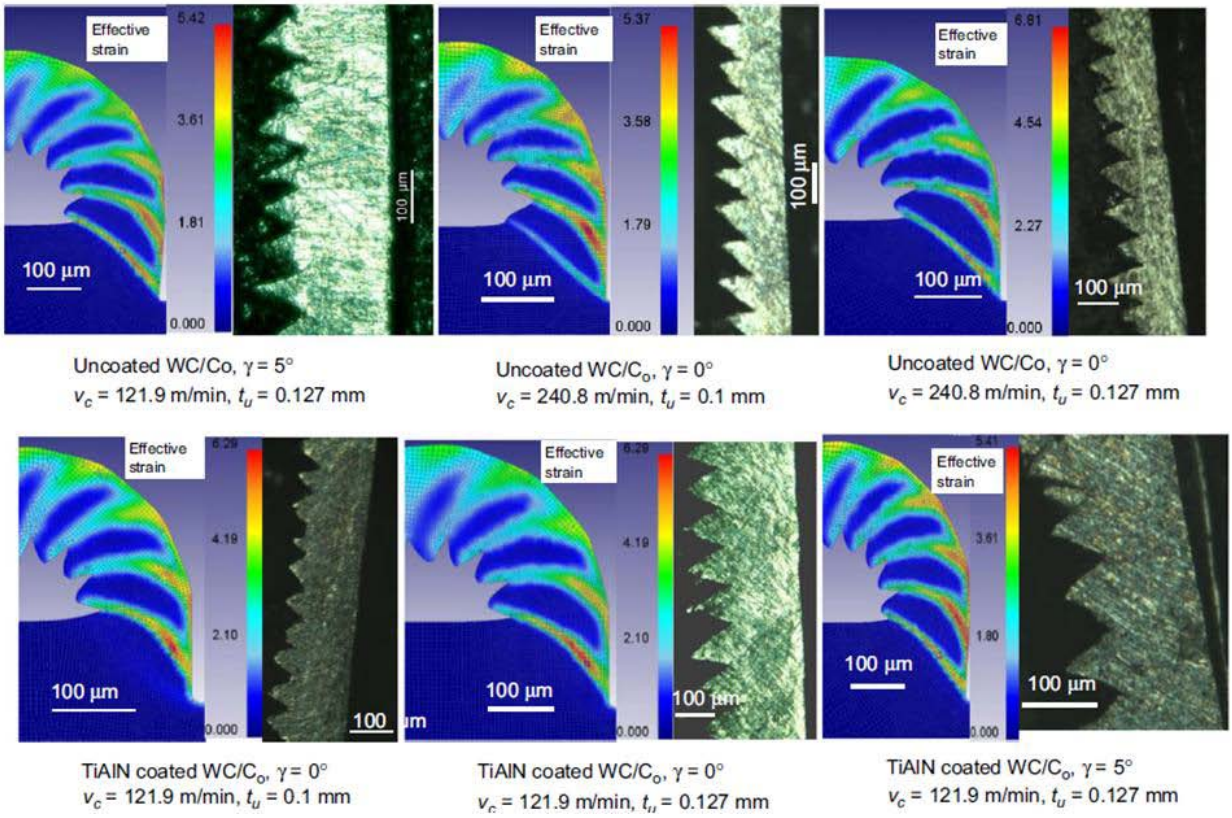

Figure 22. FE chip shape predicted by Sima and Ozel (2010) when accounting for workpiece softening produced with strain, strain rate and temperature for various cutting conditions.

Caruso et al. (2010) employed a hardness dependent flow stress model for AISI H13 tool steel to predict residual stresses following orthogonal cutting. The implementation of the novel material relationship was possible due to the development of a customised code which was linked to the FE package utilised (ABAQUS), thus giving the authors more flexibility and freedom for their purposes.

More recently, several researchers including Torrano et al. (2011), Rotella et al. (2012) and Outeiro et al. (2013) have focused on modelling workpiece mechanical and microstructural transformations following machining to identify preferred cutting conditions for preserving acceptable surface integrity. Furthermore, 3D FE formulations have become more widely used, which has helped to provide greater insight into the mechanics of different cutting processes, not previously possible with 2D models.

2.4.2 Solid mechanics fundamentals

2.4.2.1 Plasticity theory overview

The plasticity (or inelasticity) of metals is highly non-linear as well as history-dependent beyond the elastic range. This property contrasts with polymers or concrete as generally, the latter can be fairly described by means of the linear elasticity theory. When the boundary of the elastic region (known as the elastic limit) is reached with increasing stress, the metal is said to yield. This is generally characterised by a surface (known as the yield surface) when described in terms of the Cauchy stress tensor and delimits the elastic from the plastic region.

In cases when strain rate can be neglected in the analysis of a material's response, conventional plasticity theory is usually adequate for describing flow behaviour. Conversely, where rate sensitivity has a significant influence on material response (such as in metal cutting processes), the viscoplasticity theory should instead be adopted. The classical viscoplasticity definition involving rate dependent behaviour with a well defined yield criterion will be utilised in the present work.

Two key concepts in plasticity theory are the Flow Law (or Flow Rule) and Flow Potential (or Plastic Potential). In general, the former can be defined as the rate at which plastic deformation occurs (influencing therefore the shape and expansion of the yield surface), and mathematically specified by Lubliner (2008) as:

$$\dot{\varepsilon}_{ij}^{p} = g_{ij}(\sigma_{ij}, T, \beta_1) \tag{6}$$

where $g_{ij}(\sigma_{ij}, T, \beta_1)$ is the flow law and may depend on the stress tensor component σ_{ij}, the temperature T and in the simplest situation, only one internal variable α. The number of internal variables can vary according to the complexity of the model.

For convenience, the tensor function $g_{ij}(\sigma_{ij}, T, \beta_1)$ can be derived from a scalar function $g(\sigma_{ij}, T, \beta_1)$, called the flow potential, which is defined by:

$$g_{ij} = \phi(\sigma_{ij}, T, \beta_1) \frac{\partial g(\sigma_{ij}, T, \beta_1)}{\partial \sigma_{ij}} \tag{7}$$

where $\phi(\sigma_{ij}, T, \beta_1)$ is a positive scalar function, hence Eq. (6) can be rewritten as:

$$\dot{\varepsilon}_{ij}^{p} = \phi(\sigma_{ij}, T, \beta_1) \frac{\partial g(\sigma_{ij}, T, \beta_1)}{\partial \sigma_{ij}} \tag{8}$$

In general, the flow potential g is usually considered to be a function of stress only, in which case it can be defined as:

$$g\left(\sigma_{ij}, T, \beta_1\right) = J_2 \tag{9}$$

where J_2 is the second stress deviator invariant given by:

$$J_2 = \frac{1}{2} S_{ij} S_{ij} \qquad , \qquad S_{ij} = \sigma_{ij} - \frac{\sigma_{kk}}{3} \delta_{ij} \tag{10}$$

where S_{ij} is the deviatoric stress tensor and δ_{ij} is the Kronecker delta. Derivation of Eq. (9) with respect to σ_{ij} together with the use of the chain rule gives:

$$\frac{\partial g(\sigma_{ij}, T, \beta_1)}{\partial \sigma_{ij}} = \frac{\partial J_2}{\partial \sigma_{ij}} = \frac{\partial J_2}{\partial S_{kl}} \frac{\partial S_{kl}}{\partial \sigma_{ij}} = \frac{\partial}{\partial S_{kl}} \left(\frac{1}{2} S_{ij} S_{ij} \right) \frac{\partial S_{kl}}{\partial \sigma_{ij}} = S_{ij} \tag{11}$$

so that Eq. (8) can be simplified as:

$$\dot{\varepsilon}_{ij}^{p} = \phi\left(\sigma_{ij}, T, \beta_1\right) \frac{\partial g\left(\sigma_{ij}, T, \beta_1\right)}{\partial \sigma_{ij}} = \phi\left(\sigma_{ij}, T, \alpha_1\right) S_{ij} \tag{12}$$

A general flow potential Ω was proposed by Rice (1970), who showed that:

$$\dot{\varepsilon}_{ij}^{p} = \frac{\partial \Omega}{\partial \sigma_{ij}} \tag{13}$$

Particularly in ABAQUS (2010), and for some rate-independent plasticity models, the flow potential g is defined by:

$$\frac{\partial g}{\partial \sigma_{ij}} = c_i \frac{\partial f}{\partial \sigma_{ij}} \tag{14}$$

where c_i is a scalar and f is the yield function which defines the boundary of the yield surface. These models are known as "associative flow" models, which are employed in ABAQUS (except cast iron and the Cam-clay soil models) to describe plastic behaviour for metals. For strain rate dependent applications, ABAQUS offers two options, the first incorporates a rate-dependent yield strength term in the model (designed for relatively high strain rate applications, such as dynamic events or metal forming process simulations) which in general utilises an overstress power law as detailed in Eq. (15):

$$\dot{\bar{\varepsilon}}^{p} = D_a \left(\frac{\bar{\sigma}}{\bar{\sigma}_0} - 1 \right)^{m_1} \quad , \quad \bar{\sigma} \geq \bar{\sigma}_0 \tag{15}$$

where $\dot{\bar{\varepsilon}}^{p}$ is the equivalent (or effective) plastic strain rate, $\bar{\sigma}$ is the yield stress at nonzero plastic strain rate, $\bar{\sigma}_0(\bar{\varepsilon}^{p}, T, f_i)$ is the static yield stress (which may depend on the effective plastic strain $\bar{\varepsilon}^{p}$ via isotropic hardening, the temperature T and other field variables f_i), and the parameters $D_a(T, f_i)$ and $m_1(T, f_i)$ can be functions of temperature and possibly, of other predefined internal variables. The second option is to define a yield stress ratio according to Eq. (16):

$$\dot{\bar{\varepsilon}}^{p} = \dot{\bar{\varepsilon}}_0 \left(\frac{\bar{\sigma}}{\bar{\sigma}_0} \right)^{m_1} \tag{16}$$

Both options assume that the shapes of the hardening curves at different strain rates are identical. Experimentally derived static and rate-dependent stress-strain relationships can also be specified directly, in which case the yield stress at a given strain rate is interpolated directly from the recorded data.

The main concepts considered in a typical viscoplastic formulation according to Bower (2009) are described in the following subsections.

2.4.2.2 Strain rate decomposition

The strain rate tensor is linearly decomposed into elastic and plastic strain rate tensors as follows:

$$\dot{\varepsilon}_{ij} = \dot{\varepsilon}^{e}_{ij} + \dot{\varepsilon}^{p}_{ij} \tag{17}$$

2.4.2.3 Elastic stress-strain law

The elastic strains are related to the stresses according to the standard linear elastic stress-strain formulation. When volumetric changes due to variation in temperature are also considered, the relationship can be written as:

$$\varepsilon^{e}_{ij} = S_{ijkl}\,\sigma_{kl} + \alpha_2 \Delta T \delta_{ij} \tag{18}$$

where α_2 is the coefficient of thermal expansion and S_{ijkl} is the elastic compliance tensor, which is given by:

$$S_{ijkl} = \frac{1+\nu}{2E}\left(\delta_{il}\delta_{jk} + \delta_{ik}\delta_{jl}\right) - \frac{\nu}{E}\delta_{ij}\delta_{kl} \tag{19}$$

where ν and E are the Poisson's ratio and Young's modulus respectively. The inverse relation of Eq. (18) is defined as:

$$\sigma_{ij} = \frac{E}{1+\nu}\left(\varepsilon^{e}_{ij} + \frac{\nu}{1-2\nu}\varepsilon^{e}_{kk}\delta_{ij}\right) - \frac{E\alpha_2\Delta T}{1-2\nu}\delta_{ij} \tag{20}$$

2.4.2.4 Plastic flow potential

The plastic flow potential specifies the magnitude of the plastic strain rate as a function of stress as well as the resistance of the material to flow plastically, and typically defined as:

$$\dot{\bar{\varepsilon}}^p = \sqrt{\frac{2}{3}\dot{\varepsilon}_{ij}^p \dot{\varepsilon}_{ij}^p} \tag{21}$$

It is further assumed that the material is isotropic, such that the strain rate can only depend on the invariants of the deviatoric stress tensor S_{ij}. Of the two nonzero invariants the tensor has ($J_1 = 0$), the one coined as J_2 is generally chosen for the calculations, due to its relation with the Von Mises yield criterion in pure shear:

$$J_2 = \bar{k}^2 \tag{22}$$

where k is the yield strength of the material. For simple tension where the yield strength is related by $\overline{\sigma} = \bar{k}\sqrt{3}$, we have:

$$\overline{\sigma} = \sqrt{3\,J_2} = \sqrt{\frac{3}{2}\,S_{ij}S_{ij}} \tag{23}$$

In most cases, $\dot{\varepsilon}_{ij}^p$ is adopted codirectional with the outward normal to a locally smooth yield surface in the Cauchy stress space, hence the plastic strain rate tensor can also be related by:

$$\dot{\varepsilon}_{ij}^p \propto \frac{\partial f}{\partial \sigma_{ij}} \tag{24}$$

where f represents the yield criterion. Considering that the Von Mises yield criterion is frequently used, the partial derivative seen on the right hand side of Eq. (24) leads to:

$$\frac{\partial f}{\partial \sigma_{ij}} = \frac{\partial \overline{\sigma}}{\partial S_{ij}} = \frac{3}{2}\frac{1}{2}\frac{1}{\sqrt{\frac{3}{2}\,S_{kl}S_{kl}}}2S_{pq}\frac{\partial S_{pq}}{\partial \sigma_{ij}} = \frac{3}{2}\frac{1}{\sqrt{\frac{3}{2}\,S_{kl}S_{kl}}}S_{pq}\frac{\partial S_{pq}}{\partial \sigma_{ij}} \tag{25}$$

where the last derivative on the right hand side of Eq. (25) gives:

$$\frac{\partial S_{pq}}{\partial \sigma_{ij}} = \frac{\partial}{\partial \sigma_{ij}}\left(\sigma_{pq} - \frac{\sigma_{kk}}{3}\delta_{pq}\right) = \frac{\partial \sigma_{pq}}{\partial \sigma_{ij}} - \frac{1}{3}\frac{\partial}{\partial \sigma_{ij}}\left(\sigma_{kk}\delta_{pq}\right) = \delta_{ip}\delta_{jq} - \frac{1}{3}\delta_{ik}\delta_{jk}\delta_{pq} \tag{26}$$

This leads to:

$$S_{pq}\frac{\partial S_{pq}}{\partial \sigma_{ij}} = S_{pq}\left(\delta_{ip}\delta_{jq} - \frac{1}{3}\delta_{ik}\delta_{jk}\delta_{pq}\right) = S_{ij} - \left(\sigma_{pp} - \frac{\sigma_{kk}}{3}\delta_{pp}\right)\delta_{ij} = S_{ij} \tag{27}$$

Finally Eq. (25) can be simplified to:

$$\frac{\partial f}{\partial \sigma_{ij}} = \frac{3}{2}\frac{1}{\sqrt{\frac{3}{2}\,S_{kl}S_{kl}}}S_{ij} = \frac{3}{2}\frac{S_{ij}}{\overline{\sigma}} \tag{28}$$

2.4.2.5 Plastic flow law

The plastic flow law specifies the components of plastic strain rate resulting from a multiaxial state of loading. In rate-dependent plasticity, the flow law is expressed as the derivative of the yield surface with respect to stress, whereas in viscoplasticity, the flow law involves the derivative of the plastic flow potential. In the particular case of a power-law Von Mises flow potential, the flow law is defined as:

$$\dot{\varepsilon}_{ij}^{p} = \dot{\overline{\varepsilon}}^{p}\frac{\partial f}{\partial \sigma_{ij}} = \dot{\overline{\varepsilon}}^{p}\frac{3}{2}\frac{S_{ij}}{\overline{\sigma}} \qquad , \qquad \dot{\overline{\varepsilon}}^{p} = \dot{\varepsilon}_0\left(\frac{\overline{\sigma}}{\bar{\sigma}_0}\right)^{m_1} \tag{29}$$

In general when a material is considered isotropic, the hardening law is given by:

$$\bar{\sigma}_0 = \bar{\sigma}_q\left(1 + \frac{\overline{\varepsilon}^{p}}{\bar{\varepsilon}_y}\right)^{n_2} \tag{30}$$

where $\bar{\sigma}_q$ and $\bar{\varepsilon}_y$ are generic effective stress and plastic strain terms respectively while n_2 is a fitting constant.

2.4.2.6 Hardening law

The hardening law specifies the evolution of state variables with plastic straining. In the previous subsection, a simple example of isotropic hardening law for tension was defined by Eq. (30), where the accumulated effective plastic strain is calculated as:

$$\overline{\varepsilon}^{p} = \int \dot{\overline{\varepsilon}}^{p}\, dt = \int \dot{\varepsilon}_0 \left(\frac{\overline{\sigma}}{\overline{\sigma}_0}\right)^{m_1} dt \tag{31}$$

More complex models are likely to involve different types of hardening laws, however the effective plastic strain is always computed in the same fashion.

2.4.3 Workpiece material constitutive modelling

2.4.3.1 Principal characteristics

Irrespective of the manufacturing operation to be simulated, if a constitutive model is not suitably defined or does not include relevant variables which affect the material's response and are present in the actual process, numerical predictions as well as the simulation itself are likely to be inaccurate. Hence, a proper material characterisation is of extreme importance and the main foundation of any reliable FE model.

Various constitutive models have been proposed in situations (such as machining) where strain rate and temperature effects cannot be neglected, with pioneering work published by Johnson and Cook (1983) (JC). Although the JC constitutive relationship is simple in its formulation, the model is empirical in nature and does not account for metallurgical effects on the mechanical behaviour of the material. Zerilli and Armstrong (1987) (ZA) on the other hand addressed this issue by proposing two different constitutive laws to describe materials with either an fcc or bcc structure. Similarly, Follansbee and Kocks (1988) developed the Mechanical Threshold Stress (MTS) model and applied it succesfully to fcc, bcc and hcp structures in an effort to portray thermally-activated plasticity over a wide range of strain rates and temperaures in which dislocation interactions play a significant role. With the exception of the latter, the JC and ZA material models have been applied to the cutting problem with some success, however the use of JC has been predominant due to its simplicity. Power law, customised expressions (Shi et al., 2010) as well as modified JC relationships (Sartkulvanich et al., 2004; Calamaz et al., 2008; DeMange et al., 2009; Ozel, 2010) have also been utilised to accurately predict variations in flow stress with respect to plastic strain, strain rate and temperature. However, taking into account that tailored flow stress expressions and modified JC models are formulated suit to purpose, attention will be paid to the standard versions of the JC and MTS constitutive models (taking into consideration that the latter is appropriate for fcc-type materials and has not been applied to the machining process), both of them which are described in the following subsections.

2.4.3.2 Johnson-Cook (JC) model

Following extensive experimental work performed on a SHPB apparatus and succeeding analysis of the material data for OFHC copper, Armco Iron and SAE 4340 steel, Johnson and Cook (1983) proposed a single expression relating the flow stress (in tension) with the effective plastic strain $\overline{\varepsilon}^p$, the effective plastic strain rate $\dot{\overline{\varepsilon}}^p$ and the temperature T as shown in Eq. (32):

$$\overline{\sigma} = \left[A + B\left(\overline{\varepsilon}^p\right)^n\right]\left[1 + C\ ln\left(\frac{\dot{\overline{\varepsilon}}^p}{\dot{\overline{\varepsilon}}_0}\right)\right]\left[1 - \left(\frac{T - T_r}{T_m - T_r}\right)^m\right] \tag{32}$$

where:

A, B, C, n, m: material constants,

$\dot{\overline{\varepsilon}}_0$: reference strain rate for normalisation,

$T_r = 293K$ reference (ambient) temperature,

$T_m =$ melting temperature of a specific material.

The material strain and strain rate hardening effects are determined by the constants B/n and C respectively, while the influence of thermal softening is represented by the parameter m. In this regard, the general expression for the flow stress assumes that the strain, strain rate and temperature effects are independent factors with respect to the material plastic behaviour. In spite of its limitations, the JC model has commonly been applied for the FE modelling of machining processes, ranging from materials like alloy steels (Ozel and Zeren, 2007), stainless steels (Umbrello et al., 2007), titanium alloys such as Ti-6Al-4V (Molinari et al., 2013) and also Inconel 718 (Ozel et al., 2011) to mention only a few.

2.4.3.3 Mechanical Threshold Stress (MTS) model

This model was developed for high strain rate processes to obtain a constitutive relationship between the flow stress $\overline{\sigma}$, the effective plastic strain rate $\dot{\overline{\varepsilon}}^p$ and temperature T from a metallurgical/physical perspective. In its basic formulation, the MTS model uses an internal state variable, known as the mechanical threshold stress, which is defined as the flow stress at an absolute temperature $T = 0K$ (Follansbee and Kocks, 1988) as:

$$\hat{\sigma} = \hat{\sigma}_a + \hat{\sigma}_e \tag{33}$$

where $\hat{\sigma}_a$ is an athermal component (temperature independent) and $\hat{\sigma}_e$ is a term that characterises rate dependent processes. The flow stress is therefore related to the mechanical threshold stress by:

$$\overline{\sigma} = \hat{\sigma}_a + \sigma_e = \hat{\sigma}_a + s\left(\dot{\overline{\varepsilon}}^p, T\right)\hat{\sigma}_e \tag{34}$$

where $s\left(\dot{\overline{\varepsilon}}^p, T\right)$ is a fitting term (also known as scaling factor) constrained to vary between $0 \leq s\left(\dot{\overline{\varepsilon}}^p, T\right) \leq 1$. Taking into account thermal activation effects, Eq. (34) can be written as shown in Eq. (35) if $\hat{\sigma}_e = (\hat{\sigma} - \hat{\sigma}_a)$:

$$\overline{\sigma} = \hat{\sigma}_a + (\hat{\sigma} - \hat{\sigma}_a)\left[1 - \left(\frac{kT}{g_0 \mu b^3} ln\left(\frac{\dot{\overline{\varepsilon}}_0}{\dot{\overline{\varepsilon}}^p}\right)\right)^{\frac{1}{q}}\right]^{\frac{1}{p}} \tag{35}$$

where g_0 is the normalised activation energy, μ is the temperature dependent shear modulus, b is the magnitude of the Burgers vector, k is the Boltzman's constant, $\dot{\overline{\varepsilon}}_0$ is the reference strain rate and p, q are constants. The flow stress in Eq. (35) reduces to $\overline{\sigma} = \hat{\sigma}$ when $T = 0K$, which is the mechanical threshold stress as previously defined. Only one structure parameter was used to describe the material under analysis ($\hat{\sigma}_e$), however the quantity of parameters can be increased to three for most materials to account for other strengthening mechanisms affecting the flow stress. In the particular case of considering two structure parameters, the general formulation for the mechanical threshold stress following Goto et al. (2000) results in:

$$\frac{\hat{\sigma}}{\mu} = \frac{\hat{\sigma}_a}{\mu} + \sum_j \frac{\hat{\sigma}_j}{\mu} \qquad j = 1,2 \tag{36}$$

where:

$$\frac{\sigma_j}{\mu} = s_j\left(\dot{\overline{\varepsilon}}^p, T\right)\frac{\hat{\sigma}_j}{\mu_0} \qquad \rightarrow \qquad \sigma_j = s_j\left(\dot{\overline{\varepsilon}}^p, T\right)\frac{\mu}{\mu_0}\hat{\sigma}_j \tag{37}$$

μ_0 is the shear modulus at $T = 0K$ and $s_j\left(\dot{\overline{\varepsilon}}^p, T\right)$ takes the same form as previously detailed:

$$s_j = \left[1 - \left(\frac{kT}{g_{0j}\mu b^3} ln\left(\frac{\dot{\bar{\varepsilon}}_{0j}}{\dot{\bar{\varepsilon}}^p}\right)\right)^{\frac{1}{qj}}\right]^{\frac{1}{pj}} \tag{38}$$

Expanding Eq. (34) to account for two structure parameters and using subscripts *i* and *e* instead of *1* and *2* respectively, the following expression for the flow stress is obtained:

$$\overline{\sigma} = \hat{\sigma}_a + \sigma_i + \sigma_e = \sigma_a + s_i\left(\dot{\bar{\varepsilon}}^p, T\right)\frac{\mu}{\mu_0}\hat{\sigma}_i + s_e\left(\dot{\bar{\varepsilon}}^p, T\right)\frac{\mu}{\mu_0}\hat{\sigma}_e \tag{39}$$

where $\hat{\sigma}_a \equiv \sigma_a$. A more complex expression for the flow stress proposed by Chen and Gray III (1996) where the flow stress as well as the summation of terms is increased to the power of n_3 is shown in Eq. (40):

$$\begin{aligned}(\overline{\sigma})^{n_3} &= (\hat{\sigma}_a)^{n_3} + (\sigma_i)^{n_3} + (\sigma_e)^{n_3} \\ &= (\sigma_a)^{n_3} + \left(s_i\left(\dot{\bar{\varepsilon}}^p, T\right)\frac{\mu}{\mu_0}\hat{\sigma}_i\right)^{n_3} + \left(s_e\left(\dot{\bar{\varepsilon}}^p, T\right)\frac{\mu}{\mu_0}\hat{\sigma}_e\right)^{n_3}\end{aligned} \tag{40}$$

When $n_3 = 1$, the expression for the flow stress reduces to Eq. (39), which has been previously employed by several researchers (Daridon et al., 2004; da Silva and Ramesh, 1997; Follansbee and Gray III, 1989). According to Mecking and Kocks (1981), the best description of the structure evolution (total hardening rate) is accomplished by relating mechanisms such as strain hardening (dislocation accumulation) and dynamic recovery (dislocation annihilation) by means of:

$$\theta = \frac{d\hat{\sigma}_e}{d\bar{\varepsilon}^p} = \theta_h - \theta_r \tag{41}$$

where the subscript h corresponds to hardening and r to recovery mechanisms respectively. The best approach for describing θ, which is of empirical nature, is achieved by a modified Voce law that has the form:

$$\theta = \theta_0\left[1 - \frac{tanh\left(\alpha_i \frac{\hat{\sigma}_e}{\hat{\sigma}_{es}}\right)}{tanh(\alpha_i)}\right] \tag{42}$$

where α_i is a fitting term and θ_0 an experimentally obtained strain hardening rate parameter. The saturation value $\hat{\sigma}_{es}$ is obtained from the following equation:

$$ln\left(\frac{\dot{\varepsilon}_{es0}}{\dot{\varepsilon}^{p}}\right) = -\frac{g_{es0}\mu b^{3}}{kT} ln\left(\frac{\hat{\sigma}_{es}}{\hat{\sigma}_{es0}}\right) \quad (43)$$

where g_{es0} is the normalised activation energy for dislocation-dislocation interactions while the parameters $\hat{\sigma}_{es0}$ and $\dot{\varepsilon}_{es0}$ are constants.

2.4.3.4 User-defined material subroutine VUMAT - ABAQUS

2.4.3.4.1 Introduction

Built-in features (e.g. material models, frictional relationships, etc.) in commercial FE software can often be insufficient to accurately represent the mechanical, frictional or thermal properties of a material. The general purpose FE software ABAQUS provides the facility for users to develop bespoke algorithms/subroutines to supplement the default material database. In order to develop the mechanical constitutive behaviour of a material in ABAQUS, either a UMAT (for implicit analyses) or VUMAT (explicit analyses) subroutine must be specified.

Machining processes are typically modelled using explicit integration techniques and therefore VUMATs are the most suitable codes to be developed. A further advantage is that user subroutines can be easily incorporated into the ABAQUS solver thanks to the internal communication between them both once a job is submitted.

2.4.3.4.2 Main characteristics

The coding of a VUMAT can be generated using either FORTRAN 77 or C programming conventions while the definition of internal state variables through the DEPVAR option is mandatory in most cases. The subroutine must be kept in a separate file, utilises a two-state internal architecture to define values in OLD and NEW arrays respectively and in general, the Backward Euler method (implicit integration procedure) is chosen to transform the constitutive rate equations into incremental relationships.

When considering damage effects and removal of elements wants to be modelled, an element deletion flag which can take the value 0 (deletion) or 1 (active) must be defined within the DEPVAR option. A flag value of 0 implies that the tensor stress components are

set to zero and the material point must be deleted from the simulation while a value of 1 indicates that the point remains active.

Using the ABAQUS/CAE pre-processor module, the user defines the quantity of state variables associated with the material, a parameter known as *nprops*, and includes (if relevant to the situation to simulate) the deletion flag. The variables that must be established are the stress tensor components defined as *stressNew(nblock,ndir+nshr)* and the state variables *stateNew(nblock,nstatev)*, where *nblock* is the number of material points to be processed, *ndir* and *nshr* are the number of direct and indirect components in the [symmetric] stress tensor respectively, and *nstatev* is the number of user defined state variables.

If necessary (like in thermo-mechanical analyses), the internal and dissipated energies per unit mass at each material point, defined as *enerInternNew(nblock)* and *enerInelasNew(nblock)* respectively can be updated at the end of the increment. As the stress and strain tensors are symmetric, there will be in total *ndir+nshr=6* independent stress and strain tensor components. For instance, the stress tensor components are specified in ABAQUS as outlined in Table 3, for both 2D and 3D configurations.

Component	2-D Case	3-D Case
1	σ_{11}	σ_{11}
2	σ_{22}	σ_{22}
3	σ_{33}	σ_{33}
4	σ_{12}	σ_{12}
5		σ_{23}
6		σ_{31}

Table 3. Stress tensor component arrangements utilised by ABAQUS for 2D and 3D FE formulations (the fourth stress tensor component is always σ_{12}, irrespective of the dimensional scenario).

The output values are always defined within the code, which can be updated at every time increment and take the name of state-dependent variables (SDV1, SDV2, etc.). Depending on the complexity of the process modelled, the number of state-dependent variables can vary, however it is advisable to maintain a consistency in the numbering to avoid misinterpretations.

2.4.4 Type of FE analysis/formulation

2.4.4.1 Eulerian

The Eulerian formulation (or spatial description) generally defines the variations of physical quantities assessed in terms of their location in space symbolised by the spatial coordinates x, y and z together with time t (Wu, 2004). In terms of FE meshes, the elements remain fixed in space whereas the material is allowed to flow through them, thus having the advantage that their intrinsic geometrical shape is not modified with time (Childs et al., 2000). However the major drawback when applied for the modelling of machining operations is that the deformed chip shape (the free surface boundaries) must be predefined. In addition, segmented or discontinuous chip morphologies cannot be efficiently simulated with pure Eulerian formulations, which are more commonly utilised in fluid dynamic applications rather than in solid mechanics.

2.4.4.2 Lagrangian

The Lagrangian formulation considers the mesh being bonded to the workpiece material, therefore the elements are distorted accordingly when the tool advances and deforms the workpiece. Although suitable for the FE modelling of cutting processes as the chip is formed freely without any prior assumptions, highly non-linear expressions develop due to element distortion as well as rotations/translations (Childs et al., 2000).

When using pure Lagrangian models (Shih, 1996), chip formation is traditionally achieved by creating a separation surface in front of the tool tip, comprising elements which detach from the bulk workpiece through the use of a separation criterion (damage model). However, the disadvantage of this method relates to the capacity of elements to withstand the high strain, strain rate and temperature values typically found in machining (Sartkulvanich et al., 2004), which under certain circumstances could lead to a premature abortion of the analysis if no element deletion scheme was included.

2.4.4.3 Arbitrary Lagrangian Eulerian (ALE)

The ALE technique combines the features of both the Eulerian and Lagrangian approaches, which has been utilised by a number or researchers including Arrazola and Ozel

(2010) and Ozel et al. (2011) to simulate the cutting process with acceptable accuracy. The ALE method does not require a separation criterion to initiate chip formation, however excessive element distortion comparable to that encountered in pure Lagrangian models is also likely to occur.

2.4.4.4 ALE with adaptive remeshing (ALE/AR)

The utilisation of the ALE technique can be further enhanced with the addition of a remeshing procedure, so that the quality of the mesh can be maintained to avoid an early termination of the FE simulation. The technique however is inadequate for 3D simulations due to restrictions associated with the accurate prediction of chip morphology (e.g. serration, burr formation, etc.), hence only Lagrangian formulations incorporating damage models are considered to be the preferred option.

2.4.5 Friction models/contact conditions

Two distinctive frictional areas are formed at the tool-chip interface during machining, which are generally referred as the sliding (*lc*) and sticking (*lp*) regions respectively. The former is produced in the proximity of the tool tip while the latter is generated on the following portion of the tool-chip contact area, as shown in Figure 23:

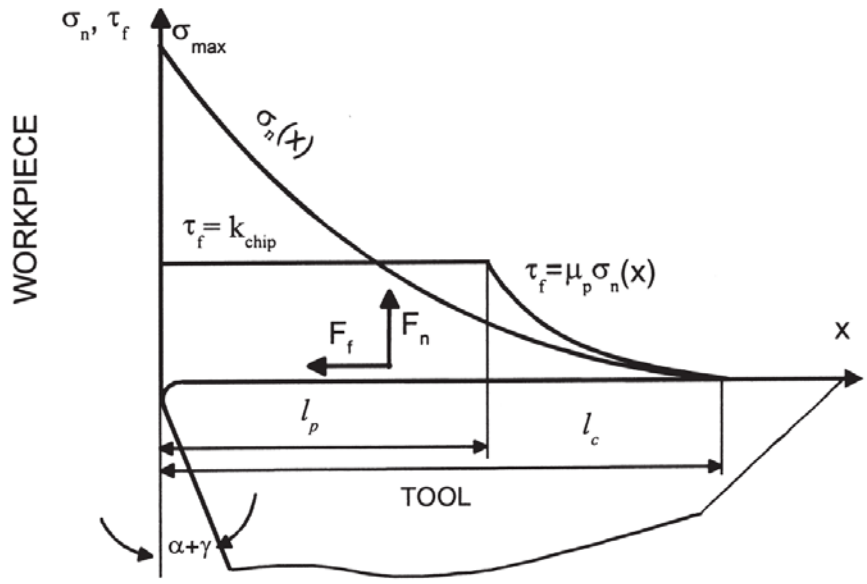

Figure 23. Sliding (*lc*) and sticking (*lp*) lengths outlined by Ozel (2006).

The maximum shear stresses $\bar{\tau}_f$ due to friction encountered at the sticking region are equivalent to the average value of the workpiece shear flow stress, hence $\bar{\tau}_f = k_{chip}$. Conversely, the shear stresses at the sliding region can be estimated using the Coulomb's friction model, therefore resulting in $\bar{\tau}_f = \mu_p \, \bar{\sigma}_n$. In general, it is difficult to calculate the lengths of the sticking and sliding regions by analytical means, with many researchers proposing empirical models as an alternative solution. In this regard, Ozel and Altan (2000) examined the influence of variable and constant friction and shear-based formulations when utilising the FE method to simulate the orthogonal cutting of low-carbon P20 mould steel (30HRc) with uncoated carbide tools at high cutting speeds. It was found that the predictions of stresses/forces together with chip morphology were more accurate when variable friction models based on experimental stress measurements were implemented. While somewhat successful, the methodology was laborious as essentially involved an iterative method to match the predicted and experimental cutting force data. Toropov and Ko (2003) studied the tool-chip contact length (which in turn determines the size of the zone where heat transfer between tool and workpiece takes place) issue by applying the analytical slip-line method in order to obtain a formula which could define the length. Following orthogonal cutting experiments on A6061 aluminium alloy, copper, SAE 1045 steel and STS 304 stainless steel at various cutting speeds with tools having rake angles of -5, 0, 5, 10 and 20º; the authors were able to demonstrate the validity/superiority of their solution for the tool-chip contact length over other ones previously obtained.

Filice et al. (2007) evaluated various friction models for the machining problem, namely Coulomb's, constant shear as well as those developed by Zorev (1963), Usui and Shirakashi (1997) and Childs et al. (2000). Even though the study was focused on AISI 1045 steel and one process configuration only, the authors found that outputs such as cutting force and contact length were not sensitive to the friction model of choice. They stressed however that friction may have more influence on the temperature distribution corresponding to the tool and that a model dealing with this issue was needed. A summary of recent contact length models available was presented by Iqbal et al. (2008), who assessed their applicability to the machining of Ti-6Al-4V alloy over a wide range of cutting speeds (60-300m/min) and feed rates (0.1-0.3mm/rev). Trials at the same feeds and different cutting speeds (198-879m/min) were also conducted on AISI 1045 steel to make useful comparisons. The investigation evidenced the inadequacy of the existing approaches to give an accurate prediction of the contact length for the cases under study, therefore the authors proposed two new models not only to cover a wider spectrum of machining conditions, but also contemplate the influence difficult-to-cut materials like Ti-6Al-4V have on friction.

An alternative recently utilised by Arrazola and Ozel (2010) to simulate the workpiece-tool interaction behaviour in metal cutting operations, defined a limiting shear stress in order to differentiate the sticking and sliding regions. By developing ALE/AR FE models comprising Eulerian and Lagrangian boundaries, the value of the limiting shear stress was found to be a major source of uncertainty as it was highly dependent on temperatures and local deformation conditions. Brocail et al. (2010) on the other hand, utilised the Coulomb's friction model when simulating the orthogonal machining of AISI 1045 steel at a cutting speed of 100m/min, a feed of 0.1mm/rev and a depth of cut of 3mm. Their formulation of the friction coefficient as being dependent on local variables such as contact pressure, tool-chip interface temperature and sliding velocity resulted in accurate predictions, however it is worth highlighting that the computation of the parameters necessitated to define μ_p was made by initially extracting the local variables from the numerical models, implying therefore that it was a time-consuming methodology.

2.4.6 Thermal effects/heat sources

Conduction heat transfer is one of the mechanisms responsible for distributing the temperature in the tool and workpiece during machining and is generally categorised as thermal contact conductance (TCC) or the heat transfer coefficient. The parameter details the temperature drop between two (ideally flat) surfaces in contact and is very sensitive to their respective mechanical states (e.g. surface roughness), as described in the early work of Cooper et al. (1969) and Mikic (1974).

The literature regarding the TCC parameter is limited, in part due to the inherent difficulties found when determining the value experimentally. Furthermore, the TCC values specified by researchers in various publications showed significant differences, which ranged from 10 to 100,000kW/m^{2}K (Iqbal et al., 2008). The lack of standards for calculating the TCC at the secondary shear zone have also conveyed to the use of arbitrary values (Torrano et al., 2011 and Courbon et al, 2011).

Practical techniques were proposed by Ceretti et al. (2007) and Jam and Fard (2011) to calculate the TCC parameter directly by correlating data obtained from machining experiments to numerical models. This leads to specific/unique TCC values for a given tool and workpiece material as well as cutting parameter combination. However the application of an average value for the thermal contact conductance can be justified when data on the thermal properties of the tool and workpiece are not available.

2.4.7 Criteria to initiate chip formation and predict its morphology

2.4.7.1 ALE/AR FEM

The modelling of the cutting process by using the ALE method assumes that plastic flow to predict chip formation/shape continuously occurs without any damage or fracture phenomenon taking place. Although this supposition can be argued from a physical point of view, the procedure of combining Eulerian and Lagrangian approaches has proved being efficient in giving reasonable predictions, as found out by Movahhedy et al. (2000). Following the use of the commercial FE software DEFORM-2D to simulate orthogonal machining assuming the cutting tool as a rigid body (with a rake angle of 10º, see Figure 24), a feed rate of 0.25mm/rev and arbitrary cutting velocities/workpiece material; the authors encountered that the ALE technique gave acceptable results without the need for using a remeshing procedure, however the analysis was preliminary and needed further refinement.

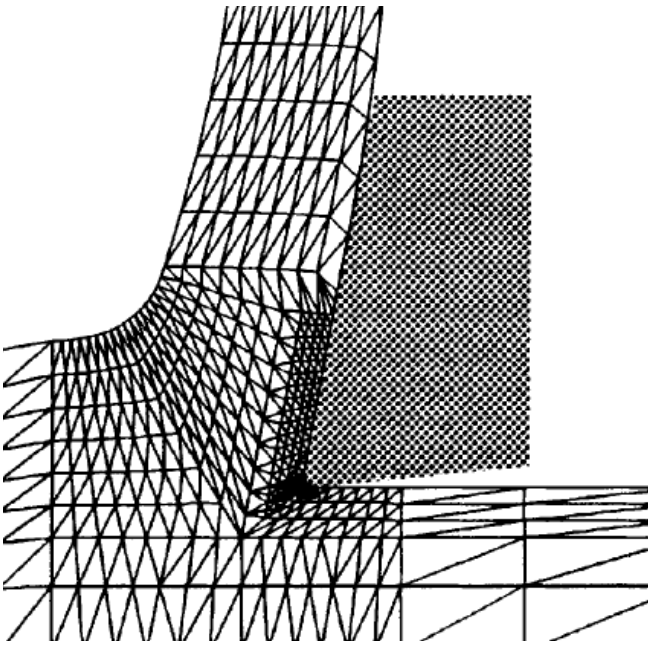

Figure 24. Resulting mesh configuration when simulating orthogonal machining using the ALE method (adapted from Movahhedy et al. (2000)).

To solve problems associated with the ALE method to develop more realistic FE models aimed at the modelling of the cutting process, researchers such as Arrazola et al. (2005) and Arrazola and Ozel (2010) incorporated the AR technique to their FE models. In the latter, a suitable mesh density at the tool tip together with adjusted remeshing parameters allowed output quantities such as energy, mechanical and thermal variables, etc. to be properly updated every time increment. Following the simulation of AISI 4340 steel when turned using uncoated carbide tools at a cutting speed of 300m/min and feed rate of

0.2mm/rev, it was showed that force predictions were as accurate as 97% and 100% for respective tangential and thrust components. Although the FE model gave acceptable results, trial and error iterations were needed to avoid a premature termination of the simulations due to mesh divergences. Lorentzon et al. (2009) incorporated a damage criterion when using the ALE/AR procedure, however fracture was produced on the chip free surface boundary rather than on the tool tip. It is thus concluded that this FE method is not appropriate to represent realistically the cutting operation, though it could be conveniently used to have a preliminary idea of it.

2.4.7.2 Damage/damage evolution models

2.4.7.2.1 Maximum principal strain

Due to its intrinsic simplicity, it is one the most employed alternatives to simulate ductile damage. The criterion basically specifies that when the maximum principal plastic strain (provided that ε_1^p, ε_2^p and ε_3^p are the principal plastic strains) exceeds a predetermined threshold effective strain value $\bar{\varepsilon}_{max}^p$, material fracture is initiated.

2.4.7.2.2 Johnson-Cook

Johnson and Cook (1985) experimentally analysed the fracture properties of OFHC copper, SAE 4340 steel and Armco Iron to develop an empirical damage model which accounted for the collective effects the strain, strain rate, temperature and pressure on the respective material's stress degradation behaviour. The level of damage (D) in an element is given by:

$$D = \frac{\Delta\bar{\varepsilon}^p}{\bar{\varepsilon}_{max}^p} \geq 0 \tag{44}$$

where $\Delta\bar{\varepsilon}^p$is the plastic strain increment, $\bar{\varepsilon}_{max}^p$ is the effective plastic strain to fracture and D is an internal (state) variable that increases monotonically with plastic deformation up to a value of 1, when total failure occurs. The term $\bar{\varepsilon}_{max}^p$, which is the equivalent plastic strain at the onset of damage, takes the form:

$$\bar{\varepsilon}^{p}_{max} = [d_1 + d_2\, exp(d_3\sigma^*)]\left[1 + d_4\, ln\left(\frac{\dot{\bar{\varepsilon}}^{p}}{\dot{\bar{\varepsilon}}_0}\right)\right]\left[1 + d_5\left(\frac{T - T_r}{T_m - T_r}\right)^{m}\right] \tag{45}$$

where $\sigma^* = \left(\sigma_{hyd}/\bar{\sigma}\right) \leq 1.5$, the hydrostatic (volumetric) stress $\sigma_{hyd} = -\sigma_{kk}\delta_{ij}/3$ and d_i $(i = 1..5)$ are damage constants. The JC damage model embedded in ABAQUS (ABAQUS, 2010) employs a slightly modified Eq. (45) and uses the exponential $-d_3$ instead of d_3, motivated by the fact that most materials experience a decrease in $\bar{\varepsilon}^{p}_{max}$ with increasing stress triaxiality; therefore d_3 will usually take positive values. Although the mathematical formulation of the fracture model is uncomplicated, considerable material fracture data are required to derive the various constants d_i.

2.4.7.2.3 Cockcroft-Latham (CL)

The damage model proposed by Cockroft and Latham (1968) states that the specific plastic work (work/volume) is the predominant mechanism for describing the failure of materials. The authors postulated that the maximum principal stress is responsible for triggering damage and consequently causing material failure. The relationship detailed in Eq. (46) was derived to describe the accumulated damage (C_1) in the material due to the applied stress:

$$C_1 = \int_0^{\bar{\varepsilon}^{p}_{max}} \sigma_1 \; d\bar{\varepsilon}^{p} \tag{46}$$

The parameter C_1 is a material constant that can be obtained from tensile tests while σ_1 is the maximum principal stress which takes the values:

$$\sigma_1 = \begin{cases} \sigma_1 & , \quad \sigma_1 > 0 \\ 0 & , \quad \sigma_1 \leq 0 \end{cases} \tag{47}$$

As discussed by Lorentzon et al. (2009), the CL model is thought to be valid when modelling damage in materials as the total plastic work generally remains constant when the material is strained. Temperature softening effects are likely to be sufficiently balanced by an increase in workpiece ductility due to strain rate effects, which is believed to be enough to assume that the total plastic work is kept constant. While the CL damage criterion can easily

be incorporated into a VUMAT subroutine, the model suggests that material failure occurs instantly upon reaching C_1, which is not usually the case for ductile metals.

2.4.7.2.4 Rittel-Wang-Merzer (RWM)

While recognising that adiabatic shear banding mechanisms are responsible for the strength degradation exhibited by certain materials under dynamic loading, Rittel et al. (2006) suggested the combined use of the elastic and plastic specific energies as the physical criterion for describing material softening, which is quantitatively described by:

$$W_{crit} = \int_0^{\bar{\varepsilon}_d^p} \sigma_{ij}\ d\varepsilon_{ij} \tag{48}$$

where σ_{ij} and ε_{ij} correspond to the stress and strain tensor components respectively. The upper integration limit $\bar{\varepsilon}_d^p$ relates to the level of strain at which the material strength begins to deteriorate. Subsequent decrease in material flow stress proceeds gradually, according to:

$$\bar{\sigma}' = \bar{\sigma}(1 - D^a) \tag{49}$$

where $\bar{\sigma}$ is the current flow stress level at a given effective plastic strain $\bar{\varepsilon}^p \geq \bar{\varepsilon}_d^p$, the term a is a constant and *D* as previously, is the degree of damage in the element (also varying from 0 to 1), which is defined in this case as:

$$D = \frac{W - W_{crit}}{W_{frac} - W_{crit}} \tag{50}$$

where W_{crit} and W_{frac} correspond to the energy values at the initiation and completion of fracture respectively.

2.5 Workpiece surface integrity

2.5.1 General aspects

Preliminary studies concerning the influence of cutting processes on resulting surface condition/quality commenced in the early 1950's (M'Saoubi et al., 2008), however the

definitions/classifications for the different characteristics of machined surfaces in terms of their mechanical and/or metallurgical attributes were only developed following the work of Field and Kahles (1964). The authors introduced the term *surface integrity* (SI) to describe the 'inherent or enhanced condition of a surface produced in machining or other surface generation operations', which included the physical, chemical and biological characteristics of the surface that can influence the functional performance of the fabricated part.

Further work by Field and Kahles (1971) and Field et al. (1972) extended the study of workpiece SI measures, which included metallurgical alterations such as microcracking, residual stresses distribution, (excessive) plastic deformation, phase/grain size alterations, craters/laps, etc. This led to the development of a methodology for defining surface integrity involving three primary data sets, each having experimental information with varying degrees of complexity, see Table 4. The selection of the respective data set (minimum, standard or extended) is typically on the likely impact of surface integrity on component functioning and application conditions.

Minimum SI data set	**Standard SI data set**	**Extended SI data set**
Surface finish Microstructure (10× or less Microcracks Macrocrack indications Microstructure Microcracks Plastic deformation Phase transformation Intergranular attack Pits, tears, laps, protrusions Built-up edge Melted and re-deposited layers Selective etching Microhardness	Minimum SI data set Fatigue test (screening) Stress corrosion test Residual stress and distortion	Standard SI data set Fatigue test (extended to obtain design data) Additional mechanical tests Tensile Stress rapture Creep Other specific tests (e.g., bearing performance, sliding friction evaluation, sealing properties of surface)

Table 4. Suggested surface integrity data sets depending on the information required (adapted from Field and Kahles (1971)).

The established SI framework was subsequently used by the majority or researchers as a basis for evaluating workpiece surface integrity following machining. Bailey et al. (1976) investigated the effects of varying speed (9.6, 18.6, 38.4, 76.2 and 152.4m/min) on surface roughness, workpiece microstructure and hardness following dry machining of tempered AISI 4340 steel (56HRc) at a fixed feed rate of 0.13mm/rev. Experimental techniques such as optical microscopy, scanning electron microscopy, X-ray microprobe analysis, microhardness

measurement and profilometry were utilised to such end, with results in all cases, except when machining at 9.6m/min, showing the appearance of a damaged surface, different in composition (consisting of a white layer of untempered martensite, a dark layer of bainite and a darker layer of overtempered martensite) and hardness from the bulk (~60-65HRc). This was believed to be caused by the high temperatures generated due to friction and high cutting speeds employed.

Brinksmeier et al. (1982) in collaboration with several research laboratories, reported on the advances in residual stresses measurement techniques (X-ray diffraction, deflection etching techniques, etc.) in metal cutting operations. It was highlighted that determination of the residual stress condition (tensor) is vital to fully evaluate the properties of a machined surface.

Matsumoto et al. (1986) assessed the effect of workpiece hardness on residual stresses following the cutting of AISI 4340 steel. By utilising a reflection electron technique, the formation of austenite and untempered martensite was detected in the machined subsurface layer, which exhibited a white-ish colour when viewed under a conventional optical microscope or scanning transmission microscope. Residual stresses were found to be compressive near the machined surface but tensile within the bulk material.

Apart from alloy steels, surface integrity investigations when machining advanced aerospace materials such as (aged) Inconel 718 superalloy, in particular when using regular and controlled contact length (0.15mm) cemented carbide tools have also been reported (Sadat, 1987). In order to limit the quantity of independent variables, orthogonal cutting conditions were specified involving a constant feed of 0.1mm/rev at variable cutting speeds of 6.6, 18, 36 and 60m/min, for both dry and wet environments. Irrespective of the type of cutting tool and environment employed, surface damage was clearly evident in all tests, which included for example cracks, cavities and grooves. It was also observed that an increase in cutting speed generally corresponded to a decrease in white layer thickness, and involved higher tensile residual stresses with maximum values near the machined surface, as shown in Figure 25:

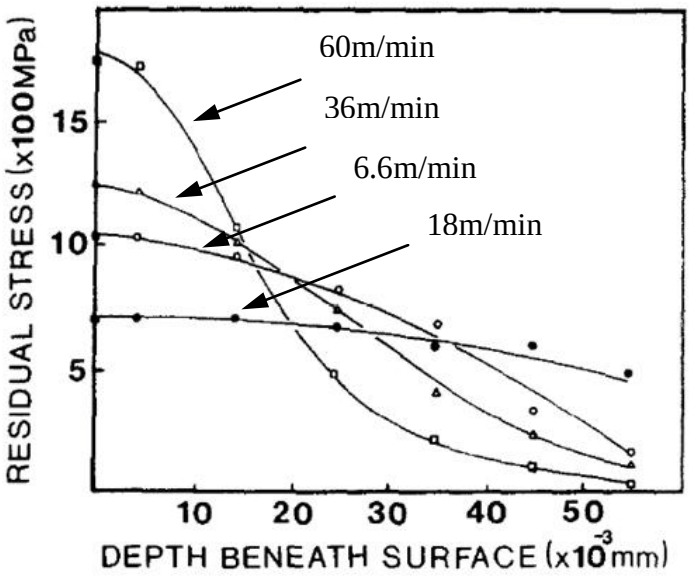

Figure 25. Residual stress distributions measured by Sadat (1987) when machining Inconel 718 with natural contact length tools at different cutting speeds.

Similarly, subsequent work by Sadat and Reddy (1992, 1993) on the turning of Inconel 718 with uncoated carbides at cutting speeds of 50 and 60m/min also showed the presence of cracks/tears together with low tensile residual stresses on the machined surface. The latter were supposed to decrease for increasing cutting speeds due to the important role tool wear would play.

Mantle and Aspinwall (1997) investigated the influence of operating parameters on surface integrity and fatigue life when turning gamma titanium aluminide using carbide tools. Baseline parameters of 25m/min with a feed of 0.1mm/rev and a depth of cut of 0.7mm were initially assessed with subsequent trials expanding the range of machining conditions from 10 to 40m/min in cutting speed, 0.05 to 0.35mm/rev in feed rate and 0.1 to 0.7mm in depth of cut, in order to identify preferred parameters levels corresponding to minimal surface damage and/or modifications. Subsequent signs of material cracks/pull-out together with a hardened white layer were seen irrespective of the cutting conditions, which had a detrimental effect of the fatigue performance.

Matsumoto et al. (1999) evaluated machinability aspects of hard turning AISI 52100 bearing steel (52-58HRc) using CBN tools as an alternative to conventional grinding operations. Despite varying tool geometries, feed rates and depths of cut, all of the machined specimens exhibited compressive surface residual stresses in contrast to results for grinding. Tool edge geometry (e.g. chamfered, honed, etc.) had a significant influence on the residual workpiece stresses distribution, while the effect of feed and depth of cut was negligible. Cross sectional micrographs however showed evidence of a ‘dark layer’ (composed of overtempered

martensite) on the machined surface comparable to that reported previously by Abrao and Aspinwall (1996).

Similarly, Barbacki et al. (2003) assessed the feasibility of hard turning using CBN20 and MC2 mixed ceramics inserts as an alternative to the grinding of hardened steels such as AISI 52100, AISI M2 and AISI L6. Although white and dark layers on the machined surface were observed in line with previous investigations, micrograins of ferrite were found in the white layer, where the thickness varied with cutting speed, depth of cut and tool wear. In general, the performance of both machining operations was shown to be approximately equivalent, with minimal differences seen in terms of workpiece microstructure, residual stresses, mesohardness and surface roughness.

Che-Haron and Jawaid (2005) carried out dry turning tests on Ti-6Al-4V aerospace alloy using carbides at cutting speeds of 45, 60, 75 and 100m/min with feeds of 0.25 and 0.35mm/rev and a constant depth of cut of 2mm. A 10µm thickness hardened white layer was evident following trials at 100m/min for the first 10s of operation, including surface tearing and severe plastic deformation (see Figure 26a). A distorted and no microstructurally altered layer was seen when cutting at 45m/min however, as shown in Figure 26b:

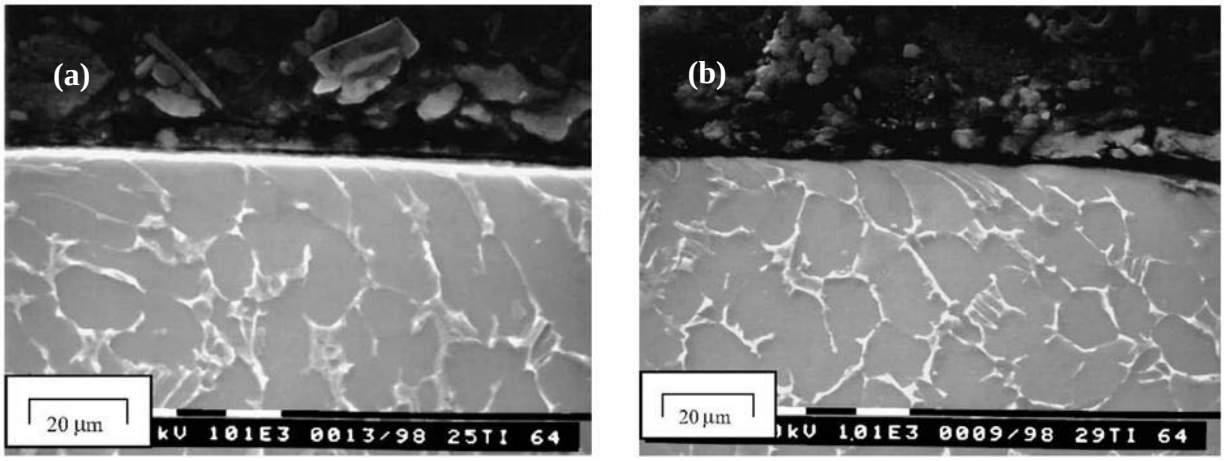

Figure 26. (a) While layer appearance when machining at 100m/min, (b) Excessive plastic deformation evidenced on the surface when cutting at 45m/min (Che-Haron and Jawaid, 2005).

Subsequent work involving AISI D2 tool steel machined with coated and uncoated carbide tools at cutting speeds of up to 600m/min undertaken by Che-Haron et al. (2007), showed that surface roughness decreased at higher cutting speeds, with uncoated tooling producing larger values. Outeiro et al. (2008) analysed the residual stresses distribution in the machined layer following turning trials on AISI 316L under dry conditions. By utilising uncoated tools at a cutting speed of 125m/min, a feed of 0.05mm/rev and a depth of cut of

2.5mm, residual stresses measured using the X-ray diffraction technique, were tensile on the surface but shifted to a compressive regime at a distance of ~10-25μm beneath the cut surface. The maximum values recorded however were generally in line with previously published results.

Following a summary of the standard procedures for measuring residual stresses when machining hardened steels, titanium alloys and nickel-based superalloys, Guo et al. (2009) presented a critical review of research relating to the modelling and prediction of surface integrity parameters. The authors concluded that micro, meso and macro scales effects must be considered collectively in FE simulations to accurately predict residual stress distributions generated in machined surfaces, in agreement with Simoneau et al. (2006).

Umbrello and Jawahir (2009) developed a FE model to predict white layer formation when machining AISI 52100 hardened steel. This was achieved accounting for material phase transformations in the constitutive model, which was implemented via a customised code that also estimated the hardness of the deformed layer. Results from the simulations showed corresponding experimental data, see Figure 27:

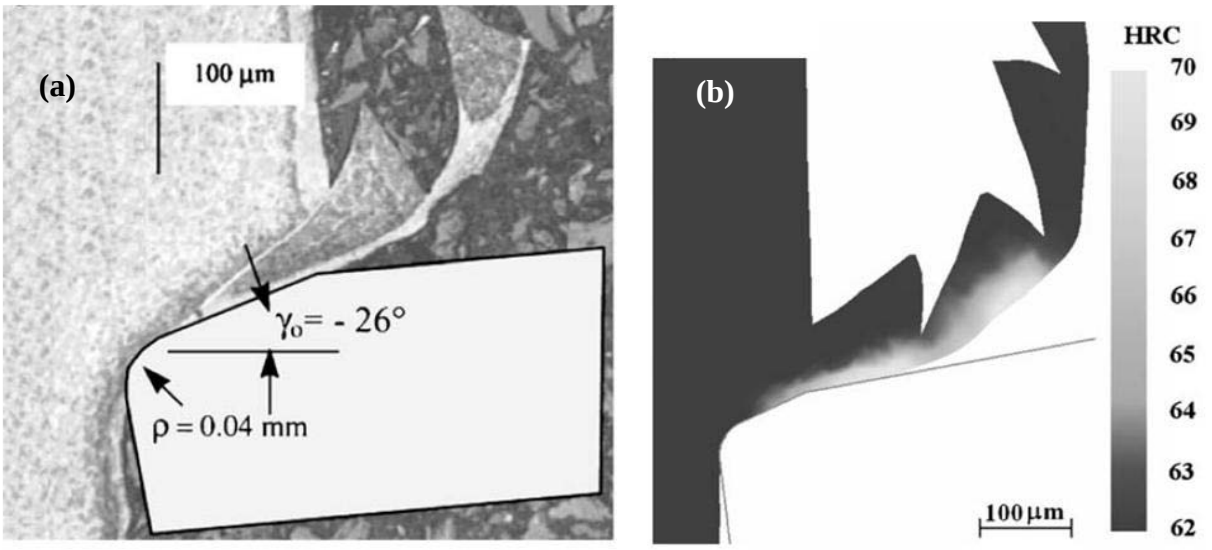

Figure 27. (a) Cross section micrograph evidencing the appearance of a white layer when cutting AISI 52100 hardened steel at 100m/min, (b) FE model predicting white layer formation, according to Umbrello and Jawahir (2009).

Although the general trend indicated that the thickness of the white layer increased with both cutting speed and feed rate and initial workpiece hardness, the FE model did not account for the formation of dark layers, hence necessitating further refinement.

In order to understand the influence of cutting parameters and tool wear on white and dark layers when orthogonally machining AISI 52100 bearing steel, Cappellini et al.

(2010) conducted a series of tests with PCBN (CBN100) tools at cutting speeds of 250 and 350m/min and feed rates of 0.1 and 0.125mm/rev. The thickness of the white layer increased with cutting speed and feed rate as opposed to a reduction in dark layer thickness.

In succeeding work, Umbrello et al. (2010) developed a numerical model to predict workpiece surface residual stresses due to alterations in the microstructure. The trials were performed in dry conditions at cutting speeds ranging from 75 to 250m/min resulting in white and dark layers on the machined surface with compressive residual stresses recorded in all situations. The research suggested that better correlation between predicted and experimental measurements of residual stresses were obtained when workpiece microstructural variations are incorporated in the FE model.

Rao et al. (2011) employed FE methods to model tool wear as well as residual stress patterns generated when face milling Ti-6Al-4V alloy. The tool wear simulation exhibited a reasonable characterisation of the experimentally observed tool chipping/notch wear, which were the primary wear patterns encountered irrespective of cutting conditions, caused by the elevated pressures and temperatures at the tool-chip interface. Average surface roughness (R_a) and residual stresses were found to be ~0.4μm and of compressive nature respectively, with the latter increasing when the feed rate did so (but only when employing high cutting speeds). It was also found that the effect of cutting speed was negligible on the generated pattern of residual stresses.

Recent publications by Jawahir et al. (2011) and Ulutan and Ozel (2011) critically assessed the latest developments and applications of advanced experimental analysis techniques for in-depth surface integrity characterisation. This included X-ray diffraction, Scanning Electron Microscopy (SEM), Electron Backscatter Diffraction (EBSD), Raman spectroscopy, acoustic methods and recrystallisation techniques for examining plastic strains, which are increasingly being employed by researchers for detailed assessment of workpiece microstructural variations and damage following machining operations.

One of the latest investigations carried out by Pu et al. (2012) on AZ31B alloy proposed to cool the cutting tool down by spraying liquid nitrogen in order to avoid surface modifications due to high machining temperatures and thus, improve the performance of the part. The orthogonal cutting strategy, known as cryogenic, was aimed at a speed of 100m/min and a feed of 0.1mm/rev together with the use of uncoated carbide tools. A white layer composed of refined grains (size of ~30nm compared to 12μm in the bulk) formed following all the trials, meaning that dynamic recrystallisation due to severe plastic deformation (and not to elevated temperature) had taken place. In conjunction with producing an enhanced surface roughness pattern and the generation of compressive residual stresses belonging to a

soft (and thus not fragile and prone to fracture) white layer, the authors were able to obtain an important understanding on how to deal with SI parameters which could degenerate the properties of the machined part.

2.5.2 Dynamic recrystallisation (DRX)

Recrystallisation is a metallurgical phenomenon that involves the formation of new grains to replace thermo-mechanically deformed microstructure typically occurring at high strains and/or temperatures. The process is usually associated with nucleation and growth mechanisms that induce an initial softening/reduction in material strength due to the strain-free (or dislocation-free) nature of the new grains and, (when used appropriately) can also act as method for controlling the final microstructure of a product, as outlined by Doherty et al. (1997).

When a material is thermo-mechanically processed in the plastic region, the average dislocation density grows along with the stored energy, which is subsequently released (reduced) in three consecutive processes; namely recovery, recrystallisation and grain growth. Three regimes characterising the grain refinement mechanism have been identified; static, dynamic and meta-dynamic (Antolovich and Evans, 2000). Static and meta-dynamic recrystallisation refer to the occurrence of grain refinement after a period of time following the plastic thermo-mechanical operation, whereas dynamic recrystallisation (DRX) takes place while the material is being deformed (Doherty et al., 1997).

Thermo-mechanical processes that result in DRX include hot rolling (Liu and Lin, 2003), hot compression (Medeiros et al., 2000) and forging (Park et al., 2001) to name but a few, where operating temperatures are typically more than half the melting temperature of the workpiece material. However, a recent study published by Murr and Pinaza (2007) proved that DRX can also occur at ambient temperature, provided that materials are deformed at relatively high strain rates (>1,000s^{-1}). The authors investigated processes where dynamic deformation is significant, such as shaped charge jet formation, rod penetration into thick targets, elevated velocity impact crater formation, projectile-induced target plug formation including failure, friction-stir welding and explosive welding, excessive plastic deformation, usually associated with the occurrence of adiabatic shear bands (ASB); and found that dynamic recrystallisation plays a major role for producing refined grains. Analysis of workpiece microstructural alterations following high-velocity/impact/friction processes

showed that DRX was the predominant mechanism leading to solid-state flow during plastic deformation. In addition, DRX was found to be generated of either local or large scale ASB.

A comprehensive study carried out by Rittel et al. (2008) involving high strain rate ($3{,}000s^{-1}$) shear deformation of Ti-6Al-4V samples using a SHPB instrument at room temperature also demonstrated that DRX can occur in the absence of elevated temperatures, and preceded the formation of ASB, see Figure 28:

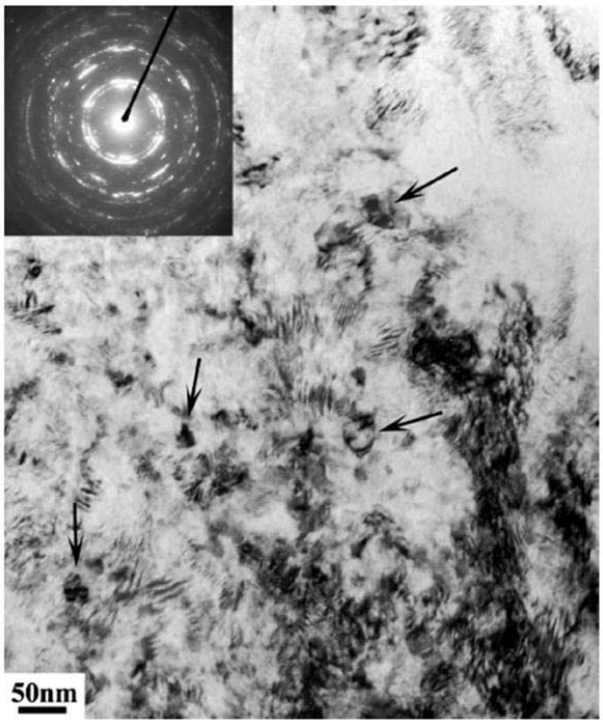

Figure 28. TEM micrograph showing recrystallised grains (arrowed) following high strain rate deformation of Ti-6Al-4V samples (Rittel et al., 2008).

Furthermore, they stated that the dynamic stored energy of cold work was responsible for generating ASB, which in turn could be thought of as the driving force for the occurrence for DRX; concluding that the DRX phenomenon was not only produced by high temperature thermo-mechanical processes, but also, it could be originated in circumstances when shear plastic deformation is severe and could lead to the appearance of ASB.

With regard to machining operations, Bushlya et al. (2011) observed the occurrence of workpiece DRX when dry machining aged Inconel 718 at cutting speeds of up to 400m/min with new/semi/worn Al_2O_3-SiC_w ceramic tools. This was apparent from the very fine recrystallised grains composing the white layer formed immediately below the cut surface as seen in high resolution transmission electron microscopy.

Similarly, Zhou et al. (2011) when evaluating the effect of tool wear on the machined surface of Inconel 718, found quantitative evidence showing that the white layer

was composed of fine grains, in particular when utilising worn tools, as shown in the EBSD maps in Figure 29:

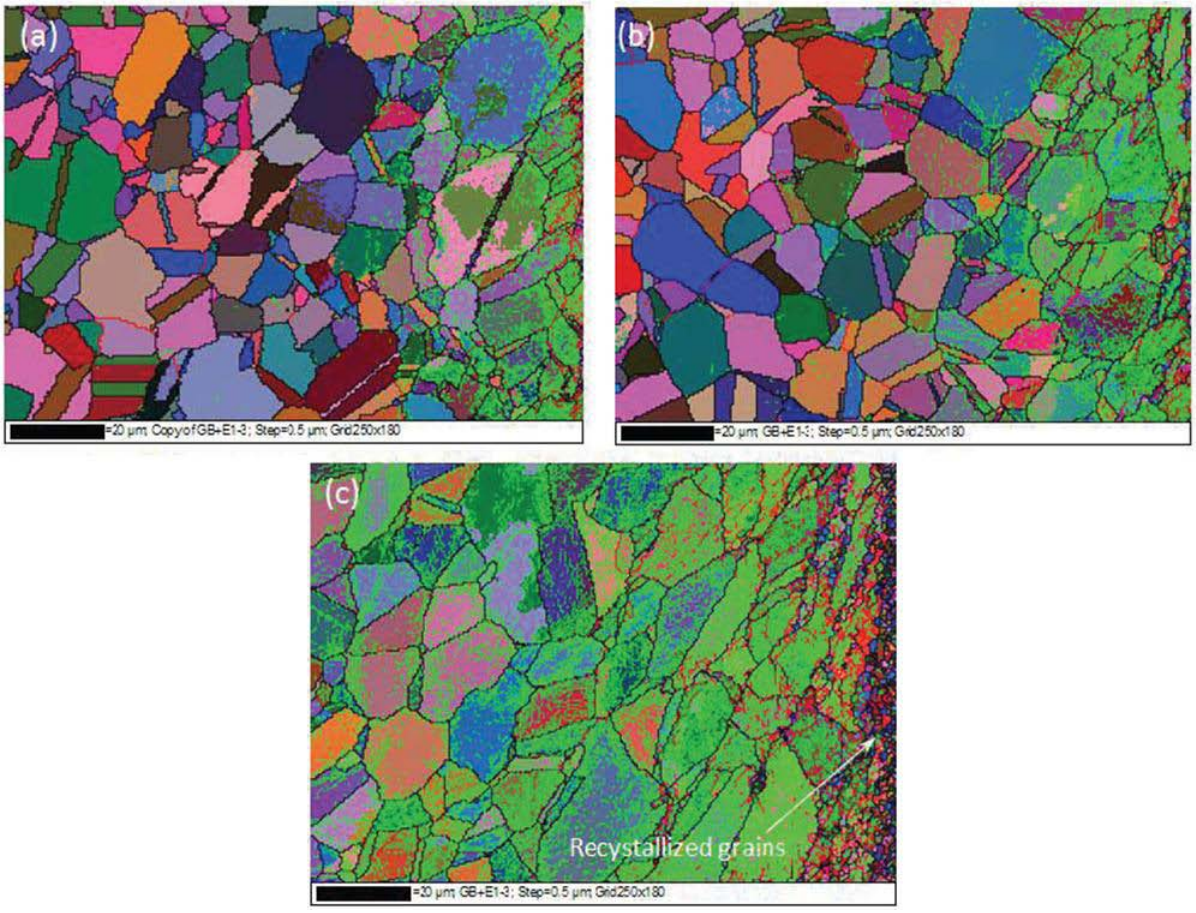

Figure 29. EBSD maps of workpiece subsurface machined with (a) new, (b) semi-worn and (c) worn tools, evidencing the appearance of refined grains in the latter, according to Zhou et al. (2011).

All tests involving new, semi-worn and worn cutting tools were performed in wet conditions using a cutting speed of 300m/min, a feed of 0.2mm/rev and a depth of cut of 0.3mm. While the tool wear condition did not appear to influence the size of the recrystallised grains (~200-300nm), the thickness of the white layer was seen to increase with wear level. By employing a range of analysis techniques including 3D optical microscopy, nano-indentation, X-ray diffraction, high resolution SEM, TEM and EBSD, M'Saoubi et al. (2012) evaluated workpiece surface integrity over different length scales following turning of Inconel 718 using polycrystalline cubic boron nitride (PCBN) and physical vapour deposition (PVD) coated cemented carbide inserts at cutting speeds of 200-300m/min and 60-90m/min respectively, while maintaining a constant feed of 0.15mm/rev and depth of cut of 0.25mm. In addition to the presence of tears and cavities on the machined surface, recrystallised fine

grains were observed on the subsurface region irrespective of the cutting tools employed, as evident from the EBSD maps shown in Figure 30:

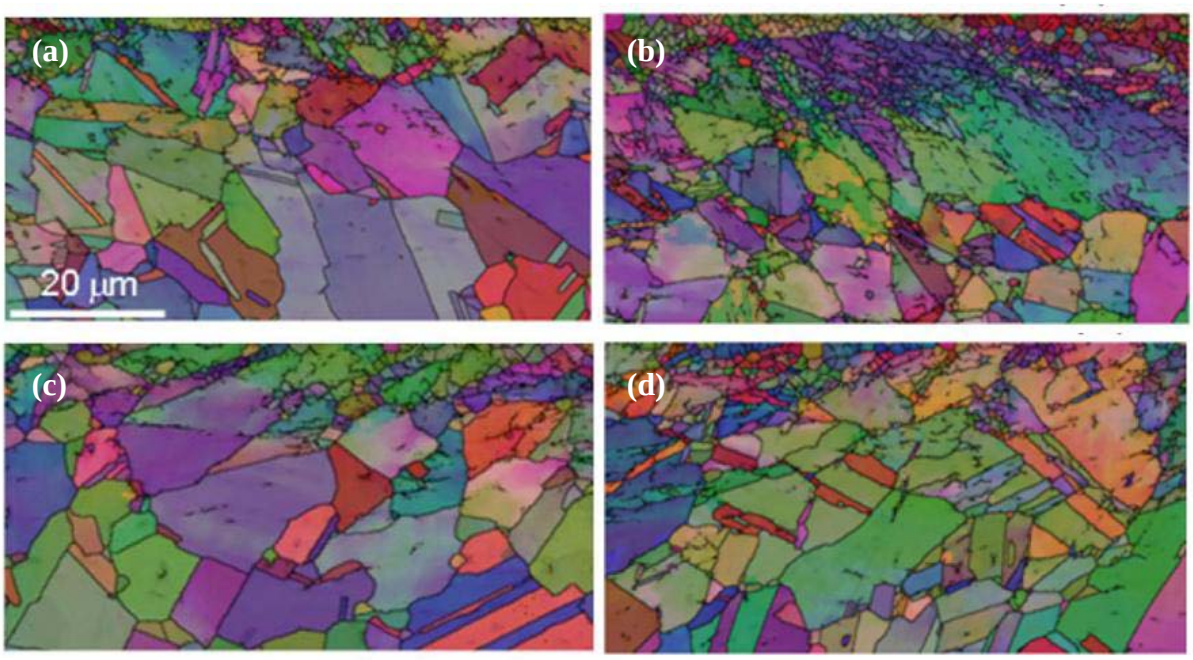

Figure 30. Cross sectional EBSD maps of workpiece microstructure showing DRX when cutting Inconel 718 with (a) new carbide at 90m/min, (b) worn carbide at 90m/min, (c) new PCBN at 300m/min, (d) worn PCBN at 300/min, according to M'Saoubi et al. (2012).

2.5.3 FEM of DRX following machining processes

Finite element techniques have been successfully employed to model material dynamic recrystallisation following hot deformation processing of Inconel 718 (e.g. forging, hot rolling, etc.). Several different numerical approaches however have been developed for the prediction of grain size due to DRX, which includes the use of state variables (Zhao et al., 2004), a meta-dynamic regime (Brand et al., 1996) as well as formulations that have involved the coupling of dislocation density, recrystallised fraction and flow softening factors (Lin et al., 2007), to cite but a few.

Conversely, research focused on simulating the recrystallisation of workpiece microstructure after machining is relatively scarce, not least due to the inherent need for developing complex user-defined codes, as well as the lack of associated experimental data. However, initial work recently commenced with Ding and Shin (2011), who proposed a criterion linking the average dislocation density to grain size in order to represent the DRX process following the orthogonal cutting of commercially pure titanium (CP Ti) at a cutting

speed of 36m/min. The principal features of the workpiece's mechanical/metallurgical behaviour were defined via a user-defined subroutine and implemented into a coupled Lagrangian-Eulerian FE model. The predicted grain size of the recrystallised material beneath the machined surface and regions in the chip was as small as 100nm. More recently, Rotella et al. (2012) developed a FE model that simulated DRX following the turning of AA7075-T651 alloy at cutting speeds of 180, 320 and 720m/min with K313 uncoated carbide tools having various tip radiuses. Due to the aggressive dry cutting conditions employed, recrystallised microstructure directly under the cut surface was observed in all cases, to decrease in size as the cutting speed and tool nose radius increased. Close correlation with experimental results however were accomplished via trial and error calibration of the model, which was a time consuming operation and suggested that further improvements were needed.

2.6 Recapitulation

The material removal operation by turning has been all this time a well recognised and utilised method in industry to fabricate parts (either simple or complex in shape) that have to satisfy several mechanical requirements. In particular for the aerospace industry, in which safety comes utterly in the first place, the machinability demands that different workpiece materials such as Ti-6Al-4V and Inconel 718 must meet are so elevated that it is essential to quantify plausible part/surface defects, imperfections and deficiencies the process could provoke so that an unexpected material failure could be avoided. In this regard, research on both advanced materials is substantially vast and has focused not only on the influence diverse cutting conditions have on the quality of the machined part/surface, but also on the benefits the use of different cutting tools could bring.

Due to the high manufacturing costs of such aerospace alloys and the increasing need for studying more in depth (and other than analytically due to its shortcomings) any workpiece surface alteration the turning process could produce, alternative techniques like those numerical (in particular the finite element method) were introduced and proved to be a more complete analysis tool. Commercial FE packages such as DEFORM, ADVANTEDGE and ABAQUS have been used by researchers to predict cutting forces, chip morphology, tool and workpiece temperatures and more recently surface integrity parameters such as white layer formation, residual stresses distribution, etc. with reasonable accuracy. Nevertheless little research has focused on the FE simulation of turning operations in 3D, due to the inherent complications of the study itself.

The Arbitrary Lagrangian Eulerian method together with the use of an Adaptive Remeshing procedure works well in 2D and has been successful in making estimations regarding chip formation/morphology, however if the analysis is upgraded to 3D the technique becomes invalid if a long chip wants to be modelled. Similarly, the implementation of artificial separation layers to generate any chip is suitable (though not realistic) only in 2D, as for more complex geometries, like those encountered in real life, the arbitrary definition of a path beforehand in which damage will take place is debatable. Hence, if a reliable representation of any cutting process is desired to draw realistic conclusions, 3D FE models including a damage criterion (irrespective of its formulation), should be the trend to follow.

Aspects not hitherto fully investigated by experimental techniques and/or numerical means can be individualised in two separate areas. The first one is associated with the sticking and sliding frictional zones that are encountered between the chip and the cutting tool, which present enormous problems when trying to quantify them in FE models, leaving researchers in some cases with no other possible resort but to utilise the simple Coulomb's friction model. The following area that has not been completely understood is concerned with the proper quantification of the thermal contact conductance, which is in general adopted arbitrarily by investigators.

Due to the fundamental characteristics of the cutting process, an appropriate workpiece material characterisation becomes critical to guarantee accurate predictions. In this sense, the most common constitutive model that has been employed is that developed by Johnson and Cook (1983), however for advanced materials such as Ti-6Al-4V and Inconel 718, it exhibits worrying limitations. In addition, the combined effects of strain, strain rate and temperature on the material's response are not well established. Hence, in an attempt to overcome the difficulties associated with the material model, investigators have arbitrary incorporated terms to make it agreeable with experimental data instead of utilising more reliable models that are readily available. An easy example of this is the physical-based Mechanical Threshold Stress model, which was developed in the late 1980's for high strain rate applications and later proved to be appropriate when high temperatures were also involved. As far as the author is concerned, no researcher has implemented this constitutive model to the machining problem, not only because it is highly complex and the quantity of constants to be calculated is numerous, but also due to the many challenges when implementing it in FE modelling.

Regardless of the constitutive model selected to work with, the generation of low/high strain rate and temperature flow stress data is essential to develop it. While in the former case standard testing machines can be employed, the latter involves the use of more

sophisticated equipment due to the extent of strain rates to achieve (>1,000s^{-1}). In this regard, the familiarly known Split Hopkinson Pressure Bar apparatus has been the preferred choice to perform tests at such extreme conditions not only to identify how the material behaves when considerable rates of deformation and temperatures occur, but also to use the data acquired to compute the constants needed for any constitutive model. The literature available presents a respectable amount of information in relation to the JC parameters for Ti-6Al-4V, however this is not the case when the attention is put on Inconel 718, where data are scarce.

Recent work on the FE modelling of machining has been carried out to contemplate situations in which alterations of the machined layer are expected to take place. As plastic strains, strain rates and temperatures are likely to be high in conventional manufacturing operations, surface damage in conjunction with other defects, such as tears, laps, cracks, etc. are possible to appear and therefore, could diminish the lifetime of the workpiece material (when not causing its catastrophic failure). When paying attention to surfaces that exhibit dynamic recrystallised grains following the turning process, a handful of studies are found, principally because of the many complications that appear when developing FE models that could predict such microstructural event.

CHAPTER 3

EXPERIMENTAL WORK

3.1 Workpiece material and tooling

3.1.1 Ti-6Al-4V alloy

The workpiece material consisted of a 105mm diameter x 100mm length bar of Ti-6Al-4V (alpha-beta alloy) in the annealed condition. A unique face grooving operation was performed in advance to produce a 1mm thick tube section so that orthogonal cutting conditions could be properly simulated, see Figure 31:

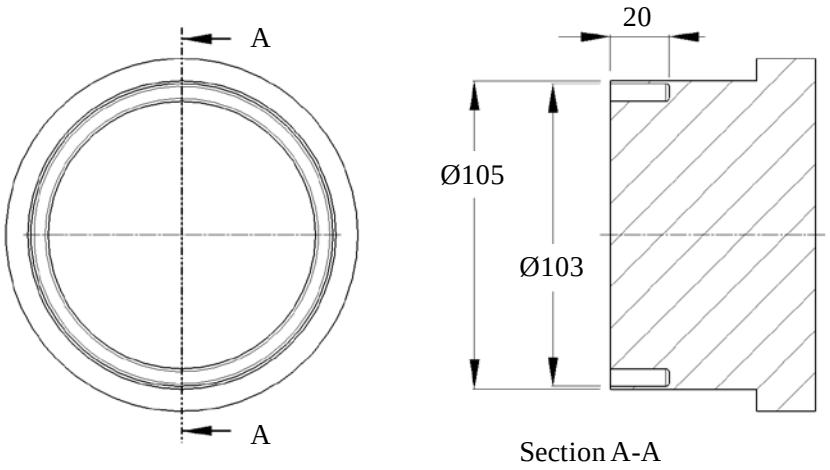

Figure 31. Resulting Ti-6Al-4V workpiece geometry derived from the unique face grooving operation (dimensions in mm), for reference only.

All experimental trials involved SANDVIK tungsten carbide inserts (K20) commercially designated as TCMW 16T308 H13A. In order to make both the 2D and 3D FE models as representative as possible (of the workpiece and the cutting tool), a measurement of the insert edge radius was performed on an Alicona G4 InfiniteFocus optical system, which is shown in Figure 32:

Figure 32. Alicona G4 InfiniteFocus optical system.

In spite of the cutting edge being normally sharp, it had a radius of 31.28μm. The 3D insert scan together with a 2D profile including some general dimensions, are given in Figure 33:

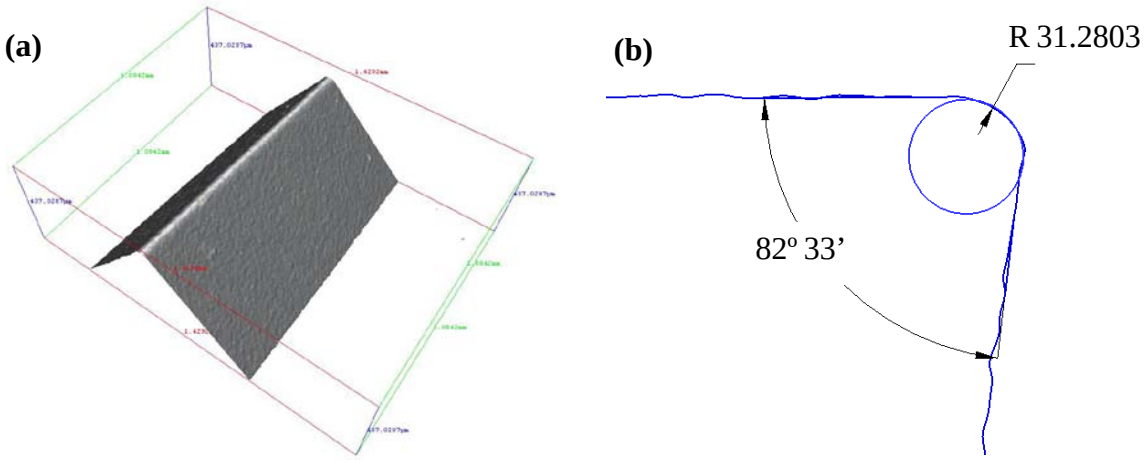

Figure 33. (a) 3D plot of the carbide insert edge captured with an Alicona G4 InfiniteFocus optical measuring system, (b) 2D profile obtained from the previous 3D plot (dimensions in μm).

The corresponding toolholder (SANDVIK STGCR 2525M 16) provided rake and clearance angles of 0º and 7º respectively. Three different cutting speeds of 60, 90 and 120m/min were used at a fixed feed of 0.125mm/rev, which were similar to those employed by Calamaz et al. (2008), Sima and Ozel (2010) and Ozel et al. (2010) in their studies.

A standard metallographic procedure was followed to reveal the workpiece material and swarf/chips microstructure. Hot compression mounting of samples was performed on a Buehler SimpliMet2 Mounting Press (see Figure 34a). Grinding and polishing operations

were carried out on an automatic single platen Buehler Alpha 2 speed grinder-polisher incorporating a Vector LC 250 Power Head, as shown in Figure 34b:

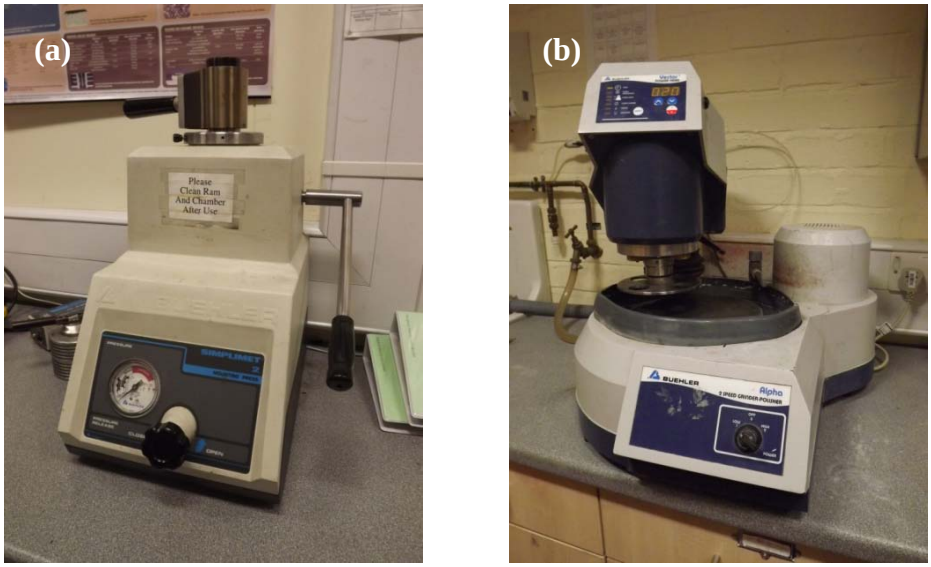

Figure 34. (a) Buehler SimpliMet2 Mounting Press, (b) Buehler Alpha 2 speed grinder-polisher.

See Table 5 for details of process sequence and abrasives.

Surface	Abrasive/Size	Force (N)	Speed (rpm)/Direction	Time (s)
Abrasive disc (waterproof paper)	600 grit SiC water cooled	27	300/Comp.	30
	800 grit SiC water cooled	Hand	-	-
	1,200 grit SiC water cooled	27	300/Comp.	300
Buehler Ultra-Pol cloth	9µm Buehler Metadi Supreme Diamond suspension	27	300/Comp.	300
	6µm Buehler Metadi Supreme Diamond suspension	27	300/Comp.	240
	3µm Buehler Metadi Supreme Diamond suspension	27	300/Comp.	240
Buehler Microcloth	0.06µm MetPrep colloidal silica	27	300/Contra.	360

Table 5. Characteristics of grinding and polishing methods performed on Ti-6Al-4V.

The final etching procedure of the highly polished specimens took place in the School of Metallurgy and Materials, using Hydrofluoric acid (HF) etchant. Figure 35 shows the microstructure of the Ti-6Al-4V workpiece material, which clearly evidences roughly equiaxed alpha and transformed beta phases.

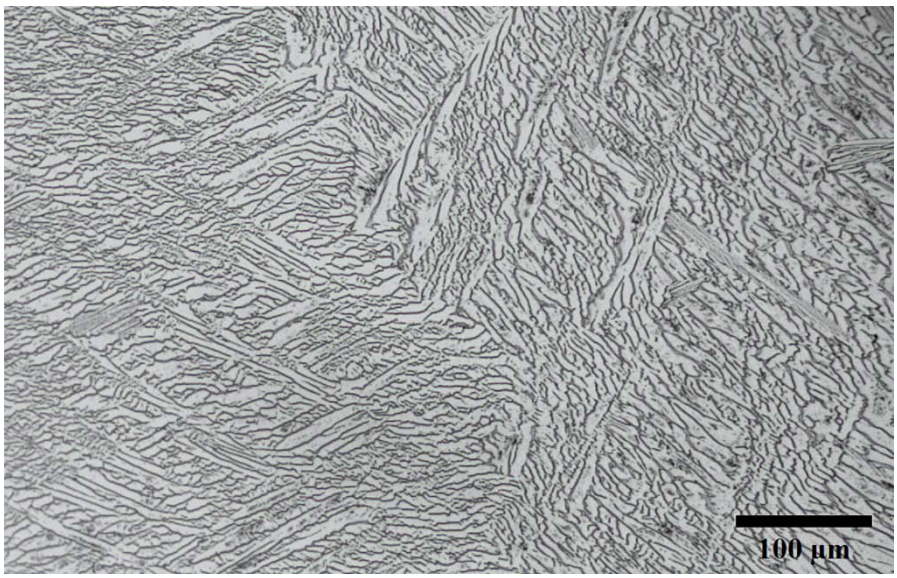

Figure 35. Microstructure of Ti-6Al-4V following etching with HF reagent.

3.1.2 Inconel 718 superalloy

The workpiece material was a bar of Inconel 718 with a chemical composition of Ni-19Cr-18.5Fe-5.1Nb-3Mo-0.9Ti-0.5Al-0.6C (wt.%) in the aged condition supplied by Rolls Royce (Soo, 2003). The hardness of the bulk material was measured utilising a Mitutoyo HM-122 microhardness instrument, shown in Figure 36, and found to be 45±1HRc.

Figure 36. Mitutoyo HM-122 microhardness testing machine.

Workpiece heat treatment involved: 1) Solution treatment at 950-980°C (1hr) followed by air cooling, 2) Precipitation treatment at 720°C (8hrs) and furnace cooling to 620°C, 3) Precipitation treatment at 620°C (8hrs) and air cooling. Table 6 details the grinding

and polishing sequences used on hot mounted samples of Inconel 718 to determine microstructure.

Surface	Abrasive/Size	Force (N)	Speed (rpm)/Direction	Time (s)
Abrasive disc (waterproof paper)	600 grit SiC water cooled	27	300/Comp.	30
	800 grit SiC water cooled	Hand	-	-
	1,200 grit SiC water cooled	Hand	-	-
Buehler Ultra-Pol cloth	9μm Buehler Metadi Supreme Diamond suspension	Hand	-	-
	6μm Buehler Metadi Supreme Diamond suspension	Hand	-	-
	3μm Buehler Metadi Supreme Diamond suspension	Hand	-	-
Buehler Microcloth	0.06μm MetPrep colloidal silica	27	300/Contra.	480

Table 6. Characteristics of grinding and polishing methods performed on Inconel 718.

The exercise proved difficult and the procedures had to be repeated several times before producing acceptable results, with many of the operations performed by hand to ensure complete removal of scratches. In order to reveal the workpiece microstructure, Kalling's N°2 reagent (40-80ml ethanol, 40ml HCl, 2g of $CuCl_2$) was utilised. As observed in Figure 37, the grain size varies from 80-100μm, while the presence of Ni_3Al and Ni_3Ti compounds are visible clearly, whose primarily function is related to the enhancement of the temperature strength and creep properties of the superalloy (Donachie and Donachie, 2002).

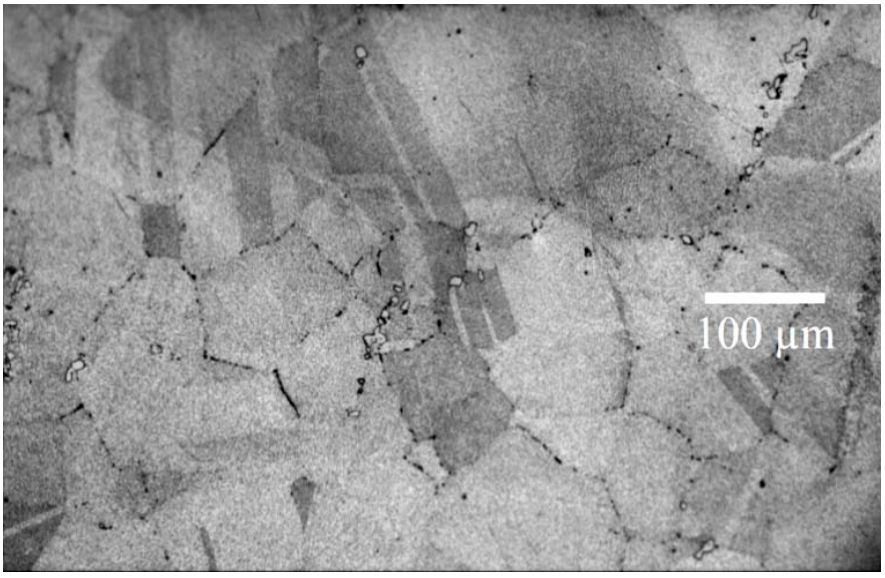

Figure 37. Microstructure of Inconel 718 following etching with Kalling's N°2 reagent.

In contrast to the Ti-6Al-4V workpiece where only one groove was machined, six grooves were produced in the Inconel 718 workpiece, three on each side of the bar so that not only orthogonal cutting conditions could be approximated as much as plausible as before, but also to later analyse the machined surfaces independently. Figure 38 shows a 2D scheme of the aspect of the workpiece material following the internal grooving operations.

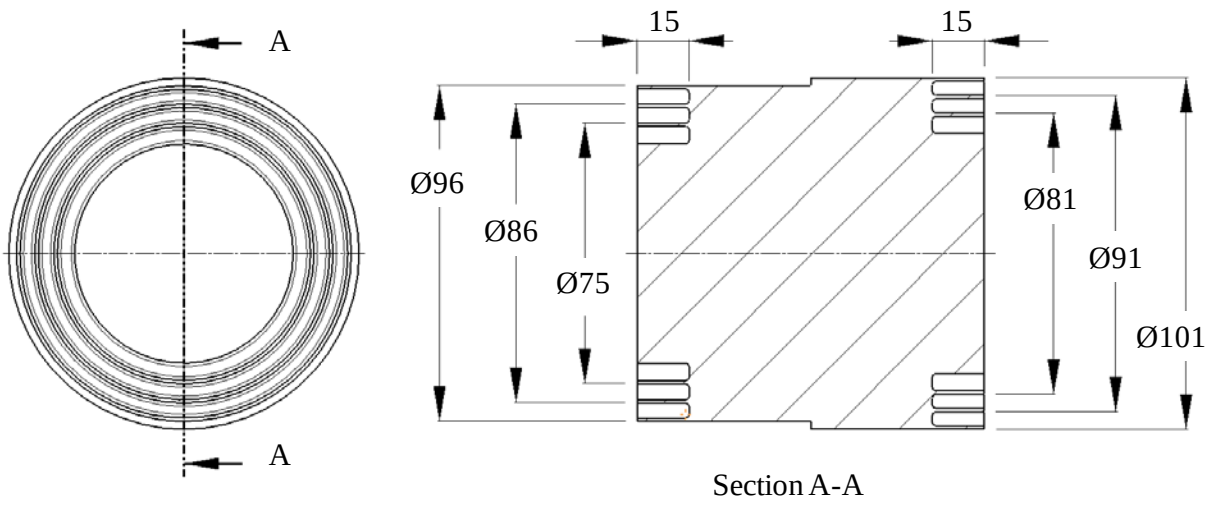

Figure 38. Resulting workpiece geometry derived from the initial six face grooving operations that took place on Inconel 718 (dimensions in mm), for reference only.

All experimental trials were performed using SECO uncoated PCBN inserts identifed as TCGW 110204S-01020-LF (CBN10). Only the top surface of the insert employed PCBN. Tool geometry involved a chamfered insert with dimensions 0.10mmx20°, which was honed. As before, edge radius was measured with the Alicona G4 InfiniteFocus optical system, giving values of 31.7605 and 11.8756µm on each edge respectively, see Figure 39:

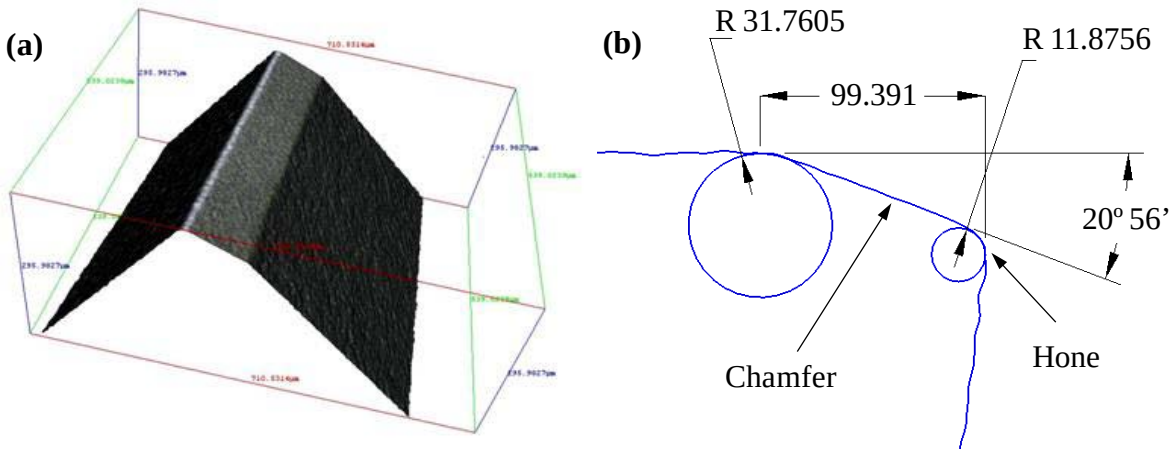

Figure 39. (a) 3D plot of the PCBN cutting tool tip captured with the Alicona optical measuring system, (b) 2D profile obtained from the previous 3D plot (dimensions in µm).

The corresponding toolholder (SECO STGCR 1616H11) provided a clearance angle of 7°. Due to the geometry of the PCBN insert, the feeds selected provided rake angles of 0° and -20º respectively. Three cutting speeds of 200, 250 and 300m/min were utilised for feeds of 0.08 and 0.2mm/rev in line with M'Saoubi et al. (2012) to increase the chances of generating workpiece microstructural surface alterations. Table 7 gives workpiece diameters and cutting parameters.

Feed (mm/rev)	**0.2**			**0.08**		
Cutting speed (m/min)	200	250	300	200	250	300
Workpiece diameter (mm)	81	91	101	96	86	75

Table 7. Inconel 718 workpiece material dimensions to perform the orthogonal tests.

3.2 Equipment

3.2.1 Elevated temperature/strain rate compression tests - Inconel 718

3.2.1.1 Gleeble - The University of Birmingham (UK)

As results of the collaborative work between the University of Birmingham and Technion that involved quasi-static/dynamic and high velocity compression tests respectively for both low and high temperatures, two sets of flow data were utilised in the present work.

The first set, generated at the University of Birmingham by Soo (2003), involved tests at strain rates of 0.001, 1, 10 and 100s^{-1} for temperatures of 20, 400, 550, 700 and 850°C utilising a Gleeble testing machine. Here, due to the intrinsic characteristics of the apparatus used for achieving different levels of strain rate, three sample configurations were employed, see Table 8.

	Length (mm)	**Diameter (mm)**	**Temperature (°C)**	**Strain rate (s^{-1})**
Design 1	13	8.5	700/850	0.001/1
Design 2	8.5	8.5	700/850	10
Design 3	9	5	20/400/550 - 700/850	0.001/1/10 - 100

Table 8. Sample dimensions for the testing conditions performed on the Gleeble apparatus. Adapted from Soo (2003).

Temperatures other than ambient were monitored by making use of a K-type thermocouple, whose wires were welded onto the centre of each workpiece specimen prior to each test.

3.2.1.2 Split Hopkinson Pressure Bar - Technion (Israel)

At commencement of the doctoral study in October 2010, there was no SHPB apparatus available at the University of Birmingham, hence the task of designing one was initiated (see Appendix I for more details). Unfortunately, due to lack of resources available, it was not possible to complete the SHBP unit. Therefore, experimental flow stress data at elevated strain rates and temperatures had to be obtained from an external source. After consultation with colleagues, it was decided to undertake testing with Prof. D. Rittel at Technion, Israel Institute of Technology.

High velocity trials were carried out utilising a SHPB apparatus at the Dynamic Fracture Laboratory, Technion, involving strain rates of ~1,000, 2,000, 3,000, 4,000, 5,000 and 6,000s^{-1} for temperatures of 20, 250 and 400°C respectively.

The preparation of the SHPB specimens, which was carried out at the University of Birmingham, involved an initial wire electrical discharge machining (WEDM) operation of 12 shafts (which were 7mm in diameter and 92mm in length) from an aged bar of Inconel 718 that had a diameter of 83mm, as shown in Figure 40a.

The small shafts were subsequently turned and hand ground on a Nu-Tool NTL 300P manual lathe with a spindle power motor of 0.5kW (0.67HP) and a maximum rotational speed of 1,400rpm to achieve a final diameter of 6±0.02mm, see Figure 40b.

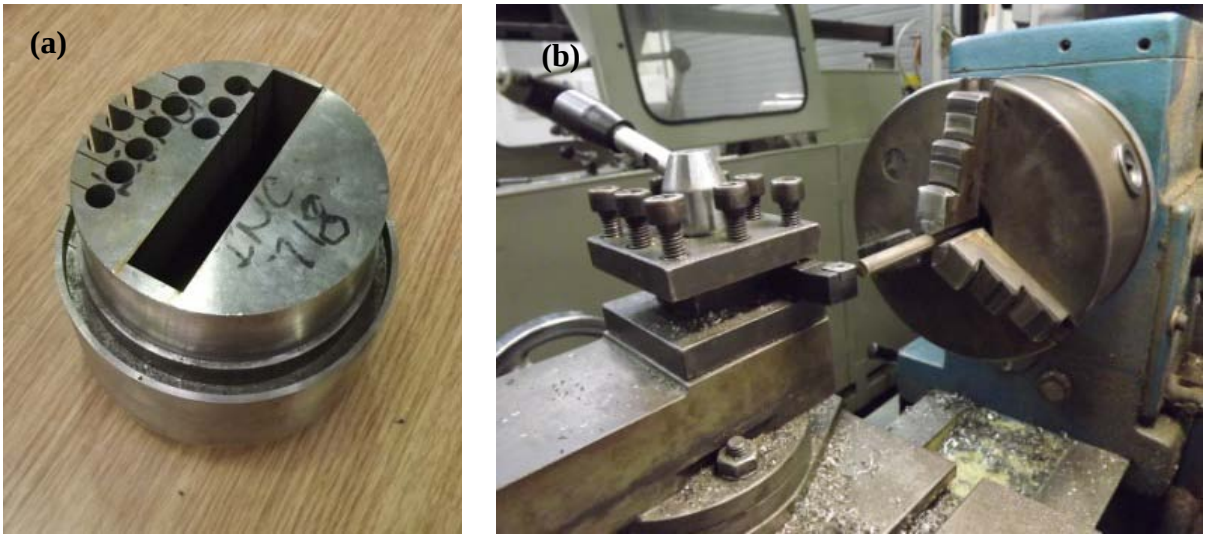

Figure 40. (a) Shafts obtained following a WEDM operation from a bar of Inconel 718, (b) Turning of a shaft to achieve a final diameter of 6±0.02mm.

Following on from this, the shafts were WEDM cut on a AGIECUT VERTEX 2003 (see Figure 41a) to produce 7mm long specimens, see Figure 41b.

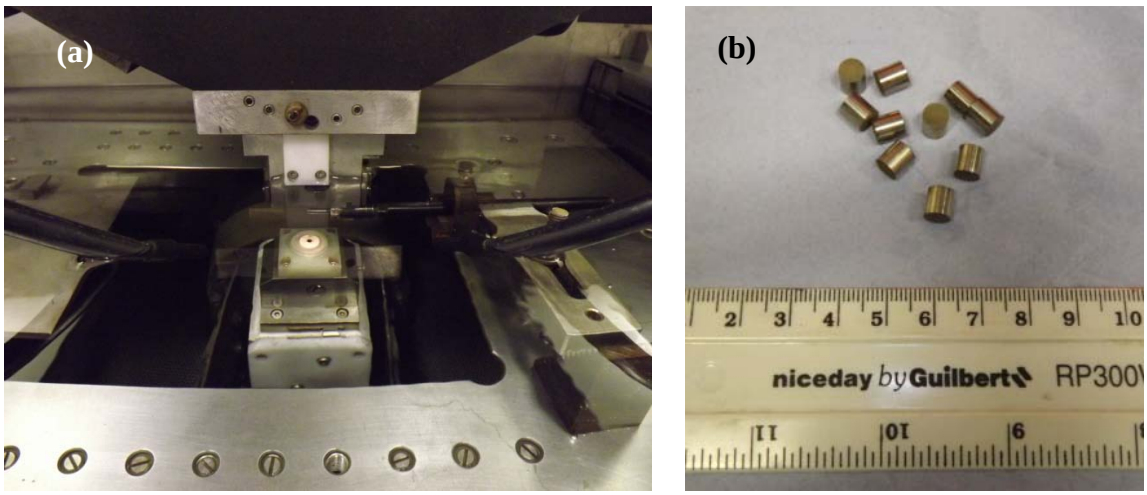

Figure 41. (a) Setup of shafts to be cut by WEDM on an AGIECUT VERTEX, (b) Samples obtained following the wire cut operation.

A final machining operation was performed to achieve the required sample length using a Jones & Shipman surface-grinder, as shown in Figure 42a. A jig was made to enable several specimens to be ground at a time, see Figure 42b.

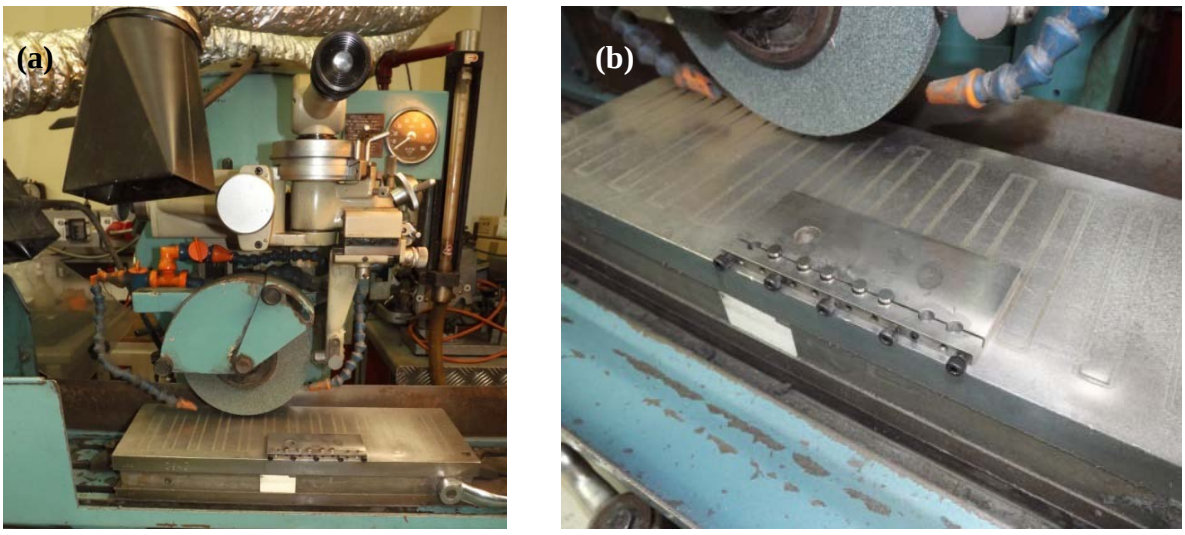

Figure 42. (a) Jones & Shipman surface-grinding machine, (b) Custom made jig to hold the cylindrical Inconel 718 samples.

A total of 72 specimens were produced (6mm diameter x 6mm long), which were ground on their ends to ensure parallelism and hence full contact with the ends of the SHPB incident and transmitter bars. In order to minimise friction between the specimen and the bars (and thus avoid artificially higher values of stress), a thin layer of Molybdenum grease was used on each end of the specimens. For each test, two replications were made in order to corroborate the findings. For trials at ambient temperature, the striker, incident and transmitter bars were made of Maraging Steel 300 (H900) while for those tests at higher temperatures,

bars of Inconel 718 were employed (all in their aged condition). In the latter case an electrical furnace was used. The specimen was connected to a K-type thermocouple and digital thermometer before being placed in the furnace which had glass fibre wool positioned at each end to avoid heat losses. Prior to all tests at temperatures higher than ambient (250 and 400°C), a thermal calibration was performed, see Figure 43.

Figure 43. Thermal calibration setup.

An average value of time to reach the desired temperature was calculated (based on five calibration experiments) so that the consequent SHPB tests could be properly conducted. The signals from the strain gauges corresponding to each test were amplified on a 240 Ohm Bridge supply, later acquired by a Nicolet 440 (12 bit, 10MHz, four channel) digitalising oscilloscope and used as an input on a bespoke Matlab program to obtain filtered true stress-strain curves. Figure 44 shows the experimental setup for tests at high temperatures.

Figure 44. Experimental SHPB setup for tests at high temperatures.

3.2.2 Machine tool for orthogonal cutting tests

The initial face grooving operation/operations as well as the complete series of orthogonal cutting tests performed on both Ti-6Al-4V alloy and Inconel 718 superalloy were carried out on a Dean Smith & Grace 1910 manual lathe with a spindle power motor of 15kW (20HP) and a maximum rotational speed of 2,000rpm, see Figure 45:

Figure 45. Dean Smith & Grace 1910 manual lathe.

3.2.3 Cutting force components measurement system

Tangential, feed and radial cutting force components were measured utilising a Kistler 9263 three-component piezoelectric dynamometer (having a natural frequency of 2.5kHz) connected to a series of model 5011 charge amplifiers via suitable coaxial cables. The data from the dynamometer were acquired using a Keithley DAS1601 analogue/digital board and processed with Dynoware software.

Measurements were recorded when machining both Ti-6Al-4V and Inconel 718 workpiece materials within the first 10-20 seconds of cutting, depending on the cutting speed and feed employed. Figure 46 shows the experimental setup for the orthogonal machining trials on aerospace alloy Ti-6Al-4V.

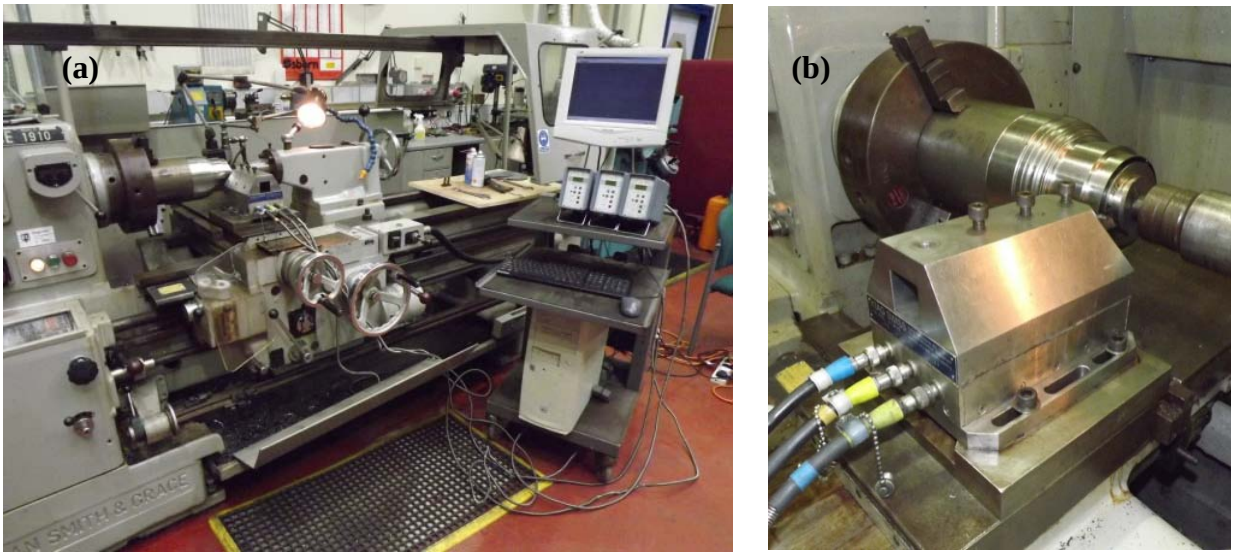

Figure 46. (a) Experimental setup for the orthogonal machining trials on aerospace alloy Ti-6Al-4V, (b) Dynamometer orientation.

3.2.4 High temperature measurement - Inconel 718

Cutting temperatures for the complete set of six machining conditions specified previously were measured with a MinoltaLand Cyclops 52 infrared camera in line with the work performed by Soo (2003), however due to the rapid and aggressive nature of the cutting operation, this proved difficult. Figure 47 details the thermal camera setup (achieved with the help of a bracket screwed onto the dynamometer).

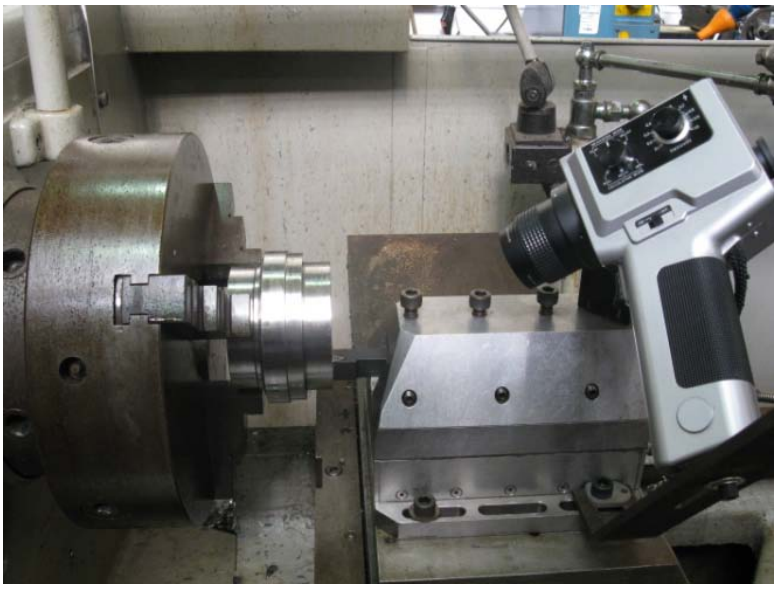

Figure 47. Thermal camera setup for the orthogonal cutting of Inconel 718 superalloy.

Figure 48 shows a number of photographs made with a FASTCAM SA1.1 high speed camera when the cutting speed and feed were 300-250m/min and 0.2-0.08mm/rev respectively. The chips generated by the machining process (either detached or continuous) made temperature measurement unrealistic due to safety and/or practical reasons.

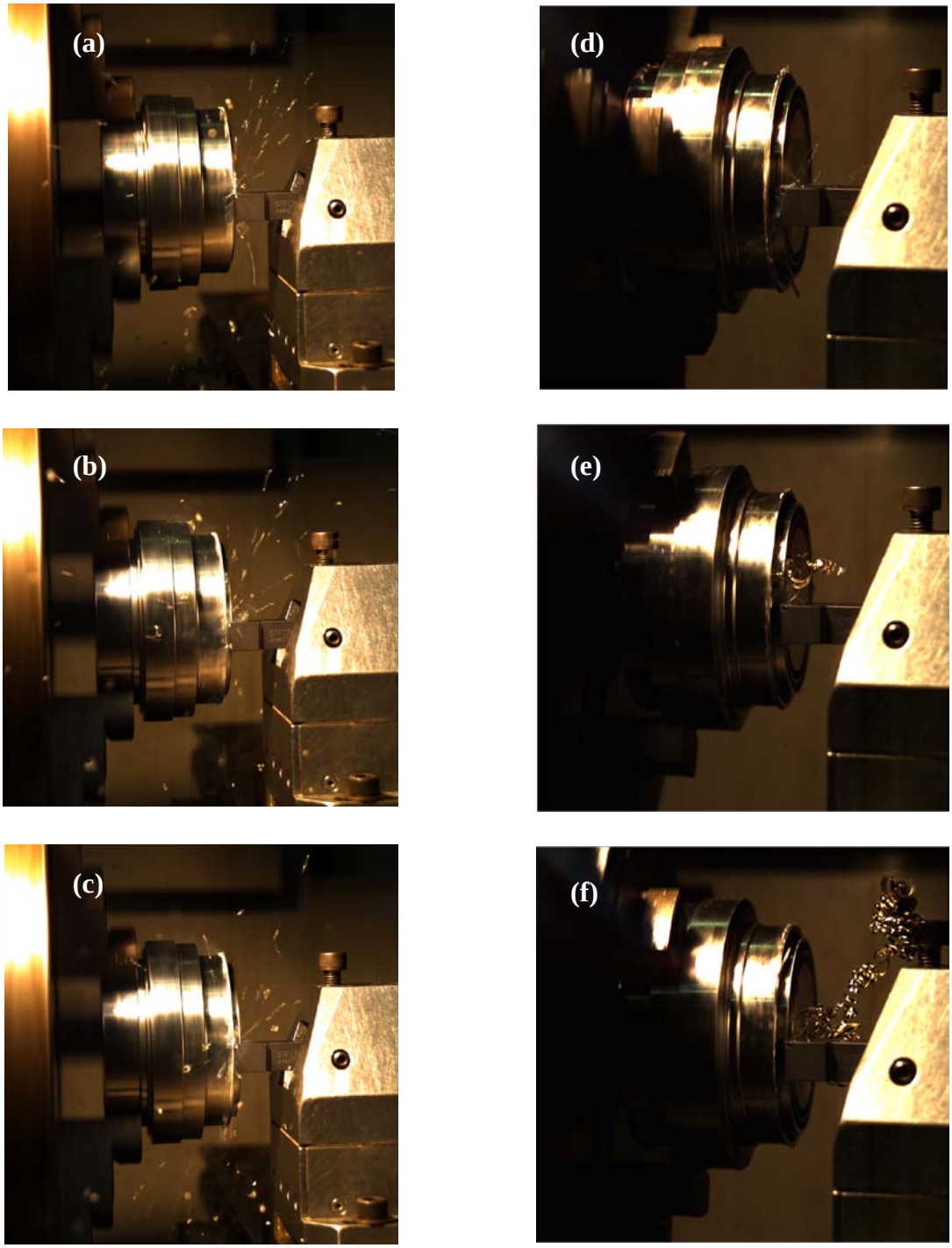

Figure 48. Photographs from a FASTCAM SA1.1 high speed camera when machining Inconel 718 at a cutting speed and feed of (a-b-c) 300m/min; 0.2mm/rev, (d-e-f) 250m/min; 0.08mm/rev. Notice how the chips break free in (b) while in (e) they are continuous. Nevertheless, temperatures were unable to be measured in either case.

Figure 49 shows the setup for the orthogonal machining experiments on Inconel 718 superalloy, which included the cutting force and temperature measurement systems together with the high-speed camera recording arrangement.

Figure 49. Complete setup prepared previous to the machining trials on Inconel 718.

3.2.5 Optical microscope, SEM/EBSD apparatus

Workpiece/chip samples for Ti-6Al-4V and Inconel 718 were observed using a Leica DM LM optical microscope with a magnification of up to 500x, as shown in Figure 50. Micrographs were taken with a Pixelink Megapixel FireWire camera (Nº PL-A662) and linked to an image processing software via Windows interface to further being printed out.

Figure 50. Leica DM LM optical microscope.

A Philips XL-30 instrument located at the Centre for Electron Microscopy, School of Metallurgy and Materials was utilised to perform all the SEM and EBSD measurements on the Inconel 718 workpiece material, as shown in Figure 51:

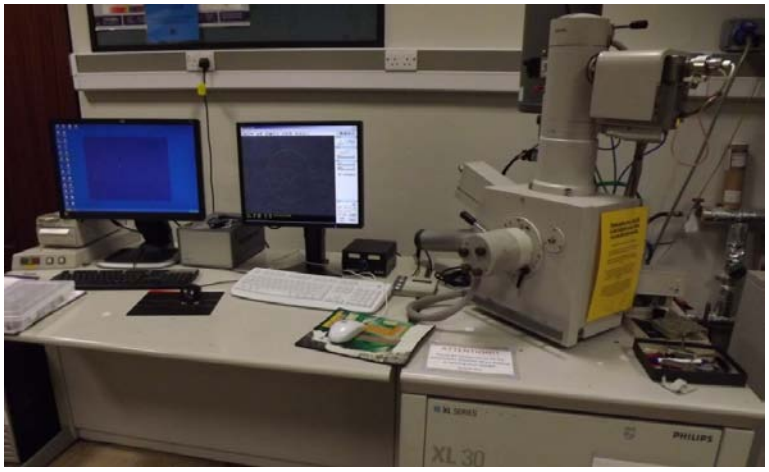

Figure 51. Philips XL-30 SEM/EBSD apparatus.

It is a general purpose 50x50 millimetre stage SEM (fitted with LaB6 filament) that incorporates Oxford Instrument INCA EDS and HKL EBSD (with Nordlys camera) systems. The HKL CHANNEL5 Tango acquisition software and a 12-bit digital CDD camera with a resolution of 1344x1024 pixels were employed for the image collection of the EBSD analysis. Working distances of 15 and 10mm were used for the EBSD and SEM analyses respectively, while the accelerating voltage remained unchanged (20kV).

Although etched samples could be used for the EBSD analysis, the best results were achieved with polished specimens (tilted to 70º) in order to better detect the Kikuchi bands in the diffraction pattern. This was made by clicking around the sample to see if bands were being detected once the beam and Live EBSP page were put in spot mode and dragged across to the right respectively (Frozen SEM option). After selecting a spot with good bands and freezing it by clicking Snap EBSP, it was made sure that 5-6 bands were marked out correctly by clicking Detect bands. Following on this, a job was created, the desired area to analyse was selected and the machine was left running till a complete scanned image was obtained.

After a lengthy series of trial and error iterations, the most suitable EBSD map (step size of 0.5μm) was obtained from a sample that was machined at a cutting speed of 300m/min and a feed of 0.2mm/rev, which exhibited smaller grains on the surface than those found in the bulk, certifying that DRX had taken place. As the principal objective was to prove that the while layer was composed of refined grains, no additional EBSD analysis was performed.

3.3 Recapitulation

Initial orthogonal cutting trials were performed on Ti-6Al-4V alloy with sharp tungsten carbide inserts at cutting speeds of 60, 90 and 120m/min and a feed of 0.125mm/rev. Tangential/feed forces were measured and the microstructure of workpiece material/chips was revealed. A further microscopy analysis of the chips was carried out to evaluate the accuracy of corresponding FE models in terms of peak, valley and pitch dimensions.

Material data for Inconel 718 were augmented to that previously generated by Soo (2003), in order to evaluate and better characterise the constitutive response of the superalloy when strain rates and temperatures surpass 1,000s^{-1} and 293K respectively. The experimental work was performed with a SHPB apparatus and contemplated respective strain rates and temperatures as elevated as ~6,000s^{-1} and 673K. Plastic stress-strain curves were obtained for all trials following an appropriate translation of the pulses generated in the process.

Mainstream cutting experiments were performed on Inconel 718 superalloy with PCBN tooling for feeds of 0.2 and 0.08mm/rev at respective cutting speeds of 300, 250 and 200m/min. Tangential and feed force components were measured for subsequent analysis and validation of the FE models. Overall process temperatures were unable to be quantified. Similarly as with Ti-6Al-4V, workpiece material and chip samples were etched to reveal microstructure. However, the metallurgical investigation not only included conventional microscopy (to observe chip features and compare them to FE simulations), but also exhaustive machined surface evaluation by performing SEM/EBSD analyses. This was made to analyse in detail possible microstructure alterations and validate FE models in order to reinforce the fact that a pronounced softening in the manufactured surface of Inconel 718 is likely to be a palpable consequence of drastic machining conditions when using PCBN inserts.

CHAPTER 4

FEM FOLLOWING ORTHOGONAL MACHINING

4.1 FEM with ABAQUS/Explicit for Ti-6Al-4V

4.1.1 2D Thermo-mechanical ALE/AR - JC and RWM

4.1.1.1 Principal features and formulation of the FE model

Model geometry was generated utilising the commercial FE pre-processor ABAQUS/CAE 6.10-1, while all numerical simulations were performed with the ABAQUS/Explicit module designed for solving dynamic non-linear problems such as machining operations. The ALE mesh formulation was initially used together with the adaptive remeshing procedure to prevent excessive element distortion due to the high levels of workpiece deformation.

The workpiece was meshed with 22,161 CPE4RT (4-node, plain strain thermally coupled, quadrilateral, bilinear displacement/temperature, reduced integration and hourglass type) elements; with typical dimensions of 6μm x 1.5μm. The corresponding cutting tool was meshed with 2,195 CPE4RT together with 63 CPE3T (3-node, plain strain thermally coupled, triangular, linear displacement and temperature type) elements; in order to account for its geometrical features. In addition, the tool cutting edge had a radius of 31.28μm in accordance with experimental measurements (see Figure 33) while operating conditions were defined in line with the orthogonal turning trials. An appropriate uniform mass scaling value of 100 was utilised in order to accelerate the calculations, without unduly influencing the numerical results (Llanos et al., 2009).

Three FE simulations were carried out comprising cutting speeds of 60, 90 and 120m/min at a constant feed of 0.125mm/rev to precisely match the experimental machining conditions.

The model configuration and geometry are shown in Figure 52a while the mesh design and corresponding boundary conditions are displayed in Figure 52b:

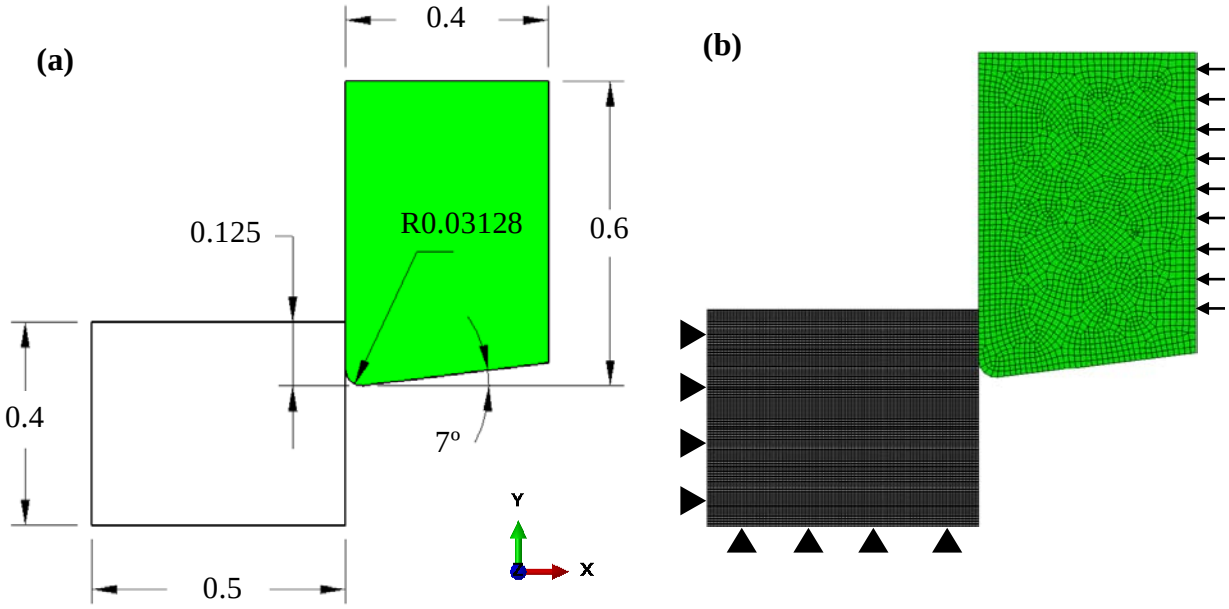

Figure 52. (a) General configuration of the 2D orthogonal cutting FE model of Ti-6Al-4V (dimensions in mm), (b) Meshed model and boundary conditions.

The Ti-6Al-4V workpiece material was described following the JC plasticity model, where the parameters A=724.7MPa, B =683.1MPa, C =0.035, n =0.47, m =1, $\dot{\bar{\varepsilon}}_0$=$10^{-5}$$s^{-1}$, T_m =1,873K and T_r=293K, according to Lee and Lin (1998). A constant Taylor-Quinney coefficient of 0.9 was specified to account for the internal heat produced in the workpiece material due to plastic deformation (inelastic heat fraction), in line with work performed by Arrazola and Ozel (2010).

Table 9 summarises the physical and mechanical properties of the Ti-6Al-4V alloy (Chen et al., 2011; Karpat, 2011) and carbide cutting tool material (Soo, 2003; Sima and Ozel, 2010) (some of which varied with temperature), together with the cutting parameters and tool geometry used in the FE simulations.

All FE analyses were performed on a computer having dual Intel(R) Xeon(R) X5550 processors (2.67GHz) with 20GB of RAM, with each run taking approximately 1h of computation.

			Ti-6Al-4V	Tool
Material Properties	Johnson-Cook constitutive model	A (MPa)	724.7	-
		B (MPa)	683.1	
		n (-)	0.47	
		C (-)	0.035	
		m (-)	1	
		T_m (K)	1,873	
		T_r (K)	293	
		$\dot{\bar{\varepsilon}}_0$($s^{-1}$)	10^{-5}	
	Density (kg/m^3)		4,430	15,000
	Poisson's Ratio (-)		0.34	0.22
	Young's modulus (GPa)		111.672-0.0577(T-273)	630
	Thermal Conductivity (W/mK)		0.015T+7.7	100
	Specific Heat Capacity (J/kgK)		$609.481e^{(0.0002T)}$	402
	Thermal Expansion Coefficient (10^{-6}/K)		-	4.7
	Inelastic Heat Fraction (-)		0.9	-
Cutting Conditions/ Tool geometry	Cutting Speed (m/min)		60/90/120	
	Depth of Cut (mm)/Feed (mm/rev)		0.125/0.125	
	Tool Tip Radius (μm)		31.28	
	Rake Angle (°)/Clearance Angle (°)		0/7	

Table 9. Mechanical and physical property data for Ti-6Al-4V alloy and the carbide cutting tool together with machining conditions/tool geometry (temperature in Kelvin).

4.1.1.2 Frictional and thermal effects

While it is generally accepted that two frictional regions exist at the tool-chip interface in cutting, e.g. sliding and sticking zones, the difficulties that appear when trying to quantify them are significant due to the influence of cutting speed, feed rate and not least tool geometry (Ozel, 2006). While Karpat (2011) specified both frictional zones in his FE formulation, Umbrello (2008) only used the constant shear model based on previous results which showed that cutting forces and chip morphology can be well predicted irrespective of the friction law used. Although the employment of a limiting shear stress is a plausible alternative to describe friction at the tool-chip interface in Lagrangian FE models portraying plastic bodies, Arrazola and Ozel (2010) deduced that this would make little sense. Moreover, the authors concluded that one of the major deficiencies stick-slip friction models have is the ambiguity of the value of limiting shear stress to work with, further stating that those should be utilised with prudence. Considering this together with the work of Filice et al. (2007) which highlighted that outputs such as cutting force and contact length are not significantly influenced by the friction model of choice and the limitations associated with ABAQUS; the

tool-chip interaction was defined according to the Coulomb's friction model with an average friction coefficient of 0.57 (Karpat, 2011; Umbrello, 2008). Despite its drawbacks, the model was therefore believed to have a marginal influence on the numerical predictions.

A thermal contact conductance (TCC) value of 100kW/m^{2}K was defined at the tool-chip interface based on information in the literature (Iqbal et al., 2008), while a heat partition coefficient of 0.5 (ratio of heat generated flowing into the workpiece and tool) was selected. In addition, 90% of the energy dissipated due to friction was assumed to be converted into heat because minimal losses are expected to occur. Table 10 lists the frictional and thermal properties employed in all FE simulations.

Contact and thermal properties	Thermal Contact Conductance (kW/m^{2}K)	100
	Heat Partition Coefficient (-)	0.5
	Friction Coefficient (-)	0.57
	Fraction of dissipated energy caused by friction that is converted to heat (%)	90
	Limit Shear Stress (MPa)	Unlimited

Table 10. Contact and thermal properties utilised to describe the interactions between the Ti-6Al-4V alloy and the K20 insert.

4.1.1.3 Damage model characteristics

The RWM relationship (see Eq. (48) to (50)) was utilised as the workpiece damage criterion to simulate material failure and hence initiate chip separation as well as adiabatic shear banding during the orthogonal cutting operation. Following a series of trial and error iterations, the best fit for parameters W_{crit}, W_{frac} and a was determined for each cutting condition and detailed in Table 11:

Feed (mm/rev)	**0.125**		
Cutting speed (m/min)	**60**	**90**	**120**
W_{crit} (J/m^3)	80	80	80
W_{frac} (J/m^3)	3,000	3,000	3,000
a (-)	0.04	0.06	0.07

Table 11. Resulting W_{crit}, W_{frac} and a values for the RWM damage model used to simulate 2D machining of Ti-6Al-4V alloy with the JC model.

The RWM criterion was added to the JC model and incorporated in ABAQUS through a VUMAT subroutine. The user customised code was written using FORTRAN 77

programming language and subsequently compiled and linked to the FE package using Intel(R) Visual FORTRAN 10.1 and Microsoft Visual Studio 2008 software respectively.

4.1.2 3D Thermo-mechanical Lagrangian - JC and CL

4.1.2.1 General formulation of the FE model

The initial 2D model of orthogonal cutting at the operating conditions previously specified (see Table 9) was extended to a full 3D configuration to better represent practical conditions. A relatively fine mesh was applied to the region of the workpiece where chip formation occurs to enhance numerical accuracy and involved 189,100 C3D8RT (8-node thermally coupled brick, trilinear displacement and temperature, reduced integration and hourglass control type) elements while the tool was meshed with a total of 23,088 C3D8RT elements respectively. Figure 53 shows a schematic of the FE model configuration including overall dimensions, whose geometry replicated a small portion of that encountered experimentally (see Figure 53).

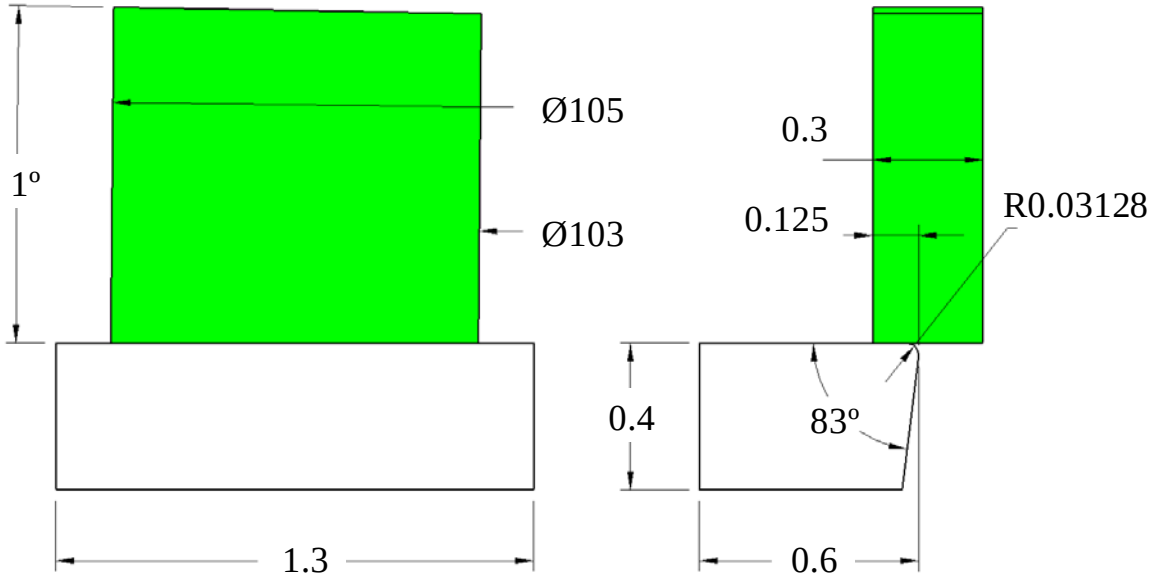

Figure 53. General configuration of the orthogonal 3D orthogonal cutting model and associated geometry (dimensions in mm).

In order to reproduce actual 3D machining conditions, a rotational boundary condition together with a constrain in the Z direction were applied to the workpiece's top and posterior faces (see Figure 54b), while the tool was fully constrained in two faces to allow for elastic deformation in X, Y and Z in the remaining ones (see Figure 54a).

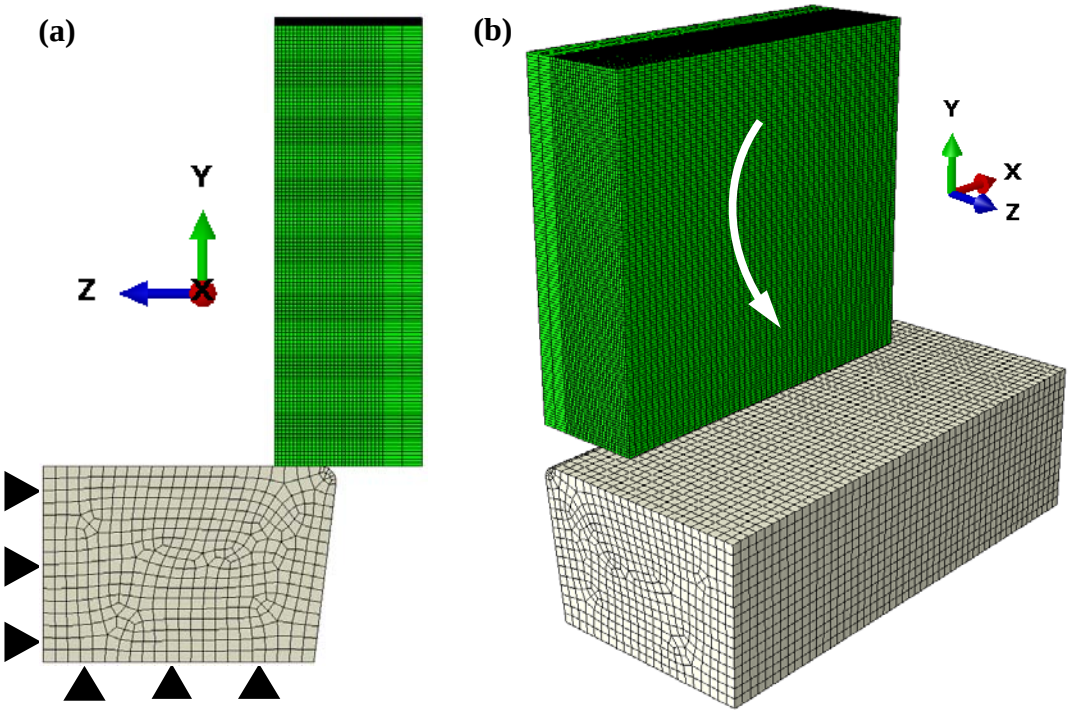

Figure 54. Meshed model showing (a) constrained and (b) rotational boundary conditions.

All of the simulations required an average computing time of 40h to achieve convergence.

4.1.2.2 Damage model characteristics

Material flow stress was represented by the JC constitutive model while workpiece damage was modelled according to the CL fracture criterion (as detailed in Eq. (46)) and implemented via a VUMAT user subroutine. A bespoke procedure to obtain the principal stress values for calculating the accumulated energy to failure was also developed (instead of using the built-in 'vsprinc' due to considerable numerical instability at initial time increments) and embedded within the primary VUMAT. A series of trial and error iterations showed that the preferred value for the parameter C_1 was 180J/m^3.

4.1.3 3D Thermo-mechanical Lagrangian - JC and RWM

4.1.3.1 Damage model characteristics

The model geometry was slightly modified from that seen in Figure 53, due to the attributes of the RWM model to generate a smaller chip compared to CL, which thus made

unnecessary to utilise a large workpiece. In specific, the angle seen in Figure 53 varied from 1º to 0.275º to give a total of 107,100 C3D8RT elements. As with the 2D FE simulations detailed previously, the appropriate values for the parameters W_{crit}, W_{frac} and a can be found in Table 12:

Feed (mm/rev)	**0.125**		
Cutting speed (m/min)	**60**	**90**	**120**
W_{crit} (J/m^3)	80	80	80
W_{frac} (J/m^3)	2,900	3,000	3,100
a (-)	0.175	0.175	0.175

Table 12. Preferred values of W_{crit}, W_{frac} and a for the RWM damage model used to simulate 3D turning of Ti-6Al-4V alloy with the JC material model.

4.2 Johnson-Cook material model for Inconel 718

4.2.1 Calculation of model parameters

4.2.1.1 Determination of n

In order to determine the hardening parameter *n*, experimental flow stress data for Inconel 718 obtained at the maximum strain rate (5,216s^{-1}) and 293K (room temperature) was utilised, in line with the calculation procedure outlined by Lesuer (2000), where $\dot{\bar{\varepsilon}}_0$=1s^{-1}. Therefore, Eq. (32) reduces to:

$$\bar{\sigma} = \left[A + B\left(\bar{\varepsilon}^p\right)^n\right] k_1 \tag{51}$$

where $k_1 = \left[1 + C\ ln\left(\frac{\dot{\bar{\varepsilon}}^p}{\dot{\bar{\varepsilon}}_0}\right)\right]$ is a constant. At a strain $\bar{\varepsilon}^p = 0$, the stress obtained corresponds to the yield strength, hence Eq. (51) reduces to:

$$\bar{\sigma} = A\ k_1 \tag{52}$$

From the experimental $\bar{\sigma} - \bar{\varepsilon}^p$ curve at the specified strain rate and temperature indicated, the yield strength was (see Table 14):

$$\bar{\sigma} = A\ k_1 = 1{,}357.66MPa \tag{53}$$

Replacing Eq. (53) into Eq. (51) and reordering terms gives:

$$\overline{\sigma} - 1{,}357.66 = B\left(\overline{\varepsilon}^{p}\right)^{n} k_1 \tag{54}$$

A logarithmic $(\overline{\sigma} - A\ k_1)$ vs. $\left(\overline{\varepsilon}^{p}\right)$ diagram was then constructed, where $\overline{\sigma}$ corresponds to the flow stress values at the specified strain rate and temperature, in order to calculate $B\ k_1$ and n. The plot obtained when $\dot{\overline{\varepsilon}}^{p} = 5{,}216 s^{-1}$ and T=293K is shown in Figure 55:

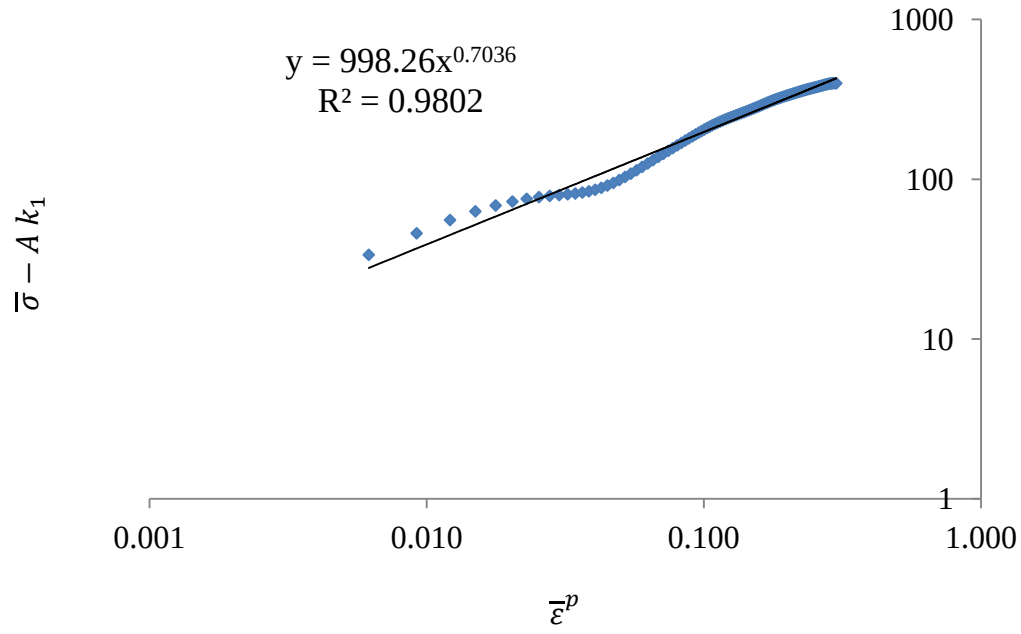

Figure 55. Logarithmic $(\overline{\sigma} - A\ k_1)$ vs. $\left(\overline{\varepsilon}^{p}\right)$ diagram to obtain n.

The data points demonstrated good correlation to a straight line, and by comparing Eq. (54) and the equation of best fit in Figure 55 it can be shown that:

$$B\ k_1 = 998.26 \tag{55}$$

$$y = \overline{\sigma} - 1{,}357.66 \quad , \quad x = \overline{\varepsilon}^{p} \quad \rightarrow \quad n = 0.7036 \tag{56}$$

4.2.1.2 Determination of C

The parameter C was obtained from the flow stress data by initially assuming a constant value of strain $\overline{\varepsilon}^{p} = 0.03$ at temperature of 293K following Lesuer (2000), so that Eq. (32) results in:

$$\overline{\sigma} = k_2\left[1 + C\ ln\left(\frac{\dot{\overline{\varepsilon}}^p}{}\right)\right] \qquad \rightarrow \qquad \frac{\overline{\sigma}}{k_2} - 1 = C\ ln\left(\frac{\dot{\overline{\varepsilon}}^p}{}\right) \tag{57}$$

A linear interpolation of the experimental flow stress data points over the range of $\overline{\varepsilon}^p = 0.03$ was initially performed, so that exact $\overline{\sigma}$ values were used. The constant k_2 was easily calculated when $\dot{\overline{\varepsilon}}^p = 1s^{-1}$ from Eq. (57), which is equivalent to the flow stress value at room temperature and $\overline{\varepsilon}^p = 0.03$, e.g. 1,329.62MPa. A semi-logarithmic $(\overline{\sigma}/1{,}329.62 - 1)$ vs. $\dot{\overline{\varepsilon}}^p$ diagram was subsequently plotted in order to determine C, see Figure 56:

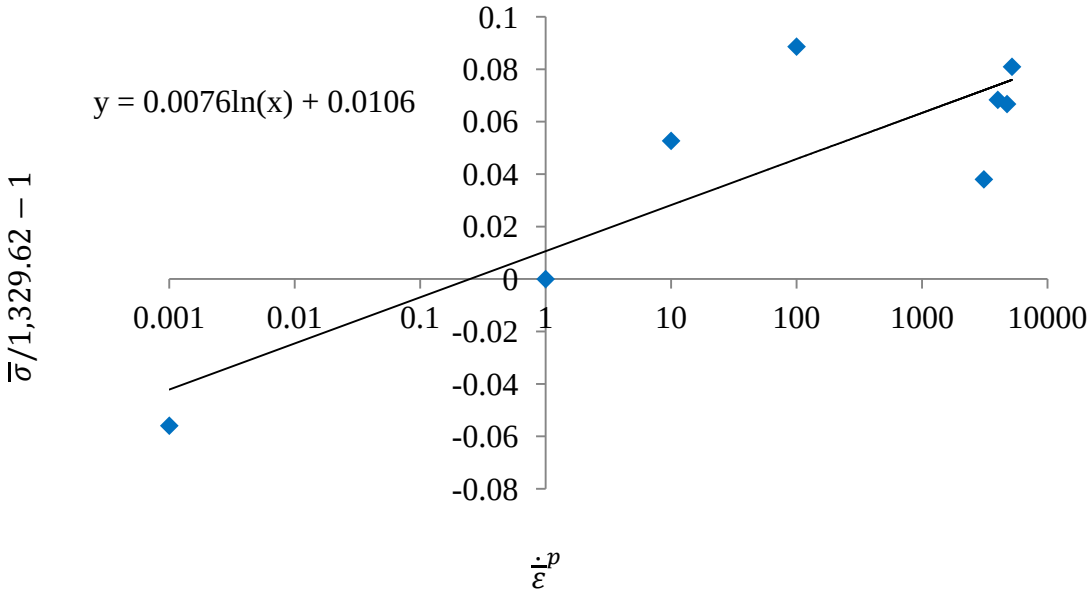

Figure 56. Semi-logarithmic $(\overline{\sigma}/1{,}329.62 - 1)$ vs. $\dot{\overline{\varepsilon}}^p$ diagram to calculate C.

By comparing the straight line equation in Figure 56 with Eq. (57), it can be seen that $C = 0.0076$. While the line should ideally pass through the origin in Figure 56, the non-zero y-intercept value observed (0.0106) was due to scatter in the data points, which also provides an indication of the quality of the fit.

4.2.1.3 Determination of A and B

To proceed with the computation of parameters A and B, the constants n and C calculated previously (at $\dot{\overline{\varepsilon}}^p = 5{,}216s^{-1}$ and T=293K) were substituted in Eq. (32) which then reduces to:

$$\overline{\sigma} = \left[A + B\left(\overline{\varepsilon}^{p}\right)^{0.7036}\right][1 + 0.0076\ ln(5{,}216)] \tag{58}$$

At zero plastic strain, Eq. (58) takes the form:

$$\overline{\sigma} = A\ [1 + 0.0076\ ln(5{,}216)] \qquad \rightarrow \qquad A = \frac{\overline{\sigma}}{[1 + 0.0076\ ln(5{,}216)]} \tag{59}$$

where $\overline{\sigma}$ corresponds to the experimental flow stress at the specified strain rate and temperature, which was 1,357.66MPa (see Eq. (53)/Table 14), and inserting this value in Eq. (59) provides:

$$A = \frac{\overline{\sigma}}{[1 + 0.0076\ ln(5{,}216)]} = \frac{1{,}357.66}{[1 + 0.0076\ ln(5{,}216)]} = 1{,}274.73\ MPa \tag{60}$$

The calculation of B was performed using Eq. (55) and substituting the value of C and $\dot{\overline{\varepsilon}}^{p}$ in k_1, giving:

$$B = \frac{998.26}{k_1} = \frac{998.26}{[1 + 0.0076\ ln(5{,}216)]} = 937.28MPa \tag{61}$$

4.2.1.4 Determination of m

Two different procedures for calculating m were employed, the first as specified by Lesuer (2000), while the second consisted of a new method that indicated higher accuracy. As m influences the softening of the workpiece material, flow stress data recorded at the highest temperature tested (1,123K) were utilised at a strain rate of $100s^{-1}$ and associated plastic strain of 0.03 for the calculations. Here, the corresponding flow stress was 1,447.49MPa. The general JC relationship in Eq. (32) can be rearranged as observed in Eq. (62):

$$\frac{\overline{\sigma}}{\left[A + B\left(\overline{\varepsilon}^{p}\right)^{n}\right]\left[1 + C\ ln\left(\frac{\dot{\overline{\varepsilon}}^{p}}{}\right)\right]} = \left[1 - \left(\frac{T - T_r}{T_m - T_r}\right)^{m}\right] \tag{62}$$

Substituting values for A, B, C and n gives:

$$\frac{\overline{\sigma}}{\left[1{,}447.49 + 937.28\left(\overline{\varepsilon}^{p}\right)^{0.7036}\right]\left[1 + 0.0076\, ln\left(\dot{\overline{\varepsilon}}^{p}\right)\right]} = \left[1 - \left(\frac{T - T_r}{T_m - T_r}\right)^{m}\right] \tag{63}$$

Therefore, the parameter m was calculated according to the relationship shown in Eq. (64):

$$m = \frac{ln\left(1 - \frac{\overline{\sigma}}{\left[1{,}447.49 + 937.28\left(\overline{\varepsilon}^{p}\right)^{0.7036}\right]\left[1 + 0.0076\, ln\left(\dot{\overline{\varepsilon}}^{p}\right)\right]}\right)}{ln\left(\frac{T - T_r}{T_m - T_r}\right)} \tag{64}$$

As the value of m will vary for different temperatures, an average value based on the data at various temperatures was calculated and found to be $m = 1.659$.

An alternative algorithm that minimises the error when calculating the parameter m was developed. Here, a variable quantity was added to or subtracted from an initial value of m ($m = 1$) which minimises the average error determined by Eq. (65) at temperatures of 673, 823, 973 and 1,123K and a strain rate of 100s^{-1} (with flow stress values corresponding to a plastic strain of 0.03).

$$error = \left[1 - \left(\frac{T - T_r}{T_m - T_r}\right)^{m}\right] - \frac{\overline{\sigma}}{\left[A + B\left(\overline{\varepsilon}^{p}\right)^{n}\right]\left[1 + C\, ln\left(\dot{\overline{\varepsilon}}^{p}\right)\right]} \tag{65}$$

This iterative procedure was performed until an error of 1x10^{-7} was achieved. This resulted in $m = 1.641$, which was adopted for the current research as the value is optimised rather than averaged, hence thought to be of higher accuracy compared to the procedure proposed by Lesuer (2000).

Table 13 displays the constants A, B, C, n and m calculated in the present work in comparison to published results for Inconel 718 and shows closest similarity with those reported by DeMange et al. (2009).

	A (MPa)	B (MPa)	n	C	m	T_m (K)	T_r (K)	$\dot{\bar{\varepsilon}}_0$ (s^{-1})	State
Present work	**1,274.7**	**937.3**	**0.7036**	**0.0076**	**1.641**	**1,573**	**293**	**1**	**AG**
Kobayashi et al. (2008)	980	1,370	0.164	0.02	1.03	1,573	298	1	AG
Shi et al. (2010)	789	700	0.22	0.0074	2.31	1,570	-	0.001	-
Sievert et al. (2003)	450	1,700	0.65	0.017	1.3	1,570	300	0.001	AN
DeMange et al. (2009)	**1,290**	**895**	**0.5260**	**0.016**	**1.55**	**1,573**	**-**	**0.03**	**AG**
	337	1,642	0.7835	0.049	1.20	1,573	-	0.03	AN
Pereira and Lerch (2001)	400	1,798	0.9143	0.0312	-	-	298	1	AN
	1,350	1,139	0.6522	0.0134	-	-	298	1	AG
Mitrofanov et al. (2005)	1,241	622	0.6522	0.0134	-	-	-	-	AG

Table 13. Johnson-Cook parameters for Inconel 718 calculated in the present research compared to published results. Note: AG and AN correspond to Aged and Annealed respectively.

4.2.2 Plastic stress-strain ($\bar{\sigma} - \bar{\varepsilon}^p$) curves

Figures 57 to 64 show the experimentally measured and corresponding JC modelled plastic stress-strain ($\bar{\sigma} - \bar{\varepsilon}^p$) curves for strain rates of 0.001, 1, 10, 100, ~3,000, 4,000, 5,000 and 6,000s^{-1} at temperatures varying from 293 to 1,123K respectively. At temperatures of up to 623K, plastic flow stress according to the JC material model showed good correlation with experimental data irrespective of strain rate, however the accuracy of the model diminished as temperatures increased. This was attributed to limitations presented by the JC model in representing the significant loss in strength of Inconel 718 as temperatures exceed ~650ºC. Nevertheless, the JC constitutive relationship demonstrated relatively good precision in characterising the yield strength and material flow hardening behaviour up to effective plastic strains of 0.3.

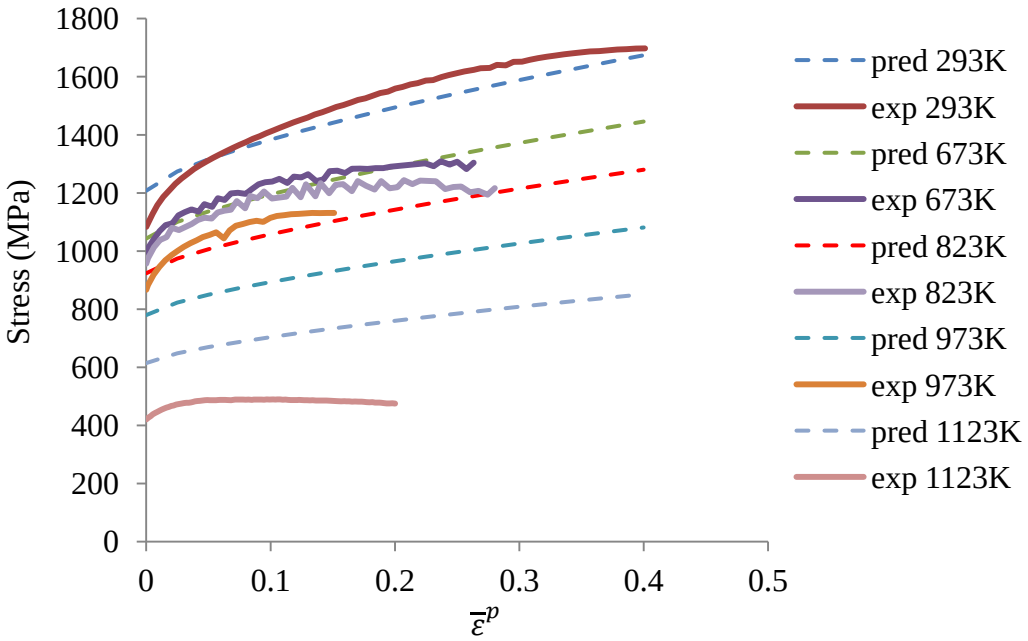

Figure 57. Comparison between experimental (exp) stress-strain curves and those predicted (pred) by the JC model at different temperatures for $\dot{\bar{\varepsilon}}^p = 0.001\ s^{-1}$.

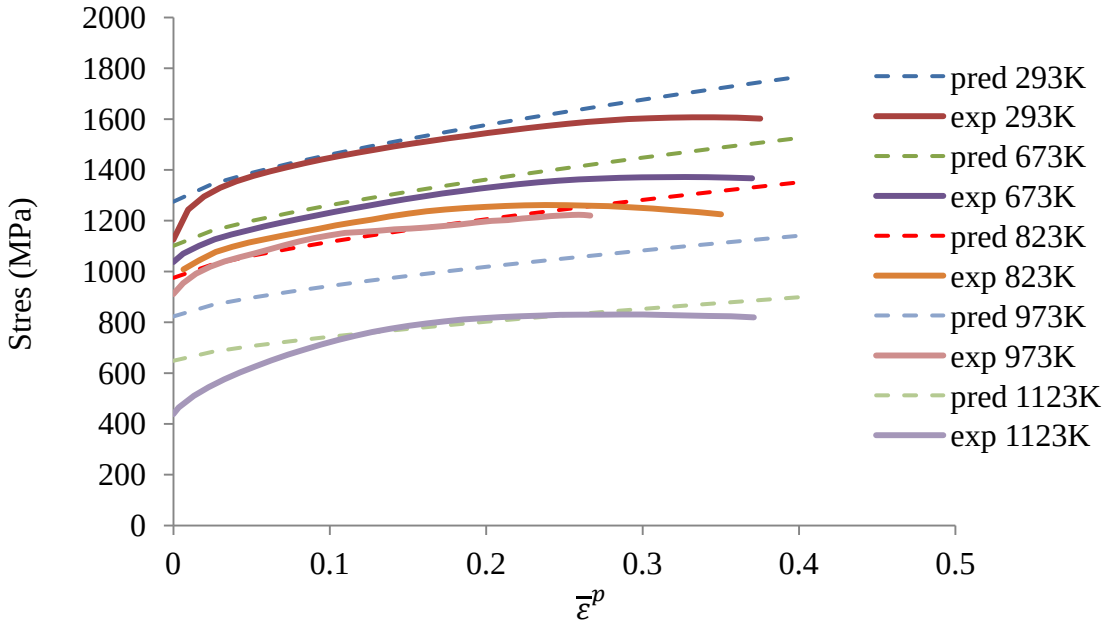

Figure 58. Comparison between experimental (exp) stress-strain curves and those predicted (pred) by the JC model at different temperatures for $\dot{\bar{\varepsilon}}^p = 1\ s^{-1}$.

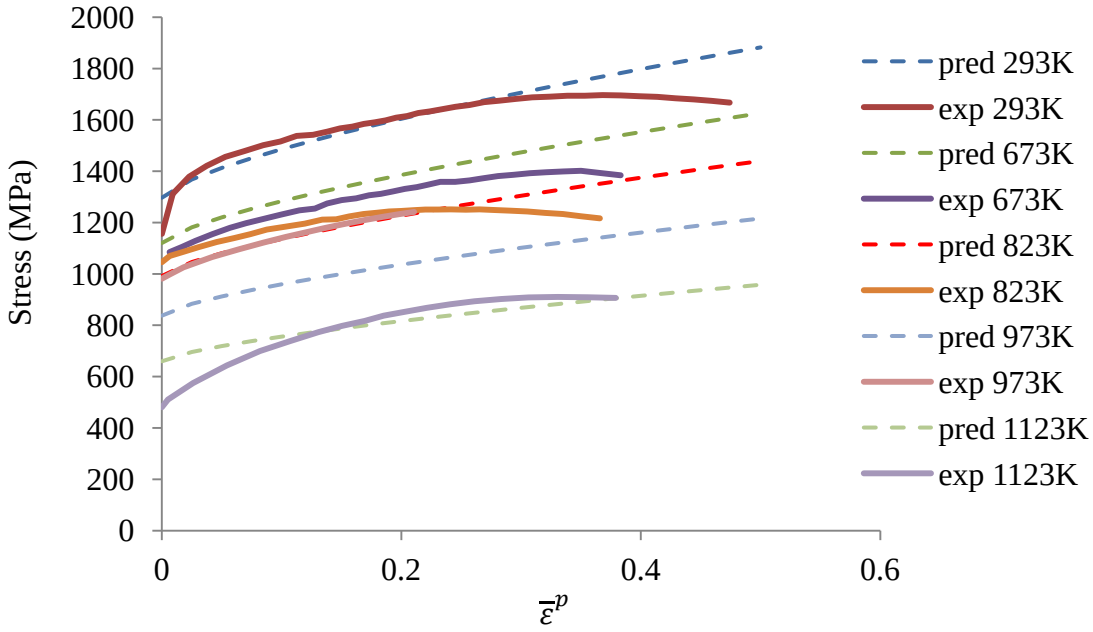

Figure 59. Comparison between experimental (exp) stress-strain curves and those predicted (pred) by the JC model at different temperatures for $\dot{\bar{\varepsilon}}^p = 10\ s^{-1}$.

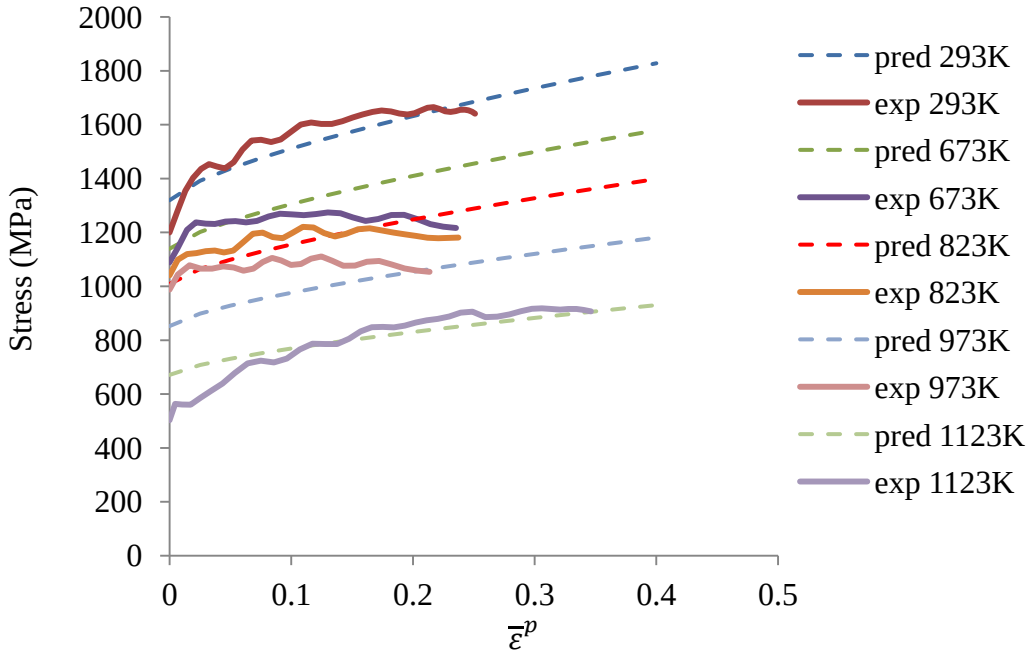

Figure 60. Comparison between experimental (exp) stress-strain curves and those predicted (pred) by the JC model at different temperatures for $\dot{\bar{\varepsilon}}^p = 100\ s^{-1}$.

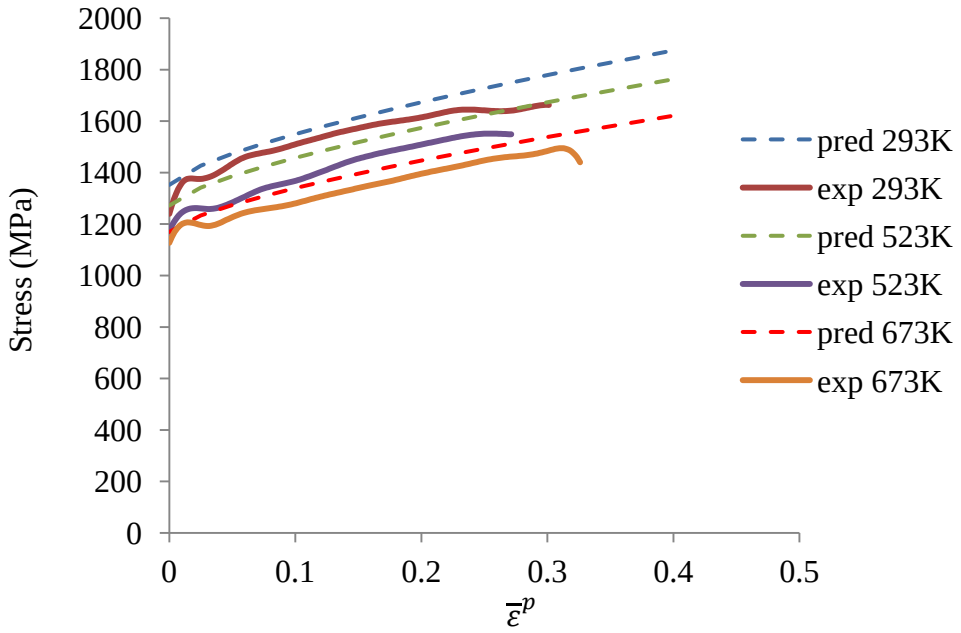

Figure 61. Comparison between experimental (exp) stress-strain curves and those predicted (pred) by the JC model at different temperatures for $\dot{\bar{\varepsilon}}^p \approx 3{,}000\ s^{-1}$.

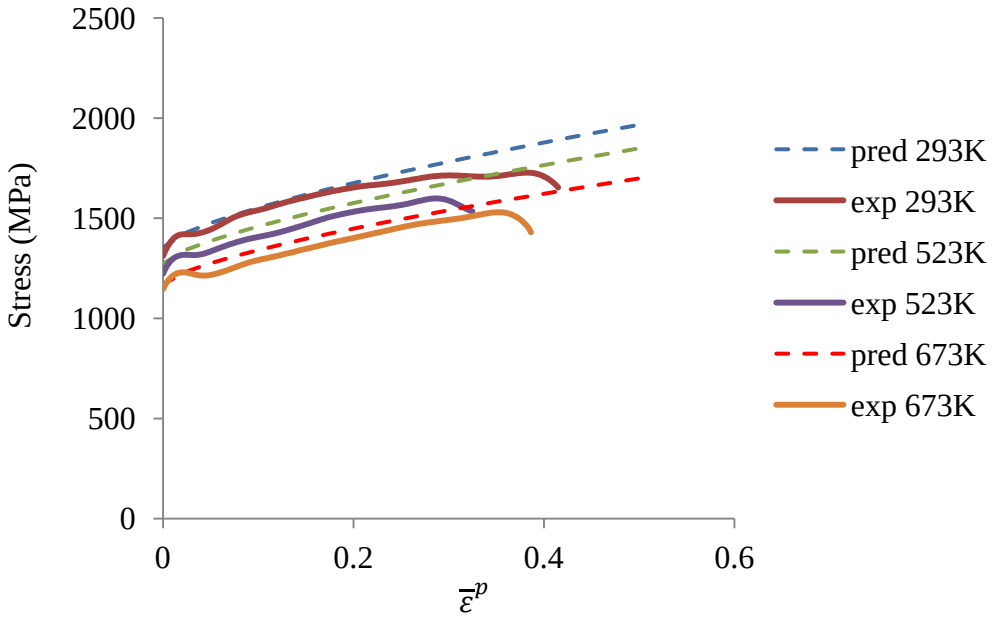

Figure 62. Comparison between experimental (exp) stress-strain curves and those predicted (pred) by the JC model at different temperatures for $\dot{\bar{\varepsilon}}^p \approx 4{,}000\ s^{-1}$.

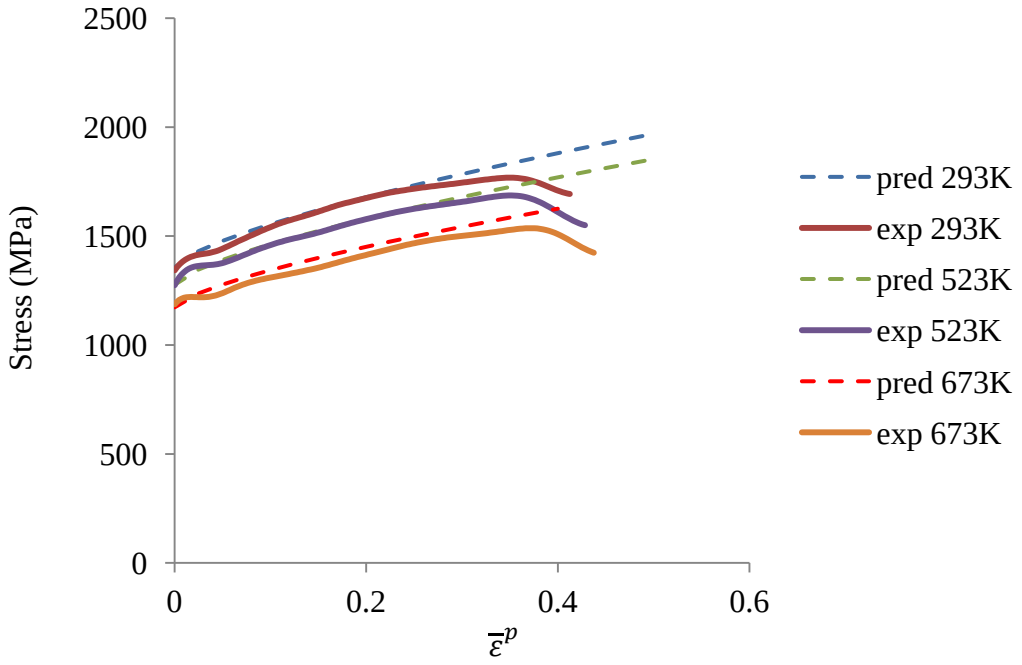

Figure 63. Comparison between experimental (exp) stress-strain curves and those predicted (pred) by the JC model at different temperatures for $\dot{\bar{\varepsilon}}^p \approx 5{,}000\ s^{-1}$.

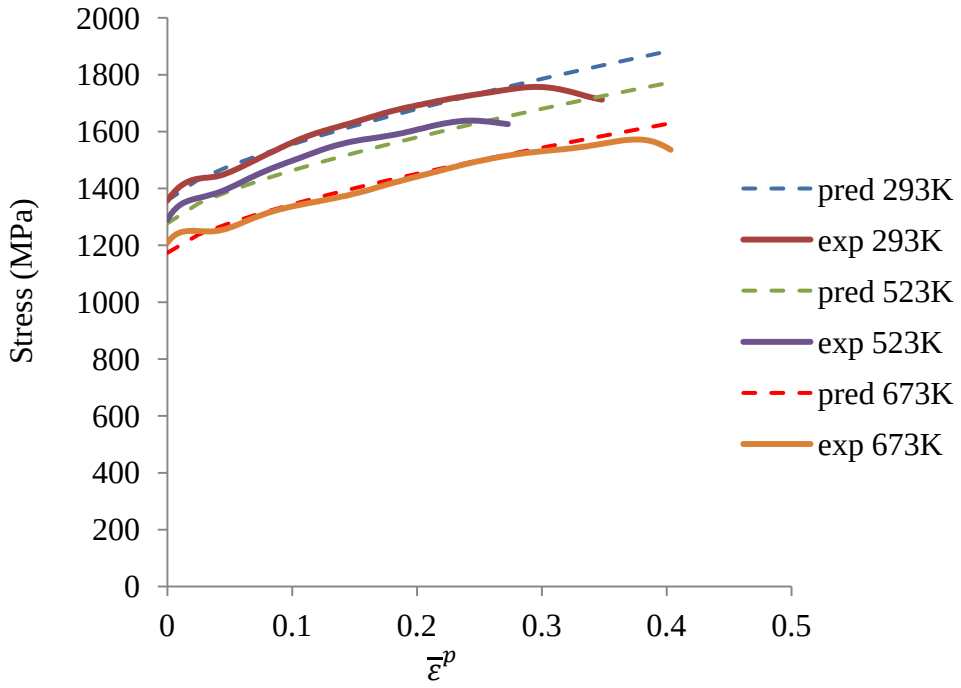

Figure 64. Comparison between experimental (exp) stress-strain curves and those predicted (pred) by the JC model at different temperatures for $\dot{\bar{\varepsilon}}^p \approx 6{,}000\ s^{-1}$.

4.2.3 Johnson-Cook VUMAT

4.2.3.1 Preliminary Power-Law Von Mises flow law analysis

Based upon the concepts of plasticity theory outlined in Chapter 2, a derivation of the flow potential was developed for a Power-law Von Mises stress formula for stresses and strains in tension, in order to extend the mathematical procedure for effectively calculating both the flow law and flow potential for the Johnson-Cook model. Initially, the expression of the flow law detailed in Eq. (29) was validated, hence according to Eq. (21) the effective plastic strain rate can be denoted as:

$$\dot{\bar{\varepsilon}}^p = \sqrt{\frac{2}{3}\dot{\varepsilon}_{ij}^p \dot{\varepsilon}_{ij}^p} = \sqrt{\frac{2}{3}\left(\dot{\bar{\varepsilon}}^p \frac{3}{2}\frac{S_{ij}}{\bar{\sigma}}\right)\left(\dot{\bar{\varepsilon}}^p \frac{3}{2}\frac{S_{ij}}{\bar{\sigma}}\right)} = \sqrt{\frac{2}{3}\frac{9}{4}\left(\frac{\dot{\bar{\varepsilon}}^p}{\bar{\sigma}}\right)^2 S_{ij}S_{ij}} \tag{66}$$

By replacing S_{ij} in Eq. (10) and $\bar{\sigma}$ in Eq. (23) in the above gives:

$$\dot{\bar{\varepsilon}}^p = \sqrt{\frac{2}{3}\frac{9}{4}\left(\frac{\dot{\bar{\varepsilon}}^p}{\bar{\sigma}}\right)^2 2J_2} = \sqrt{3\left(\frac{\dot{\bar{\varepsilon}}^p}{\bar{\sigma}}\right)^2 J_2} = \frac{\dot{\bar{\varepsilon}}^p}{\bar{\sigma}}\sqrt{3J_2} = \frac{\dot{\bar{\varepsilon}}^p}{\bar{\sigma}}\bar{\sigma} = \dot{\bar{\varepsilon}}^p \tag{67}$$

confirming that Eq. (67) verifies the expression of the flow law shown in Eq. (29). As the flow law is the derivative of the generalised flow potential (Ω) with respect to σ_{ij} (Eq. (13)), integration of the latter gives the plastic flow potential, as detailed in Eq. (68):

$$\Omega = \dot{\bar{\varepsilon}}^p \frac{\bar{\sigma}}{m_1+1} = \dot{\bar{\varepsilon}}_0 \left(\frac{\bar{\sigma}}{\bar{\sigma}_0}\right)^{m_1} \frac{\bar{\sigma}}{m_1+1} \tag{68}$$

The proof for Eq. (68) is detailed in Eq. (69):

$$\begin{aligned}\frac{\partial\Omega}{\partial\sigma_{ij}} &= \frac{\partial}{\partial\sigma_{ij}}\left(\dot{\bar{\varepsilon}}_0\left(\frac{\bar{\sigma}}{\bar{\sigma}_0}\right)^{m_1}\frac{\bar{\sigma}}{m_1+1}\right) = \frac{\partial}{\partial\sigma_{ij}}\left(\left(\frac{\dot{\bar{\varepsilon}}_0}{m_1+1}\right)\frac{\bar{\sigma}^{m_1+1}}{\bar{\sigma}_0{}^{m_1}}\right) \\ &= \left(\frac{\dot{\bar{\varepsilon}}_0}{m_1+1}\right)\frac{1}{\bar{\sigma}_0{}^{m_1}}\frac{\partial}{\partial\sigma_{ij}}\left(\bar{\sigma}^{m_1+1}\right) \\ &= \left(\frac{\dot{\bar{\varepsilon}}_0}{m_1+1}\right)\frac{1}{\bar{\sigma}_0{}^{m_1}}\left(m_1+1\right)\left(\bar{\sigma}^{m_1}\right)\frac{\partial\bar{\sigma}}{\partial\sigma_{ij}}\end{aligned} \tag{69}$$

Replacing $\overline{\sigma}$ in Eq. (23) in the above shows:

$$\frac{\partial \Omega}{\partial \sigma_{ij}} = \frac{\dot{\bar{\varepsilon}}_0}{{\bar{\sigma}_0}^{m_1}} \left(\overline{\sigma}^{m_1}\right) \frac{\partial \overline{\sigma}}{\partial \sigma_{ij}} = \frac{\dot{\bar{\varepsilon}}_0}{{\bar{\sigma}_0}^{m_1}} \left(\overline{\sigma}^{m_1}\right) \sqrt{3} \frac{\partial {J_2}^{1/2}}{\partial \sigma_{ij}} \tag{70}$$

where it can be deduced that:

$$\frac{\partial {J_2}^{1/2}}{\partial \sigma_{ij}} = \frac{1}{2} {J_2}^{-1/2} \frac{\partial J_2}{\partial \sigma_{ij}} = \frac{1}{2} {J_2}^{-1/2} S_{ij} = \frac{S_{ij}}{2\sqrt{J_2}} \tag{71}$$

Substituting Eq. (71) into Eq. (70), the flow law can be derived as detailed in Eq. (72), which corroborates Eq. (29) and validates Eq. (68).

$$\frac{\partial \Omega}{\partial \sigma_{ij}} = \frac{\dot{\bar{\varepsilon}}_0}{{\bar{\sigma}_0}^{m_1}} \left(\overline{\sigma}^{m_1}\right) \sqrt{3} \frac{S_{ij}}{2\sqrt{J_2}} = \dot{\bar{\varepsilon}}^p \sqrt{3} \frac{S_{ij}}{2\sqrt{J_2}} = \dot{\bar{\varepsilon}}^p \sqrt{3} \frac{S_{ij}}{2\frac{\overline{\sigma}}{\sqrt{3}}} = \dot{\bar{\varepsilon}}^p \frac{3}{2} \frac{S_{ij}}{\overline{\sigma}} \tag{72}$$

The equations for the flow law and flow potential vary when analysed for shear conditions, where the plastic strain rate magnitude is defined as:

$$\dot{\bar{\gamma}}^p = \sqrt{2 \dot{\gamma}_{ij}^p \dot{\gamma}_{ij}^p} \tag{73}$$

which is related to the plastic strain rate magnitude in tension, shown in Eq. (21), by:

$$\dot{\bar{\gamma}}^p = \sqrt{3}\, \dot{\bar{\varepsilon}}^p \tag{74}$$

Therefore, substituting Eq. (74) in Eq. (29) and recalling that $\overline{\sigma} = \bar{k}\sqrt{3}$, the plastic flow law for shear takes the form:

$$\dot{\gamma}_{ij}^p = \dot{\bar{\gamma}}^p \frac{\partial f}{\partial \sigma_{ij}} = \frac{\dot{\bar{\gamma}}^p}{2} \frac{S_{ij}}{\overline{k}} \qquad , \qquad \dot{\bar{\gamma}}^p = \dot{\bar{\gamma}}_0 \left(\frac{\overline{k}}{\overline{k}_0}\right)^{m_1} \tag{75}$$

where in general for an isotropic material the hardening law is:

$$\bar{k}_0 = \bar{k}_q \left(1 + \frac{\overline{\gamma}^p}{\bar{\gamma}_y}\right)^{n_2} \tag{76}$$

To verify the expression of the shear plastic flow law seen in Eq. (75), it can be shown from Eq. (73) that:

$$\dot{\bar{\gamma}}^p = \sqrt{2\dot{\gamma}_{ij}^p \dot{\gamma}_{ij}^p} = \sqrt{2\left(\frac{\dot{\bar{\gamma}}^p}{2}\frac{S_{ij}}{\bar{k}}\right)\left(\frac{\dot{\bar{\gamma}}^p}{2}\frac{S_{ij}}{\bar{k}}\right)} = \sqrt{2\frac{1}{4}\left(\frac{\dot{\bar{\gamma}}^p}{\bar{k}}\right)^2 S_{ij}S_{ij}} = \sqrt{2\frac{1}{4}\left(\frac{\dot{\bar{\gamma}}^p}{\bar{k}}\right)^2 2J_2} \tag{77}$$

Replacing $J_2 = \bar{k}^2$ in Eq. (22) in the above yields:

$$\dot{\bar{\gamma}}^p = \sqrt{\left(\frac{\dot{\bar{\gamma}}^p}{\bar{k}}\right)^2 J_2} = \frac{\dot{\bar{\gamma}}^p}{\bar{k}}\sqrt{J_2} = \frac{\dot{\bar{\gamma}}^p}{\bar{k}}\bar{k} = \dot{\bar{\gamma}}^p \tag{78}$$

Integration of the flow law therefore gives the plastic potential, which can be detailed as:

$$\Omega = \frac{\dot{\bar{\gamma}}^p}{m_1+1}\bar{k} = \frac{\dot{\bar{\gamma}}_0}{m_1+1}\left(\frac{\bar{k}}{\bar{k}_0}\right)^{m_1}\bar{k} \tag{79}$$

By utilising a similar procedure as with the case in tension, it can be shown that the flow law is:

$$\begin{aligned}\frac{\partial\Omega}{\partial\sigma_{ij}} &= \frac{\partial}{\partial\sigma_{ij}}\left(\frac{\dot{\bar{\gamma}}_0}{m_1+1}\left(\frac{\bar{k}}{\bar{k}_0}\right)^{m_1}\bar{k}\right) = \frac{\partial}{\partial\sigma_{ij}}\left(\frac{\dot{\bar{\gamma}}_0}{m_1+1}\frac{\bar{k}^{m_1+1}}{\bar{k}_0{}^{m_1}}\right) \\ &= \frac{\dot{\bar{\gamma}}_0}{m_1+1}\frac{1}{\bar{k}_0{}^{m_1}}\frac{\partial}{\partial\sigma_{ij}}\left(\bar{k}^{m_1+1}\right) = \frac{\dot{\bar{\gamma}}_0}{m_1+1}\frac{1}{\bar{k}_0{}^{m_1}}(m_1+1)\left(\bar{k}^{m_1}\right)\frac{\partial\bar{k}}{\partial\sigma_{ij}}\end{aligned} \tag{80}$$

Recalling that $J_2 = \bar{k}^2$ (Eq. (22)), the above gives:

$$\frac{\partial\Omega}{\partial\sigma_{ij}} = \frac{\dot{\bar{\gamma}}_0}{\bar{k}_0{}^{m_1}}\left(\bar{k}^{m_1}\right)\frac{\partial\bar{k}}{\partial\sigma_{ij}} = \frac{\dot{\bar{\gamma}}_0}{\bar{k}_0{}^{m_1}}\left(\bar{k}^{m_1}\right)\frac{\partial J_2{}^{1/2}}{\partial\sigma_{ij}} \tag{81}$$

and replacing Eq. (71) in the above, it is seen that:

$$\frac{\partial\Omega}{\partial\sigma_{ij}} = \frac{\dot{\bar{\gamma}}_0}{\bar{k}_0{}^{m_1}}\left(\bar{k}^{m_1}\right)\frac{S_{ij}}{2\sqrt{J_2}} \tag{82}$$

Further manipulation reduces to Eq. (82):

$$\frac{\partial \Omega}{\partial \sigma_{ij}} = \dot{\overline{\gamma}}^{p} \frac{S_{ij}}{2\sqrt{J_2}} = \frac{\dot{\overline{\gamma}}^{p}}{2} \frac{S_{ij}}{\overline{k}} \tag{83}$$

which equates Eq. (75) and therefore validates Eq. (79).

4.2.3.2 Main characteristics

The JC relationship to describe the flow behaviour of a material is given by Eq. (32), however an alternative form of the flow stress for shear is provided by Ozlu et al. (2010), who stated that:

$$\overline{k} = \frac{1}{\sqrt{3}} \left[A + B \left(\frac{\overline{\gamma}^{p}}{\sqrt{3}} \right)^{n} \right] \left[1 + C \, ln \left(\frac{\dot{\overline{\gamma}}^{p}}{\dot{\overline{\gamma}}_0} \right) \right] \left[1 - \left(\frac{T - T_r}{T_m - T_r} \right)^{m} \right] \tag{84}$$

where substituting $\overline{\sigma} = \overline{k}\sqrt{3}$ and taking from Eq. (74) the effective plastic strain $\overline{\varepsilon}^{p} = \overline{\gamma}^{p}/\sqrt{3}$ as well as $\dot{\overline{\gamma}}^{p}/\dot{\overline{\gamma}}_0 = \dot{\overline{\varepsilon}}^{p}/\dot{\overline{\varepsilon}}_0$, the formula is equivalent to that in tension. Based on this, an initial expression for the flow law and flow potential for shear was developed, which was subsequently used to further determine the flow law and flow potential in tension.

The plastic flow potential was initially derived from the expression of the equivalent plastic strain rate, which from Eq. (84) was calculated as:

$$ln \left(\frac{\dot{\overline{\gamma}}^{p}}{\dot{\overline{\gamma}}_0} \right) = \frac{1}{C} \left(\frac{\overline{k}}{\frac{1}{\sqrt{3}} \left[A + B \left(\frac{\overline{\gamma}^{p}}{\sqrt{3}} \right)^{n} \right] \left[1 - \left(\frac{T - T_r}{T_m - T_r} \right)^{m} \right]} - 1 \right) \tag{85}$$

where substituting $A_k = A/\sqrt{3}$ and $B_k = B/\sqrt{3}$, the effective shear strain rate can be expressed according to Eq. (86):

$$\dot{\overline{\gamma}}^{p} = \dot{\overline{\gamma}}_0 \, exp \left[\frac{1}{C} \left(\frac{\overline{k}}{\left[A_k + B_k \left(\frac{\overline{\gamma}^{p}}{\sqrt{3}} \right)^{n} \right] \left[1 - \left(\frac{T - T_r}{T_m - T_r} \right)^{m} \right]} - 1 \right) \right] \tag{86}$$

Eq. (86) can be reduced to:

$$\dot{\bar{\gamma}}^{p} = \dot{\bar{\gamma}}_{0}\, exp\left[C_k\left(\frac{\sqrt{J_2}}{k_s} - 1\right)\right] \tag{87}$$

where:

$$k_s = \left[A_k + B_k\left(\frac{\bar{\gamma}^{p}}{\sqrt{3}}\right)^{n}\right]\left[1 - \left(\frac{T - T_r}{T_m - T_r}\right)^{m}\right] \quad , \quad C_k = \frac{1}{C} \quad , \quad \bar{k} = \sqrt{J_2} \tag{88}$$

Finally, the equation for the flow law takes the form of:

$$\frac{\partial \Omega}{\partial \sigma_{ij}} = \frac{\dot{\bar{\gamma}}^{p}}{2}\frac{S_{ij}}{\bar{k}} = \frac{\dot{\bar{\gamma}}_{0}}{2} exp\left[C_k\left(\frac{\sqrt{J_2}}{k_s} - 1\right)\right]\frac{S_{ij}}{\sqrt{J_2}} \tag{89}$$

where following integration, the flow potential is:

$$\Omega = \frac{\dot{\bar{\gamma}}_{0}}{C_k} exp\left[C_k\left(\frac{\sqrt{J_2}}{k_s} - 1\right)\right] k_s \tag{90}$$

Subsequent derivation of the flow potential to validate the flow law shown in Eq. (89) gives:

$$\begin{aligned}
\frac{\partial \Omega}{\partial \sigma_{ij}} &= \frac{\partial}{\partial \sigma_{ij}}\left(\frac{\dot{\bar{\gamma}}_{0}}{C_k} exp\left[C_k\left(\frac{\sqrt{J_2}}{k_s} - 1\right)\right] k_s\right) \\
&= \frac{\dot{\bar{\gamma}}_{0}}{C_k} k_s\, exp\left[C_k\left(\frac{\sqrt{J_2}}{k_s} - 1\right)\right]\frac{\partial}{\partial \sigma_{ij}}\left[C_k\left(\frac{\sqrt{J_2}}{k_s} - 1\right)\right] \\
&= \frac{\dot{\bar{\gamma}}_{0}}{C_k} k_s\, exp\left[C_k\left(\frac{\sqrt{J_2}}{k_s} - 1\right)\right]\frac{C_k}{k_s}\frac{\partial \sqrt{J_2}}{\partial \sigma_{ij}} \\
&= \frac{\dot{\bar{\gamma}}_{0}}{C_k} k_s\, exp\left[C_k\left(\frac{\sqrt{J_2}}{k_s} - 1\right)\right]\frac{C_k}{k_s}\frac{S_{ij}}{2\sqrt{J_2}}
\end{aligned} \tag{91}$$

which yields:

$$\frac{\partial \Omega}{\partial \sigma_{ij}} = \frac{\dot{\bar{\gamma}}_{0}}{2} exp\left[C_k\left(\frac{\sqrt{J_2}}{k_s} - 1\right)\right]\frac{S_{ij}}{\sqrt{J_2}} \tag{92}$$

Eq. (92) can finally be reduced as detailed in Eq. (93) and is equivalent to Eq. (89):

$$\frac{\partial \Omega}{\partial \sigma_{ij}} = \frac{\dot{\overline{\gamma}}^{p}}{2} \frac{S_{ij}}{\overline{k}} \tag{93}$$

The plastic flow potential in tension is derived from the expression of the equivalent plastic strain rate, which from Eq. (32) is given by:

$$\dot{\overline{\varepsilon}}^{p} = \dot{\overline{\varepsilon}}_0 \, exp\left[\frac{1}{C}\left(\frac{\overline{\sigma}}{\left[A + B\left(\overline{\varepsilon}^{p}\right)^{n}\right]\left[1 - \left(\frac{T - T_r}{T_m - T_r}\right)^{m}\right]} - 1\right)\right] \tag{94}$$

Similarly for shear, Eq. (94) can be reduced to:

$$\dot{\overline{\varepsilon}}^{p} = \dot{\overline{\varepsilon}}_0 \, exp\left[C_k\left(\frac{\sqrt{3\,J_2}}{\sigma_s} - 1\right)\right] \tag{95}$$

where:

$$\sigma_s = \left[A + B\left(\overline{\varepsilon}^{p}\right)^{n}\right]\left[1 - \left(\frac{T - T_r}{T_m - T_r}\right)^{m}\right] \quad , \quad C_k = \frac{1}{C} \quad , \quad \overline{\sigma} = \sqrt{3\,J_2} \tag{96}$$

Therefore, the plastic flow law takes the form:

$$\frac{\partial \Omega}{\partial \sigma_{ij}} = \dot{\overline{\varepsilon}}^{p} \frac{3}{2} \frac{S_{ij}}{\overline{\sigma}} = \frac{3}{2} \dot{\overline{\varepsilon}}_0 \, exp\left[C_k\left(\frac{\sqrt{3\,J_2}}{\sigma_s} - 1\right)\right] \frac{S_{ij}}{\sqrt{3\,J_2}} \tag{97}$$

and after integrating Eq. (97), the flow potential results to be:

$$\Omega = \frac{\dot{\overline{\varepsilon}}_0}{C_k} \, exp\left[C_k\left(\frac{\sqrt{3\,J_2}}{\sigma_s} - 1\right)\right] \sigma_s \tag{98}$$

Subsequent derivation of the flow potential to corroborate the flow law seen in Eq. (97) gives:

$$\begin{aligned}\frac{\partial \Omega}{\partial \sigma_{ij}} &= \frac{\partial}{\partial \sigma_{ij}}\left(\frac{\dot{\bar{\varepsilon}}_0}{C_k}\, exp\left[C_k\left(\frac{\sqrt{3\,J_2}}{\sigma_s}-1\right)\right]\sigma_s\right)\\ &= \frac{\dot{\bar{\varepsilon}}_0}{C_k}\,\sigma_s\, exp\left[C_k\left(\frac{\sqrt{3\,J_2}}{\sigma_s}-1\right)\right]\frac{\partial}{\partial \sigma_{ij}}\left[C_k\left(\frac{\sqrt{3\,J_2}}{\sigma_s}-1\right)\right]\\ &= \frac{\dot{\bar{\varepsilon}}_0}{C_k}\,\sigma_s\, exp\left[C_k\left(\frac{\sqrt{3\,J_2}}{\sigma_s}-1\right)\right]\frac{C_k\sqrt{3}}{\sigma_s}\frac{\partial \sqrt{J_2}}{\partial \sigma_{ij}}\\ &= \frac{\dot{\bar{\varepsilon}}_0}{C_k}\,\sigma_s\, exp\left[C_k\left(\frac{\sqrt{3\,J_2}}{\sigma_s}-1\right)\right]\frac{C_k\sqrt{3}}{\sigma_s}\frac{S_{ij}}{2\sqrt{J_2}}\end{aligned} \tag{99}$$

which finally yields:

$$\frac{\partial \Omega}{\partial \sigma_{ij}} = \frac{\sqrt{3}}{2}\dot{\bar{\varepsilon}}_0\, exp\left[C_k\left(\frac{\sqrt{3\,J_2}}{\sigma_s}-1\right)\right]\frac{S_{ij}}{\sqrt{J_2}} = \frac{\sqrt{3}}{2}\dot{\bar{\varepsilon}}^p\,\frac{S_{ij}}{\frac{\bar{\sigma}}{\sqrt{3}}} = \dot{\bar{\varepsilon}}^p\,\frac{3}{2}\frac{S_{ij}}{\bar{\sigma}} \tag{100}$$

holding true for Eq. (97) and thus, validating Eq. (98).

4.2.3.3 Constitutive equations

Some of the equations that were used to write the thermo-mechanical VUMAT subroutine for the JC constitutive model were derived following the example given in ABAQUS (2010) for a rate-dependent isotropic elasto-plastic material, while the rest needed to complete the code were determined based on previous subsections as well as from the literature. In this work, the elasticity was assumed to be linear and isotropic with parameters (Young's modulus and shear modulus) assumed temperature dependent. In consequence, the elasticity can be written in terms of three material parameters that are the bulk modulus K, the shear modulus μ (sometimes also known as G) and the Lame's constant λ, which are defined as:

$$K = \frac{E}{3(1-2\nu)} \tag{101}$$

$$\mu = \frac{E}{2(1+\nu)} \tag{102}$$

$$\lambda = \frac{\nu E}{(1+\nu)(1-2\nu)} \tag{103}$$

where recall that E and ν are the Young's modulus and Poisson's ratio respectively. Eq. (102) provides a relationship between E and μ, however with no temperature effects being taken into consideration. To include these, the physical laws for describing the variation of E and μ with temperature were obtained from the literature (Soo, 2003 and Davis, 1997 respectively), and thus an appropriate value of ν was calculated in order to keep the experimental evidence valid. Data for both E and μ are unknown beyond a temperature of ~1,100K, therefore the parameter ν was assumed to be variable in the range 273-1,100K in order to corroborate Eq. (102). As the drop with increasing temperature is more noticeable in μ than E and as such, it would make Eq. (102) to lose validity, it was considered that a quadratic fit to the data points for E holds from 1,100K afterwards together with the assumption that $\nu = 0.276$ is constant (computed as the mean value in the range of 273-1,100K). In consequence, μ was computed according to Eq. (102) beyond 1,100K so that agreement with data and material elastic relationships is achieved**.** The elasticity can be written in volumetric p_{ij} and deviatoric S_{ij} tensor components respectively as follows:

$$p_{ij} = -\frac{1}{3}\sigma_{kk}\delta_{ij} = -\lambda\varepsilon^e_{kk}\delta_{ij} \tag{104}$$

$$S_{ij} = \sigma_{ij} + p_{ij} = \sigma_{ij} - \frac{\sigma_{kk}}{3}\delta_{ij} = \sigma_{ij} - \lambda\varepsilon_{kk}\delta_{ij} = 2\mu\varepsilon^e_{ij} \tag{105}$$

A further detailed analysis of Eq. (105) shows that the stress components in the elastic region can be described according to Eq. (106):

$$\sigma_{ij} = S_{ij} - p_{ij} = 2\mu\varepsilon^e_{ij} + \lambda\varepsilon^e_{kk}\delta_{ij} = \frac{E}{(1+\nu)}\varepsilon^e_{ij} + \frac{\nu E}{(1+\nu)(1-2\nu)}\varepsilon^e_{kk}\delta_{ij} \tag{106}$$

This neglects any influence on the stress tensor from changes in the bulk workpiece volume due to increases in temperature (see Eq. (20)), which is insignificant in conventional cutting operations.

When extending the analysis to the plastic region, the flow law is governed by Eq. (97), which is required for the material to satisfy a uniaxial stress-plastic strain/strain rate/temperature relationship and calculation of the plastic strain increment $\Delta\bar{\varepsilon}^p$. As the material is rate and temperature dependent, the relationship follows the uniaxial flow rate

detailed in Eq. (95), where integrating using the backward Euler method and substituting $\overline{\sigma} = \sqrt{3\,J_2}$, results in Eq. (107) for the effective plastic strain increment:

$$\Delta\overline{\varepsilon}^{p} = \Delta t\,\dot{\overline{\varepsilon}}^{p} = \Delta t\,\dot{\varepsilon}_0\,exp\left[C_k\left(\frac{\overline{\sigma}}{\sigma_s} - 1\right)\right] \tag{107}$$

Eq. (107) can be inverted numerically to define $\overline{\sigma}$ as a function of $\overline{\varepsilon}^{p}$ at the end of the increment $(t + \Delta t)$, which yields the JC relationship:

$$\overline{\sigma} = \left[A + B\left(\overline{\varepsilon}^{p} + \Delta\overline{\varepsilon}^{p}\right)^{n}\right]\left[1 + C\;ln\left(\frac{\overline{\varepsilon}^{p} + \Delta\overline{\varepsilon}^{p}}{(t + \Delta t)\,\dot{\varepsilon}_0}\right)\right]\left[1 - \left(\frac{T - T_r}{T_m - T_r}\right)^{m}\right] \tag{108}$$

where the time increment is explicitly included. For any time increment where plastic flow is occurring (which is confirmed by evaluating $\overline{\sigma}$ based on purely elastic response and verifying that σ_s is exceeded), Eq. (101) to Eq. (108) must be integrated and solved for the state at the end of the increment. In ABAQUS, the integration procedure is accomplished by applying the backward Euler method to the flow law given by Eq. (13), thus the plastic strain rate is:

$$\dot{\varepsilon}_{ij}^{p} = \frac{\partial\Omega}{\partial\sigma_{ij}} = \frac{\Delta\varepsilon_{ij}^{p}}{\Delta t} = \dot{\overline{\varepsilon}}_0\,exp\left[C_k\left(\frac{\overline{\sigma}}{\sigma_s} - 1\right)\right]\frac{3}{2}\frac{S_{ij}}{\overline{\sigma}} \tag{109}$$

Therefore the plastic strain yields:

$$\Delta\varepsilon_{ij}^{p} = \Delta t\,\dot{\overline{\varepsilon}}_0\,exp\left[a\left(\frac{\overline{\sigma}}{\sigma_s} - 1\right)\right]\frac{3}{2}\frac{S_{ij}}{\overline{\sigma}} = \Delta\overline{\varepsilon}^{p}\,\frac{3}{2}\frac{S_{ij}}{\overline{\sigma}} \tag{110}$$

Combining Eq. (110) with Eq. (105) together with the strain rate decomposition defined in Eq. (17), which after time integration results in the total strain increment $\Delta\varepsilon_{ij} = \Delta\varepsilon_{ij}^{e} + \Delta\varepsilon_{ij}^{p}$, an associated increment in the deviatoric stresses is given by Eq. (111):

$$\Delta S_{ij} = 2\mu\Delta\varepsilon_{ij}^{e} = 2\mu\left(\Delta\varepsilon_{ij} - \Delta\varepsilon_{ij}^{p}\right) = 2\mu\left(\Delta\varepsilon_{ij} - \Delta\overline{\varepsilon}^{p}\,\frac{3}{2}\frac{S_{ij}}{\overline{\sigma}}\right) \tag{111}$$

The total deviatoric stress component at the time $t + \Delta t$ is then defined by Eq. (112):

$$S_{ij} = S_{ij}^0 + \Delta S_{ij} = S_{ij}^0 + 2\mu\left(\Delta\varepsilon_{ij}^e - \Delta\varepsilon_{ij}^p\right) = 2\mu\,\varepsilon_{ij}^e\big|_t + 2\mu\left(\Delta\varepsilon_{ij}^e - \Delta\varepsilon_{ij}^p\right) = \\ = 2\mu\left(\varepsilon_{ij}^e\big|_t + \Delta\varepsilon_{ij}^e\right) - 2\mu\Delta\varepsilon_{ij}^p \tag{112}$$

Utilising the integrated flow law observed in Eq. (110), the first term on the right hand side of Eq. (112) becomes:

$$2\mu\left(\varepsilon_{ij}^e\big|_t + \Delta\varepsilon_{ij}^e\right) = S_{ij} + 2\mu\Delta\varepsilon_{ij}^p = S_{ij}\left(1 + \frac{2\mu\Delta\varepsilon_{ij}^p}{S_{ij}}\right) = S_{ij}\left(1 + \frac{2\mu\Delta\overline{\varepsilon}^p\,\frac{3}{2}\frac{S_{ij}}{\overline{\sigma}}}{S_{ij}}\right) \\ = S_{ij}\left(1 + \frac{3\mu}{\overline{\sigma}}\Delta\overline{\varepsilon}^p\right) \tag{113}$$

To simplify notation, the term $\varepsilon_{ij}^e\big|_t + \Delta\varepsilon_{ij}^e$ is denoted as $\hat{\varepsilon}_{ij}$, hence Eq. (113) yields:

$$2\mu\hat{\varepsilon}_{ij} = S_{ij}\left(1 + \frac{3\mu}{\overline{\sigma}}\Delta\overline{\varepsilon}^p\right) \tag{114}$$

Taking the inner product of Eq. (114) with itself gives:

$$(2\mu)^2\hat{\varepsilon}_{ij}\hat{\varepsilon}_{ij} = S_{ij}S_{ij}\left(1 + \frac{3\mu}{\overline{\sigma}}\Delta\overline{\varepsilon}^p\right)^2 = 2\,J_2\left(1 + \frac{3\mu}{\overline{\sigma}}\Delta\overline{\varepsilon}^p\right)^2 = \frac{2\,\overline{\sigma}^2}{3}\left(1 + \frac{3\mu}{\overline{\sigma}}\Delta\overline{\varepsilon}^p\right)^2 \tag{115}$$

Multiplication of Eq. (115) by $2/3$ gives:

$$(2\mu)^2\frac{2}{3}\hat{\varepsilon}_{ij}\hat{\varepsilon}_{ij} = \frac{4\,\overline{\sigma}^2}{9}\left(1 + \frac{3\mu}{\overline{\sigma}}\Delta\overline{\varepsilon}^p\right)^2 \tag{116}$$

which can be simplified as:

$$2\mu\sqrt{\frac{2}{3}\hat{\varepsilon}_{ij}\hat{\varepsilon}_{ij}} = \frac{2\,\overline{\sigma}}{3}\left(1 + \frac{3\mu}{\overline{\sigma}}\Delta\overline{\varepsilon}^p\right) \tag{117}$$

to eventually obtain:

$$3\mu\tilde{\overline{\varepsilon}} = \overline{\sigma} + 3\mu\Delta\overline{\varepsilon}^p \qquad , \qquad \tilde{\overline{\varepsilon}} = \sqrt{\frac{2}{3}\hat{\varepsilon}_{ij}\hat{\varepsilon}_{ij}} \tag{118}$$

Rearranging terms it is obtained:

$$3\mu\left(\tilde{\bar{\varepsilon}} - \Delta\bar{\varepsilon}^{p}\right) - \bar{\sigma} = 0 \tag{119}$$

Eq. (119) describes a non-linear relationship for $\Delta\bar{\varepsilon}^{p}$ in the general case when $\bar{\sigma}$ depends on the effective plastic strain (e.g. when the material is rate-dependent, or when there is nonzero work hardening), but it is linear when the workpiece response is rate-dependent perfectly plastic. The influence of temperature in the constitutive response of the material considered is the description for $\bar{\sigma}$ in Eq. (32). Solving Eq. (115) using the Newton's method, the following generic function $f\left(\Delta\bar{\varepsilon}^{p}\right)$ and its first derivative $f'\left(\Delta\bar{\varepsilon}^{p}\right)$ can be defined:

$$f\left(\Delta\bar{\varepsilon}^{p}\right) = 3\mu\left(\tilde{\bar{\varepsilon}} - \Delta\bar{\varepsilon}^{p}\right) - \bar{\sigma} \tag{120}$$

$$f'\left(\Delta\bar{\varepsilon}^{p}\right) = \frac{\Delta f\left(\Delta\bar{\varepsilon}^{p}\right)}{\Delta\bar{\varepsilon}^{p}} = 3\mu(0-1) - \frac{\Delta\bar{\sigma}}{\Delta\bar{\varepsilon}^{p}} = -3\mu - \frac{\Delta\bar{\sigma}}{\Delta\bar{\varepsilon}^{p}} = -3\mu - H \tag{121}$$

For the JC plasticity model, the analytical form of the hardening parameter H can be computed as:

$$H = \frac{d\bar{\sigma}}{d\bar{\varepsilon}^{p}} = \left[B\, n\left(\bar{\varepsilon}^{p}\right)^{n-1}\right]\left[1 + C\, ln\left(\frac{\bar{\varepsilon}^{p}}{t\,\dot{\bar{\varepsilon}}_{0}}\right)\right]\left[1 - \left(\frac{T - T_{r}}{T_{m} - T_{r}}\right)^{m}\right] \tag{122}$$

where $\bar{\varepsilon}^{p}$ is the accumulated plastic strain and t is the current step time. Now it can be made:

$$c_{p} = -\frac{f_{a}\left(\Delta\bar{\varepsilon}^{p}\right)}{f'_{a}\left(\Delta\bar{\varepsilon}^{p}\right)} = -\frac{3\mu\left(\tilde{\bar{\varepsilon}} - \Delta\bar{\varepsilon}^{p}\right) - \bar{\sigma}}{-3\mu - H} = \frac{3\mu\left(\tilde{\bar{\varepsilon}} - \Delta\bar{\varepsilon}^{p}\right) - \bar{\sigma}}{3\mu + H} \tag{123}$$

where c_{p} is a generic term defined for simplification purposes. Therefore the plastic strain increment is calculated according to Eq. (124) using an iterative procedure until convergence is achieved:

$$\Delta\bar{\varepsilon}^{p} = \Delta\bar{\varepsilon}_{0}^{p} + c_{p} = \Delta\bar{\varepsilon}_{0}^{p} + \frac{3\mu\left(\tilde{\bar{\varepsilon}} - \Delta\bar{\varepsilon}^{p}\right) - \bar{\sigma}}{3\mu + H} = \Delta\bar{\varepsilon}_{0}^{p} + \frac{3\mu\tilde{\bar{\varepsilon}} - 3\mu\Delta\bar{\varepsilon}^{p} - \bar{\sigma}}{3\mu + H} \tag{124}$$

All parameters can be easily identified in Eq. (124) but $3\mu\tilde{\bar{\varepsilon}}$. Expanding the function in Eq. (125) corresponds to the effective Von Mises stress calculated at the current time step ($\bar{\sigma}_{C}$):

$$3\mu\tilde{\bar{\varepsilon}} = 3\mu\sqrt{\frac{2}{3}\hat{\varepsilon}_{ij}\hat{\varepsilon}_{ij}} = \sqrt{9\mu^2\frac{2}{3}\hat{\varepsilon}_{ij}\hat{\varepsilon}_{ij}} = \sqrt{6\mu^2\hat{\varepsilon}_{ij}\hat{\varepsilon}_{ij}} = \sqrt{\frac{6}{4}\left(2\mu\hat{\varepsilon}_{ij}\right)\left(2\mu\hat{\varepsilon}_{ij}\right)} = \sqrt{\frac{3}{2}\,S_{ij}S_{ij}} \quad (125)$$

Eq. (124) converges when $\Delta\bar{\varepsilon}^p \cong \Delta\bar{\varepsilon}_0^p$ (depending on the value of the tolerance chosen, but always close to zero), which means that $3\mu\tilde{\bar{\varepsilon}} - 3\mu\Delta\bar{\varepsilon}^p - \bar{\sigma} \cong 0$. Therefore it can be assumed that $3\mu\tilde{\bar{\varepsilon}} - \bar{\sigma} \cong 0$, because $\Delta\bar{\varepsilon}^p$ is small when compared to $3\mu\tilde{\bar{\varepsilon}}$ and $\bar{\sigma}$. Consequently, in some cases it is straightforward to approximate $\Delta\bar{\varepsilon}^p$ as:

$$\Delta\bar{\varepsilon}^p = \frac{\bar{\sigma}_C - \bar{\sigma}}{3\mu + H} \quad (126)$$

which yields practically the same value when calculated with the Newton's method. Once $\Delta\bar{\varepsilon}^p$ is found, the solution can be fully determined by first updating the deviatoric stresses in Eq. (114) as follows:

$$\left[S_{ij}\right]_{new} = \frac{1}{1 + \frac{3\mu}{\bar{\sigma}_{new}}\Delta\bar{\varepsilon}^p}\,2\mu\hat{\varepsilon}_{ij} = \frac{\bar{\sigma}_{new}}{\bar{\sigma}_{new} + 3\mu\Delta\bar{\varepsilon}^p}\left(2\mu\hat{\varepsilon}_{ij}\right) = \frac{\bar{\sigma}_{new}}{\bar{\sigma}_{new} + 3\mu\Delta\bar{\varepsilon}^p}\left[S_{ij}\right]_{old} \quad (127)$$

where $\bar{\sigma}_{new}$ is the updated flow stress computed at the end of the increment taking into account $\Delta\bar{\varepsilon}^p$. Finally, the tensor stress components at the end of the increment are calculated as:

$$\left[\sigma_{ij}\right]_{new} = \left[S_{ij}\right]_{new} - \left[p_{ij}\right]_{new} = \frac{\bar{\sigma}_{new}}{\bar{\sigma}_{new} + 3\mu\Delta\bar{\varepsilon}^p}\left(2\mu\hat{\varepsilon}_{ij}\right) + \frac{1}{3}\left[\sigma_{kk}\right]_{new}\delta_{ij} \quad (128)$$

To obtain accurate predictions when performing fully coupled thermo-mechanical FE simulations involving plasticity, it is mandatory to update both the specific internal and dissipated energies. In the former situation, the energy per unit volume can be calculated according to Bower (2009) as:

$$U = \frac{1}{\rho_o}\left(\frac{1}{2}\sigma_{ij}\varepsilon_{ij}^e\right) \quad (129)$$

where the tensor and strain quantities are known and ρ_o is the density of the material. For numerical purposes though, the calculation is performed as the sum of accumulated trapezoids leading to Eq. (130):

$$U_{new} = U_{old} + \frac{\Delta\varepsilon_{ij}^{e}}{2\rho_o}\left(\left[\sigma_{ij}\right]_{old} + \left[\sigma_{ij}\right]_{new}\right) \tag{130}$$

To compute the dissipated plastic energy (the area under the stress-strain curve) per unit volume, the situation follows a similar procedure prior to material yielding as shown in Eq. (131):

$$U_{new}^{p} = U_{old}^{p} + \frac{\Delta\overline{\varepsilon}^{p}}{2\rho_o}(\overline{\sigma} + \overline{\sigma}_{new}) \tag{131}$$

The validity of the JC-based VUMAT subroutine was evaluated by comparing it against the built-in JC model within ABAQUS before modelling the machining process. A detailed comparative analysis of the results from both simulations is shown in Appendix II.

4.3 Mechanical Threshold Stress model for Inconel 718

4.3.1 Calculation of model parameters

4.3.1.1 Determination of σ_a

In correspondence with previous research (Follansbee and Kocks, 1988; Goto et al., 2000), σ_a was estimated as 40MPa and assumed to remain constant with strain. This value was utilised for the present work without any further modification.

4.3.1.2 Determination of g_{0i} and $\hat{\sigma}_i$

In an initial attempt to describe the viscoplastic characteristics of Inconel 718, a two-term MTS model was developed, whose description of the flow stress is given by Eq. (39). The values of g_{0i} and $\hat{\sigma}_i$ were calculated based on a modified Arrhenius (Fisher) diagram, with input values taken from the $\overline{\sigma} - \overline{\varepsilon}^{p}$ data generated following elevated strain rate and temperature compression tests using the Gleeble and SHPB testing apparatuses. The plot was first constructed by constraining the model assuming that $\hat{\sigma}_e = 0$ when $\overline{\varepsilon}^{p} = 0$ (strain value at which yielding takes place) with chosen values for pi, qi and $\dot{\overline{\varepsilon}}_{0i}$ beforehand, thus from Eq. (39) it is obtained:

$$\left(\frac{\overline{\sigma}-\sigma_a}{\mu}\right)^{pi} = \left[1-\left(\frac{kT}{g_{0i}\mu b^3}ln\left(\frac{\dot{\overline{\varepsilon}}_{0i}}{\dot{\overline{\varepsilon}}^p}\right)\right)^{\frac{1}{qi}}\right]\left(\frac{\hat{\sigma}_i}{\mu_0}\right)^{pi} = \left(\frac{\hat{\sigma}_i}{\mu_0}\right)^{pi} - \left(\frac{1}{g_{0i}}\right)^{\frac{1}{qi}}\left(\frac{\hat{\sigma}_i}{\mu_0}\right)^{pi}\left(\frac{kT}{\mu b^3}ln\left(\frac{\dot{\overline{\varepsilon}}_{0i}}{\dot{\overline{\varepsilon}}^p}\right)\right)^{\frac{1}{qi}} \quad (132)$$

An example of how the plot is constructed will be given for T=293K, with values for the constants appearing in Eq. (132) assumed to be: $b = 2.48\text{x}10^{-10}m$ and $k = 1.38\text{x}10^{-23}J/K$ according to Goto et al. (2000), whereas $\dot{\overline{\varepsilon}}_{0i} = 1\text{x}10^{7}s^{-1}$, $p_i = 1$ and $q_i = 1$ were selected based on trial and error iterations. The shear modulus μ was assumed to be temperature dependent according to the following expression (Davis, 1997):

$$\mu\,(MPa) = 80{,}272.3 - 20.146\,(T-273) - 0.00888298\,(T-273)^2 \quad , \quad T(K) \qquad (133)$$

where it follows that $\mu_0 = \mu(T = 0K) = 85{,}114.1\ MPa$. Finally, a plot of the type:

$$\left(\frac{\overline{\sigma}-\sigma_a}{\mu}\right)^{pi} \text{ vs. } \left(\frac{kT}{\mu b^3}ln\left(\frac{\dot{\overline{\varepsilon}}_{0i}}{\dot{\overline{\varepsilon}}^p}\right)\right)^{\frac{1}{qi}}$$

was constructed whose input values were the experimental yield strength $\overline{\sigma}$ together with the strain rate and temperature at which such yielding occurred as explained before.

The data generated with the SHPB apparatus at strain rates of ~1,000 and 2,000s^{-1} however were disregarded in the development of the present constitutive model because their corresponding yield strength values were found to be lower when compared to results using the Gleeble machine at lower strain rates (see Figure 65). This discrepancy was believed to occur in the region where the strain rate sensitivity of Inconel 718 takes place, somehow resembling the results Lee et al. (2011) experimentally obtained.

A similar situation evidencing the sudden increase in yield strength was recorded by DeMange et al. (2009) when testing aged Inconel 718 at low and high strain rates, with values that varied from 1,350MPa (0.04s^{-1}) to 2,075MPa (2,339s^{-1}) respectively. It has been shown that in fcc metals (such as Inconel 718) the rate-controlling mechanism relates to the overcoming of dislocation forests made by individual dislocations, but taking into account that the activation volume is much higher for fcc than for bcc metals, the strain rate sensitivity of the former compared to the latter is much lesser (Liang and Khan, 1999). However the modification in strain rate sensitivity on fcc metals such as 0.999Cu is due to the strain rate sensitivity of structure evolution, as corroborated by Follansbee and Kocks (1988).

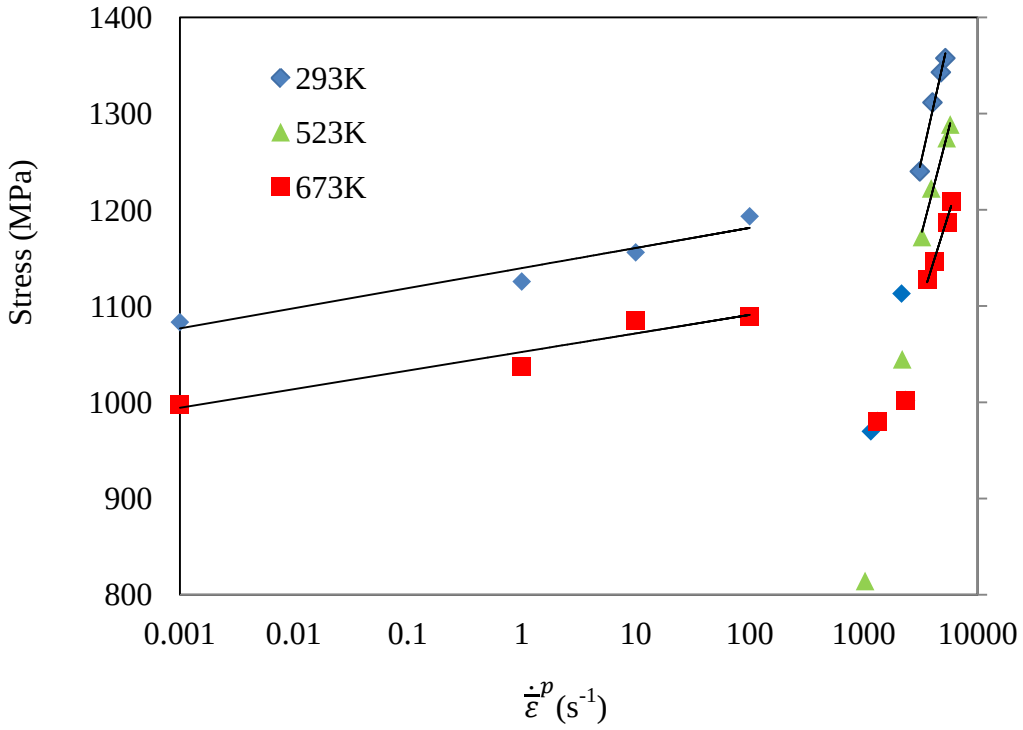

Figure 65. Semi-log graph showing that yield strength data points belonging to strain rates of ~1,000 and 2,000s^{-1} do not conform to the trend seen from the first (Gleeble) to the second (SHPB) set of data, which would resemble that seen in Figure 18.

Taking into account that the highest testing temperature (673K) is not capable of degrading significantly the strength of the superalloy and that at high strain rates (>1,000s^{-1}) hardening due to dislocation interaction is more energetic, the increase in the strain rate sensitivity pattern observed in Figure 65 is much more noticeable compared to that at low strain rates (<1,000s^{-1}).

Table 14 details a summary of the yield strength values recorded following compression tests at room temperature (T=293K) for different strain rates.

	Yield Strength (MPa)							
	First set of data - Gleeble				**Second set of data - SHPB**			
293K	1,083.3 (0.001)	1,125.5 (1)	1,155.8 (10)	1,193.3 (100)	1,239.96 (3,113)	1,311.6 (4,020)	1,343.03 (4,762)	1,357.66 (5,216)

Table 14. Yield strength (MPa) for a temperature of 293K (values in parenthesis indicate the strain rates at which yielding occurred).

In the example outlined here, the results obtained to construct the Fisher plot utilising the yield strength values taken from Table 14 together with the constants previously assumed, were as displayed in Figure 66.

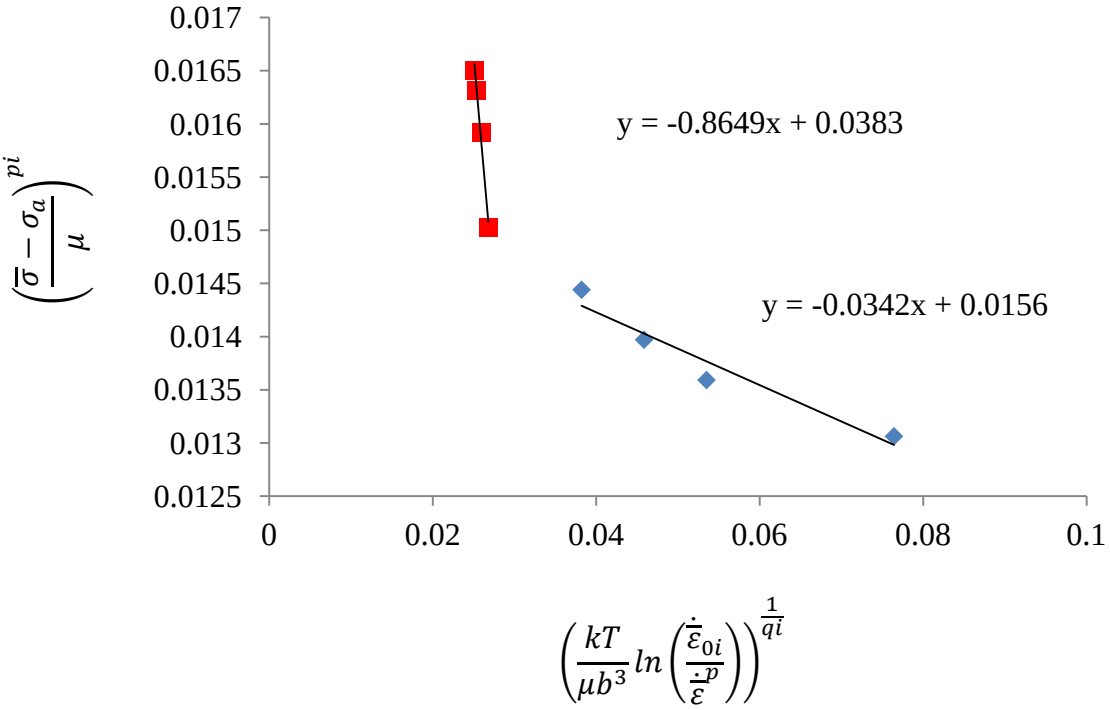

Figure 66. Fisher plot constructed from generated data and utilised to calculate $\hat{\sigma}_i$ and g_{0i} when T=293K.

It is generally assumed that g_{0i} and $\hat{\sigma}_i$ remain constant for all temperatures and strain rates that compose the testing domain, most of the time for simplification purposes as considered by Follansbee and Kocks (1988). The Fisher diagram shown in Figure 66 implies however that there were two slopes whose values were noticeable different, hence such assumption of constancy for g_{0i} and $\hat{\sigma}_i$ could no longer be withhold. Here, the linear fit corresponding to the lowest slope corresponds to data generated with the Gleeble machine (quasi static – 100s^{-1}) whereas the remaining line seen in the plot relates to data which were generated with the SHPB apparatus (≥1,000s^{-1}).

The trend found in this investigation is in accordance with previously published work by Chen and Gray III (1996) on tantalum, although it has a bcc structure. For Ni-C alloys (fcc) however, the appearance of the Fisher plot is also similar to that seen in Figure 66, although a single line to fit the data points was only used (Follansbee et al., 1990).

To account for the behaviour seen in Figure 66, it was assumed in consequence that in those two distinctive regions where the slopes become different, two different values of g_{0i} and $\hat{\sigma}_i$ that include all strain rates under analysis must be calculated for each temperature under consideration. As described before, the adjustment of all data points was made with a straight line for each case, where in the region comprising low strain rates (first set of data) can be observed:

$$x = \left(\frac{kT}{\mu b^3} ln\left(\frac{\dot{\bar{\varepsilon}}_{0i}}{\dot{\bar{\varepsilon}}^p}\right)\right)^{\frac{1}{qi}} = 0 \quad , \quad y = \left(\frac{\overline{\sigma} - \sigma_a}{\mu}\right)^{pi} = \left(\frac{\hat{\sigma}_i}{\mu_0}\right)^{pi} = 0.0156$$

where $\hat{\sigma}_i = 1327.78\, MPa$. With this value already calculated the next step was to obtain the value of g_{0i} when $y = 0$, calculation procedure which was made as follows:

$$0 = -0.0342\, x + 0.0156 = -\left(\frac{1}{g_{0i}}\right)^{\frac{1}{qi}} \left(\frac{\hat{\sigma}_i}{\mu_0}\right)^{pi} \left(\frac{kT}{\mu b^3} ln\left(\frac{\dot{\bar{\varepsilon}}_{0i}}{\dot{\bar{\varepsilon}}^p}\right)\right)^{\frac{1}{qi}} + 0.0156$$

where finally $g_{0i} = 0.4561$.

By repeating the same procedure for high strain rates (second set of data), the other two values of $\hat{\sigma}_i$ and g_{0i} were obtained, which were $3{,}259.87\, MPa$ and 0.04428 respectively. In order to calculate all other g_{0i} and $\hat{\sigma}_i$ values, it is mandatory to know the yield strength for every strain rate and temperature as it can be concluded from Eq. (132) and the example shown at T=293K. This is simple and straightforward to do with the data already generated, however for numerical purposes it was necessary to complete the 'gaps' in the yield strength values that were missing from the testing conditions in order to have a fully defined domain which in consequence could allow the FE software to run free of divergences in such regions of interest.

For example, Figure 67 shows a 3D scheme of all $\hat{\sigma}_i$ values calculated from the available second set of data (SHPB) with respect to strain rate and temperature, in which case the XC, YC and ZC axes correspond to the temperature (K), strain rate (in log axis displayed, s^{-1}) and $\hat{\sigma}_i$ respectively (MPa). From the graph, it is evidenced that $\hat{\sigma}_i$ values corresponding to temperatures higher than 673K (for all strain rates ranging from 0.001 to ~6,000s^{-1}) must be fulfilled in order to have a totally defined FE model in the tested domains.

In principle, the behaviour of $\hat{\sigma}_i$ in the strain rate range of 100s^{-1} to 3,113s^{-1} at all temperatures under consideration (293, 523 and 673K) was assumed to be linear mostly due to the resulting shape of all Fisher plots, which (in some cases) made the computation of an 'intersection strain rate' impossible, because had such calculation process taken place, some experimental data points would have been ignored.

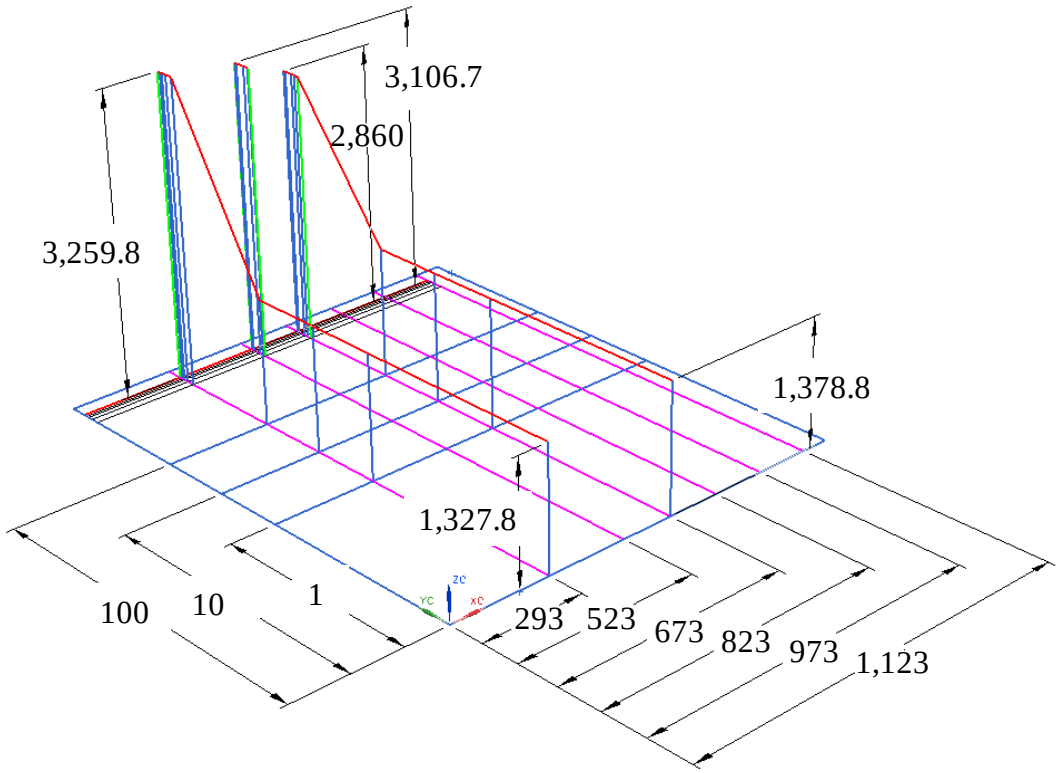

Figure 67. 3D scheme of $\hat{\sigma}_i$ with respect to strain rate and temperature. The gaps found at 523K and outside the tested region must be completed in order to run a FE model free of numerical divergences.

This can be clearly evidenced in the Fisher plot constructed for a temperature of 823K as shown in Figure 68:

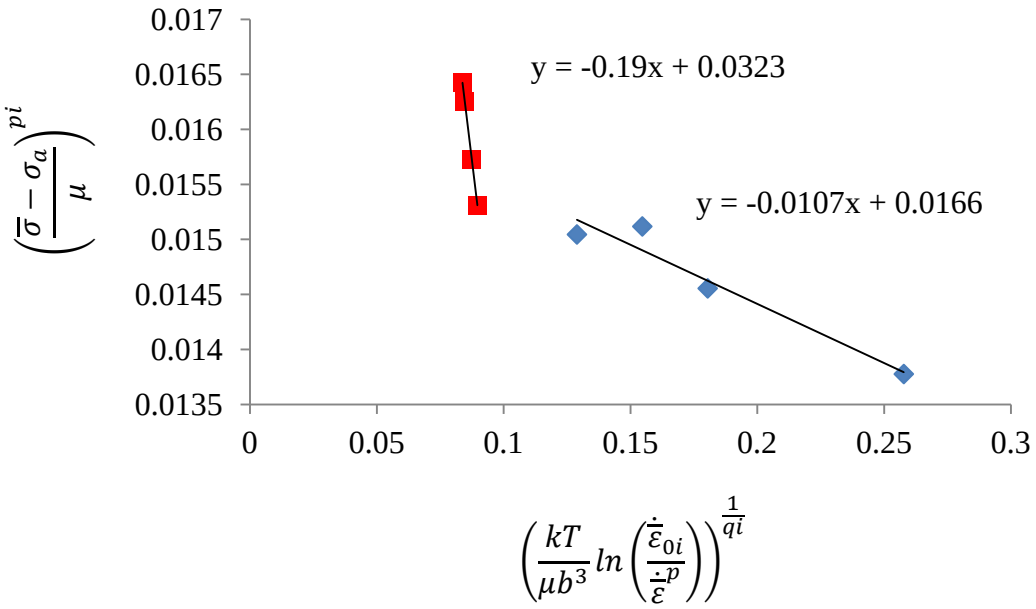

Figure 68. Fisher plot constructed from available and estimated data and utilised to calculate $\hat{\sigma}_i$ and g_{0i} when T=823K.

A simple calculation of the 'intersection strain rate' comprising both straight lines would give a value of 1,153s^{-1}, which in principle would seem correct as it lies between 1,000s^{-1} to 3,113s^{-1}, however from Figure 68 it can be noticed that such intersection would be produced at a point in which at least one data value (either calculated from experiments or estimated) had to be ignored. In order to avoid a situation like this one therefore, the joining of data points from strain rates of 100s^{-1} to 3,113s^{-1} was done with a straight line.

In order to accomplish the task of filling the gaps seen in Figure 67, the yield strength values in the low strain rate regime (0.001, 1, 10 and 100s^{-1}) at a temperature T=523K (250°C) were needed to calculate the respective $\hat{\sigma}_i$ missing values**.** Therefore in order to calculate them, a graph of Yield Strength vs. Temperature taking into account temperatures of 293K and 673K for a strain rate of 0.001s^{-1} was constructed as shown in Figure 69.

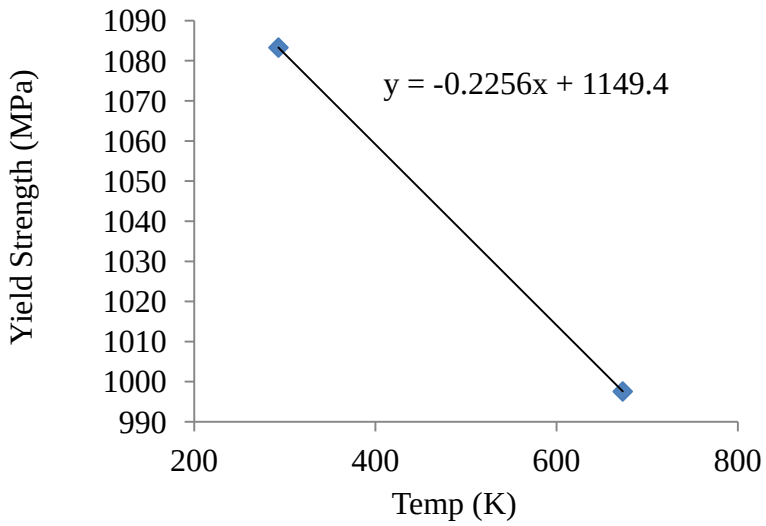

Figure 69. Graph plotted taking into account the values of the yield strength corresponding to temperatures of 293 and 673K.

It was assumed that the missing yield strength value between 293K and 673K lies within the straight line that connects both data points, therefore for 523K at 0.001s^{-1} the estimated yield strength was:

$$yield\ strength\ (estimated) = -0.2256 * 523 + 1{,}149.4 = 1{,}031.4MPa$$

The calculation for the remaining three yield strength values corresponding to the other low strain rates followed. A slightly different procedure was used to calculate the yield strength values for elevated strain rates (~3,000-6,000s^{-1}) and temperatures (823-1,123K) though,

mostly because they would lie outside the boundaries of the data generated, hence assumptions needed to be stronger than before. Initially, a semi log graph Yield Strength vs. Strain Rate with the whole second set of data (SHPB) was constructed as shown in Figure 70:

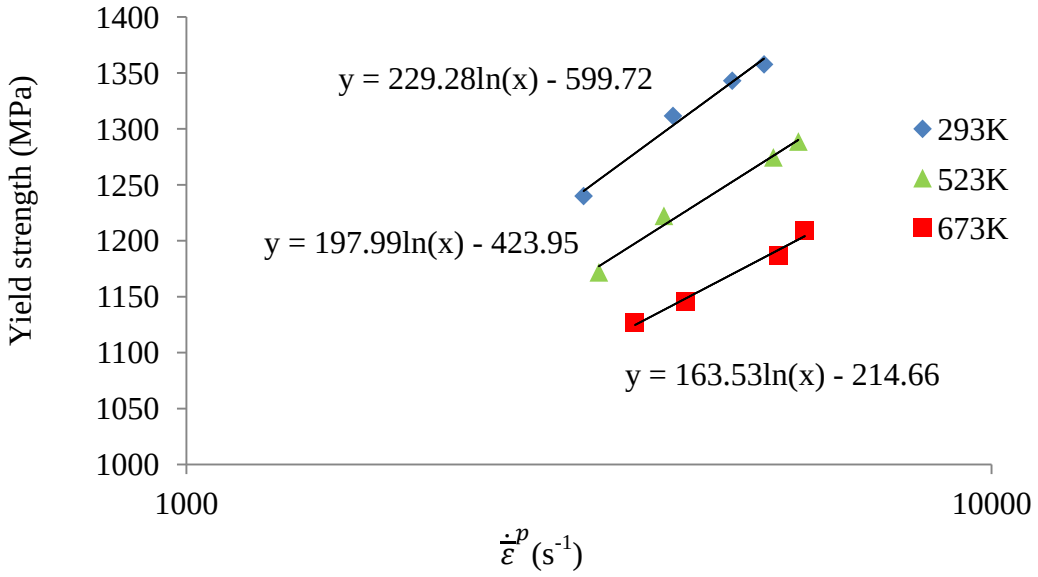

Figure 70. Semi-log graph plotted taking into account the values of the yield strength for strain rates that varied from ~3,000 to 6,000s^{-1} corresponding to temperatures of 293, 523 and 673K respectively.

A linear fit was assumed for each of the data points plotted that corresponded to the same temperature and varied with strain rate. Then, another two graphs of the slope values and the [absolute value of the] independent terms that resulted from the previous calculations and can be identified in Figure 70, (both being considered with respect to temperature) were made as shown in Figures 71a and 71b.

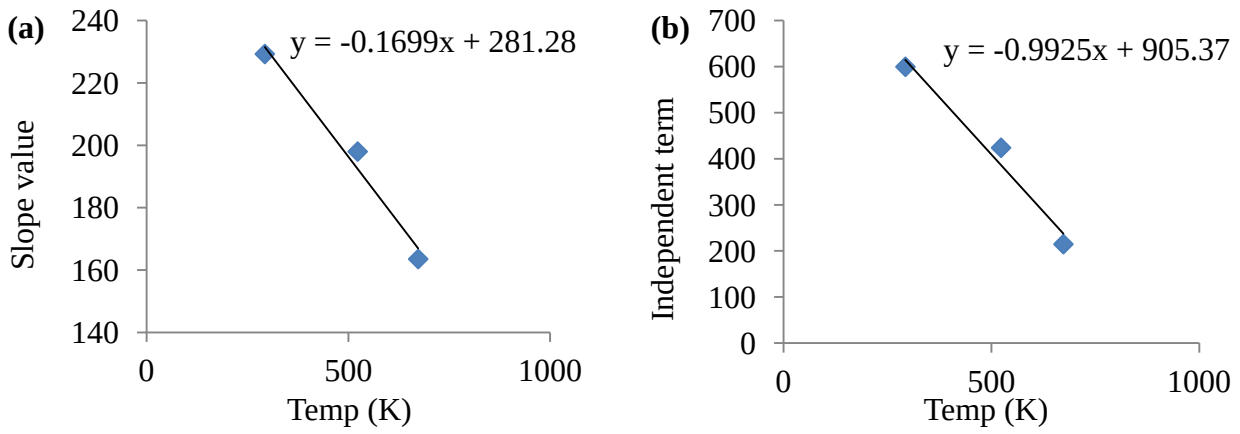

Figure 71. (a) Graph plotted taking into account the values of the slopes seen in Figure 76, (b) Graph plotted taking into account the absolute value of the independent terms seen in Figure 70.

A linear fit was made for the data points plotted observed in Figures 71a and 71b, which was assumed not to have significant oscillations for temperatures higher than 673K, irrespective of strain rate. In order to estimate the yield strength for a temperature of 823K at a strain rate of ~3,000s^{-1}, the calculated slope and absolute value of the independent term were found to be 141.45 and 88.54 respectively. As the SHPB tests were not performed at exactly 3,000s^{-1} (due to the machine's operating characteristics the firing pressures were set equal instead, therefore the achieved strain rates were similar), the calculation of the yield strength was then made by taking an average value of strain rate from the second set of data:

$$strain\ rate\ (823K) = \frac{(3{,}113 + 3{,}252 + 3{,}606)}{3} = 3{,}324s^{-1}$$

So that the estimated yield strength would be:

$$yield\ strength\ (823K - 3{,}324s^{-1}) = 141.45 * \ln(3{,}324) - 88.543 = 1{,}058.5\ MPa$$

The calculation of the remaining yield strength values up to temperatures of 973K was made following the same procedure. As the yield strength of Inconel 718 degrades very rapidly above temperatures of 923K (650°C) as stated before, a different estimation of such values for strain rates of ~3,000-6,000s^{-1} needed to be made for a temperature of 1,123K. This behaviour which softens the superalloy is clearly marked at low strain rates (the plot includes the already calculated values of yield strength for 523K) as it can be deduced from Figure 72.

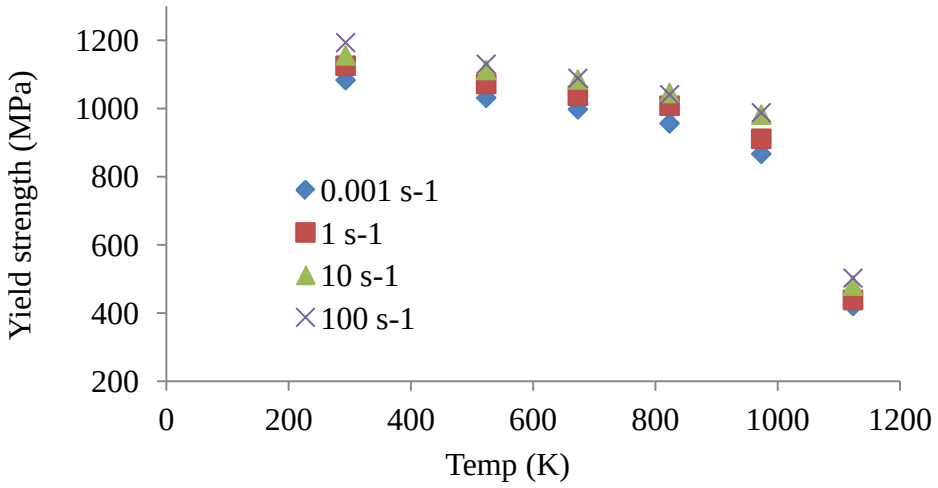

Figure 72. Graph plotted considering yield strength values for strain rates that varied from ~0.001 to 100s^{-1} corresponding to temperatures of 293, 523, 673, 823, 973 and 1,123K respectively.

In order to keep consistency, it was assumed that degradation of the yield strength at elevated strain rates followed an equivalent trend when the strain rates were low. In the construction of a graph Yield Strength vs. Temperature in the interval delimitated by the temperatures 973K and 1,123K when accounting for low strain rates, an interesting pattern was found and can be clearly noticed in Figure 73:

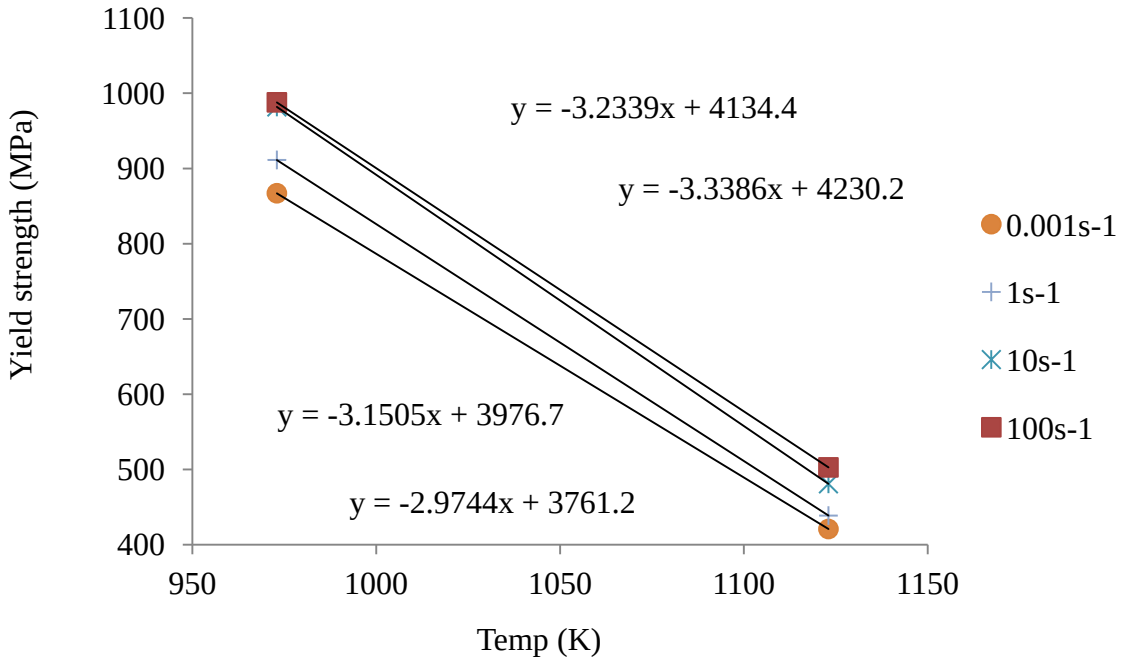

Figure 73. Graph plotted taking into account the values of the yield strength for strain rates that varied from ~0.001 to 100s^{-1} corresponding to temperatures of 973 and 1,123K respectively.

The slopes of the fitting lines can practically be considered parallel for all data points, therefore in order to minimise errors an average value of slope was calculated, which was -3.17435. In order to keep uniformity in the calculations, the independent term (B_1) that was needed to compute the new yield strength was given by the yield strength previously estimated at 973K for the averaged strain rate of 3,324s^{-1} and was calculated as follows:

$$yield\ strength\ (973K - 3324s^{-1}) = -3.17435 * 973 + B_1 = 1{,}000.7 \quad , \quad B_1 = 4{,}089.33$$

Finally, the yield strength at T=1,123K and $\dot{\bar{\varepsilon}}^{p} = 3{,}324s^{-1}$ was estimated as follows:

$$yield\ strength\ (1{,}123K - 3{,}324s^{-1}) = -3.17435 * 1123 + 4{,}089.33 = 524.3\ MPa$$

Table 15 summarises the experimental yield strength values corresponding to Inconel 718 obtained from the Gleeble and SHPB testing apparatuses together with the estimated values that were utilised for the construction of the Fisher plot and the subsequent calculation of g_{0i} and $\hat{\sigma}_i$ parameters necessitated for numerical purposes within the MTS framework.

Temperature (K)						
293	523	673	823	973	1,123	
Yield strength (MPa)						
1,083.3 (0.001)	**1,031.4 (0.001)**	997.57 (0.001)	956.45 (0.001)	867.06 (0.001)	420.89 (0.001)	**Gleeble**
1,125.5 (1)	**1,072.4 (1)**	1,037.3 (1)	1,008.22 (1)	911.3 (1)	438.72 (1)	
1,155.8 (10)	**1,113.1 (10)**	1,085.16 (10)	1,045.67 (10)	981.71 (10)	480.92 (10)	
1,193.3 (100)	**1,130.2 (100)**	1,088.94 (100)	1,040.82 (100)	987.86 (100)	502.78 (100)	
1,239.96 (3,113)	1,171.77 (3,252)	1,127.13 (3,606)	**1,058.5 (3,324)**	**1,000.7 (3,324)**	**524.3 (3,324)**	**SHPB**
1,311.6 (4,020)	1,222.28 (3,917)	1,146.02 (4171)	**1,085.9 (4,036)**	**1,023.2 (4,036)**	**547.1 (4,036)**	
1,343.03 (4,762)	1,274.54 (5,357)	1,186.95 (5,432)	**1,121.3 (5,184)**	**1,052.2 (5,184)**	**576.1 (5,184)**	
1,357.66 (5,216)	1,288.71 (5,754)	1,208 (5,864)	**1,132.6 (5,611)**	**1,061.4 (5,611)**	**585.3 (5,611)**	

Table 15. Experimental and estimated (in bold) yield strength (MPa) values for various temperatures (K) used to develop, for numerical purposes, the MTS constitutive model. Values in parenthesis indicate the real and averaged strain rates (also in bold) at which yielding was supposed to have taken place.

All g_{0i} and $\hat{\sigma}_i$ values had to be calculated for all strain rates and temperatures (with particular complexity in the region where strain rates and temperatures were higher than ~3,000s^{-1} and 673K respectively), not only for those obtained from the SHPB tests, but also for those calculated as average values.

The aim of this task was to construct a piecewise bilinear surface with a regular grid whose intermediate g_{0i} and $\hat{\sigma}_i$ (each of the variables being considered with respect to strain and temperature) values could be derived from, in which case an uncomplicated linear interpolation scheme in the local domain of interest was performed.

4.3.1.3 Determination of $\hat{\sigma}_{es0}$ and g_{es0}

It is generally assumed for the development of the MTS model that the quantities $\hat{\sigma}_{es0}$ and g_{es0} remain constant irrespective of all testing conditions, very much similar to what it is considered with g_{0i} and $\hat{\sigma}_i$. In order to calculate $\hat{\sigma}_{es0}$ (saturation stress at $T = 0K$) from Eq. (43), it is first necessary to calculate $\hat{\sigma}_{es}$ (saturation stress), value which is obtained from a $\hat{\sigma}_e - \overline{\varepsilon}^p$ graph when $\hat{\sigma}_e$ reaches a constant value (when it is found to be stable). Another option outlined by Banerjee (2007) is to calculate $\hat{\sigma}_{es}$ from a $d\hat{\sigma}_e/d\overline{\varepsilon}^p$ vs. $\hat{\sigma}_e$ graph at the point when $d\hat{\sigma}_e/d\overline{\varepsilon}^p = 0$. From Eq. (39) the term $\hat{\sigma}_e$ takes the form of:

$$\hat{\sigma}_e = \frac{1}{s_e\left(\dot{\overline{\varepsilon}}^p, T\right)}\left(\frac{\mu_0}{\mu}(\overline{\sigma} - \sigma_a) - \hat{\sigma}_i\, s_i\left(\dot{\overline{\varepsilon}}^p, T\right)\right) \tag{134}$$

where in order to calculate $s_e\left(\dot{\overline{\varepsilon}}^p, T\right)$, the parameters $\dot{\overline{\varepsilon}}_{0e}$, $\dot{\varepsilon}_{es0}$, p_e, q_e and g_{0e} have to be assumed beforehand.

Commonly to simplify things, it is postulated that g_{0e} always remains constant, however in most situations this is not the case as considerable variability exists (Follansbee and Kocks, 1988), thereby making the use of an 'average value' questionable. In general, most researchers have employed $g_{0e} = 1.6$ (Chen and Gray III, 1996; Goto et al., 2000; Banerjee, 2007) following the work initiated by Follansbee and Kocks (1988), although the basis of this value was not outlined by the authors.

In this work however, as the activation energy g_{0i} was assumed to be variable with strain rate and temperature, it was stipulated that g_{0e} would follow the same fashion. The problem with making g_{0e} variable implied that one more variable wais introduced into the general formulation of the model (therefore increasing its complexity), however an intuitive method which minimised the errors encountered when $\hat{\sigma}_{es0}$ and g_{es0} were calculated in the usual way was proposed in this work. Initially and in line with the common method for calculating $\hat{\sigma}_{es0}$ and g_{es0}, a graph of the type:

$$\frac{kT}{\mu b^3}\, ln\left(\frac{\dot{\varepsilon}_{es0}}{\dot{\overline{\varepsilon}}^p}\right) \text{ vs. } ln\,(\hat{\sigma}_{es})$$

was constructed from the Gleeble and SHPB data as it is shown in Figure 74:

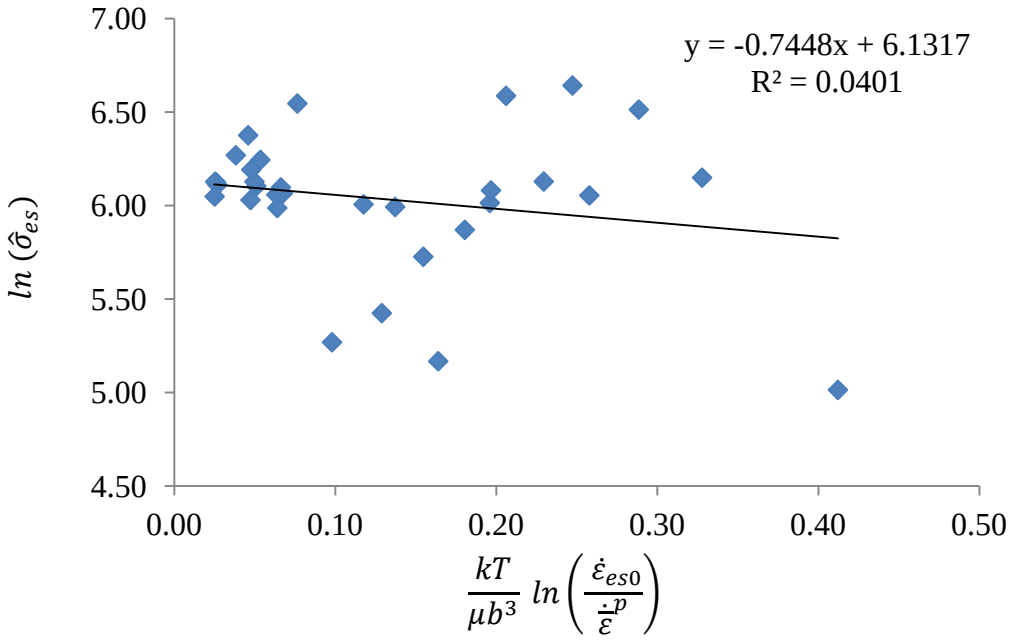

Figure 74. Graph constructed from available experimental data in order to calculate the parameters $\hat{\sigma}_{es0}$ and g_{es0} when considering $g_{0e} = 1.6$.

From Eq. (43) and Figure 74 it was deduced that:

$$ln(\hat{\sigma}_{es}) = ln(\hat{\sigma}_{es0}) - \frac{1}{g_{es0}} \frac{kT}{\mu b^3} ln\left(\frac{\dot{\varepsilon}_{es0}}{\dot{\varepsilon}^p}\right)$$

Therefore it is easy to notice that:

$$x = \frac{kT}{\mu b^3} ln\left(\frac{\dot{\varepsilon}_{es0}}{\dot{\varepsilon}^p}\right) = 0 \quad , \quad y = ln(\hat{\sigma}_{es}) = ln(\hat{\sigma}_{es0}) = 6.1317$$

hence $\hat{\sigma}_{es0} = e^{6.1317} = 460.22MPa$. With this parameter already calculated the next step was to obtain the value of g_{es0} when $y = 0$:

$$0 = -0.7448\,x + 6.1317 = -\frac{1}{g_{es0}}\left[\frac{kT}{\mu b^3} ln\left(\frac{\dot{\varepsilon}_{es0}}{\dot{\varepsilon}^p}\right)\right] + 6.1317$$

By inspection, it can be seen that: $-1/g_{es0} = -0.7448$, therefore $g_{es0} = 1.343$.

The scatter in the data points seen in Figure 74 was considerable to believe that the assumption of constancy for $g_{0e} = 1.6$ would give accurate predictions (evidenced by the low R-squared value of the fit made).

For this reason, it was decided to make this parameter variable with temperature and strain rate. The method to calculate the different g_{0e} values proposed in this work consisted of keeping $g_{es0} = 1.343$ invariable and made $\hat{\sigma}_{es0}$ to fluctuate, because in some cases the analytical computation of g_{0e} by working with Eq. (43) and Eq. (39):

$$g_{0e} = \frac{\frac{kT}{\mu b^3}\, ln\left(\frac{\dot{\bar{\varepsilon}}_{0e}}{\dot{\bar{\varepsilon}}^p}\right)}{\left[1 - \left(\frac{\frac{\mu_0}{\mu}(\bar{\sigma} - \sigma_a) - s_i\left(\dot{\bar{\varepsilon}}^p, T\right)\hat{\sigma}_i}{\hat{\sigma}_{es}}\right)^{pe}\right]^{qe}} \tag{135}$$

where the constants are $\dot{\bar{\varepsilon}}_{0e} = 1\text{x}10^7 s^{-1}$, $p_e = 1$, $q_e = 1$ and $\hat{\sigma}_{es}$ is obtained from a $\hat{\sigma}_e - \bar{\varepsilon}^p$ curve; could provide negative values, which is erroneous for activation energies.

It is seen from Eq. (135) that in order to avoid negative values of g_{0e}, $\hat{\sigma}_{es}$ values as high as possible are required. Therefore from the data generated, all $\hat{\sigma}_{es}$ values were gathered considering Eq. (39) (initially by stipulating $g_{0e} = 1.6$, otherwise there would be more variables than equations to solve) and used to compute $\hat{\sigma}_{es0}$ for every strain rate and temperature accordingly.

It is simple to deduce from Eq. (43) that $\hat{\sigma}_{es}$ increases when $\hat{\sigma}_{es0}$ increases, hence the criterion here was to choose the maximum value of those $\hat{\sigma}_{es0}$ previously obtained to recalculate all $\hat{\sigma}_{es}$ values. Once this was done, all g_{0e} were computed by making use of Eq. (135), ensuring in the end that no negative values were found. It is worth mentioning that both methods for calculating $\hat{\sigma}_{es0}$ and g_{es0} (the general and the one proposed in this work) end up with the same quantity for g_{es0}, however the approach proposed in this work completely clears out the poor fit initially calculated and effectively provided constant values of $\hat{\sigma}_{es0}$ and g_{es0} throughout all the testing conditions.

While assuming an arbitrary constant value for g_{0e} is simple to do and has been the preferred choice by many researchers, it could also produce an inadequate linear regression. On the other hand, the adjustment of the data points by working back the constitutive equations as described before is highly likely to eliminate this source of imperfection (see Figure 75), but with the disadvantage of obtaining a slightly different value of $\hat{\sigma}_{es0}$ as well as augmenting the complexity of the viscoplastic model (and in consequence, its implementation into the FE model through the VUMAT subroutine).

Finally, $\hat{\sigma}_{es0} = \exp(6.8265) = 921.96MPa$ while g_{es0} remained the same as before.

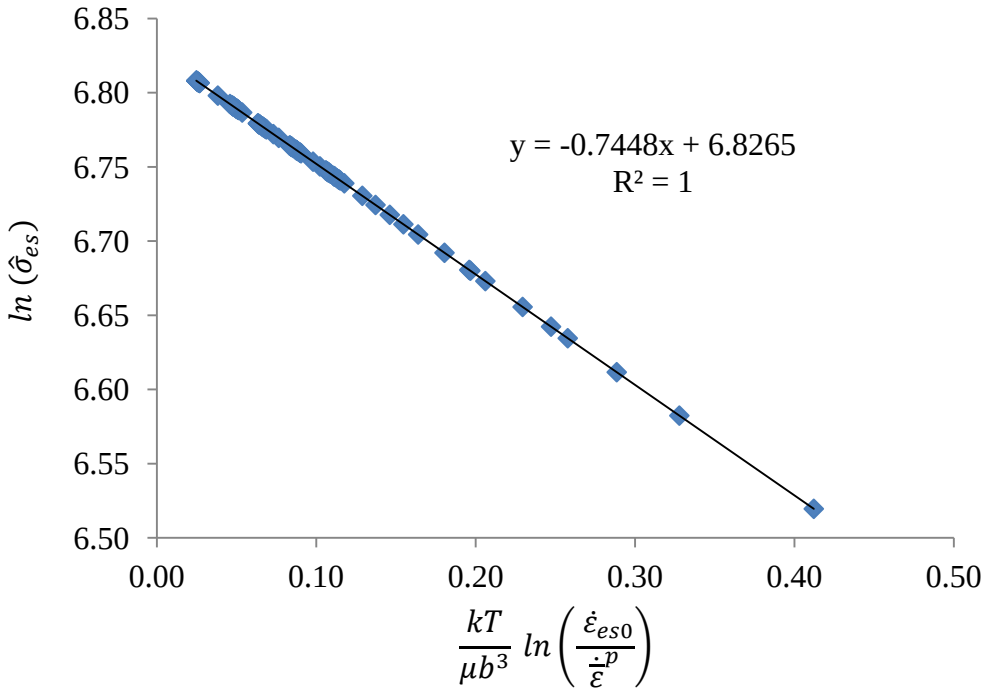

Figure 75. Graph constructed following the assumption that g_{0e} was variable instead of having the value of 1.6 in order to obtain constant values for $\hat{\sigma}_{es0}$ and g_{es0} throughout all the testing condition and therefore, increase the accuracy of the predictions.

4.3.1.4 Determination of θ_0

According to Eq. (42) when $\hat{\sigma}_e = 0$, the parameter $\theta = d\hat{\sigma}_e/d\overline{\varepsilon}^p = \theta_0$. Therefore, the values of θ_0 are easily calculated from the slope of the graph $\hat{\sigma}_e - \overline{\varepsilon}^p$ at zero strain. It is worth noticing that in an ideal condition $\hat{\sigma}_e = 0$ at zero strain as assumed in subsection 4.3.1.2, however due to the relatively high spread encountered in the data points when initially calculating the parameters $\hat{\sigma}_i$ and g_{0i}, the values of $\hat{\sigma}_e$ computed from Eq. (39) may slightly differ from zero.

Although this source of error is known, θ_0 was be calculated as $\Delta\hat{\sigma}_e/\Delta\overline{\varepsilon}^p$. The computation of the slope was done using the initial pair of resulting $\hat{\sigma}_e$ points corresponding to those $\overline{\varepsilon}^p$. For example, Figure 76 shows the resulting $\hat{\sigma}_e - \overline{\varepsilon}^p$ curves for a temperature of 293K and a strain rate of $0.001s^{-1}$ when the $g_{0e} = 1.6$ and when it is variable, noticing that no big differences in the shape of the curves are encountered, therefore reinforcing the assumption made in subsection 4.3.1.3 that considers a good approach to have constant values of $\hat{\sigma}_{es0}$ and g_{es0} for all testing conditions.

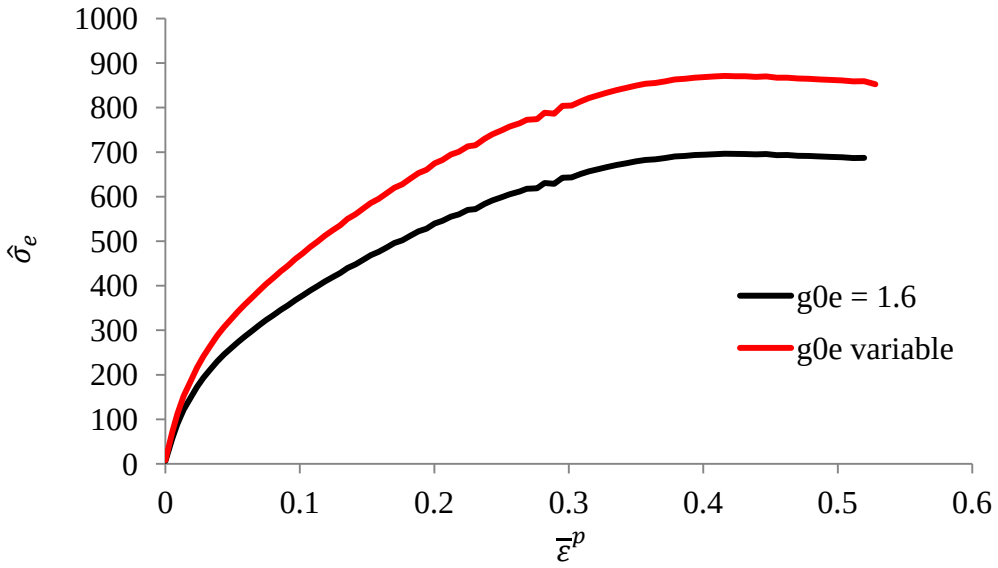

Figure 76. Resulting $\hat{\sigma}_e - \bar{\varepsilon}^p$ curves when the strain rate is 0.001s^{-1} and the temperature is 293K, taking into account different values of g0e. In this case θ_0 was calculated from the curve seen in red, which corresponded to a g0e variable.

4.3.2 Plastic stress-strain ($\bar{\sigma} - \bar{\varepsilon}^p$) curves

Figures 77 to 84 show the predicted and experimental plastic $\bar{\sigma} - \bar{\varepsilon}^p$ curves for strain rates of 0.001, 1, 10, 100, ~3,000, 4,000, 5,000 and 6,000s^{-1} at temperatures that varied from 293 to 1,123K, depending on the testing conditions. At quasi-static testing conditions, the predictions made by the MTS model are undoubtedly accurate when compared to the experimental data, even at plastic strains as high as 0.4 (corresponding to room temperature tests) as it can be deduced from Figure 77.

The softening effect increasing temperatures have on the mechanical strength of the superalloy can be identified from both experimental and predicted plastic $\bar{\sigma} - \bar{\varepsilon}^p$ curves; which is, as expected, more pronounced when temperatures surpass the threshold in the region of 650°C.

A similar softening behaviour produced by temperatures can be observed in Figure 78, where it is also highlighted that predictions imparted by the constitutive model showed an increasingly deviation from their experimental analogous plastic $\bar{\sigma} - \bar{\varepsilon}^p$ curves as strains were higher than ~0.1 in average.

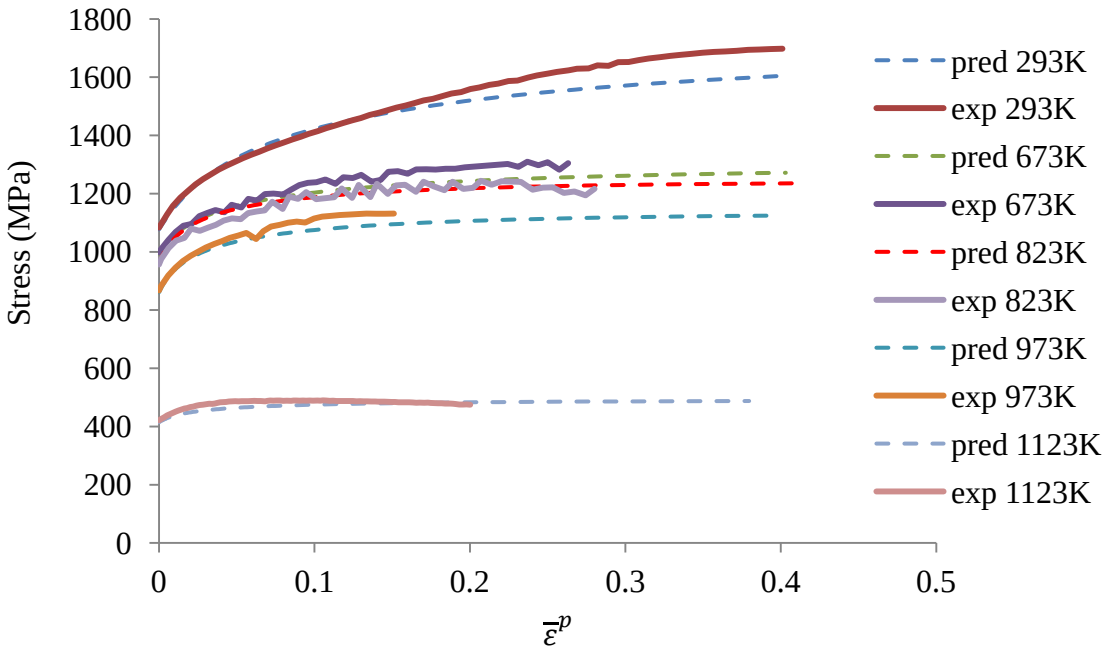

Figure 77. Comparison between experimental (exp) stress-strain curves and those predicted (pred) by the MTS model at different temperatures for $\dot{\bar{\varepsilon}}^p = 0.001\ s^{-1}$.

However the errors encountered were less than ~10% for all temperatures under study, suggesting that the MTS model was still able to confer values of flow stress with respect to strain with an acceptable level of accuracy (also seen in Figures 79 and 80 for a strain rate of 10 and 100s^{-1} respectively).

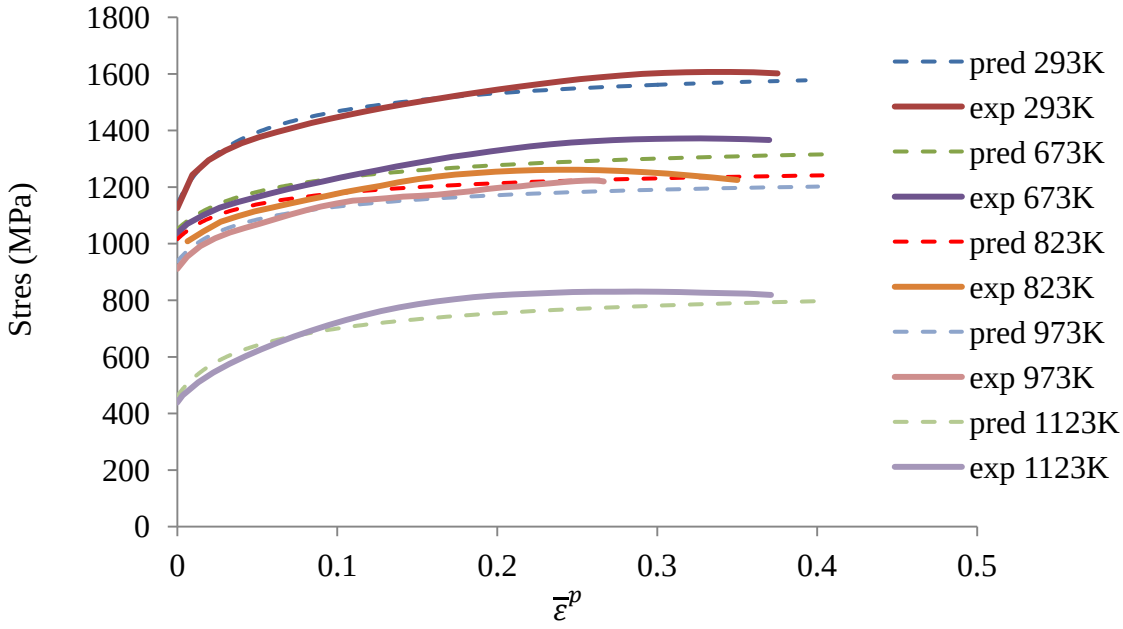

Figure 78. Comparison between experimental (exp) stress-strain curves and those predicted (pred) by the MTS model at different temperatures for $\dot{\bar{\varepsilon}}^p = 1\ s^{-1}$.

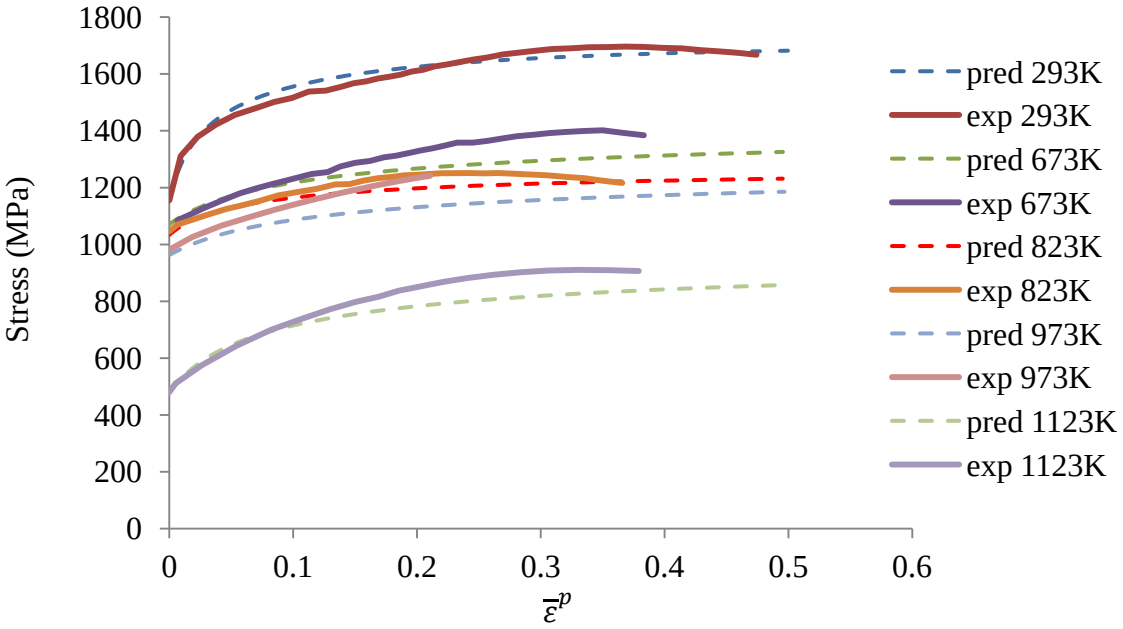

Figure 79. Comparison between experimental (exp) stress-strain curves and those predicted (pred) by the MTS model at different temperatures for $\dot{\bar{\varepsilon}}^p = 10\ s^{-1}$.

Oscillations found in the experimental findings regarding a strain rate of $100s^{-1}$ had no influence whatsoever in the predicted plastic $\bar{\sigma} - \bar{\varepsilon}^p$ curves as it can be seen in Figure 79, supporting the idea that the MTS model is robust enough in its principles to handle with such irregularities that could be of intrinsic nature of the testing method employed.

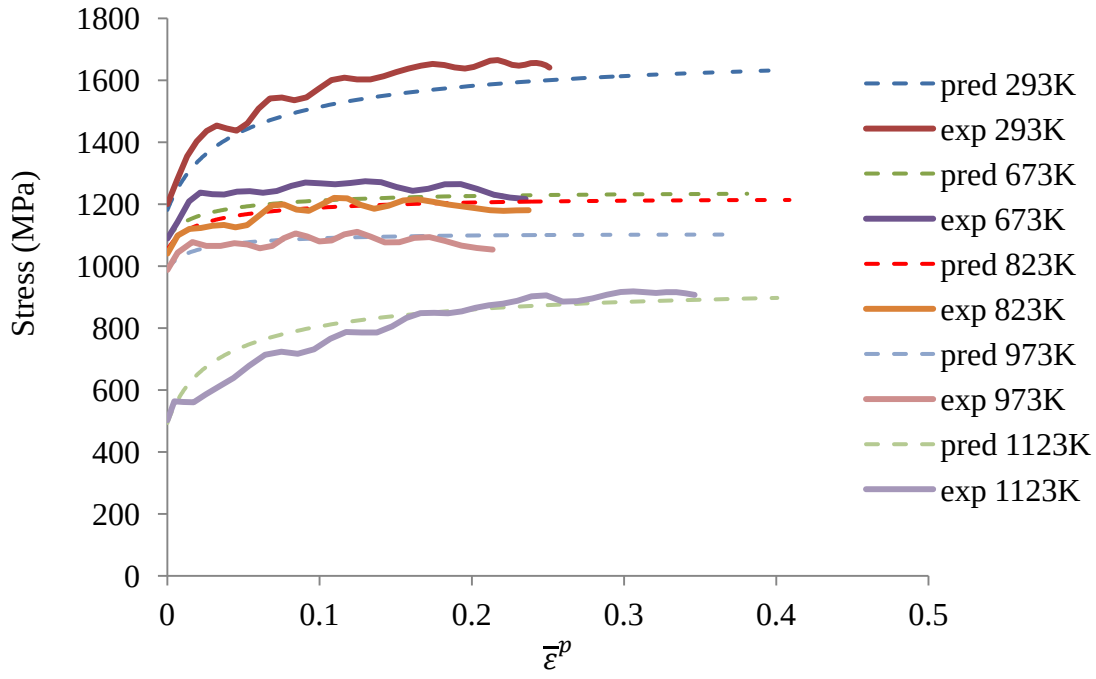

Figure 80. Comparison between experimental (exp) stress-strain curves and those predicted (pred) by the MTS model at different temperatures for $\dot{\bar{\varepsilon}}^p = 100\ s^{-1}$.

For all compression tests that involved the use of the SHPB apparatus, the accuracy in the predictions slightly decreased, although in the shape of the $\bar{\sigma} - \bar{\varepsilon}^p$ curves rather than in the overall flow values.

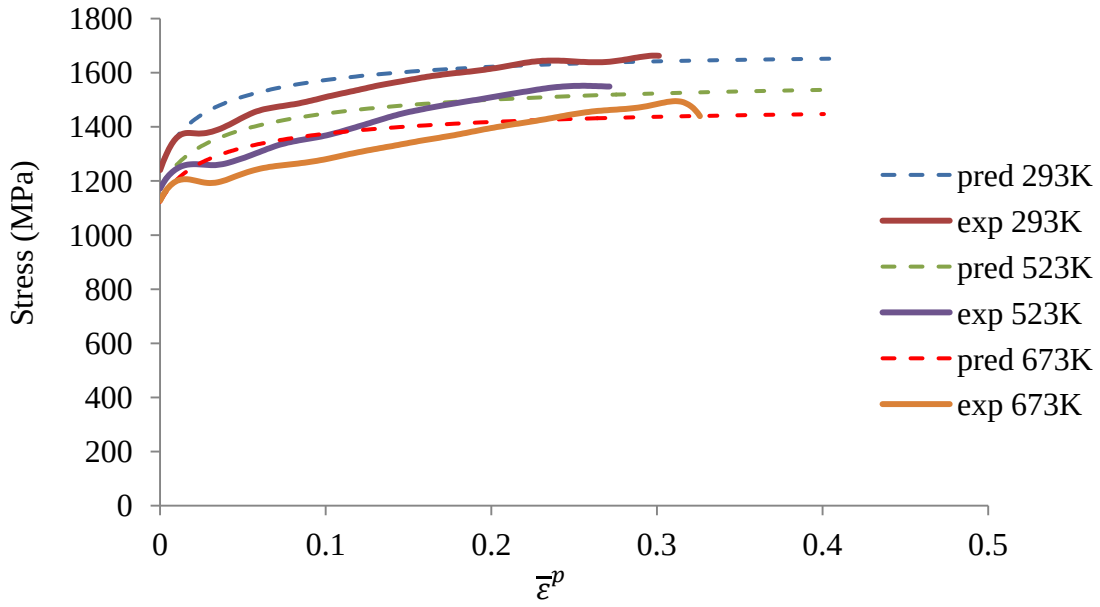

Figure 81. Comparison between experimental (exp) stress-strain curves and those predicted (pred) by the MTS model at different temperatures for $\dot{\bar{\varepsilon}}^p \approx 3{,}000\ s^{-1}$.

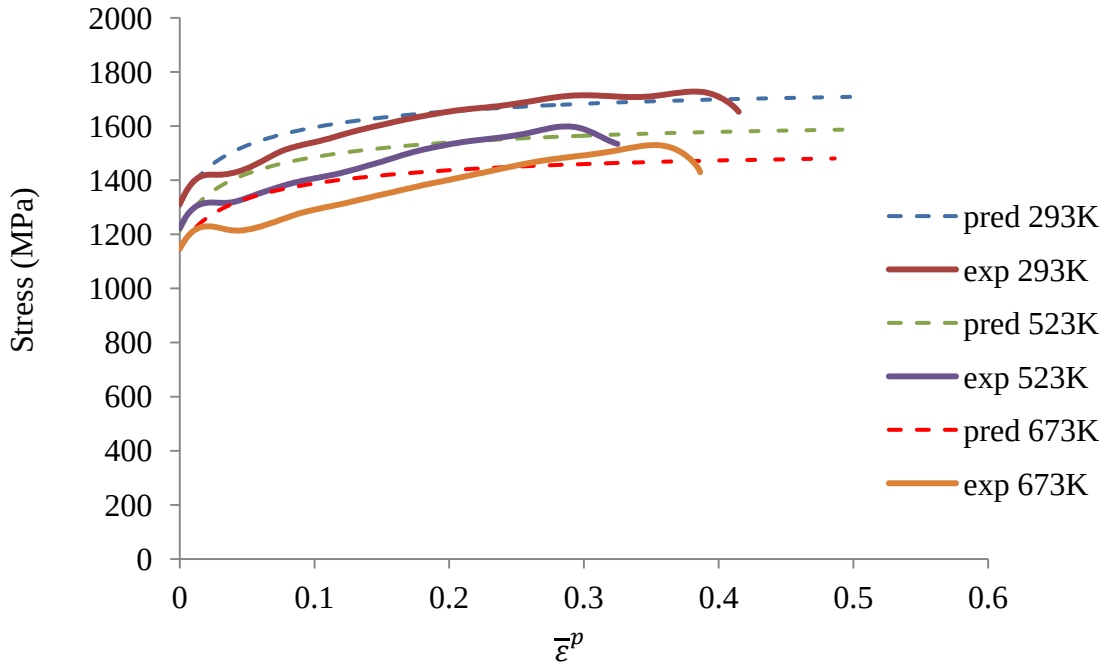

Figure 82. Comparison between experimental (exp) stress-strain curves and those predicted (pred) by the MTS model at different temperatures for $\dot{\bar{\varepsilon}}^p \approx 4{,}000\ s^{-1}$.

This was believed to happen due to the election of the modified Voce law, whose formulation was based on empirical findings and in accordance with the authors who first developed the MTS model (Follansbee and Kocks, 1988), assumed to be questionable from a more rigorous, either metallurgical or physical, point of view.

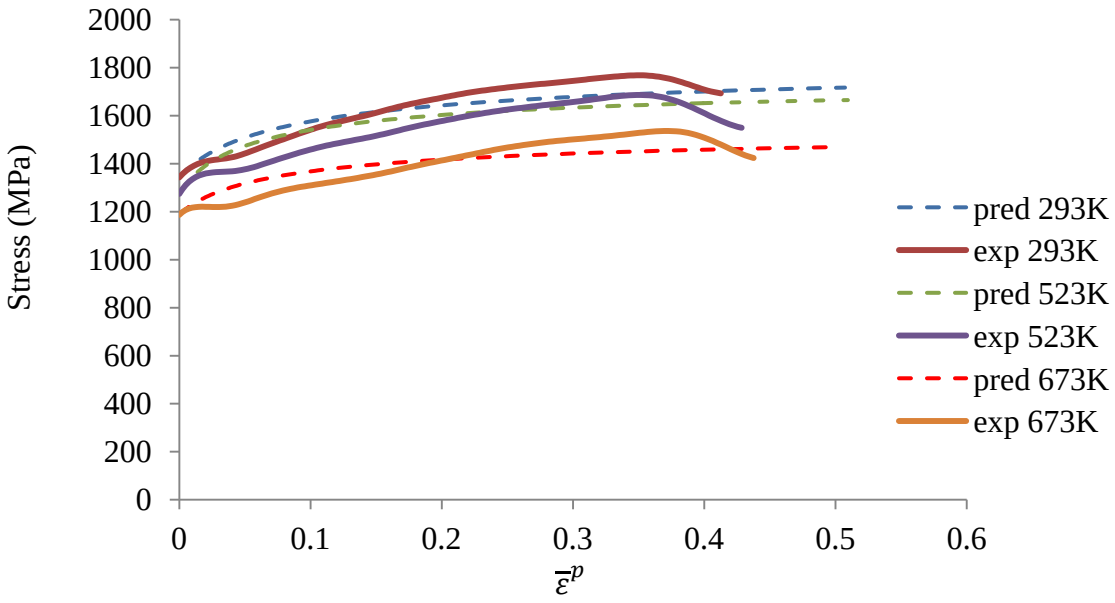

Figure 83. Comparison between experimental (exp) stress-strain curves and those predicted (pred) by the MTS model at different temperatures for $\dot{\bar{\varepsilon}}^p \approx 5{,}000\ s^{-1}$.

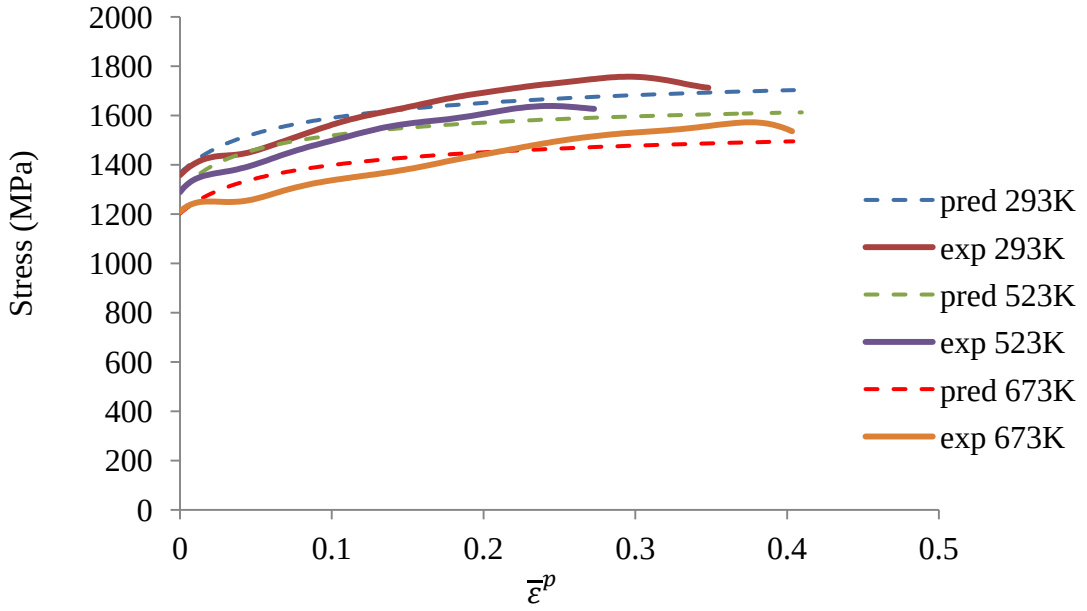

Figure 84. Comparison between experimental (exp) stress-strain curves and those predicted (pred) by the MTS model at different temperatures for $\dot{\bar{\varepsilon}}^p \approx 6{,}000\ s^{-1}$.

The initial peak in the flow stress observed in all plastic $\bar{\sigma} - \overline{\varepsilon}^{p}$ curves obtained from the SHPB machine (and not seen from Gleeble tests) was believed to correspond to the commencement of the yielding of Inconel 718, which was influenced by impurities and/or alloying elements that are present in it together with the appearance of thermal softening due to a rise in the adiabatic temperature.

As deformation at elevated strain rates progressed, the hardening rate (parameter given by the slope of the plastic $\bar{\sigma} - \overline{\varepsilon}^{p}$ curve) increased when compared to tests performed with the Gleeble testing apparatus, confirming that a rise in strain rate is related to a greater level of hardening in the material. On the contrary, temperatures softened the material regardless of the degree of plastic hardening produced by the augmentation of strain rates, therefore it was believed that Eq. (42), even with its apparent disadvantages, was a fair description of the complex mechanisms that were taking part in the softening/hardening of the Inconel 718 superalloy.

4.3.3 Mechanical Threshold Stress VUMAT

4.3.3.1 Constitutive equations

From a numerical viewpoint, there are no major differences between the VUMAT for the MTS model and that developed for the JC relationship, as both are flow models in which the criterion $\overline{\sigma} = \sqrt{3\,J_2}$ holds. The plastic strain increment was still computed by Eq. (124), however it has to be marked that the hardening parameter H needed to be calculated as follows instead:

$$\begin{aligned} H = \frac{d\overline{\sigma}}{d\overline{\varepsilon}^{p}} &= \frac{d}{d\overline{\varepsilon}^{p}}\left(\hat{\sigma}_a + \sigma_i + \sigma_e\right) = \frac{d}{d\overline{\varepsilon}^{p}}\left(\sigma_a + s_i\left(\dot{\overline{\varepsilon}}^{p}, T\right)\frac{\mu}{\mu_0}\hat{\sigma}_i + s_e\left(\dot{\overline{\varepsilon}}^{p}, T\right)\frac{\mu}{\mu_0}\hat{\sigma}_e\right) \\ &= \frac{d}{d\overline{\varepsilon}^{p}}\left(\sigma_a\right) + \frac{d}{d\overline{\varepsilon}^{p}}\left(s_i\left(\dot{\overline{\varepsilon}}^{p}, T\right)\frac{\mu}{\mu_0}\hat{\sigma}_i\right) + \frac{d}{d\overline{\varepsilon}^{p}}\left(s_e\left(\dot{\overline{\varepsilon}}^{p}, T\right)\frac{\mu}{\mu_0}\hat{\sigma}_e\right) \\ &= \frac{\mu}{\mu_0}\left[\frac{d\left(s_i\left(\dot{\overline{\varepsilon}}^{p}, T\right)\right)}{d\overline{\varepsilon}^{p}}\hat{\sigma}_i + \frac{d\hat{\sigma}_i}{d\overline{\varepsilon}^{p}}\left(s_i\left(\dot{\overline{\varepsilon}}^{p}, T\right)\right)\right] \\ &+ \frac{\mu}{\mu_0}\left[\frac{d\left(s_e\left(\dot{\overline{\varepsilon}}^{p}, T\right)\right)}{d\overline{\varepsilon}^{p}}\hat{\sigma}_e + \frac{d\hat{\sigma}_e}{d\overline{\varepsilon}^{p}}\left(s_e\left(\dot{\overline{\varepsilon}}^{p}, T\right)\right)\right] \end{aligned} \tag{136}$$

Assuming that the variation of the variables $s_i\left(\dot{\bar{\varepsilon}}^p, T\right)$ and $s_e\left(\dot{\bar{\varepsilon}}^p, T\right)$ with respect to plastic strain is negligible, after some manipulation it is found:

$$H = \frac{\mu}{\mu_0}\frac{d\hat{\sigma}_e}{d\bar{\varepsilon}^p}\left(s_e\left(\dot{\bar{\varepsilon}}^p, T\right)\right) = \frac{\mu}{\mu_0}\theta\left(s_e\left(\dot{\bar{\varepsilon}}^p, T\right)\right) \tag{137}$$

which is easily obtained for any strain rate and temperature. Once the magnitude $\Delta\bar{\varepsilon}^p$ was in consequence computed, the internal state variable $\hat{\sigma}_e$ was further updated so that $\bar{\sigma}_{new}$ could be calculated and therefore, so the remaining constitutive equations belonging to the VUMAT subroutine.

The numerical code developed for the MTS model was written following the one that had been developed for the JC model, which was extensively checked against the built-in the FE software ABAQUS provides in order to make sure it was appropriate. Similarly as done previously, a simple FE simulation was initially carried out to assess the VUMAT subroutine for the MTS model and compared against the results given by that generated for the JC viscoplastic relationship before attempting to apply it to the orthogonal machining situation. The corresponding example in conjunction with a detailed analysis of the numerical findings can be found in Appendix III.

4.4 FEM with ABAQUS/Explicit for Inconel 718

4.4.1 2D Thermo-mechanical ALE/AR - JC and RWM

4.4.1.1 Principal features and formulation of the FE model

In a similar fashion as it was done when simulating the orthogonal cutting of Ti-6Al-4V in 2D, here the workpiece was meshed with 11,039 CPE4RT type elements; whose general size was 6μm x 1.5μm. The cutting tool on the other hand, was meshed with 1,643 CPE4RT type elements in conjunction with 29 CPE3T 3-node, plain strain thermally coupled, triangular, linear displacement and temperature type elements; in order to properly account for its geometrical features.

Operating conditions were defined in such a way to match as close as possible those employed in the orthogonal cutting experiments. Furthermore, a convenient uniform mass scaling value of 100 was utilised in all situations.

A total of six FE simulations were carried out, comprising cutting velocities of 200, 250 and 300m/min at feeds of 0.08 and 0.2mm/rev for a variable step time depending on each machining condition.

For instance, the FE model configuration utilised when the feed was 0.2mm/rev is shown in Figure 85a while the corresponding meshed workpiece and tool together with the boundary conditions are displayed in Figure 85b:

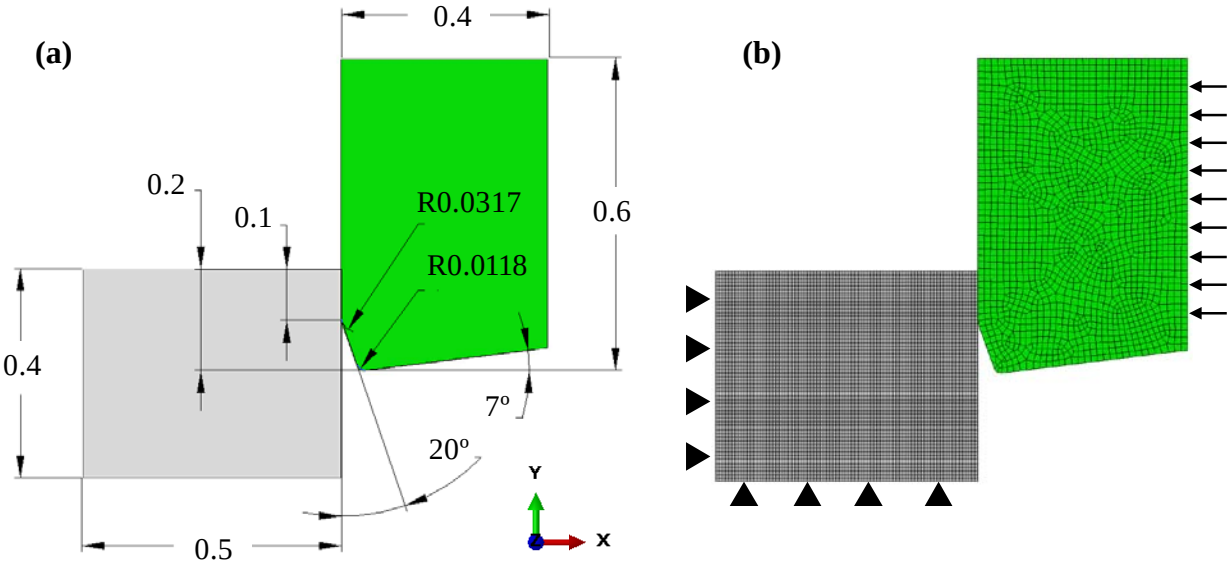

Figure 85. (a) General dimensions of the orthogonal FE model to simulate 2D orthogonal cutting of Inconel 718 superalloy, (b) Meshed bodies and boundary conditions.

The Inconel 718 workpiece material was described according to the JC plasticity model, where the constants were calculated in subsection 4.2.1. It was in addition assumed that a constant Taylor-Quinney coefficient of 0.9 best described the internal heat generated in the workpiece that was consequence of the plastic deformation. Table 16 summarises the mechanical/physical properties of Inconel 718 (Soo, 2003) and the PCBN cutting tool used in the FE simulations, the majority of them being temperature dependent. FE simulations carried out for feeds of 0.2 and 0.08mm/rev took ~25min and 1h of computation respectively.

4.4.1.2 Frictional and thermal effects

In this situation, the interaction between the tool and workpiece material was also defined according to the Coulomb's friction model, however with an average friction coefficient of 0.35 instead, which was obtained from the literature (Coelho et al., 2007).

			Inconel 718	**Tool**
Material Properties	Johnson-Cook constitutive model	A (MPa)	1,274.73	-
		B (MPa)	937.28	
		n (-)	0.7036	
		C (-)	0.0076	
		m (-)	1.641	
		T_m (K)	1,573	
		T_r (K)	293	
		$\dot{\bar{\varepsilon}}_0$($s^{-1}$)	1	
	Density (kg/m^3)		8,220	4,084.14 (293K) 4,055.03 (773K) 4,028.4 (1,273K)
	Poisson's Ratio (-)		0.276 (T>1,100K), else variable to maintain Eq. (102) valid	0.15
	Young's modulus (GPa)		200 (293K) 171 (813K) 163 (923K) 154 (1,033K) 139 (1,143K)	587
	Thermal Conductivity (W/mK)		11.4 (294K) 19.6 (811K) 24.9 (1,144K)	38 (293K) 42 (773K) 38 (1,293K)
	Specific Heat Capacity (J/kgK)		430.0 (294K) 449.7 (373K) 474.7 (473K) 499.9 (573K) 525.0 (673K) 560.0 (811K) 575.8 (873K) 601.2 (973K) 645.5 (1,144K)	669 (293K) 1,177 (773K) 1,190 (1,273K)
	Thermal Expansion Coefficient (10^{-6}/K)		-	4.55 (293K) 5.57 (773K) 6.40 (1,273K)
	Inelastic Heat Fraction (-)		0.9	-
Cutting Conditions/ Tool Geometry	Cutting Speed (m/min)		200/250/300	
	Depth of Cut (mm)		0.2/0.08	
	Feed (mm/rev)		0.2/0.08	
	Tool Tip Radius (μm)		11.87	
	Rake Angle (°)		0/-20	
	Clearance Angle (°)		7	

Table 16. Mechanical and physical property data for Inconel 718 superalloy and the PCBN cutting tool together with machining conditions/tool geometry employed. Data corresponding to the tool were provided by courtesy of Dr. M'Saoubi at SECO Tools.

In addition, an average TCC value of 100kW/m^{2}K was adopted in concordance with previous FE simulations to maintain a fixed criterion. Moreover, it was stipulated that equal quantities of the heat generated in the cutting process were transferred to the workpiece material and tool.

Table 17 summarises therefore, the presupposed frictional and thermal properties utilised in all FE simulations.

Contact and thermal properties	Thermal Contact Conductance (kW/m^{2}K)	100
	Heat Partition Coefficient (-)	0.5
	Friction Coefficient (-)	0.35
	Fraction of dissipated energy caused by friction that is converted to heat (%)	90
	Limit Shear Stress (MPa)	Unlimited

Table 17. Contact and thermal properties utilised to describe the interactions between the Inconel 718 superalloy and the PCBN insert.

4.4.1.3 Damage model characteristics

In line with the RWM criterion to describe material failure, only positive values of energy W were considered, where after a series of trial and error iterations, the best fit for the parameters W_{crit}, W_{frac} and a was found to be as it can be observed in Table 18.

Feed (mm/rev)	**0.2**			**0.08**		
Cutting speed (m/min)	**200**	**250**	**300**	**200**	**250**	**300**
W_{crit} (J/m^3)	120	120	120	120	120	120
W_{frac} (J/m^3)	7,600	7,600	7,600	7,600	7,600	7,600
a (-)	0.05	0.05	0.08	0.106	0.115	0.115

Table 18 Resulting W_{crit}, W_{frac} and a values for the RWM damage model used to simulate 2D machining of Inconel 718 superalloy with the JC model.

4.4.2 3D Thermo-mechanical Lagrangian - JC and RWM

4.4.2.1 General formulation of the FE model

Following the same 3D modelling strategy that was performed when simulating orthogonal cutting on Ti-6Al-4V alloy, the bar and cutting tool were completely designed to match their original geometries.

The radiuses encountered in both the chamfer edges of the tool were included while operating conditions/parameters were defined identical to those employed in the orthogonal turning trials.

In all the FE scenarios, the workpiece was strategically edge-seeded to refine the element size in those regions of principal interest while the tool was meshed automatically with no recourse of such option, in which case both bodies were comprised of C3D8RT type elements. Due to the resulting 3D FE model was relatively large together with the relevant fact that it had to be linked to external software every time increment for its proper execution, a suitable uniform mass scaling value was utilised in order to speed up the calculations, in concordance with previous circumstances.

The step time, in spite of being variable for each simulation for perceptible reasons, was defined large enough to make sure the steady state condition could be reached. For example, the 3D FE model design that was generated when the cutting speed was 300m/min and the feed 0.2mm/rev is shown in Figure 86:

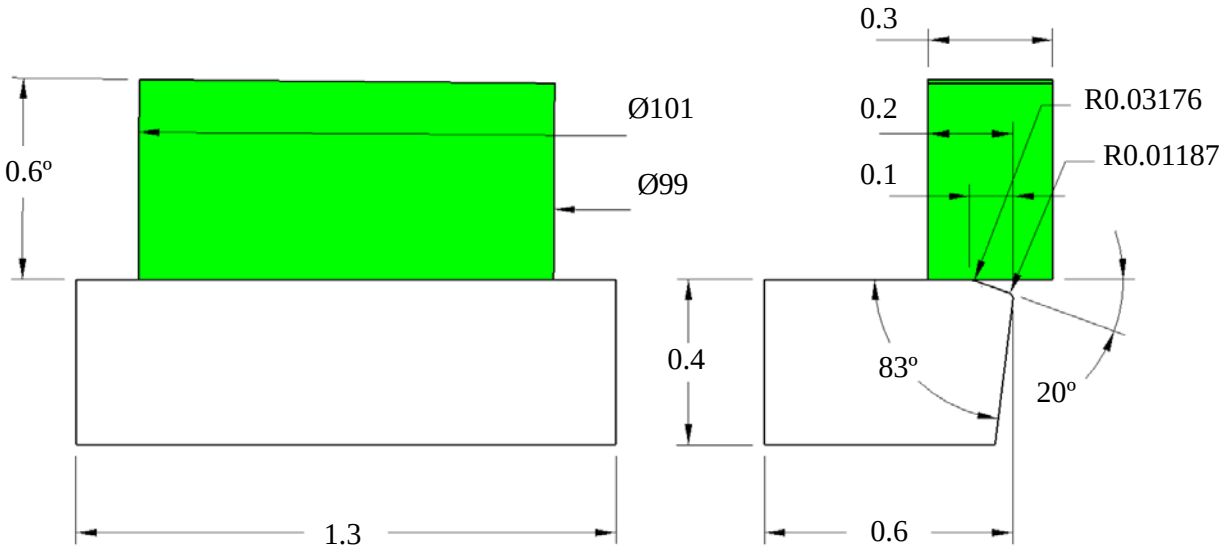

Figure 86. General configuration of the FE model to simulate 3D orthogonal cutting of Inconel 718 aerospace superalloy (dimensions in mm).

The constrained faces of the tool together with the rotational boundary condition applied to the workpiece are shown in the meshed assembly observed in Figures 87a and 87b respectively.

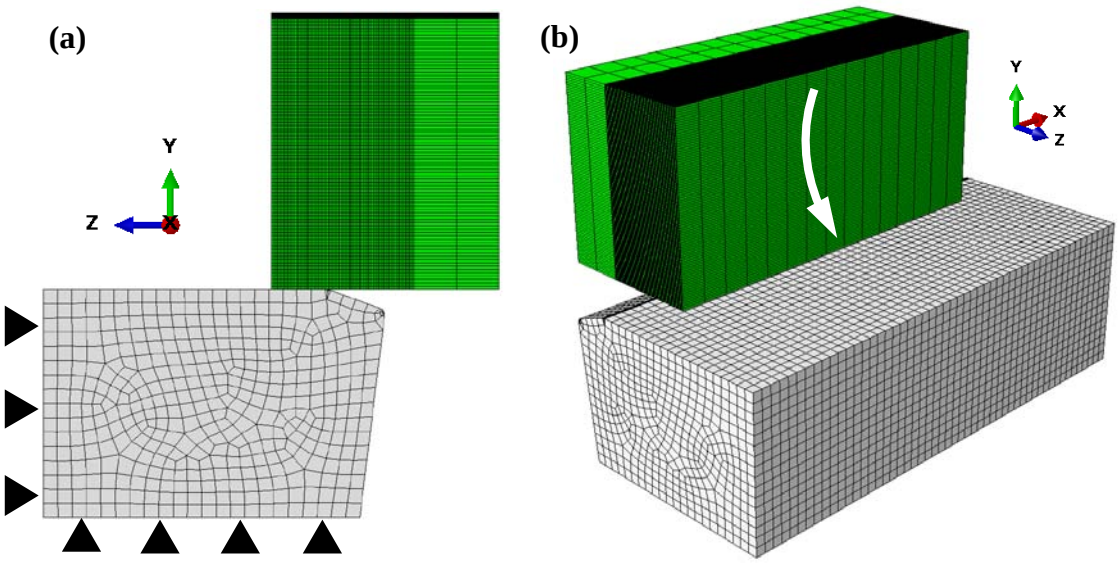

Figure 87. 3D perspectives of the FE model to simulate orthogonal cutting of Inconel 718 superalloy (a) Constrained faces, (b) Boundary condition.

As the dimensions of the real workpiece varied from test to test as described in Figure 38, the mesh corresponding to each cutting scenario to perform the FE simulations had to do so; while the meshed tool did not experience any variation in the quantity of elements, as perceived in Table 19 for each cutting speed and feed.

Feed (mm/rev)	**0.2**			**0.08**		
Cutting speed (m/min)	**200**	**250**	**300**	**200**	**250**	**300**
Workpiece	119,850	109,650	103,275	217,140	244,860	272,580
Tool	23,036	23,036	23,036	23,036	23,036	23,036

Table 19. Quantity of finite elements for workpiece and PCBN tool for each 3D machining simulation when using the JC and RWM models.

All 3D FE simulations performed comprising feeds of 0.2 and 0.08mm/rev took an average of 7h and 11h of computation respectively.

4.4.2.2 Damage model characteristics

In agreement with the RWM damage model, only positive values of energy W were considered, where after a series of trial and error iterations, the best fit for the parameters W_{crit}, W_{frac} and a was found to be as detailed in Table 20.

Feed (mm/rev)	**0.2**			**0.08**		
Cutting speed (m/min)	**200**	**250**	**300**	**200**	**250**	**300**
W_{crit} (J/m^3)	150	150	150	150	150	150
W_{frac} (J/m^3)	3,450	3,500	3,600	3,550	3,600	3,700
a (-)	0.125	0.121	0.155	0.115	0.115	0.11

Table 20. Resulting W_{crit}, W_{frac} and a values for the RWM damage model used to simulate 3D machining of Inconel 718 superalloy with the JC model.

4.4.3 3D Thermo-mechanical Lagrangian - MTS and RWM

4.4.3.1 General formulation of the FE model

As the constitutive model varied in this case uniquely, the 3D FE models for each cutting speed and feed were the same as those described in subsection 4.4.2.1, therefore the properties/size of the mesh corresponding to the workpiece material and cutting tool remained unchanged in both situations. The complete set of 3D FE simulations performed which comprehended cutting feeds of 0.2 and 0.08mm/rev took an average of 17h and 32h of computation respectively. The corresponding example (including a detailed analysis of the numerical findings) when the MTS and RWM models are used can be found in Appendix IV.

4.4.3.2 Damage model characteristics

As previously commented, not only positive values of energy W were considered in these modelling scenarios, but also a trial and error procedure which took place to obtain the constants W_{crit}, W_{frac} and a. Following some iterations that were carried out therefore, the most appropriate values that were encountered for the energy terms are summarised in Table 21 for each cutting condition.

Feed (mm/rev)	**0.2**			**0.08**		
Cutting speed (m/min)	**200**	**250**	**300**	**200**	**250**	**300**
W_{crit} (J/m^3)	150	150	150	150	150	150
W_{frac} (J/m^3)	3,500	3,600	3,750	3,700	3,800	3,850
a (-)	0.145	0.145	0.145	0.145	0.15	0.15

Table 21. Resulting W_{crit}, W_{frac} and a values for the RWM damage model used to simulate 3D machining of Inconel 718 superalloy with the MTS model.

4.5 FEM with ABAQUS/Explicit for Inconel 718 to predict DRX

4.5.1 Recrystallisation

4.5.1.1 Introduction

In order to predict grain refinement, the parameter known as Zener-Hollomon (Z) has usually been utilised to accomplish such purpose, which is normally defined as (Medeiros et al., 2000):

$$Z = \dot{\bar{\varepsilon}}^{p} \; exp\left(\frac{Q}{RT}\right) \tag{138}$$

where recall that $\dot{\bar{\varepsilon}}^{p}$ is the effective plastic strain rate (s^{-1}), T the temperature (K), R the universal gas constant (K^{-1}) and Q the activation energy (J/mol), the latter being established as the energy needed for a dislocation to overcome a barrier with the assistance of thermal energy. Generally, for the hot working of Inconel 718 in its annealed state, it has been assumed that Q remains constant and has a value of 400kJ/mol (Medeiros et al., 2000; Zhou and Baker, 1994). However, the study presented by Meyers et al. (2002) shows that this quantity varies with strain rate and temperature according to the next expression:

$$\Delta G = kT \; ln\left(\frac{\dot{\bar{\varepsilon}}_0}{\dot{\bar{\varepsilon}}^{p}}\right) \tag{139}$$

where k is the Boltzman's constant, $\dot{\varepsilon}_0$ is the reference strain rate and similarly as before, ΔG is the activation energy (J). By working with Eq. (138) and Eq. (139) a relation between both activation energies Q and ΔG could be found, as an analysis of the units of Eq. (138) gives:

$$\left[\frac{Q}{RT}\right] = \left[\frac{\frac{J}{mol}}{\frac{1}{mol\,K}K}\right] = [J]$$

Therefore:

$$\left[\frac{Q}{RT}\right] = \left[\frac{Q}{Na\;KT}\right] = \left[\frac{\Delta G}{KT}\right] = \left[\frac{J}{\frac{1}{K}K}\right] = [J] \qquad \rightarrow \qquad \frac{Q}{RT} = \frac{\Delta G}{KT} \tag{140}$$

where Na is the Avogadro constant ($6.02214129 \times 10^{23} mol^{-1}$) and $\Delta G = Q/Na$. Had an analogy been found between Q and ΔG, the study consequently worked with the latter. Recrystallisation takes place in hot metal forming processes in general, like forging and rolling, where the elevated temperatures play an important role to this end, though strain rates might not be too elevated. Several studies have related the grain size d to Z with good results (Park et al., 2001), typically using expressions of the type:

$$d = K_d \, Z^{-K_z} \tag{141}$$

where K_d and K_z are always positive constants. By replacing Eq. (138) in Eq. (141) it is straightforward to observe that the grain size is associated with the activation energies as follows:

$$d = K_d \, \dot{\bar{\varepsilon}}^{p} \, exp\left(\frac{Q}{RT}\right)^{-K_z} = K_d \, \dot{\bar{\varepsilon}}^{p} \, exp\left(\frac{\Delta G}{KT}\right)^{-K_z} \tag{142}$$

Hence, it can be deduced that $d \propto 1/\Delta G$, relationship which implies that once dynamic recrystallisation begins, the grain size decreases consistently when the activation energy increases (or in other words when the parameter Zener-Hollomon Z increases). The same conclusion can be derived from Medeiros et al. (2000), who experimentally found that:

$$\log(d) = -0.027 \log(Z) - \frac{7{,}454}{T} + \ 8.49 \tag{143}$$

Results of the character seen in Eq. (141) and Eq. (143), in which the recrystallised grain size is related to Z (and therefore to the activation energy) in an inverse mode are common when studying processes that present such microstructural alteration.

4.5.1.2 Mathematical link to the MTS and RWM models

The activation energy ΔG in the initial one-term MTS model developed by Follansbee and Kocks (1988) is given by the following phenomenological expression:

$$\Delta G = g_0 \mu b^3 \left[1 - \left(\frac{\bar{\sigma}}{\sigma_t}\right)^{p}\right]^{q} \tag{144}$$

Replacing Eq. (139) in Eq. (144) it is seen that:

$$kT\ ln\left(\frac{\dot{\bar{\varepsilon}}_0}{\dot{\bar{\varepsilon}}^p}\right) = g_0\mu b^3\left[1-\left(\frac{\bar{\sigma}}{\sigma_t}\right)^p\right]^q$$

Where after some manipulation the general formulation for $s\left(\dot{\bar{\varepsilon}}^p, T\right)$ can be obtained:

$$s\left(\dot{\bar{\varepsilon}}^p, T\right) = \frac{\bar{\sigma}}{\sigma_t} = \left[1-\left(\frac{kT}{g_0\mu b^3}ln\left(\frac{\dot{\bar{\varepsilon}}_0}{\dot{\bar{\varepsilon}}^p}\right)\right)^{\frac{1}{q}}\right]^{\frac{1}{p}} \tag{145}$$

As a two-term MTS model for Inconel 718 has been developed in the present work, two scaling terms can be individualised:

$$s_i\left(\dot{\bar{\varepsilon}}^p, T\right) = \left[1-\left(\frac{\Delta G_i}{g_{0i}\mu b^3}\right)^{\frac{1}{qi}}\right]^{\frac{1}{pi}} \quad , \quad \Delta G_i = kT\ ln\left(\frac{\dot{\bar{\varepsilon}}_{0i}}{\dot{\bar{\varepsilon}}^p}\right)$$

$$s_e\left(\dot{\bar{\varepsilon}}^p, T\right) = \left[1-\left(\frac{\Delta G_e}{g_{0e}\mu b^3}\right)^{\frac{1}{qe}}\right]^{\frac{1}{pe}} \quad , \quad \Delta G_e = kT\ ln\left(\frac{\dot{\bar{\varepsilon}}_{0e}}{\dot{\bar{\varepsilon}}^p}\right)$$

Thus replacing in the general equation of the flow stress it is obtained:

$$\bar{\sigma} = \sigma_a + \left[1-\left(\frac{\Delta G_i}{g_{0i}\mu b^3}\right)^{\frac{1}{qi}}\right]^{\frac{1}{pi}}\frac{\mu}{\mu_0}\hat{\sigma}_i + \left[1-\left(\frac{\Delta G_e}{g_{0e}\mu b^3}\right)^{\frac{1}{qe}}\right]^{\frac{1}{pe}}\frac{\mu}{\mu_0}\hat{\sigma}_e \tag{146}$$

Although it may not be very clear to infer at a first glance, it can be deduced from Eq. (146) that $\bar{\sigma} \propto 1/\Delta G_i$ and $\bar{\sigma} \propto 1/\Delta G_e$ because p_i, q_i, p_e and p_e are all positive values. Recalling that $d \propto 1/\Delta G$ (derived from Eq. (142)), it can further be concluded that:

$$\bar{\sigma} \propto d \tag{147}$$

The result given by Eq. (147) seems to indicate that the grain size increases when the material strain hardens, however note that this would not be the case, as Eq. (142) was obtained from analyses in which recrystallisation took place. The only conjecture that could be drawn from

Eq. (146) is that the MTS model appears to be a potential candidate for the prediction of the flow stress when the grains decrease, dependence that is usually seen experimentally, see Figure 88.

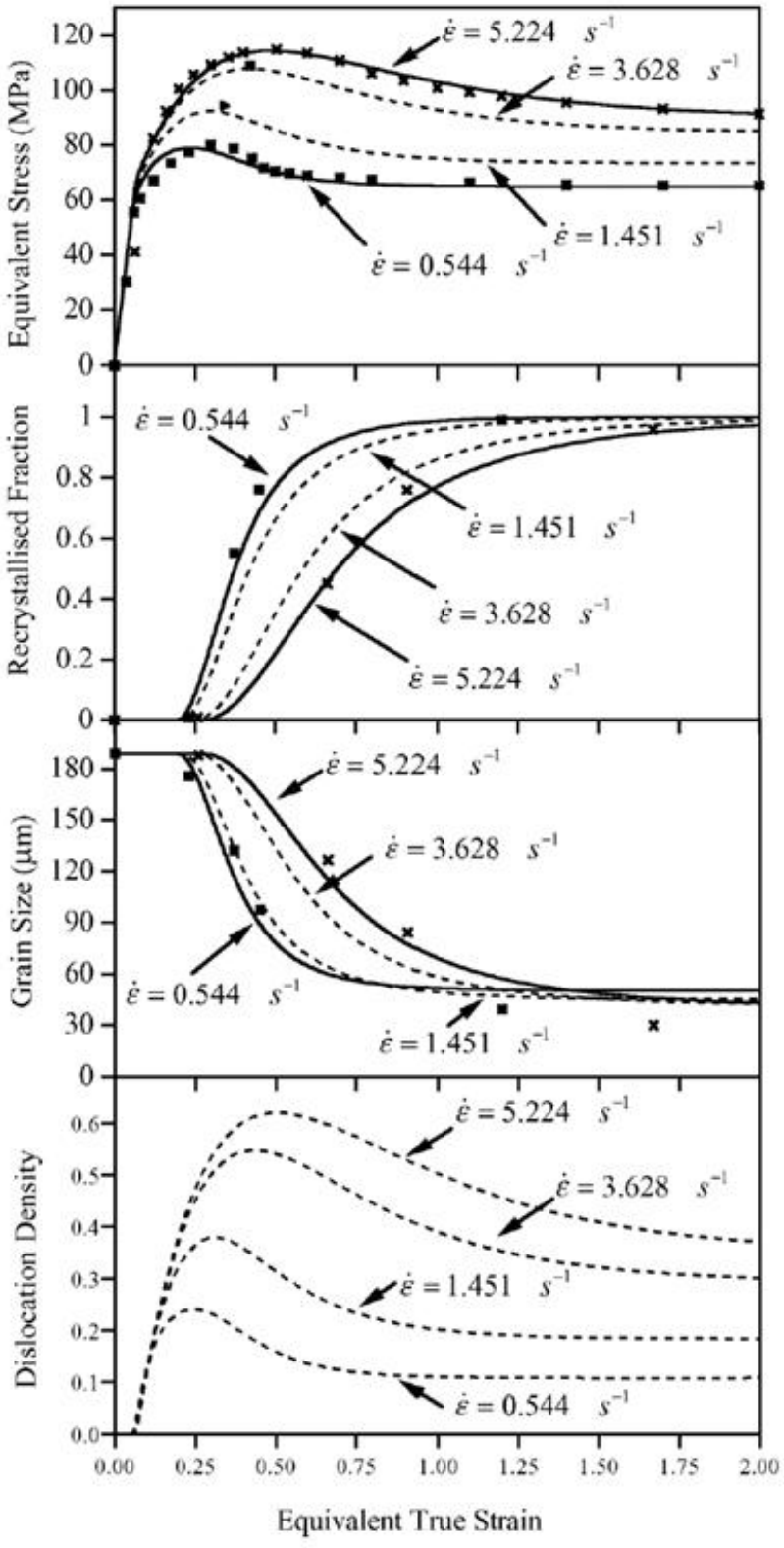

Figure 88. Dependence of equivalent stress, recrystallised fraction, grain size and dislocation density with equivalent true strain for low carbon steel, according to Lin et al. (2005).

In the particular case when some quantities have certain values, like the ones resulting from the development of the MTS model here, namely $\dot{\bar{\varepsilon}}_{0i} = \dot{\bar{\varepsilon}}_{0e}$ together with $p_i = q_i = p_e = q_e = 1$, it can be observed from Eq. (139) that $\Delta G_i = \Delta G_e = \Delta G$, which leads to a simplification of Eq. (146):

$$\bar{\sigma} = \sigma_a + \left[1 - \left(\frac{\Delta G}{g_{0i}\mu b^3}\right)^{\frac{1}{qi}}\right]^{\frac{1}{pi}} \frac{\mu}{\mu_0}\hat{\sigma}_i + \left[1 - \left(\frac{\Delta G}{g_{0e}\mu b^3}\right)^{\frac{1}{qe}}\right]^{\frac{1}{pe}} \frac{\mu}{\mu_0}\hat{\sigma}_e \tag{148}$$

where after some manipulation it is obtained:

$$\bar{\sigma} = \sigma_a + \frac{\mu}{\mu_0}(\sigma_i + \sigma_e) - \Delta G\left(\frac{\hat{\sigma}_i}{g_{0i}\mu b^3} + \frac{\hat{\sigma}_e}{g_{0e}\mu b^3}\right) \tag{149}$$

thus, easing the visualisation of Eq. (147).

The fact that the flow stress decreases when the grain refines is a typical consequence of the strain-free nature of the latter once they are re-grown, provoking the softening DRX is in general associated with. Such moderate softening on the flow stress of materials has been found experimentally in numerous cases not only for Inconel 718 (Zhao et al., 2004; Brand et al., 1996), but also for alloy steels (Lin et al., 2005) to name but a few.

The MTS model, in principle, seems to be an appropriate constitutive description to further predict dynamic recrystallisation, as it could link the flow stress with grain size (through the physical concept of activation energy) in a manner that would be in accordance with experimental findings. However as the MTS model only predicts hardening in its standard formulation, it would be necessary to develop new expressions to account for the softening produced by dynamic recrystallisation. From Eq. (139) it is seen that:

$$\frac{\Delta G}{kT} = ln\left(\frac{\dot{\bar{\varepsilon}}_0}{\dot{\bar{\varepsilon}}^p}\right) \tag{150}$$

and from Eq. (138):

$$ln\left(\frac{Z}{\dot{\bar{\varepsilon}}^p}\right) = \frac{Q}{RT} \tag{151}$$

Taking into account the analogy encountered in Eq. (140) it could, in principle, be stated from Eq. (150) and Eq. (151) that:

$$ln\left(\frac{\dot{\bar{\varepsilon}}_0}{\dot{\bar{\varepsilon}}^p}\right) = ln\left(\frac{Z}{\dot{\bar{\varepsilon}}^p}\right) \quad \rightarrow \quad \dot{\bar{\varepsilon}}_0 = Z \tag{152}$$

As $\dot{\bar{\varepsilon}}_0$ is a constant and generally has a high value, it could be deduced that Eq. (152) does not hold, meaning that the parameter Zener-Hollomon Z does not seem to be applicable to high strain rate processes, like metal cutting. Although Caruso et al. (2012) and Rotella et al. (2012) have used Z to predict grain size evolution following machining of AISI 52100 steel and AA7075-T651 alloy respectively, the authors did it as *de facto* providing little evidence to support the choice. A constant activation energy value of $Q = 116.7kJ/mol$ was selected by Rotella et al. (2012), however Medeiros et al. (2000) showed that in some situations Q is not likely to remain constant when considering a wide range of strain rates and temperatures. Similarly, Shekhar et al. (2012) utilised Z for high severe plastic deformation processes (when $\bar{\varepsilon}^p$>2 and $\dot{\bar{\varepsilon}}^p$ ~1,000 s^{-1}), in particular when machining self-diffusivity copper by considering $Q = 197kJ/mol$. It is interesting to note however that 25% of the samples did not actually correlate grain size with Z. Ding and Shin (2011) on the other hand, proposed a dislocation-based FE model to predict grain refinement when cutting CP Ti at 36m/min and a feed rate of 0.3mm/rev which made no use of Z. Validation of the simulations proved the accuracy of the model for recrystallised grains as fine as 93nm (10% error).

When modelling microstructure evolution in multipass hot rolling of C-Mn steel (maximum $\dot{\bar{\varepsilon}}^p$ =5.224s^{-1} while T=1,373K), Lin et al. (2005) did not use Z either, instead they pioneered the area of research by developing their own model (dislocation-based also). Based on their results the authors concluded that the set of unified viscoplastic constitutive equations to portray grain size, static/dynamic recrystallisation and dislocation density were appropriate to predict microstructure evolution after hot working.

As observed therefore, the employment of the parameter Z is still a matter of debate between researchers worldwide and sometimes it is not adopted to simulate grain refinement in manufacturing processes. This in particular is evidenced in the FE modelling of metal cutting, however it needs to be highlighted that while the activation energy Q is chosen constant in the majority (if not all) cases, it may vary depending on the process conditions as pointed out by Medeiros et al. (2000). Taking these findings into account, the derivation from Eq. (152) and the fact that plastic stress-strain curves predicted by the MTS model developed for Inconel 718 are in high accordance with experimental data (further suggesting that its main equations are acceptable for their later use in drawing additional conclusions), Z is not utilised in the present work. Instead, a model linking grain size with dislocation density will be assumed.

Now that a connection between grain size and the MTS constitutive model has been found, the intention is to extend the analysis to further detect a probable link between grain size and the RWM damage model too. Recall that it was experimentally found by Rittel et al. (2008) and Rittel (2009) that the stored energy of cold work which led to the generation of dynamic recrystallised grains, was the main agent that provoked ulterior softening/damage by adiabatic shear banding in materials such as Ti-6Al-4V. Based on these findings, the RWM damage model was developed to trigger material failure when a certain value of energy was reached, to then produce softening by adiabatic shear banding until complete flow tress deterioration was accomplished.

Considering therefore that dynamic recrystallisation precedes adiabatic shear banding, it can therefore be plausible to think (without contradicting experimental evidence) that a value of energy lower than the one needed to begin damage could exist to account for onset of dynamic recrystallisation. If a value of energy:

$$W_R = k_W\, W_{crit} \quad , \quad 0 < k_W < 1 \tag{153}$$

(where k_W is a constant) was considered to trigger recrystallisation, it could effectively be observed that the RWM model could be utilised to trigger not only damage due to adiabatic shear banding, but also softening by grain refinement. Although it may activate it, the flow stress softening encountered soon after the grains are refined (see Figure 88) could not be predicted by the RWM model, necessitating a new law or expression to account for this effect before damage is produced.

In conclusion, a relevant connection between grain size distribution and the flow stress predicted by the MTS model has been found, through the analysis that included and linked activation energies found in both of their formulations. Furthermore, as the predicted plastic stress-strain curves given by the constitutive model exhibited a reasonable degree of accuracy, they led to the conclusion that the parameter Z (usually employed in processes that reach strain rates of the order of ~10-50s^{-1}) does not seen to be suitable to predict grain size distribution when high strain rates are involved.

Finally, it was proved that the RWM model could not only account for onset of damage by shear banding, but also by dynamic recrystallisation. To accomplish this in the context of the MTS model, the definition of a novel law to predict such microstructural event would be necessitated, matter that is discussed in the following subsection.

4.5.1.3 Proposed DRX model

The relationship between the flow stress and the dislocation density was well described in the past by Estrin and Mecking (1984) for Cu. It has also been found that when Inconel 718 hardens at strain rates varying from 1,000 to 5,000s^{-1} (though in its annealed state) the flow stress is related to the dislocation density according to Lee et al. (2011) by:

$$\bar{\sigma} = \sigma_0 + \alpha_1 \mu b \sqrt{\rho} \tag{154}$$

where σ_0 and α_1 are constants, and as usual μ is the (temperature dependent) shear modulus, b is the magnitude of the Burgers vector and ρ corresponds to the average dislocation density. The formula includes not only the effect dislocations have on other dislocations (second term on the right hand side), but also some other contributions have on the plastic resistance (first term on the right hand side) e.g. lattice resistance, solution hardening, grain size effects, etc.

Assuming that Eq. (154) holds true when the Inconel 718 superalloy is in its aged condition and considering that the two-term MTS model developed in this work fairly represents its flow behaviour, Eq. (154) can be differentiated with respect to the plastic strain $\bar{\varepsilon}^p$ as follows:

$$\frac{d}{d\bar{\varepsilon}^p}(\bar{\sigma} - \sigma_0) = \alpha_1 \mu b \frac{d}{d\bar{\varepsilon}^p}\sqrt{\rho} \tag{155}$$

$$\frac{d}{d\bar{\varepsilon}^p}\left(\sigma_a + s_i\left(\dot{\bar{\varepsilon}}^p, T\right)\frac{\mu}{\mu_0}\hat{\sigma}_i + s_e\left(\dot{\bar{\varepsilon}}^p, T\right)\frac{\mu}{\mu_0}\hat{\sigma}_e - \sigma_0\right) = \alpha_1 \mu b \frac{1}{2}\rho^{-1/2}\frac{d\rho}{d\bar{\varepsilon}^p} \tag{156}$$

$$\frac{d\sigma_a}{d\bar{\varepsilon}^p} + \frac{\mu}{\mu_0}\frac{d}{d\bar{\varepsilon}^p}\left(s_i\left(\dot{\bar{\varepsilon}}^p, T\right)\hat{\sigma}_i\right) + \frac{\mu}{\mu_0}\frac{d}{d\bar{\varepsilon}^p}\left(s_e\left(\dot{\bar{\varepsilon}}^p, T\right)\hat{\sigma}_e\right) - \frac{d\sigma_0}{d\bar{\varepsilon}^p} = \alpha_1 \mu b \frac{1}{2}\rho^{-1/2}\frac{d\rho}{d\bar{\varepsilon}^p} \tag{157}$$

$$\begin{aligned}\frac{d\sigma_a}{d\bar{\varepsilon}^p} + \frac{\mu}{\mu_0}\left[\frac{d\left(s_i\left(\dot{\bar{\varepsilon}}^p, T\right)\right)}{d\bar{\varepsilon}^p}\hat{\sigma}_i + \frac{d\hat{\sigma}_i}{d\bar{\varepsilon}^p}\left(s_i\left(\dot{\bar{\varepsilon}}^p, T\right)\right)\right] \\ + \frac{\mu}{\mu_0}\left[\frac{d\left(s_e\left(\dot{\bar{\varepsilon}}^p, T\right)\right)}{d\bar{\varepsilon}^p}\hat{\sigma}_e + \frac{d\hat{\sigma}_e}{d\bar{\varepsilon}^p}\left(s_e\left(\dot{\bar{\varepsilon}}^p, T\right)\right)\right] - \frac{d\sigma_0}{d\bar{\varepsilon}^p} \\ = \alpha_1 \mu b \frac{1}{2}\rho^{-1/2}\frac{d\rho}{d\bar{\varepsilon}^p}\end{aligned} \tag{158}$$

In order to keep consistency, the same assumption that involved $s_i\left(\dot{\bar{\varepsilon}}^p, T\right)$ and $s_e\left(\dot{\bar{\varepsilon}}^p, T\right)$ being negligible with respect to the plastic strain was made, thus:

$$s_e\left(\dot{\bar{\varepsilon}}^p, T\right)\frac{\mu}{\mu_0}\frac{d\hat{\sigma}_e}{d\bar{\varepsilon}^p} = \alpha_1 \mu b \frac{1}{2}\rho^{-1/2}\frac{d\rho}{d\bar{\varepsilon}^p} \tag{159}$$

According to Mecking and Kocks (1981) the variation of dislocation density with respect to the plastic strain is given by:

$$\frac{d\rho}{d\bar{\varepsilon}^p} = K_a\sqrt{\rho} - K_b\rho \tag{160}$$

where K_a and K_b are constants. The first term represents the contribution to hardening provided by dislocation accumulation while the second term is related to dynamic recovery (dislocation annihilation), effect that decreases the dislocation density and therefore softens the material. Two main functions have been proposed for the hardening rate $d\hat{\sigma}_e/d\bar{\varepsilon}^p$ given by Eq. (41) over the years, namely a Voce law:

$$\frac{d\hat{\sigma}_e(\bar{\varepsilon}^p)}{d\bar{\varepsilon}^p} = \theta_0\left(1 - \frac{\hat{\sigma}_e(\bar{\varepsilon}^p)}{\hat{\sigma}_{es}}\right) \tag{161}$$

and a phenomenological (or modified Voce) law, which recalling Eq. (42) is defined as:

$$\frac{d\hat{\sigma}_e(\bar{\varepsilon}^p)}{d\bar{\varepsilon}^p} = \theta_0\left[1 - \frac{tanh\left(\alpha_i\ \frac{\hat{\sigma}_e(\bar{\varepsilon}^p)}{\hat{\sigma}_{es}}\right)}{tanh(\alpha_i)}\right]$$

In the standard MTS model, the structure parameter $\hat{\sigma}_e$ commands the evolution of the hardening rate, and consequently of the flow stress. In its general formulation, the constitutive model states that the material hardens with strain until the stress $\hat{\sigma}_e$ reaches the saturation value $\hat{\sigma}_{es}$, mathematically expressed as:

$$\frac{d\hat{\sigma}_e}{d\bar{\varepsilon}^p} = 0 \tag{162}$$

It is clearly seen that the Voce law specified by Eq. (161) does not account for the softening produced by dynamic recrystallisation, the only softening mechanism considered is the one

produced by dynamic recovery. To address this issue, a new law for the evolution is proposed in this work, which takes into consideration the additional softening produced when the grain size is reduced. Starting with Eq. (160) and assuming that a law $h\left(\overline{\varepsilon}^p, \rho\right)$ accounted for this further softening, it would be found that:

$$\frac{d\rho}{d\overline{\varepsilon}^p} = K_a\sqrt{\rho} - K_b\rho - h\left(\overline{\varepsilon}^p, \rho\right) \tag{163}$$

and replacing this into Eq. (159) results in:

$$s_e\left(\dot{\overline{\varepsilon}}^p, T\right)\frac{\mu}{\mu_0}\frac{d\hat{\sigma}_e}{d\overline{\varepsilon}^p} = \alpha_1\mu b\frac{1}{2}\rho^{-1/2}\left(K_a\sqrt{\rho} - K_b\rho - h(\overline{\varepsilon}^p, \rho)\right) \tag{164}$$

where $d\hat{\sigma}_e/d\overline{\varepsilon}^p$ (unlike before) would represent the 'new' evolution law that would account not only for the softening produced dynamic recovery, but also by grain refinement. The objective of this work is therefore to find an appropriate $d\hat{\sigma}_e/d\overline{\varepsilon}^p$ equation that could contemplate strain hardening together with combined dynamic recovery and recrystallisation softening effects in addition to provide reliable predictions. To deduce such unknown expression, a mathematical approach based on comprehensive observations made from the literature will be developed instead of doing so from fundamental physical concepts.

Unfortunately, the difficulties associated with the objective of finding theoretical-based relationships completely derived from physical principles that could portray softening due to dynamic recrystallisation led to this practical alternative; however it is believed that the preliminary method/equations proposed in this work might provide insightful ideas for researchers in the future to recommend stronger theories.

Initially, the original Voce law is adopted as the evolution expression to start from to construct the desired $d\hat{\sigma}_e/d\overline{\varepsilon}^p$ (after all, the modified Voce law seen in Eq. (42) is nothing but a redefined version of the original one). Eq. (161) is therefore an ordinary differential equation which contains strain dependent terms, and in a similar way a function of the type $h(\overline{\varepsilon}^p, \rho)$ was added to Eq. (160) to account for dynamic recrystallisation effects, a strain-based function $f_a\left(\overline{\varepsilon}^p\right)$ can be added to this equation in order to maintain Eq. (164) valid, hence the 'new' evolution law would have, in principle, the following aspect:

$$\frac{d\hat{\sigma}_e(\overline{\varepsilon}^p)}{d\overline{\varepsilon}^p} = \theta_0\left(1 - \frac{\hat{\sigma}_e(\overline{\varepsilon}^p)}{\hat{\sigma}_{es}}\right) - f_a\left(\overline{\varepsilon}^p\right) \tag{165}$$

Recall that recrystallisation softens the workpiece material after a peak (corresponding to a critical strain) in flow stress is reached, hence it is straightforward to think that $f_a(\bar{\varepsilon}^p)$ has to portray this effect after such limit is attained. It is important to stress at this stage that the variable $\hat{\sigma}_e(\bar{\varepsilon}^p)$ influences the aspect of the resulting stress-strain curve and makes the flow stress $\bar{\sigma}$ to vary in a proportional way with it, therefore a decrease in $\hat{\sigma}_e(\bar{\varepsilon}^p)$ will produce a decrease in $\bar{\sigma}$.

In consequence, the shape of $f_a(\bar{\varepsilon}^p)$ can be visualised/recognised by looking at experimental stress-strain curves in which recrystallisation is present. Established from extensive analyses made by observation, the aspect of $f_a(\bar{\varepsilon}^p)$ following the peak in flow stress would usually resemble a *sin*-like curve (see Figure 88), hence:

$$f_a(\bar{\varepsilon}^p) \propto \sin(\bar{\varepsilon}^p) \tag{166}$$

Once the appearance of $f_a(\bar{\varepsilon}^p)$ is known, the resulting $d\hat{\sigma}_e/d\bar{\varepsilon}^p$ law needs the necessary degrees of freedom so that it could dynamically handle not only maximum values of flow stress, but also strains at which this happens (~0.5 for $\dot{\bar{\varepsilon}}^p$ = 5.224s^{-1} in Figure 88) together with the strains corresponding to the flow values at which the maximum softening is produced (~2 for $\dot{\bar{\varepsilon}}^p$ = 5.224s^{-1} in Figure 88). Mathematically speaking, the new evolution law $d\hat{\sigma}_e/d\bar{\varepsilon}^p$ could be defined in a general manner as follows:

$$\frac{d\hat{\sigma}_e(\bar{\varepsilon}^p)}{d\bar{\varepsilon}^p} = \theta_0\left(k_a - k_b\frac{\hat{\sigma}_e(\bar{\varepsilon}^p)}{\hat{\sigma}_{es}}\right) - k_c\sin(k_d\bar{\varepsilon}^p) \tag{167}$$

where k_a, k_b, k_c and k_d are constants. Note that when no recrystallisation takes place, $k_a = k_b = 1$ and $k_c = k_d = 0$, therefore the new evolution law given by Eq. (167) could be considered as a more general expression of that seen in Eq. (160). Replacing Eq. (167) into Eq. (164) it is obtained:

$$\begin{aligned} s_e\left(\dot{\bar{\varepsilon}}^p, T\right)\frac{\mu}{\mu_0}\left[\theta_0\left(k_a - k_b\frac{\hat{\sigma}_e(\bar{\varepsilon}^p)}{\hat{\sigma}_{es}}\right) - k_c\sin(k_d\bar{\varepsilon}^p)\right] \\ = \alpha_1\mu b\frac{1}{2}\rho^{-1/2}\left(K_a\sqrt{\rho} - K_b\rho - h(\bar{\varepsilon}^p,\rho)\right) \end{aligned} \tag{168}$$

where it can be easily indentified that:

$$\left(s_e\left(\dot{\bar{\varepsilon}}^p, T\right)\frac{\mu}{\mu_0}\right) k_c \sin\left(k_d \bar{\varepsilon}^p\right) = \left(\alpha_1 \mu b \frac{1}{2}\rho^{-1/2}\right) h\left(\bar{\varepsilon}^p, \rho\right) \tag{169}$$

After regrouping some of the terms into a general constant K_g it is concluded that:

$$h\left(\bar{\varepsilon}^p, \rho\right) = K_g \rho^{\frac{1}{2}} \sin\left(k_d \bar{\varepsilon}^p\right) \tag{170}$$

which confirms that h, as initially assumed, is a function of $\bar{\varepsilon}^p$ and ρ. Moreover, recall that when no recrystallisation is present $k_d = 0$, hence $h\left(\bar{\varepsilon}^p, \rho\right) = 0$ maintaining Eq. (160) valid. Alike Eq. (161), Eq. (167) is an ordinary differential equation that requires only one boundary condition to be fully defined, consequently it can be stated that:

$$\hat{\sigma}_e(\bar{\varepsilon}^p)\left(\bar{\varepsilon}^p = 0\right) = 0 \tag{171}$$

After solving Eq. (167) considering the restriction given by Eq. (171), an exact solution to the problem is to be found, which has the form:

$$\hat{\sigma}_e\left(\bar{\varepsilon}^p\right) = \frac{\hat{\sigma}_{es}}{K_1}\left[K_2 e^{-\left(\frac{\theta_0 k_b \bar{\varepsilon}^p}{\hat{\sigma}_{es}}\right)} - K_3 + K_4 \cos\left(k_d \bar{\varepsilon}^p\right) - K_5 \sin\left(k_d \bar{\varepsilon}^p\right)\right] \tag{172}$$

where:

$$K_1 = k_b(\theta_0^2 k_b^2 + k_d^2 \hat{\sigma}_{es}^2)$$

$$K_2 = -k_a k_b^2 \theta_0^2 - k_a k_d^2 \hat{\sigma}_{es}^2 - k_b k_c k_d \hat{\sigma}_{es}$$

$$K_3 = K_2 + k_b k_c k_d \hat{\sigma}_{es} = -k_a k_b^2 \theta_0^2 - k_a k_d^2 \hat{\sigma}_{es}^2$$

$$K_4 = k_b k_c k_d \hat{\sigma}_{es}$$

$$K_5 = \frac{K_4 \theta_0 k_b}{k_d \hat{\sigma}_{es}} = \theta_0 k_b^2 k_c$$

It is observed that Eq. (172) only depends on the strain $\bar{\varepsilon}^p$, thus making it very useful when computing the flow stress $\bar{\sigma}$ as observed below:

$$\bar{\sigma} = \sigma_a + s_i\left(\dot{\bar{\varepsilon}}^p, T\right)\frac{\mu}{\mu_0}\hat{\sigma}_i + s_e\left(\dot{\bar{\varepsilon}}^p, T\right)\frac{\mu}{\mu_0}\frac{\hat{\sigma}_{es}}{K_1}\left[K_2 e^{-\left(\frac{\theta_0 k_b \bar{\varepsilon}^p}{\hat{\sigma}_{es}}\right)} - K_3 + K_4\cos\left(k_d\bar{\varepsilon}^p\right) - K_5\sin\left(k_d\bar{\varepsilon}^p\right)\right] \tag{173}$$

Replacing Eq. (173) in Eq. (154) and assuming that the latter holds when grain refinement takes place, it is seen that:

$$\sigma_a + s_i\left(\dot{\bar{\varepsilon}}^p, T\right)\frac{\mu}{\mu_0}\hat{\sigma}_i + s_e\left(\dot{\bar{\varepsilon}}^p, T\right)\frac{\mu}{\mu_0}\frac{\hat{\sigma}_{es}}{K_1}\left[K_2 e^{-\left(\frac{\theta_0 k_b \bar{\varepsilon}^p}{\hat{\sigma}_{es}}\right)} - K_3 + K_4\cos\left(k_d\bar{\varepsilon}^p\right) - K_5\sin\left(k_d\bar{\varepsilon}^p\right)\right] - \sigma_0 = \alpha_1\mu b\sqrt{\rho} \tag{174}$$

Therefore the average dislocation density that results from considering both flow softening mechanisms, namely dynamic recovery and dynamic recrystallisation could be calculated as:

$$\sqrt{\rho} = \frac{1}{\alpha_1 b}\left(\frac{\sigma_a - \sigma_0}{\mu} + s_i\left(\dot{\bar{\varepsilon}}^p, T\right)\frac{\hat{\sigma}_i}{\mu_0} + s_e\left(\dot{\bar{\varepsilon}}^p, T\right)\frac{\hat{\sigma}_{es}}{\mu_0 K_1}\left[K_2 e^{-\left(\frac{\theta_0 k_b \bar{\varepsilon}^p}{\hat{\sigma}_{es}}\right)} - K_3 + K_4\cos\left(k_d\bar{\varepsilon}^p\right) - K_5\sin\left(k_d\bar{\varepsilon}^p\right)\right]\right) \tag{175}$$

With regard to grain size evolution, it is known that when recrystallisation takes places the dislocation density decreases in the same fashion the flow stress does so after having reached a critical value (in reality the reduction produced in the in dislocation density is the responsible for the softening seen in the flow stress). As the dislocation density keeps decreasing the grain size does so, therefore a general expression of the type:

$$d = d_{ini} - h_1\rho^{h_2} \tag{176}$$

in which d_{ini}, h_1 and h_2 are the initial grain size of the material and fitting constants respectively is proposed. In conclusion, Eq. (176) is considered to be representative of how

the grain varies in size with dislocation density and therefore, was used to predict grain refinement in this research work.

4.5.1.4 Calculation of constants/VUMAT implementation

In order to calculate the flow stress when recrystallisation takes place, it is observed that Eq. (172) depends on the constants k_a, k_b, k_c and k_d to be fully defined, implying therefore that four constrains were necessitated. The saturation value $\hat{\sigma}_{es}$ is that of $\hat{\sigma}_e(\overline{\varepsilon}^p = \overline{\varepsilon}^p_{ecrit})$ because the material softens after having reached a peak in flow stress (in the recrystallisation regime), hence only three more boundary conditions need to be defined beforehand to fully delineate Eq. (172). In principle, they could be specified as the critical strain which defines onset of recrystallisation, the maximum strain accounting for the maximum degree of softening and the value of $\hat{\sigma}_e(\overline{\varepsilon}^p)$ that corresponds to it.

Now, the two values of strains could be calculated by the values of energy that predict commencement of recrystallisation and damage respectively, therefore we can see that the RWM model could implicitly link critical strains to values of energy, something that seems to have a better physical background than assuming values of strains arbitrarily.

For the calculation of $\hat{\sigma}_e(\overline{\varepsilon}^p = \overline{\varepsilon}^p_{max})$, it has been observed from numerous studies that commonly, the flow stress at the maximum strain could be:

$$\bar{\sigma}_{max} = \bar{\sigma}(\overline{\varepsilon}^p = \overline{\varepsilon}^p_{max}) = 80 - 90\% \left[\bar{\sigma}(\overline{\varepsilon}^p = \overline{\varepsilon}^p_{ecrit})\right] \quad (177)$$

where neither $\overline{\varepsilon}^p_{ecrit}$, $\bar{\sigma}_{max}$ nor $\overline{\varepsilon}^p_{max}$ are kwon in this work. Due to lack of data therefore, an average value of 85% was assumed to calculate the flow stress at the maximum strain irrespective of temperature and strain rate. The value $\bar{\sigma}_{crit} = \bar{\sigma}(\overline{\varepsilon}^p = \overline{\varepsilon}^p_{ecrit})$ corresponds to a value $\hat{\sigma}_e(\overline{\varepsilon}^p = \overline{\varepsilon}^p_{ecrit})$, hence $\hat{\sigma}_e(\overline{\varepsilon}^p = \overline{\varepsilon}^p_{max})$ is calculated by a simple algorithm that searches for $\hat{\sigma}_e$ values until the equality $\bar{\sigma}_{max} = 0.85\text{x}\bar{\sigma}_{crit}$ is achieved. As concluded from subsection 4.3.2, the MTS model on its own is capable of predicting the hardening behaviour of Inconel 718 with a reasonable accuracy until $\overline{\varepsilon}^p_{ecrit}$ (when recrystallisation is not included), however it is noticed that Eq. (173) can also predict hardening from zero plastic strain up to this critical point.

Therefore in order to maintain a logical criterion, the MTS constitutive model was applied from zero to $\overline{\varepsilon}^{p}_{ecrit}$, whereas Eq. (173) was considered valid from this point onwards. This corollary would result in having $\hat{\sigma}_{es} = \hat{\sigma}_{e}\left(\overline{\varepsilon}^{p} = \overline{\varepsilon}^{p}_{ecrit}\right)$ as said before, because once softening begins, the maximum value in flow stress would correspond to that given by the saturation stress $\hat{\sigma}_{es}$.

Although the establishment of the parameters $\overline{\varepsilon}^{p}_{ecrit}$, $\overline{\varepsilon}^{p}_{max}$, $\hat{\sigma}_{es}$ and $\hat{\sigma}_{e}\left(\overline{\varepsilon}^{p} = \overline{\varepsilon}^{p}_{max}\right)$ may give the notion that all four restrictions to delineate the 'recrystallised' stress-strain curve are appropriate, it is noted from Eq. (172) that $\hat{\sigma}_{e}$ is a function of $\overline{\varepsilon}^{p}$, which means that the stresses and strains are dependent, and thus it reduces the quantity of independent constrains to two only. Therefore two additional boundary conditions are needed so that the resulting plastic stress-strain curve could be properly defined. Consequently, it could be undoubtedly stated that:

$$\frac{d\hat{\sigma}_{e}(\overline{\varepsilon}^{p} = \overline{\varepsilon}^{p}_{ecrit})}{d\overline{\varepsilon}^{p}} = 0 \tag{178}$$

$$\frac{d\hat{\sigma}_{e}(\overline{\varepsilon}^{p} = \overline{\varepsilon}^{p}_{max})}{d\overline{\varepsilon}^{p}} = 0 \tag{179}$$

Once all the boundary conditions needed are specified (and mathematically checked that they are independent), the calculation of the parameters k_a, k_b, k_c and k_d was achieved by using preliminary algorithms that estimate every parameter individually, to then use those initial values to refine them in one final algorithm until specific tolerance values for $\overline{\varepsilon}^{p}_{ecrit}$, $\overline{\varepsilon}^{p}_{max}$ and $\hat{\sigma}_{e}\left(\overline{\varepsilon}^{p} = \overline{\varepsilon}^{p}_{max}\right)$ are met.

For example, if it was assumed that at a temperature of 1,123K and strain rate of $10s^{-1}$ recrystallisation took place at a critical plastic strain of 0.2 (given for instance as the resultant value of energy provided by the RWM damage model), the predicted maximum flow stress would be ~783MPa. Furthermore, assume that $\overline{\varepsilon}^{p}_{max}$= 1, which in consequence would correspond to a flow stress of ~665MPa (85% of 783MPa).

The numerical algorithm developed in this work to calculate the constants k_a, k_b, k_c and k_d based on the restrictions aforesaid would result in a plastic stress-strain curve as shown in Figure 89:

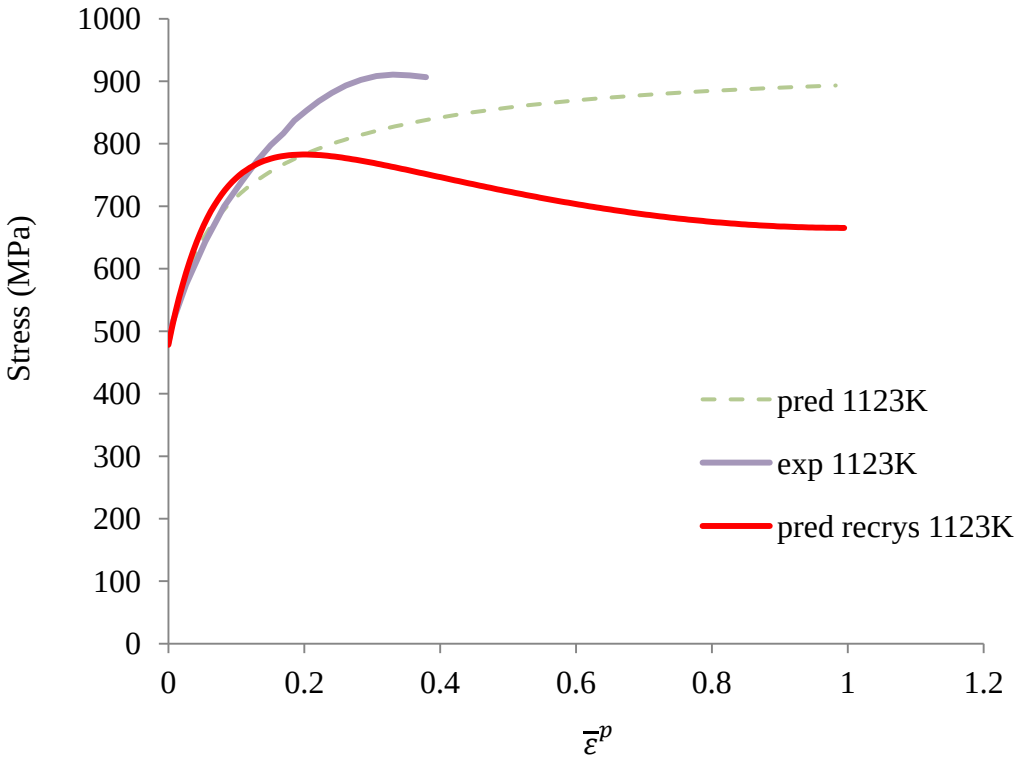

Figure 89. Theoretical predicted stress-strain curve by the model proposed in this work when recrystallisation effects are taken into consideration.

From Figure 89 it can be seen that Eq. (173) is flexible enough to predict softening due to grain refinement and that the algorithms developed are robust (and simple from a programmer's perspective) to give accurate predictions based on the constrains defined. In addition, it can be corroborated that the predicted flow stress at a plastic strain of 1 (~665MPa) is 85% of the peak found at a strain of 0.2 (~783MPa) together with the fact that the derivatives at such strain values were zero.

It is important to note that at $\bar{\varepsilon}^p_{max}$, complete stress degradation will have taken place, therefore Figure 89 is missing the further softening provoked by the application of the RWM damage model. In order to compute $\bar{\varepsilon}^p_{max}$, an approximation method based on the calculation of energies is proposed, which rectifies the resulting recrystallised stress-strain curve into straight lines and divides it into three specific regions of energy, see the scheme plotted in Figure 90:

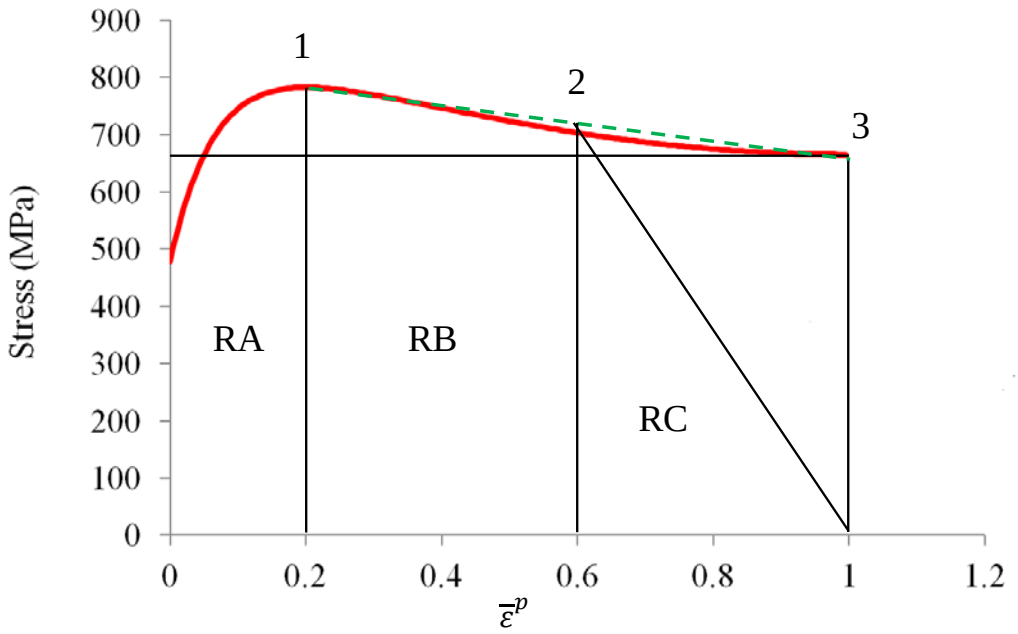

Figure 90. Rectified stress-strain curve to calculate $\overline{\varepsilon}^p_{max}$.

In region RA, the value of energy U_1^p under the stress-strain curve is calculated by Eq. (131), however it should be highlighted that $U_1^p \neq W_R$, hence if it is made:

$$W_R = k_W\, W_{crit} = k_E\, U_1^p \tag{180}$$

where k_E is a constant, in principle it is obtained:

$$k_E = \frac{k_W\, W_{crit}}{U_1^p} \tag{181}$$

A linear approximation (dashed green line) to the real shape of the recrystallised stress-strain curve is made between point 1 (corresponding to $\overline{\varepsilon}^p_{ecrit}$ and $\bar{\sigma}_{crit}$ which are known) and point 3 (corresponding to $\overline{\varepsilon}^p_{max}$ and $\bar{\sigma}_{max}$), in which case its mathematical expression would give the variation of the flow stress with plastic strain in such region:

$$\bar{\sigma} = \left[\bar{\sigma}_{crit} + \left(\frac{\bar{\sigma}_{crit} - \bar{\sigma}_{max}}{\overline{\varepsilon}^p_{max} - \overline{\varepsilon}^p_{ecrit}}\right)\overline{\varepsilon}^p_{ecrit}\right] - \left(\frac{\bar{\sigma}_{crit} - \bar{\sigma}_{max}}{\overline{\varepsilon}^p_{max} - \overline{\varepsilon}^p_{ecrit}}\right)\overline{\varepsilon}^p \tag{182}$$

where $\overline{\varepsilon}^p_{ecrit} < \overline{\varepsilon}^p < \overline{\varepsilon}^p_{max}$ and $\bar{\sigma}_r$ and $\overline{\varepsilon}^p_r$ are the unknown values of flow stress and plastic strain in which damage would be triggered (point 2). It is easy to verify from Eq. (182) that:

$$\bar{\sigma}\left(\bar{\varepsilon}^p = \bar{\varepsilon}^p_{ecrit}\right) = \left[\bar{\sigma}_{crit} + \left(\frac{\bar{\sigma}_{crit} - \bar{\sigma}_{max}}{\bar{\varepsilon}^p_{max} - \bar{\varepsilon}^p_{ecrit}}\right)\bar{\varepsilon}^p_{ecrit}\right] - \left(\frac{\bar{\sigma}_{crit} - \bar{\sigma}_{max}}{\bar{\varepsilon}^p_{max} - \bar{\varepsilon}^p_{ecrit}}\right)\bar{\varepsilon}^p_{ecrit} = \bar{\sigma}_{crit} \tag{183}$$

$$\bar{\sigma}\left(\bar{\varepsilon}^p = \bar{\varepsilon}^p_{max}\right) = \left[\bar{\sigma}_{crit} + \left(\frac{\bar{\sigma}_{crit} - \bar{\sigma}_{max}}{\bar{\varepsilon}^p_{max} - \bar{\varepsilon}^p_{ecrit}}\right)\bar{\varepsilon}^p_{ecrit}\right] - \left(\frac{\bar{\sigma}_{crit} - \bar{\sigma}_{max}}{\bar{\varepsilon}^p_{max} - \bar{\varepsilon}^p_{ecrit}}\right)\bar{\varepsilon}^p_{max} = \bar{\sigma}_{max} \tag{184}$$

The value of energy U_2^p which corresponds to region RB is then given by:

$$U_2^p = \frac{\bar{\sigma}_{crit} + \bar{\sigma}_r}{2}\left(\bar{\varepsilon}^p_r - \bar{\varepsilon}^p_{ecrit}\right) \tag{185}$$

and doing so with region RC, the resulting energy is:

$$U_3^p = \frac{\bar{\sigma}_r}{2}\left(\bar{\varepsilon}^p_{max} - \bar{\varepsilon}^p_r\right) \tag{186}$$

Hence, in order to calculate $\bar{\varepsilon}^p_r$ (which instantly gives $\bar{\sigma}_r$ and then U_2^p) to further obtain $\bar{\varepsilon}^p_{max}$, a coupled algorithm was developed which consisted of first giving arbitrary values to $\bar{\varepsilon}^p_{max}$ to later enter this value into Eq. (182). This operation was followed by also giving arbitrary values to $\bar{\varepsilon}^p$ in Eq. (182) until the expression:

$$W_{crit} = k_E\left(U_1^p + U_2^p\right) \tag{187}$$

was corroborated to a specific tolerance. Then, with the preliminary values of $\bar{\varepsilon}^p_r$ and $\bar{\sigma}_r$ already calculated, the algorithm checked that the following expression:

$$W_{frac} = k_E\left(U_1^p + U_2^p + U_3^p\right) \tag{188}$$

was true. If this was not the case, the loop would recommence and give a new value to $\bar{\varepsilon}^p_{max}$ so that not only Eq. (187) could be validated again, but also Eq. (188). Once the parameters $\bar{\varepsilon}^p_{crit}$, $\bar{\varepsilon}^p_{max}$, $\bar{\sigma}_{crit}$ and $\bar{\sigma}_{max}$ together with the restrictions given by Eq. (178) and Eq. (179) are defined, the constants k_a, k_b, k_c and k_d can be calculated.

All the numerical techniques described here to finally predict softening due to DRX were implemented into the VUMAT subroutine in conjunction with the developed codes of the MTS and RWM models initially developed.

4.5.2 3D Thermo-mechanical Lagrangian - MTS and RWM

4.5.2.1 General formulation of the FE model

The unique aspect that varied in this case was the addition of the DRX model to the MTS constitutive model, therefore the 3D FE arrangement specified for each of the previous conditions following orthogonal machining Inconel 718, remained the same as that described in subsection 4.4.2. As a consequence of this, workpiece and tool mesh properties continued unchanged. All FE simulations took an average of 170hs of computation. An example (including a detailed analysis of the numerical findings) when the MTS, RWM and DRX models are used can be found in Appendix V.

4.5.2.2 Damage model characteristics

Following the same reasoning perpetuated in all previous numerical approaches, not only positive values of energy W were considered, but also a trial and error method was performed to obtain the most suitable parameters W_{crit}, W_{frac} and a, which are displayed in Table 22:

Feed (mm/rev)	**0.2**			**0.08**		
Cutting speed (m/min)	**200**	**250**	**300**	**200**	**250**	**300**
W_{crit} (J/m^3)	150	150	150	150	150	150
W_{frac} (J/m^3)	3,500	3,600	3,750	3,710	3,810	3,850
a (-)	0.145	0.145	0.145	0.145	0.15	0.15

Table 22. Resulting W_{crit}, W_{frac} and a values for the RWM damage model used to simulate 3D machining of Inconel 718 superalloy with the MTS and DRX models.

4.5.2.3 DRX model characteristics

Based on the explanations given previously to develop the custom-made DRX model, the average dislocation density seen in Eq. (175) was calculated by a trial an error iteration, which used a value for the parameter α_1 of 0.52 while $\sigma_0 = 575MPa$ to follow in the footsteps of Lee et al. (2011). In consequence, the computation of the mean grain size according to Eq. (176), was performed with refined h_1 and h_2 parameters, that according to the units used in ABAQUS turned out to be 1/380 and 0.3 respectively.

4.6 Recapitulation

Fully coupled thermo-mechanical numerical simulations (2D/3D) imitating the real dimensions of the Ti-6Al-4V workpiece material and carbide tool were performed in order to evaluate more precisely the predictions of both modelling techniques in terms of cutting forces, temperatures and chip formation/morphology. In 2D, the JC relationship together with the RWM damage model were employed while the ALE/AR method was used in an attempt to better accommodate the elevated workpiece element distortion that is produced when simulating chip formation/morphology. When the modelling exercise was done in 3D, the CL damage model was also employed in order to make quantifiable comparisons with RWM in order to mark the path to follow for the mainstream FE work on Inconel 718.

With the flow stress data generated by utilising the SHPB apparatus together with that already had in hand from the Gleeble machine, the laborious task of calculating novel constants for the JC model in conjunction with a detailed development of a two-term MTS constitutive model took place. Both viscoplastic models showed a competent correlation with experimental plastic stress-strain curves at low ($<1{,}000s^{-1}$) and high (up to $\sim6{,}000s^{-1}$) strain rates, however the MTS model was more accurate than JC at values of temperature that surpassed the strength threshold of the superalloy (~923K). This implies that the latter model would need modifications and at the same time, proves the former as being a convenient option (in spite of its intrinsic complexity) when trying to describe the constitutive behaviour of the Inconel 718 workpiece material at a wide spectrum of strain rates and temperatures.

FE modelling work following orthogonal cutting of Inconel 718 was (in all cases) carried out using the RWM damage criterion together with the JC and MTS constitutive models to draw comparisons between them both and further state which one performed better. 2D and 3D fully coupled thermo-mechanical FE models at real scale were developed in an attempt to make them as close to actual machining conditions as possible.

Having developed the MTS strength model as a plausible alternative to JC and also demonstrated its prediction capabilities, a further and more complex step was taken in order to replicate microstructural alterations on the machined surface of Inconel 718. To address this problem, a tailored mathematical criterion (based on experimental evidence) suit to purpose was developed and linked to the MTS and RWM models, where the latter was in charge of triggering the grain refinement effect. The additional flow softening provoked by the grain refinement mechanism was achieved by adjusting the evolution law of the constitutive model to finally prove that the new expression could forecast continuous (differentiable) plastic stress-strain curves and handle with no major obstacles different prerequisites.

CHAPTER 5

RESULTS AND DISCUSSION

5.1 Orthogonal cutting of Ti-6Al-4V alloy

Based on a detailed study as well as extensive results gathered from the literature following machining of Ti-6Al-4V alloy, Molinari et al. (2013) indicated that cutting forces are influenced by the generation of shear bands (also witnessed in this work, see Figure 92), which make them oscillate with a frequency calculated as $f_{force} = 1/(\Delta t)_{force}$, where $(\Delta t)_{force}$ corresponds to the time interval between two consecutive force peaks. The authors however made use of averaged tangential and feed force values in their analysis, in agreement with Sima and Ozel (2010) and Ozel et al. (2010), who likewise performed turning trials on Ti-6Al-4V alloy. Therefore, mean values were also utilised in the present work, with results condensed in Table 23 following orthogonal machining at cutting speeds of 60, 90 and 120m/min and a feed of 0.125mm/rev.

Feed (mm/rev)	**0.125**		
Cutting speed (m/min)	**60**	**90**	**120**
Experimental tangential force (N)	143	138	132
Experimental feed force (N)	55	52	48

Table 23. Experimental tangential and feed forces when turning Ti-6Al-4V alloy.

The pattern exhibited by both force components is in agreement with numerous studies (Karpat, 2011; Li and Shih, 2005), that is the values decreased as a direct consequence of the escalating cutting speeds. This behaviour is due to the considerable temperatures and plastic strains generated by the machining process which softened the workpiece material at a higher degree when those increased (in consequence deteriorating the intrinsic capability of the aerospace alloy to withstand increasing loads).

5.2 Orthogonal cutting of Inconel 718 superalloy

Similarly as with Ti-6Al-4V alloy, chip serration has also been widely observed when machining Inconel 718 superalloy at high cutting speeds as reported by Thakur et al. (2009) and more recently by Zhang et al. (2013), with the characteristic that this work is not the exception (see Figure 100). Fluctuation in cutting forces is therefore evidenced in the same fashion it occurs with Ti-6Al-4V, as according to the latter study the periodical variation in tangential and feed force values can be attributed to chip thickness modifications when the serrated chips are generated. Nevertheless, it has also been a customary practise adopted by researchers to work with average cutting force values not only in purely-based experimental investigations (Choudhury and El-Baradie, 1998; Pawade et al., 2007), but also those which focus on FE modelling (Courbon et al., 2011; Lorentzon et al., 2009).

Based on the above, Table 24 summarises the tangential and feed force values that were averaged following their measurement during the orthogonal turning procedure which employed cutting velocities of 200, 250 and 300m/min at feed rates of 0.2 and 0.08mm/rev respectively.

Feed (mm/rev)	**0.2**			**0.08**		
Cutting speed (m/min)	**200**	**250**	**300**	**200**	**250**	**300**
Experimental tangential force (N)	370	390	405	200	260	195
Experimental feed force (N)	140	150	170	100	125	110

Table 24. Experimental tangential and feed forces when turning Inconel 718 superalloy.

It is interesting to note from the recordings that when the feed was 0.2mm/rev, an increase in cutting speed was accompanied by an increase in tangential and feed forces too. This phenomenon may contradict some findings (Choudhury and El-Baradie, 1998) as when the cutting speed increases it would be expected a rise in the temperature of the workpiece material, which would soften it to then reduce the cutting forces. Alike remarks can be made for experimental forces obtained when the feed was 0.08mm/rev.

As all trials were effectuated in dry conditions and at cutting speeds which were elevated however, it is believed that such experimental results were mainly caused by the high level of wear/damage produced on the tool cutting edge, which therefore affected the cutting forces at a great extent as derived from the generated data. For example, Figure 91 shows the aspect of the PBCN insert cutting edges when the orthogonal cutting operation was carried

out at cutting speeds of 200, 250 and 300m/min and a feed rate of 0.2mm/rev, in which tool wear together with edge damage/breakage are clearly visible.

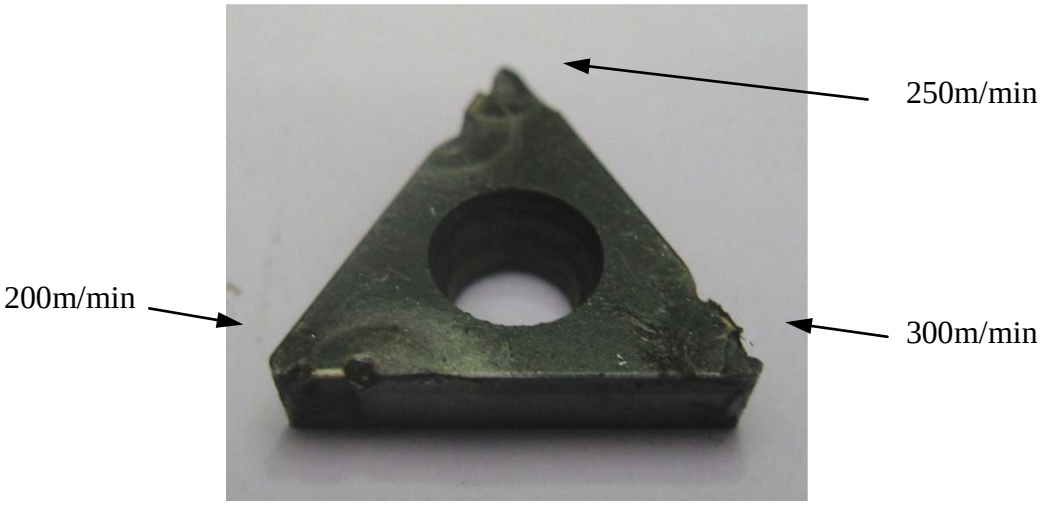

Figure 91. High tool wear/damage evidenced following machining of Inconel 718 at various cutting speeds and a feed of 0.2mm/rev.

Similar findings together with a comparable trend in cutting force values when cutting Inconel 718 in dry conditions, although at significantly lower cutting speeds (40, 60 and 80m/min) and with a different tool material (coated CVD), were also encountered by other researchers (Devillez et al., 2011), hence it is of no surprise that the pattern found in this work which relates cutting velocities to both tangential and feed force components behaves randomly.

5.3 FEM following machining

5.3.1 2D orthogonal cutting on Ti-6Al-4V with JC and RWM

5.3.1.1 Chip formation/morphology

A detailed dimensional analysis of the predicted chips together with those found experimentally following the corresponding etching procedure is shown in Figure 92. It is relevant to highlight that chip serration was produced in all cases irrespective of the cutting speed employed. Furthermore, the phenomenon of shear banding generation was clearly evidenced due to the elevated mesh distortion, which was caused by the softening effect the damage model utilised had on the workpiece. As observed, predicted chip morphology did not involve the use of the element deletion technique due to the difficulties the version of ABAQUS used has in dealing with such features in 2D environments.

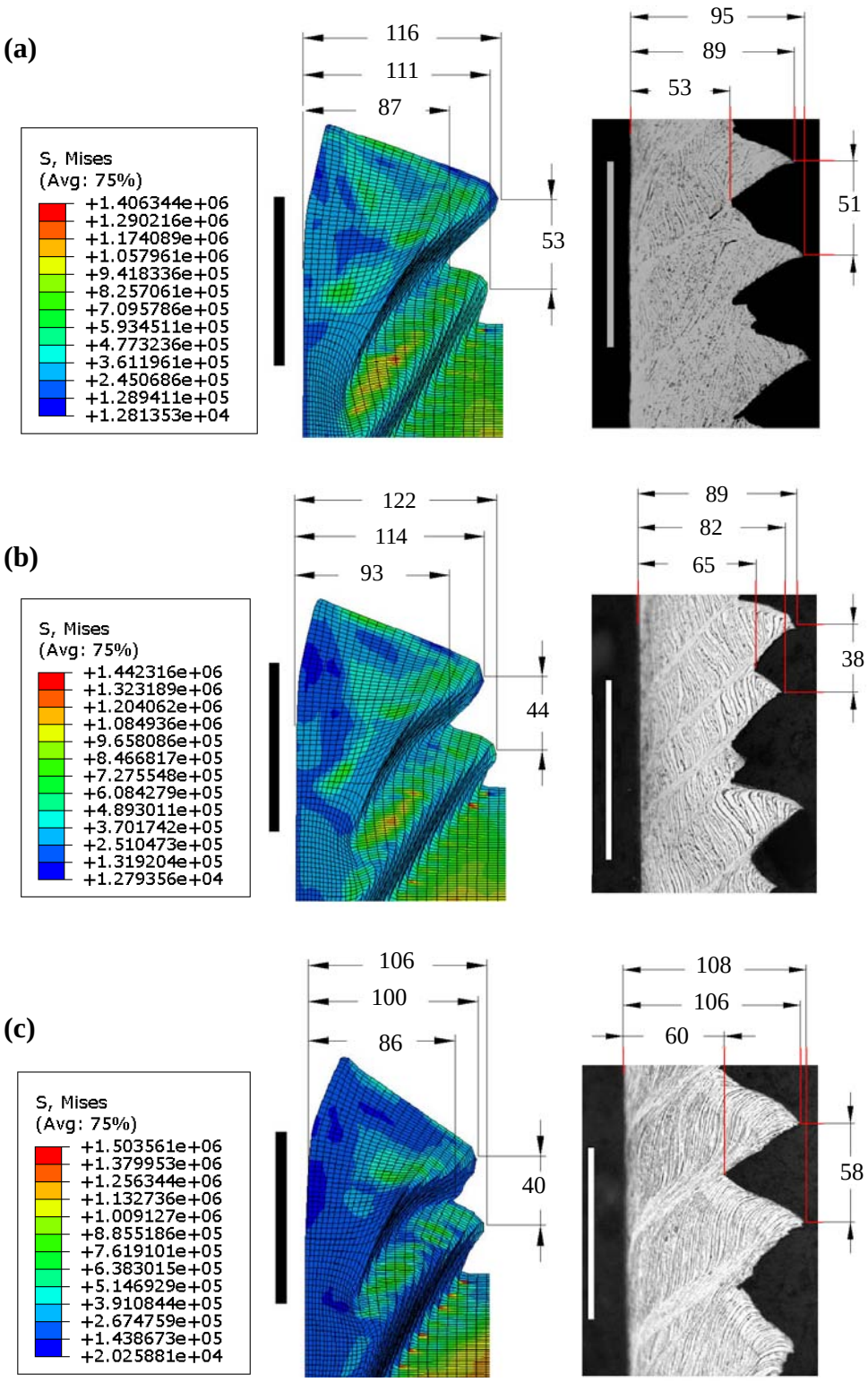

Figure 92. Comparison between experimental and predicted chip morphology (μm) for a feed of 0.125mm/rev and a cutting speed of (a) 120m/min, (b) 90m/min, (c) 60m/min when simulating 2D machining of Ti-6Al-4V with the JC and RWM models. The scale bars correspond to 100μm while the variable S to the Von Mises stress (10^{-3} MPa).

Although differences between predicted and experimental chip features are always expected to occur, these seemed to be minimal for all machining situations modelled. For example, a good agreement between predicted and experimental chip pitch was achieved,

which involved an average error of 9%. It is important to stress that in all cases, chip valley was overestimated by almost 50%, which indicated that the generation of the second saw-tooth occurred faster than it should have been. With regard to the thickness of the predicted shear bands, it was deduced that a higher degree of softening was needed so that they could be as slender as those encountered following the orthogonal cutting trials.

Due to the tremendous distortion suffered by the mesh comprising the workpiece, all FE simulations aborted shortly after the second saw-tooth was completely formed. This was somehow expected to happen due to the method chosen to simulate orthogonal cutting, which neither include any artificial separation layer nor a full workpiece remeshing technique (only a few columns of elements in front of the tool tip in order to achieve realistic adiabatic shear bands).

5.3.1.2 Cutting forces

The corresponding output field variables for all nodes comprising the cutting tool were extracted from the FE simulations and utilised to estimate both force components. Table 25 puts together the mean experimental and predicted tangential and feed forces when the cutting speed varied from 60 to 120m/min.

Feed (mm/rev)	**0.125**		
Cutting speed (m/min)	**60**	**90**	**120**
Experimental tangential force (N)	143	138	132
ABAQUS prediction (N)	148.8 (4%)	156.6 (13.5%)	162.1 (22.8%)
Experimental feed force (N)	55	52	48
ABAQUS prediction (N)	55.5 (1%)	63.8 (22.7%)	66.2 (37.9%)

Table 25. Comparison between averaged experimental and predicted forces including error deviation when simulating 2D machining of Ti-6Al-4V with the JC and RWM models.

In accordance with recordings obtained experimentally, both force components increased as machining progressed until a sharp drop of ~10% was evidenced, corresponding to initiation of saw-tooth chip profile. This response was repeated continuously with the stresses rapidly oscillating between the maximum and minimum values over the entire process duration in line with the experimental force data.

In all FE simulations, tangential forces were overestimated, highlighting that their accuracy increased when the cutting speed decreased (the best estimation having a ~4% error for a cutting speed of 60m/min). The same trend was found for the predicted feed forces,

which were not only overestimated in all cases, but also comprised better predictions when the cutting speed decreased (in which case the best estimation involved an error of ~1%, also corresponding to a cutting speed of 60m/min).

The fact that numerical predictions became more inaccurate (irrespective of the temperatures generated in the process) at higher cutting speeds, implied that the constitutive model employed was not capable of entirely capturing the strain softening Ti-6Al-4V exhibits (Sima and Ozel, 2010), situation which becomes more perceptible when cutting speeds are increased, because plastic strains are expected to be undoubtedly high.

5.3.1.3 Workpiece/tool temperature distribution

Figure 93 displays the predicted temperatures in tool and workpiece that followed the 2D FE simulation for the cutting conditions aforementioned.

As it was expected, general process temperatures increased when cutting speeds increased, which were more accentuated in the workpiece. Nevertheless, the maximum temperature values estimated in the workpiece (~720K when cutting at 120m/min) do not seem to be high enough to help provoke the softening required to keep decreasing the cutting force values exhibited in the previous subsection. Although the cutting tool utilised has an elevated thermal conductivity value when compared to the tool's, the maximum temperature was predicted to be ~320K for a cutting speed of 120m/min, which in principle seemed to be not too high and therefore indicated that adjustments are necessitated. Regardless of the operating conditions however, the overall temperature distribution showed its highest peaks at the tool-chip interface, in accordance with experimental findings available in the literature (Sima and Ozel, 2010).

Interestingly to say is that a noticeable increase in temperature was not included in the internal composition of the predicted shear bands (for example, the highest temperature had a value of ~550K when machining at 120m/min), fact that was considered to be mostly due to the rapid flow softening produced by the RWM damage model, which as a result influenced (decreased) the plastic energy generated.

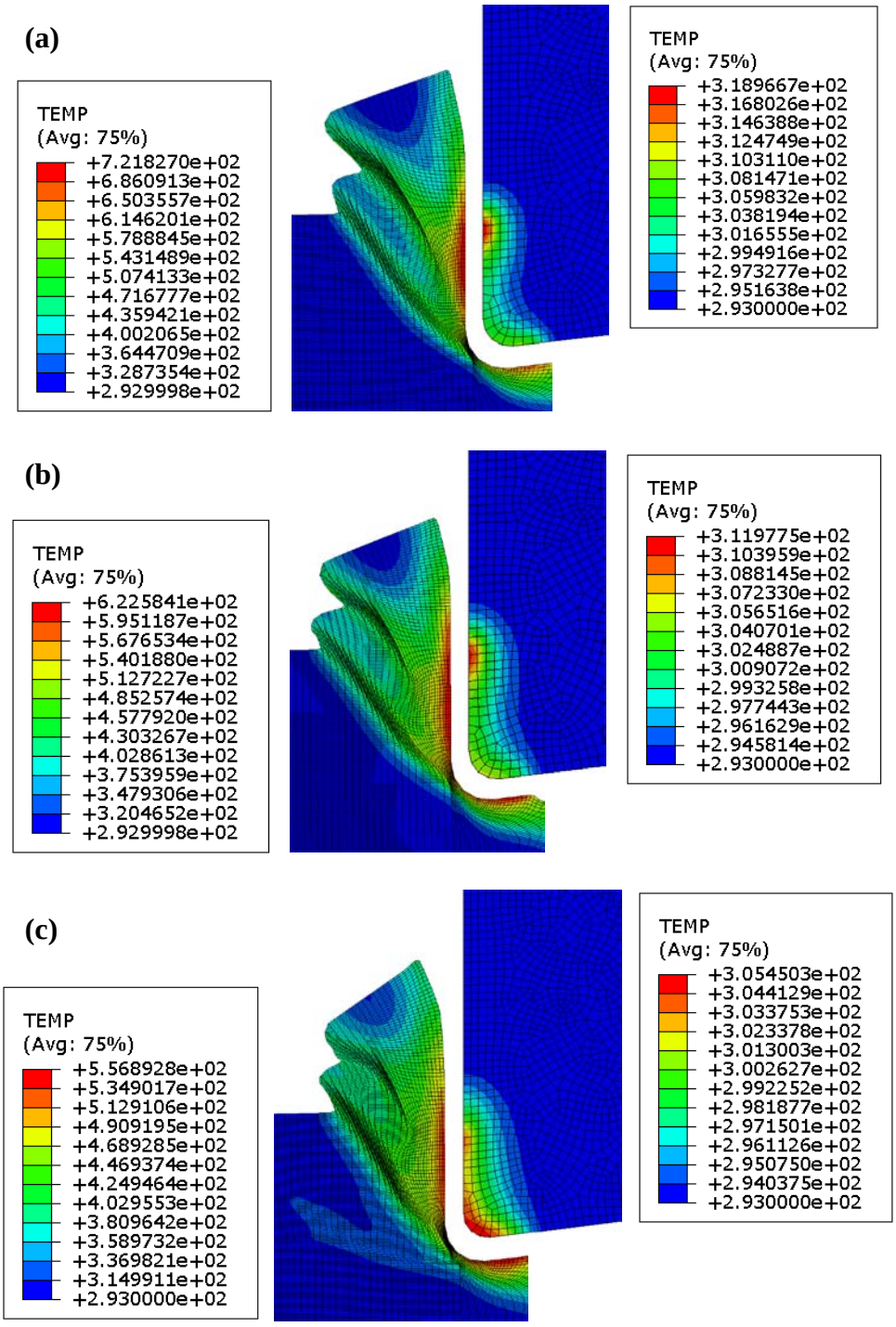

Figure 93. Predicted temperature distribution in tool and workpiece (K) for a feed of 0.125mm/rev and a cutting speed of (a) 120m/min, (b) 90m/min, (c) 60m/min when simulating 2D machining of Ti-6Al-4V with the JC and RWM models.

5.3.2 3D orthogonal cutting on Ti-6Al-4V with JC and CL/RWM

5.3.2.1 Chip formation/morphology

Figure 94 displays views of the workpiece material Von Mises stress distribution in a three dimensional environment seen from two angles for all cutting conditions simulated.

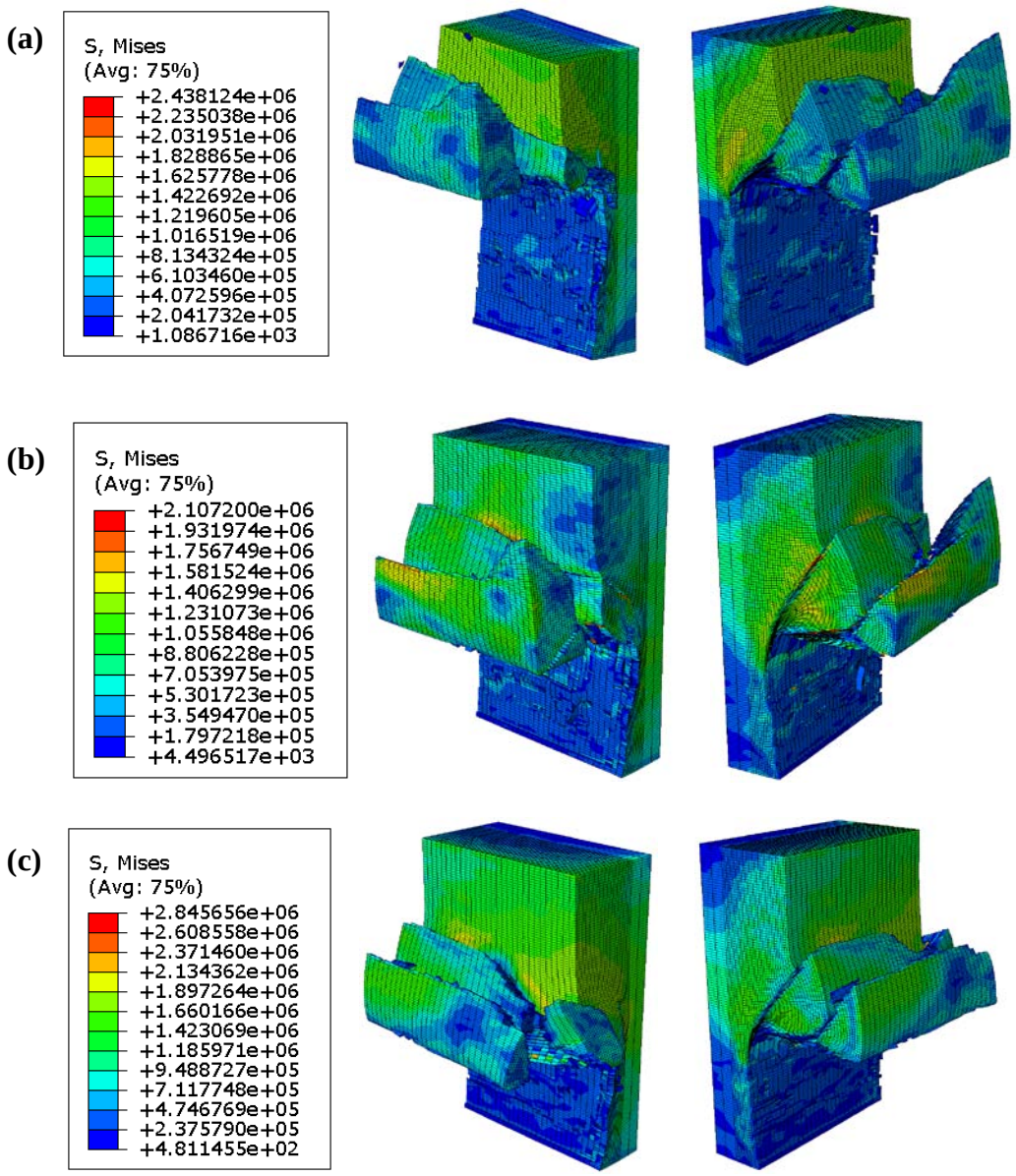

Figure 94. 3D view images of Von Mises stress distribution in workpiece (10^{-3}MPa) for a feed of 0.125mm/rev and a cutting speed of (a) 120m/min, (b) 90m/min, (c) 60m/min when simulating 3D machining of Ti-6Al-4V with the JC and CL models.

An important aspect to take into account that is common to all FE simulations, is the fact that the saw-tooth chip produced did not have a constant section across the 1mm wall thickness of the workpiece, which is clearly evidencing the benefits of 3D modelling in order to capture essential features that are most of the time neglected in two-dimensional situations. Chip serration was predicted in all cutting situations and the generation of a softened and irregular machined surface is easily noticed, however the level of damage produced by the CL fracture criterion on the workpiece is believed to be too aggressive because the formation of adiabatic shear bands involved deleted rather than highly distorted elements. On the other hand as shown in Figure 95, the RWM damage model generated not only adiabatic shear bands that were continuous for each cutting condition, but also a burr which resembled a

remarkable similarity with common experimental findings. The predicted workpiece surfaces following the cutting operation remained soft in nature as before (~11MPa in average), however they were not as soft as those generated by the CL damage model (~2MPa in average) because it is likely that the degree of damage exerted to the workpiece was 'shared' by both surface and adiabatic shear bands.

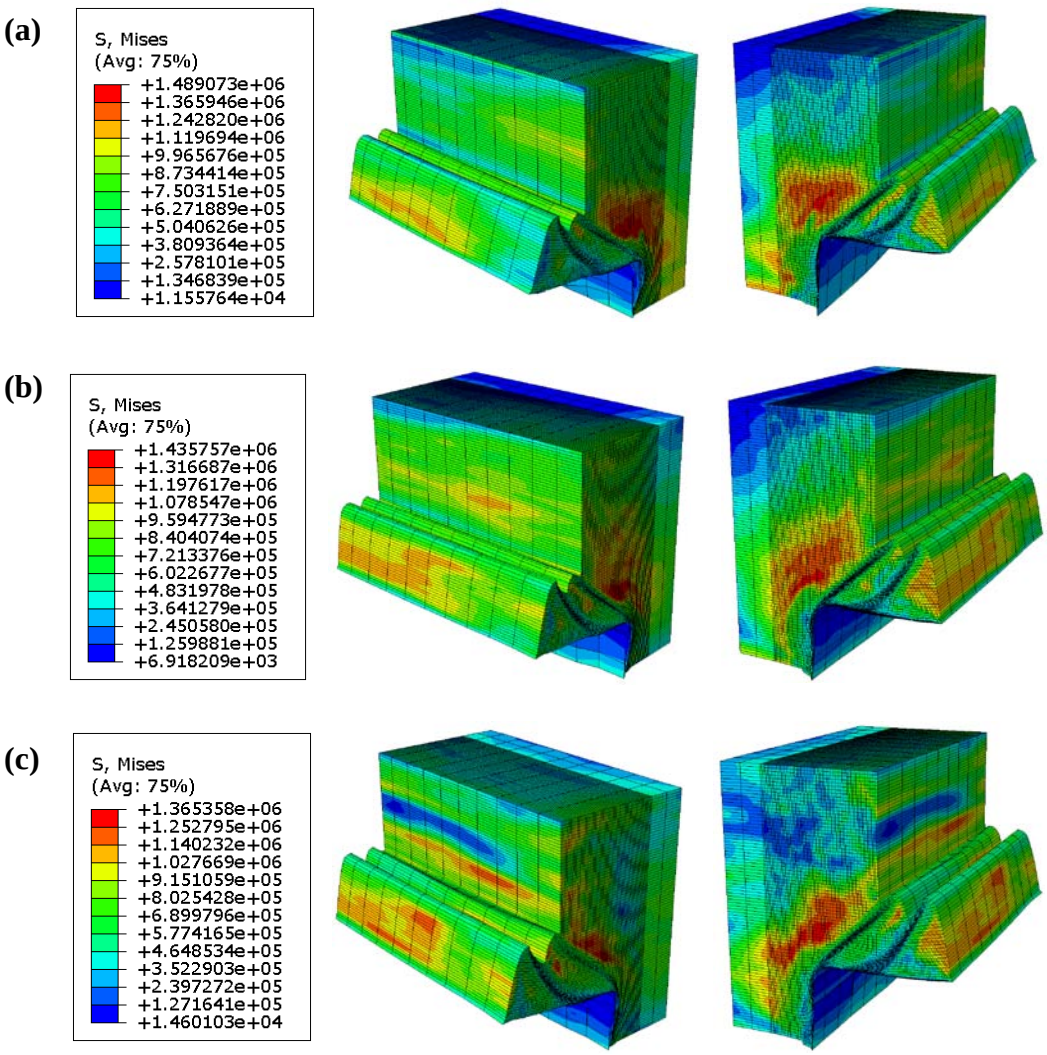

Figure 95. 3D view images of Von Mises stress distribution in workpiece (10^{-3}MPa) for a feed of 0.125mm/rev and a cutting speed of (a) 120m/min, (b) 90m/min, (c) 60m/min when simulating 3D machining of Ti-6Al-4V with the JC and RWM models.

In accordance with results observed from experiments, serrated chips were formed by elements that suffered from nodal flow softening to a great extent, which ultimately led to the evident continuous shear bands that were predicted in all cases. Damage occurred indeed, however it was primarily reached to mesh elements which were located at the tool tip instead of those situated at the newly formed shear bands. Figure 96 shows the predicted chip morphology as well as the accumulated energy distribution C_1 seen in Eq. (46) from the FE

models together with corresponding cross sectional micrographs of chips collected following the experimental trials.

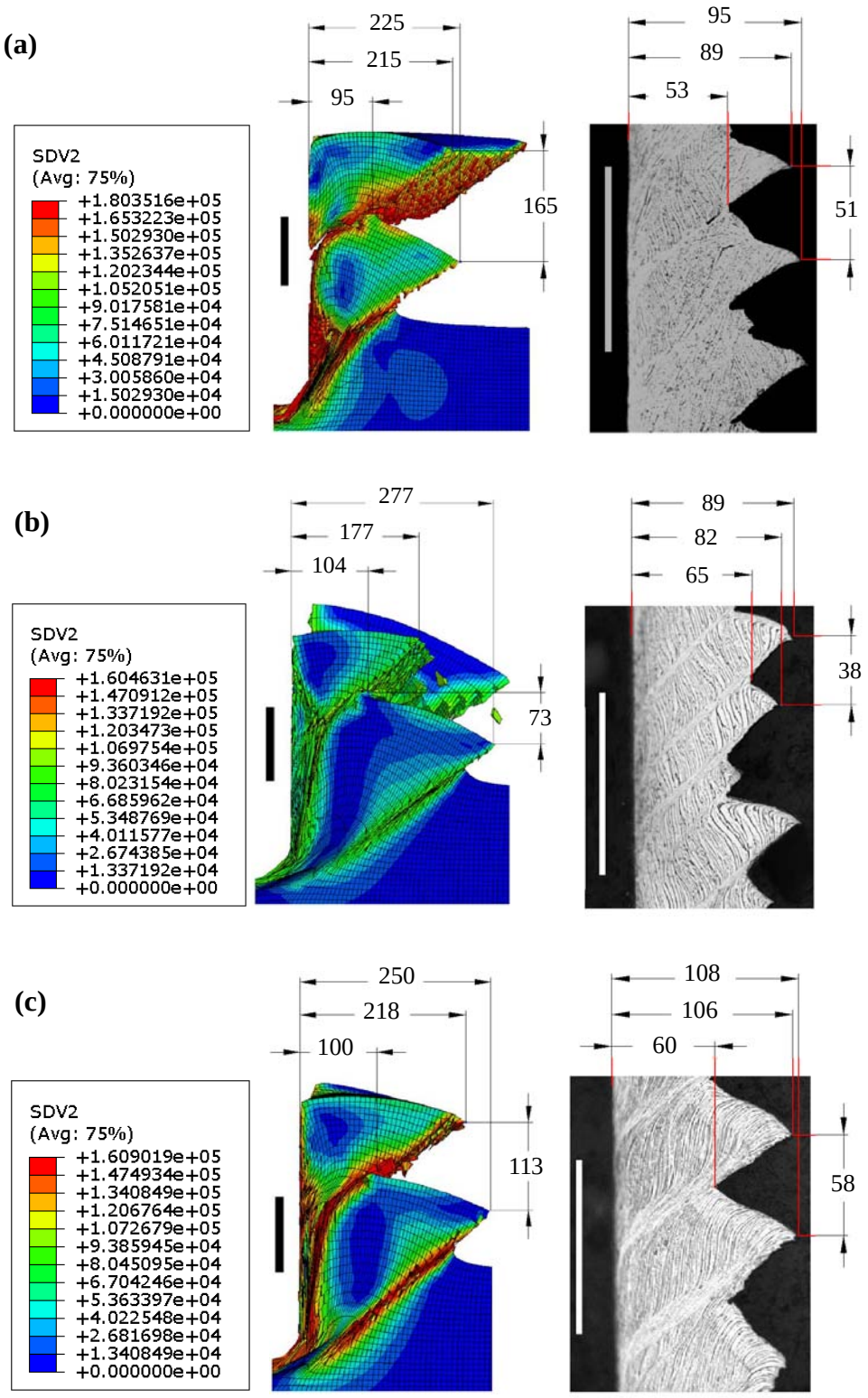

Figure 96. Comparison between experimental and predicted chip morphology (μm) for a feed of 0.125mm/rev and a cutting speed of (a) 120m/min, (b) 90m/min, (c) 60m/min when simulating 3D machining of Ti-6Al-4V with the JC and CL models. The scale bars correspond to 100μm while the variable SDV2 to C_1 in Eq. (46).

Serrated chip formation was patently simulated irrespective of cutting speed, which reflected the morphology of swarf detailed in the optical micrographs.

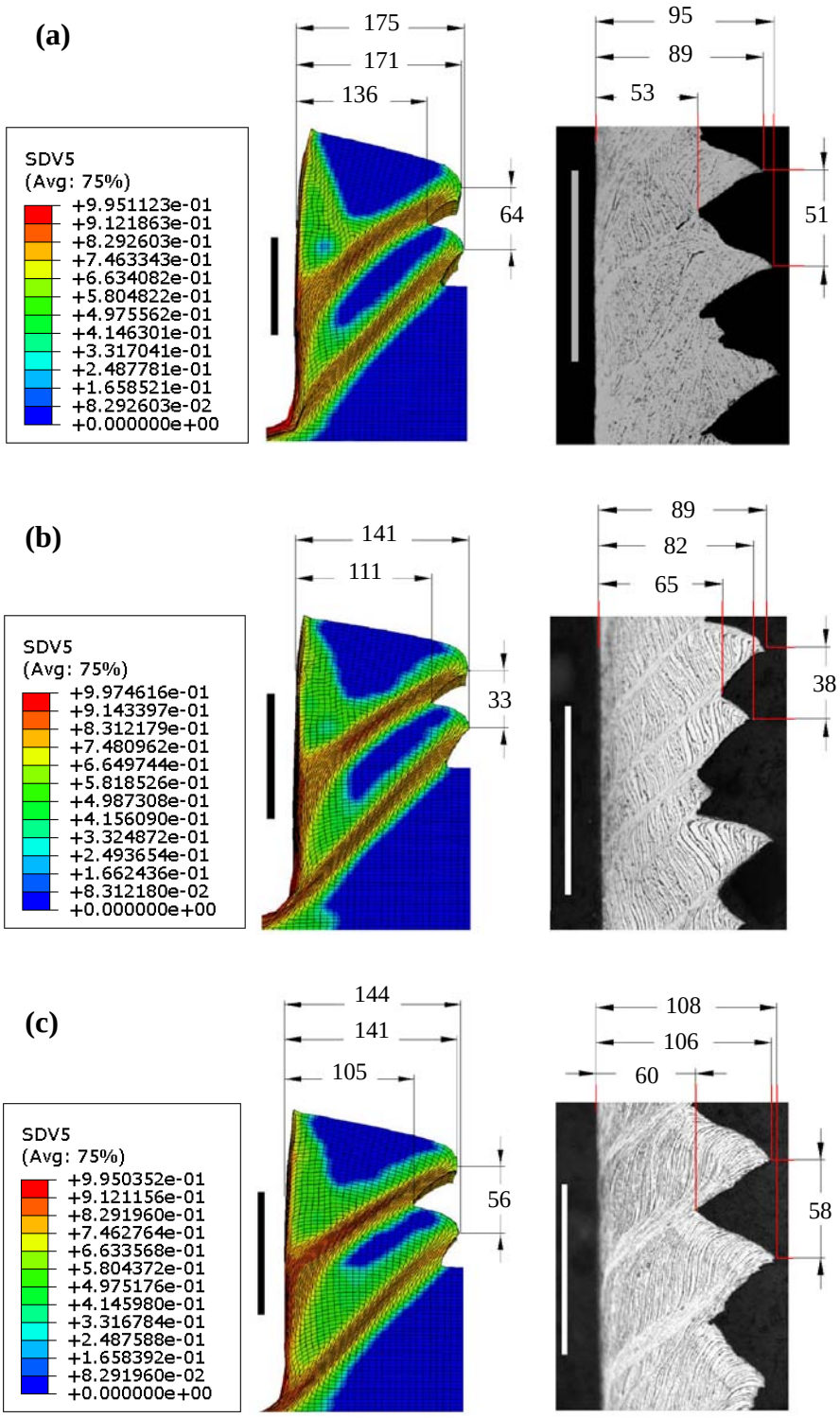

Figure 97. Comparison between experimental and predicted chip morphology (μm) for a feed of 0.125mm/rev and a cutting speed of (a) 120m/min, (b) 90m/min, (c) 60m/min when simulating 3D machining of Ti-6Al-4V with the JC and RWM models. The scale bars correspond to 100μm while the variable SDV5 to D^{α} in Eq. (49).

As commented before and seen more in detail here, the predicted chips were discontinuous with premature separation of the segments along the shear bands, which suggests that the CL damage model specified requires further refinement in order to improve the accuracy of the simulations. Furthermore, the mismatch between all the predicted and experimental chip features was with no doubt considerable, with overall dimensions of the former being roughly twice the size of the latter.

The RWM damage model on the contrary, provided a better accuracy with regard to chip pitch, valley and peak for all machining conditions simulated as observed in Figure 97, however such values were still overestimated and comprised a considerable error of 50% approximately. As well evidenced from the plotted images when compared to the etched micrographs, the adiabatic shear bands were accurately predicted though they were slightly thicker than their experimental counterparts. In addition, the maximum values of the variable SDV5 which corresponded to D^a in Eq. (49) were initially encountered at the tool tip with likely inference along the tool-chip interface.

5.3.2.2 Cutting forces

The comparison between experimental forces and numerical predictions was made by averaging the cutting and thrust (feed) forces at steady state. Table 26 summarises the experimental and predicted cutting and thrust forces resulting from the FE simulations carried out when the CL damage criterion was utilised.

Feed (mm/rev)	**0.125**		
Cutting speed (m/min)	**60**	**90**	**120**
Experimental tangential force (N)	143	138	132
ABAQUS prediction (N)	342.1 (139%)	347.3 (151%)	350.7 (166%)
Experimental feed force (N)	55	52	48
ABAQUS prediction (N)	217.1 (295%)	226.4 (335%)	216 (350%)

Table 26. Comparison between averaged experimental and predicted forces including error deviation when simulating 3D machining of Ti-6Al-4V with the JC and CL models.

As seen from the table, cutting and feed forces were overestimated by a substantial percentage of 152% and 327% respectively in average. This was most likely due to the insufficient both strain and thermal softening effects had on the constitutive response of the alloy. Although the selection of different JC constants that are available in the literature may have a quantifiable effect on the prediction of forces, the high discrepancies encountered here

are believed to be exclusively because important softening mechanisms were not taken into consideration. Consequently, the effective stresses (and therefore the forces) predicted in this investigation were understandably higher when compared to those found in the experimental orthogonal cutting trials.

Table 27 outlines instead, the experimental and predicted tangential and thrust forces for the different cutting conditions employed when the RWM model was applied. Although the FE simulated forces were still overestimated in all situations, the maximum discrepancy was reduced to an average value of 39% and 100% for cutting and feed components respectively, suggesting that the incorporation of the RWM damage relationship into the 3D FE model was more acceptable and/or reasonable.

Feed (mm/rev)	**0.125**		
Cutting speed (m/min)	**60**	**90**	**120**
Experimental tangential force (N)	143	138	132
ABAQUS prediction (N)	185.8 (30%)	187.9 (36.1%)	200.6 (52%)
Experimental feed force (N)	55	52	48
ABAQUS prediction (N)	95.1 (73%)	99.4 (91.1%)	114.5 (138%)

Table 27. Comparison between averaged experimental and predicted forces including error deviation when simulating 3D machining of Ti-6Al-4V with the JC and RWM models.

5.3.2.3 Workpiece/tool temperature distribution

Figure 98 displays the predicted temperature distribution in both workpiece/chip and tool for the different cutting speeds evaluated following the application of the CL damage model. Tool-chip contact length generally decreased as cutting speed was increased, with corresponding maximum rake face temperatures of up to ~470K when turning at 120m/min. This was typically concentrated along the cutting edge (maximum depth of cut position) with a ‘parabola-like’ temperature distribution pattern extending to the point where the chip loses contact with the tool.

The highest temperatures in the workpiece were recorded along the secondary shear zone primarily due to frictional interactions between the chip and cutting tool surface and secondly, due to excessive plastic deformation in such region. This was estimated to exceed ~1,800K when operating at 120m/min, which was approximately in line with results reported by Sima and Ozel (2010). This confirms that the majority of heat generated remains confined in the chip with greater dissipation of thermal energy through the cutting tool as a result of the higher thermal conductivity in the latter.

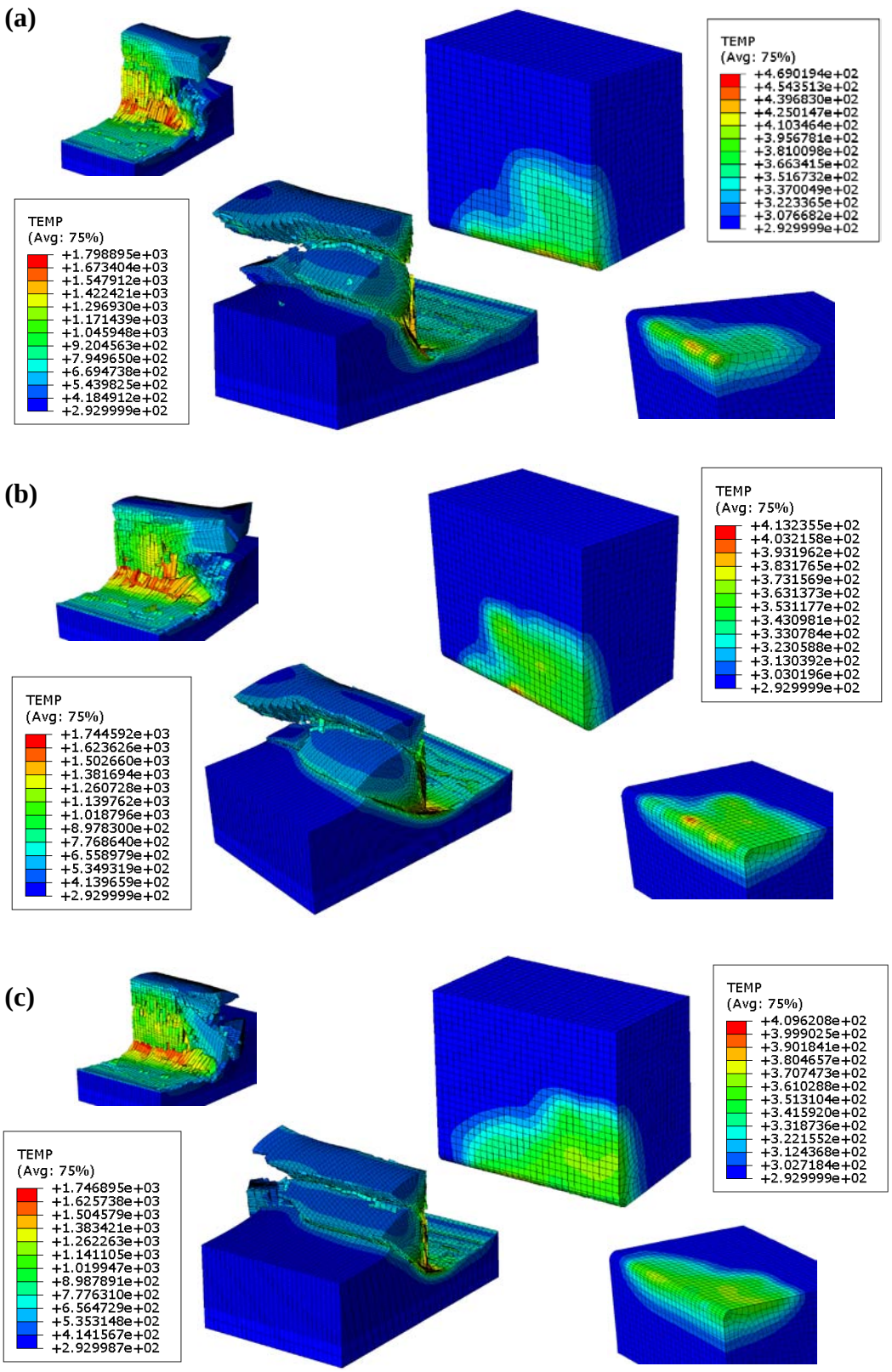

Figure 98. Predicted temperature distribution in tool and workpiece (K) for a feed of 0.125mm/rev and a cutting speed of (a) 120m/min, (b) 90m/min, (c) 60m/min when simulating 3D machining of Ti-6Al-4V with the JC and CL models.

Although the maximum predicted temperatures fluctuated from significant values of ~1,750K to 1,800K for cutting speeds of 60 to 120m/min respectively, their effect in

softening the alloy to obtain precise cutting forces was not really appreciable, strengthening the reasoning that a modified constitutive model which could account for additional softening mechanisms would be more appropriate. Alternatively, predicted process temperatures by making use of the RWM damage model are observed in the images plotted in Figure 99.

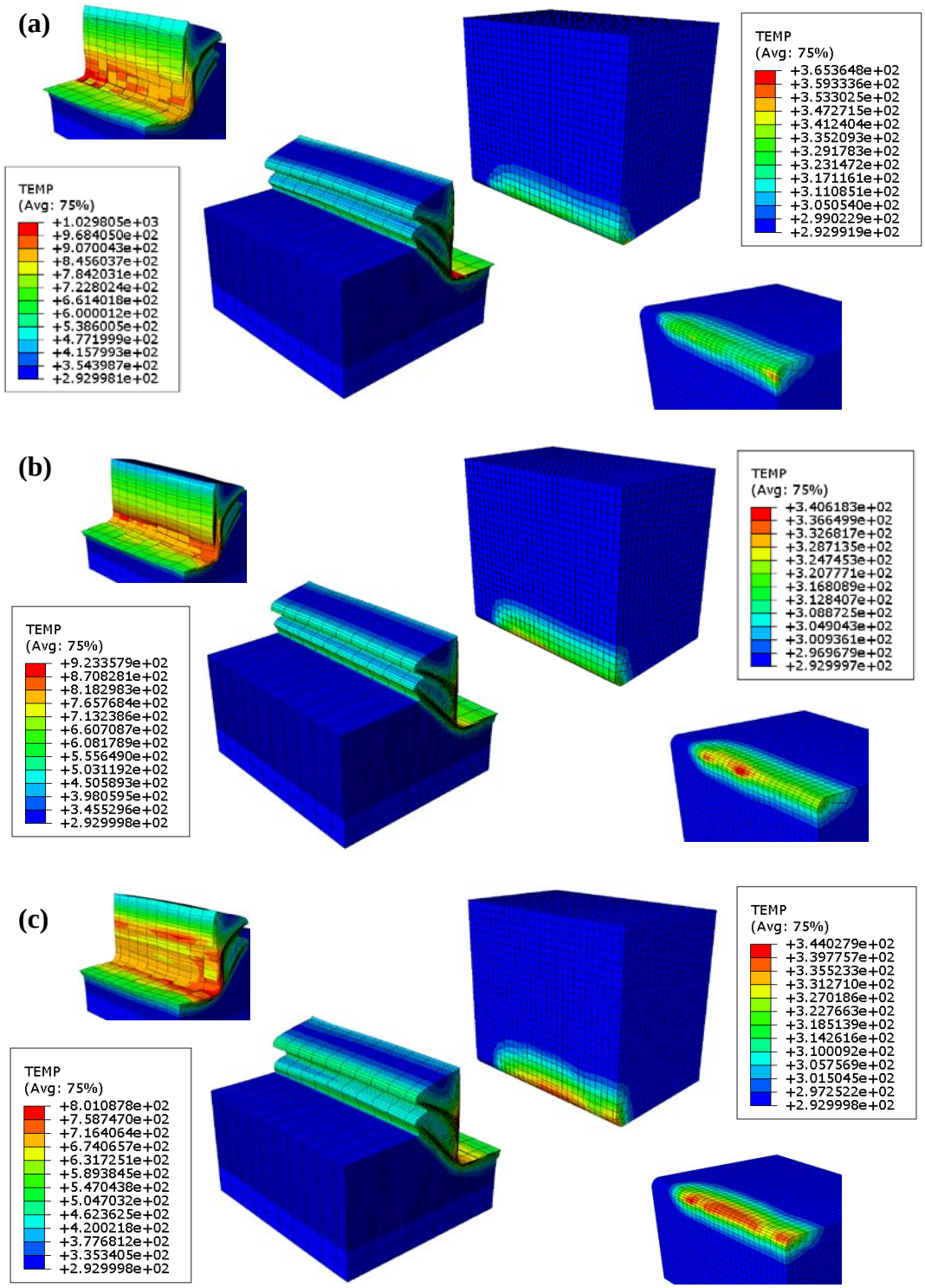

Figure 99. Predicted temperature distribution in tool and workpiece (K) for a feed of 0.125mm/rev and a cutting speed of (a) 120m/min, (b) 90m/min, (c) 60m/min when simulating 3D machining of Ti-6Al-4V with the JC and RWM models.

As it could have been anticipated, peak temperatures were considerably lower than before (~1,000K when machining at 120m/min) because of the marked softening provoked by the RWM model, which decreased the energy that causes temperature rise due to plastic deformation. Although important, frictional effects did not play a notable role in increasing predicted cutting temperatures either, implying that their effect could be assumed as secondary when compared to that the material constitutive response has.

Temperatures in the primary shear zone were generally found to vary from ~600 to 1,000K depending upon the cutting speed and the interval of time evaluated. This, in conjunction with the flow degradation produced by the RWM damage model, was expected to cause thermal and flow softening of the Ti-6Al-4V aerospace alloy respectively, as the material strength typically deteriorates rapidly above temperatures of ~350-400°C, which would explain the observed formation of adiabatic shear bands leading to the continuous serrated chip morphology. Unlike before, temperatures on the tool rake face for all FE simulations were more evenly distributed, in particular with a visible localisation of the maximum values along the cutting edge when cutting at 60m/min. Similarly to what occurred to the workpiece, estimated tool temperatures were lower than those obtained with the CL damage model, showing an average diminution of ~100K in all cases.

5.3.3 2D orthogonal cutting on Inconel 718 with JC/MTS and RWM

5.3.3.1 Chip formation/morphology

Taking into account that the 2D and 3D FE modelling work carried out on Ti-6Al-4V alloy was utilised as a benchmark to evaluate the performance of the CL and RWM damage models for mainstream work on Inconel 718, it was therefore decided to apply the latter in all subsequent simulations to predict chip formation/morphology due to its advantages in terms of chip formation/morphology over the former.

For reasons that remain unclear, all the 2D FE simulations which included the MTS constitutive model aborted in the very beginning, hence only the JC relationship was utilised to make useful comparisons. As such, Figures 100 and 101 show a dimensional assessment of predicted 2D chip profiles (whose Von Mises stress distribution was plotted) together with their experimental etched analogues when the cutting speeds are 300, 250 and 200m/min for feeds of 0.2 and 0.08mm/rev respectively. At the higher feed, predicted chip peaks presented a remarkable correlation with those experimentally obtained, with an average error that barely increased when the cutting speed appreciably decreased.

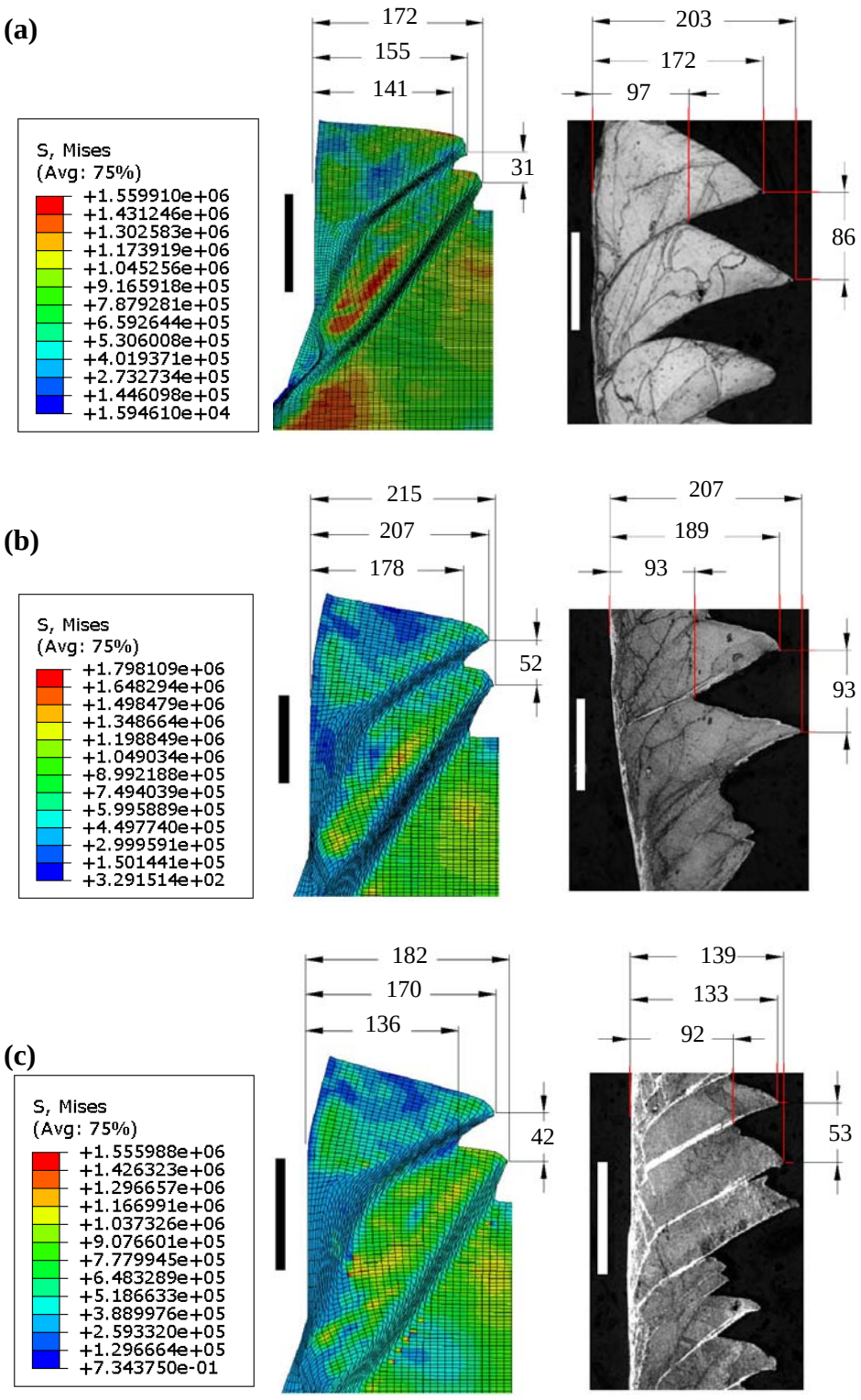

Figure 100. Comparison between experimental and predicted chip morphology (μm) for a feed of 0.2mm/rev and a cutting speed of (a) 300m/min, (b) 250m/min, (c) 200m/min when simulating 2D machining of Inconel 718 with the JC and RWM models. The scale bars correspond to 100μm while the variable S to the Von Mises stress (10^{-3} MPa).

For instance, the first saw-tooth formed when operating at 300m/min had a mismatch of ~10%, which approximately remained constant until it reached a value of ~27% (17% of variation) when the cutting speed decreased to 200m/min (33% of variation).

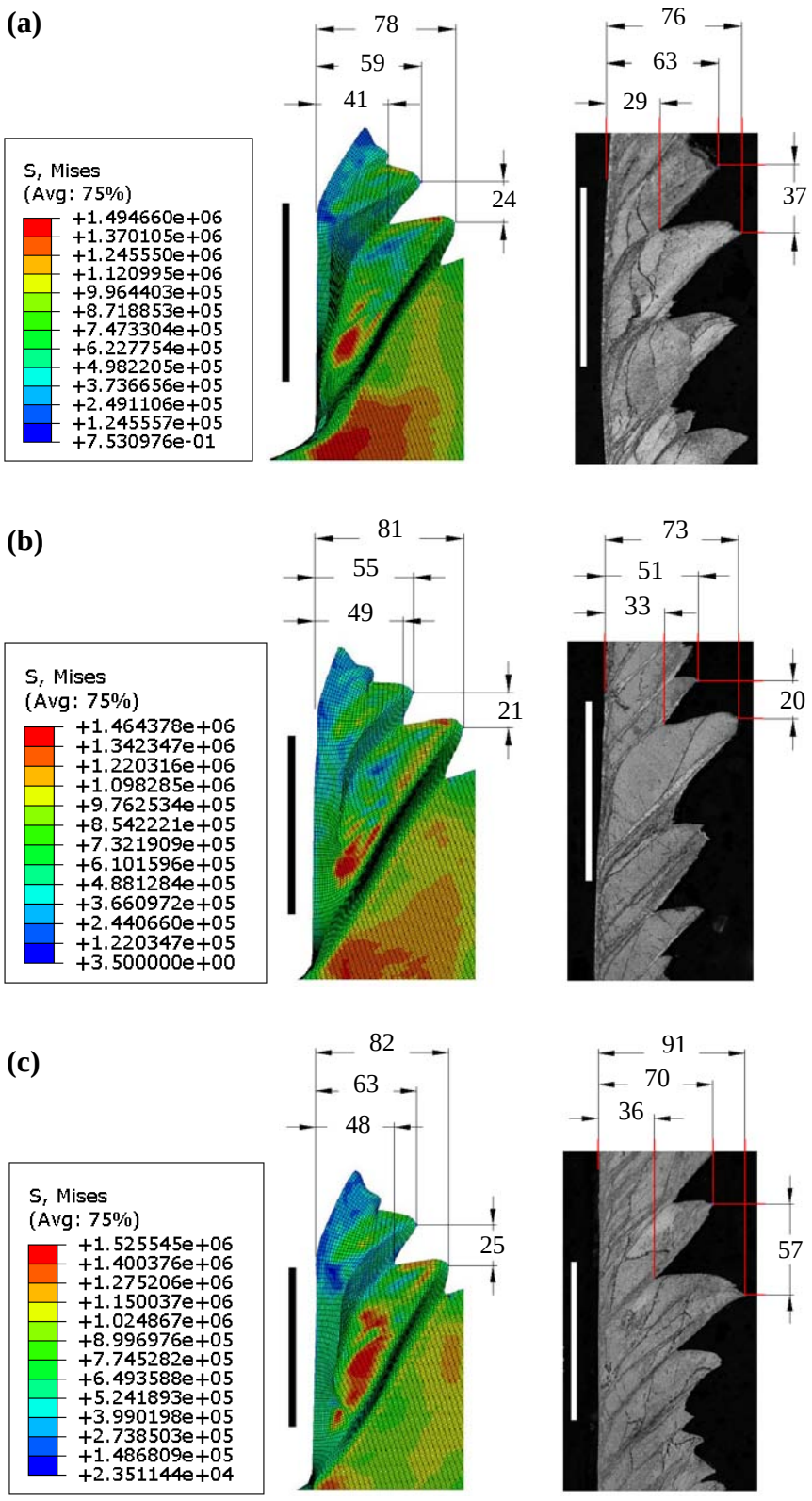

Figure 101. Comparison between experimental and predicted chip morphology (μm) for a feed of 0.08mm/rev and a cutting speed of (a) 300m/min, (b) 250m/min, (c) 200m/min when simulating 2D machining of Inconel 718 with the JC and RWM models. The scale bars correspond to 100μm while the variable S to the Von Mises stress (10^{-3} MPa).

The accuracy of the predictions augmented when the feed was 0.08mm/rev, in which case the error varied roughly from 3% to 10% when the cutting speed decreased from

300 to 200m/min. A comparable trend could be established for the second predicted saw-tooth in this regard, however the same tendency does not apply when the chip valley is under study, neither when the cutting speeds nor the feeds varied. In general terms when considering this characteristic aspect of the chip, the disparity between the numerical results and those experimental had a mean value of ~40%, with peaks of ~90% in a very few cases. Chip pitch for a feed of 0.2mm/rev on the other hand, evidenced a growing exactness when the maximum cutting speed converged to 200m/min, whose value involved an accuracy of ~80%. An equivalent circumstance (though comprising a deviation of 5%) was achieved when the cutting speed attained the intermediate value of 250m/min, however for a feed of 0.08mm/rev. All these results seemed to postulate that the precision of the numerical predictions is related to the feed, provided that the former increases when the latter decreases.

Irrespective of the cutting speed under investigation, the thickness of the predicted adiabatic shear bands appeared to be thinner for higher feeds, which was more in line with experimental findings. In spite of well declaring that the workpiece element size might influence the prediction of such feature, it could also be presumed (perhaps with a stronger argument in hand) that the combined thermal and flow softening effects were not sufficient to cause the essential element degradation that would lead beyond question to paper-thin shear bands.

5.3.3.2 Cutting forces

Table 28 sums up the experimental and predicted tangential and feed forces for cutting velocities of 200, 250 and 300m/min at feeds of 0.2 and 0.08mm/rev respectively.

Feed (mm/rev)	**0.2**			**0.08**		
Cutting speed (m/min)	**200**	**250**	**300**	**200**	**250**	**300**
Experimental tangential force (N)	370	390	405	200	260	195
ABAQUS prediction (N)	282.9 (30.8%)	288.3 (35.3%)	307.9 (31.5%)	160.4 (19.8%)	156.8 (39.7%)	149.9 (23.1%)
Experimental feed force (N)	140	150	170	100	125	110
ABAQUS prediction (N)	116.6 (20%)	125.1 (20%)	121.9 (39.5%)	96.4 (3.6%)	100.3 (19.8%)	102.1 (7.2%)

Table 28. Comparison between averaged experimental and predicted forces including error deviation when simulating 2D machining of Inconel 718 with the JC and RWM models.

In accordance with results documented succeeding the experimental trials, forces increased as machining progressed until a sharp drop of ~10% was evidenced, corresponding to initiation of saw-tooth chip profile. In all cutting situations that comprised a feed of 0.2mm/rev, predicted tangential forces were underestimated, highlighting that their accuracy increased when the cutting speed decreased (the best estimation having a ~31% error for a cutting speed of 200m/min). Interestingly, an opposite trend was found for the predicted feed forces, which were not only overestimated in all cases, but also comprised better predictions when the cutting speed increased (in which case the best estimation involved an error of ~20%, also corresponding to a cutting speed of 200m/min). All in all, estimated feed forces presented a superior accuracy (~26.5% in average) when contrasted to their tangential analogous components (~32.5% in average), findings that suggest that the suppositions realised when developing the 2D FE model were adequate/acceptable.

5.3.3.3 Workpiece/tool temperature distribution

The predicted tool and workpiece/chip temperature distribution for the different cutting speeds evaluated following the employment of the JC and RWM models is shown in Figures 102 and 103, each of them corresponding to a respective feed rate of 0.2 and 0.08mm/rev.

Although forecasted maximum temperatures were as high as ~1,200 and ~890K for the feeds mentioned above respectively (when cutting at 300m/min) and augmented when the cutting speeds did so, they seemed not to rise plentifully to more adequate values that might be expected after operating at such excessive machining conditions (>1,400K). Nonetheless, the greatest temperatures in the workpiece were highly confined in the tool-chip interface as well as in the tool tip for all cutting speeds and either feed considered. A more evident thermal distribution was seen concentrated along the adiabatic shear bands when cutting at 0.2mm/rev than when doing so at 0.08mm/rev, however numerical predictions in overall conveyed the impression of being representative of the actual machining operation, as due to the elevated plastic straining in conjunction with frictional effects, (high) temperatures were plausible to be found in such particular regions.

Thermal allocation in the tool on the other hand, showed an expanding domain when reducing the feed from 0.2 to 0.08mm/rev, mostly because the period of time involved in removing the same amount material was reduced in the former situation.

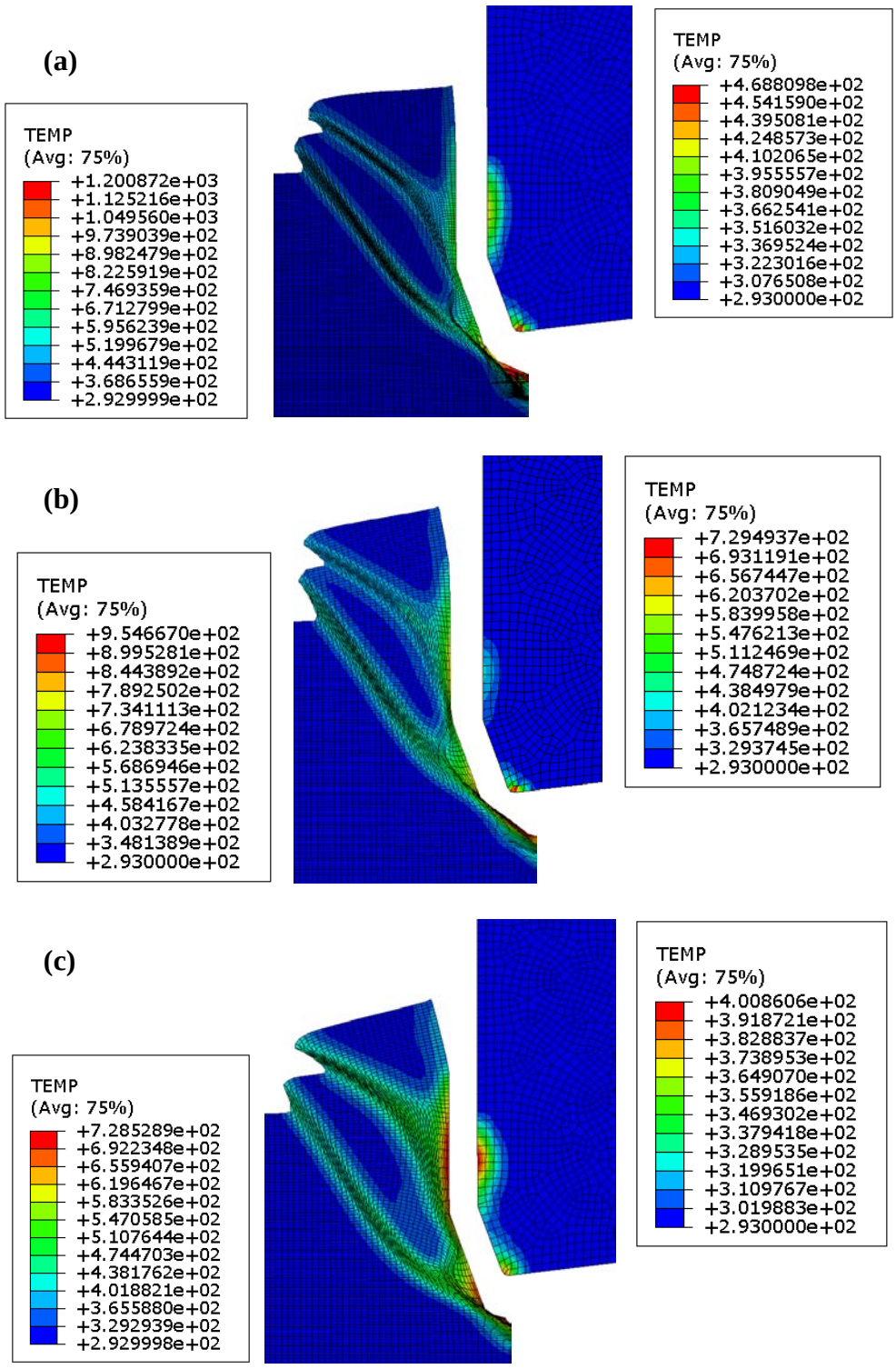

Figure 102. Predicted temperature distribution in tool and workpiece (K) for a feed of 0.2mm/rev and a cutting speed of (a) 300m/min, (b) 250m/min, (c) 200m/min when simulating 2D machining of Inconel 718 with the JC and RWM models.

In agreement with predictions made for the workpiece, locations where the maximum temperatures in the tool were encountered, oscillated between the cutting tip and the rake face (tool-chip interface) with peak values of ~470K and ~400K for feeds of 0.2 and 0.08mm/rev respectively.

The computations, despite the fact that the thermal conductivity of the tool is greater than that of the aerospace superalloy (38 compared to 11.4W/mK) and it would in consequence dissipate heat faster, still evidenced the previous inference that temperatures should have been higher.

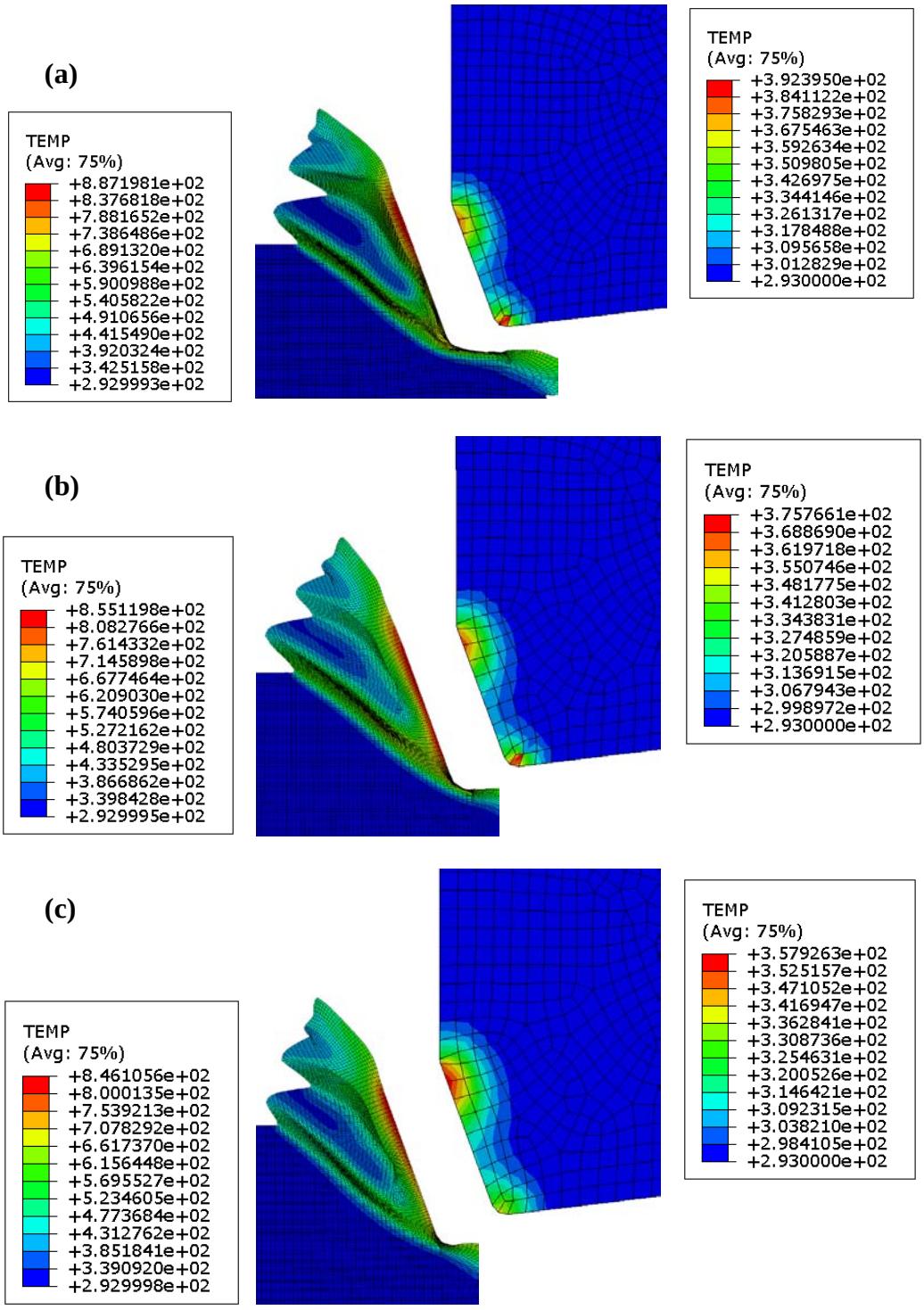

Figure 103. Predicted temperature distribution in tool and workpiece (K) for a feed of 0.08mm/rev and a cutting speed of (a) 300m/min, (b) 250m/min, (c) 200m/min when simulating 2D machining of Inconel 718 with the JC and RWM models.

5.3.4 3D orthogonal cutting on Inconel 718 with JC/MTS and RWM

5.3.4.1 Chip formation/morphology

Figures 104 and 105 display views of the workpiece material's Von Mises stress distribution in a three dimensional environment observed from two angles when the JC viscoplastic model is employed for feeds of 0.2 and 0.08mm/rev respectively. In all circumstances, it is clearly seen the saw-tooth aspect of the chip predicted by the software while the formation of a large burr is also noticed.

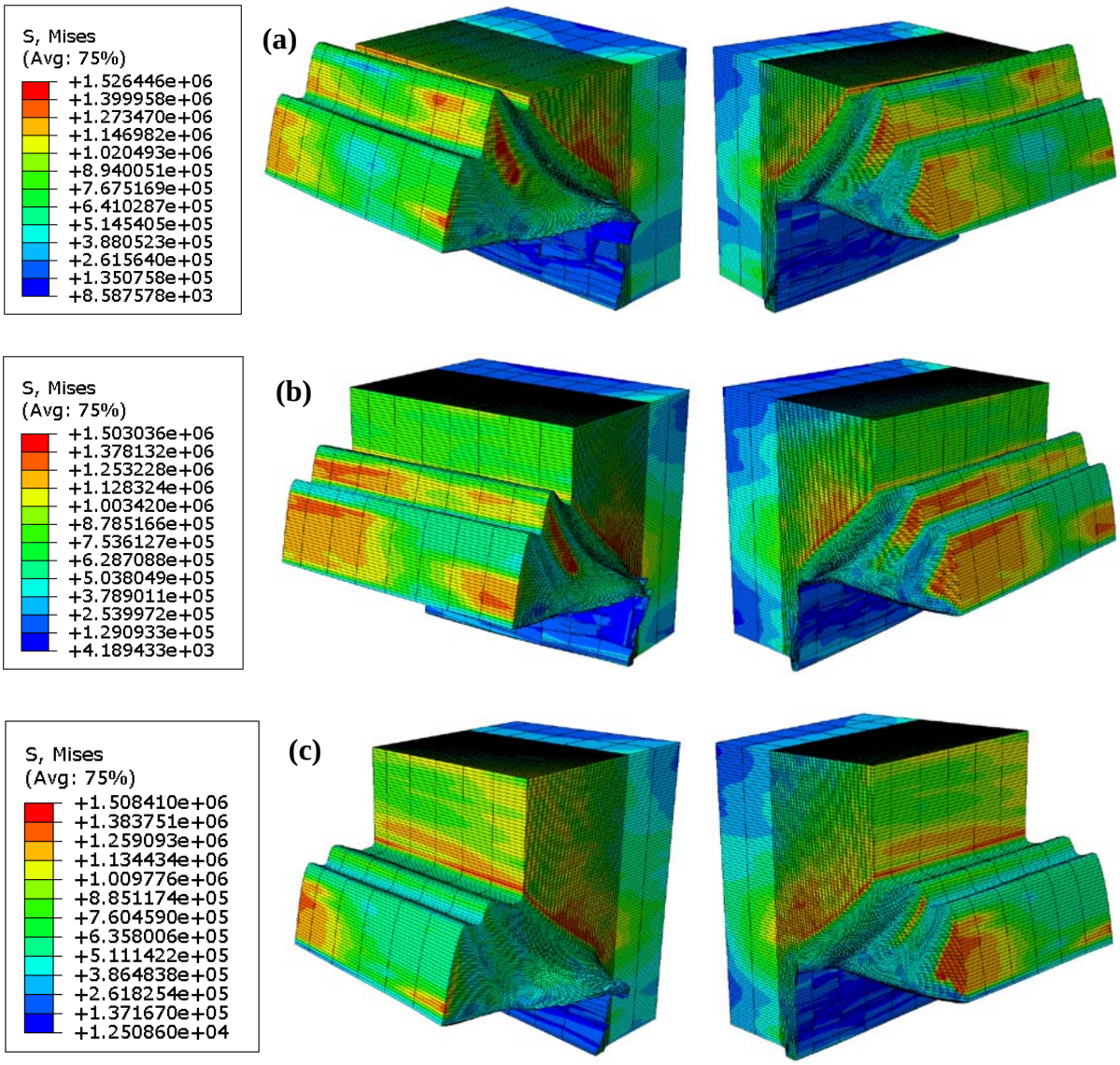

Figure 104. 3D view images of Von Mises stress distribution in workpiece (10^{-3}MPa) for a feed of 0.2mm/rev and a cutting speed of (a) 300m/min, (b) 250m/min, (c) 200m/min when simulating 3D machining of Ti-6Al-4V with the JC and RWM models.

A very particular discovery which deserves to be highlighted when operating at the higher feed is that predicted chip formation mechanism seems to be directly influenced by the

cutting speed, with the former being accelerated when the latter decreases, as in theory there would be more time for such an event to take place. This trend however, was not repeated when the feed decreased to 0.08mm/rev, suggesting that tool geometry together with variable machining parameters are likely to modify tendencies and as such, are variables that need to be investigated more in depth, either individually or coupled.

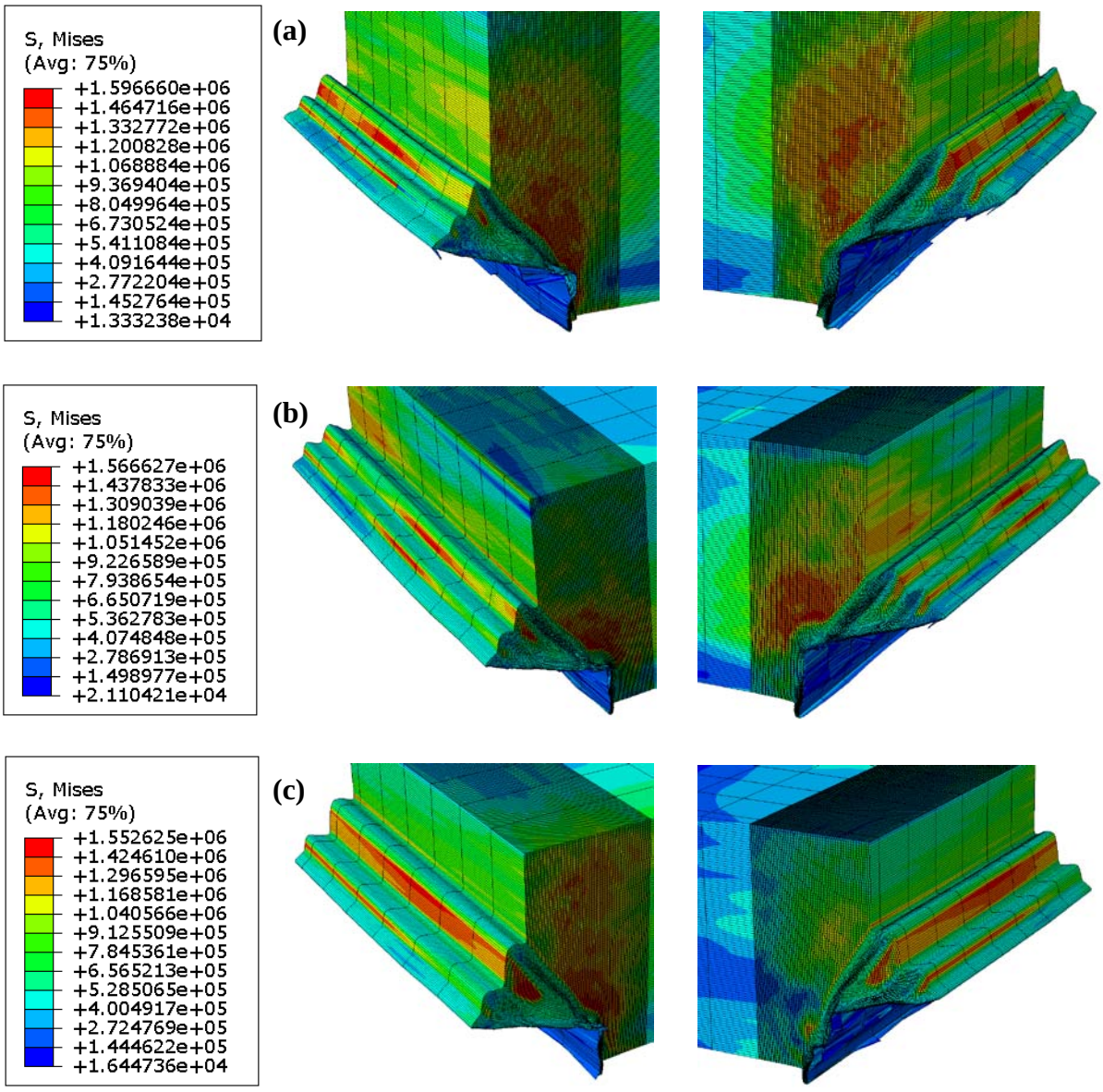

Figure 105. 3D view images of Von Mises stress distribution in workpiece (10^{-3}MPa) for a feed of 0.08mm/rev and a cutting speed of (a) 300m/min, (b) 250m/min, (c) 200m/min when simulating 3D machining of Ti-6Al-4V with the JC and RWM models.

Chip serration was predicted in all cases in line with previous 3D FE simulations performed when machining Ti-6Al-4V alloy, confirming not only the versatility of the RWM damage model in dealing with different materials, but also its intrinsic robustness which is based on energy considerations. Flow softening, which commands saw-tooth chip formation

and leads to damage concentrated at the tool tip, is an evident consequence of the physics of the cutting process and was consequently reproduced in the FE simulations. According to the numerical predictions, the machined surface persisted soft irrespective of cutting speed and feed whereas regions belonging to the chip exhibited a mixed hardened-softened contour as deduced from the images.

Similarly, Figures 106 and 107 show the workpiece Von Mises stress distribution for all cutting conditions stated before, but when the MTS constitutive model is utilised instead.

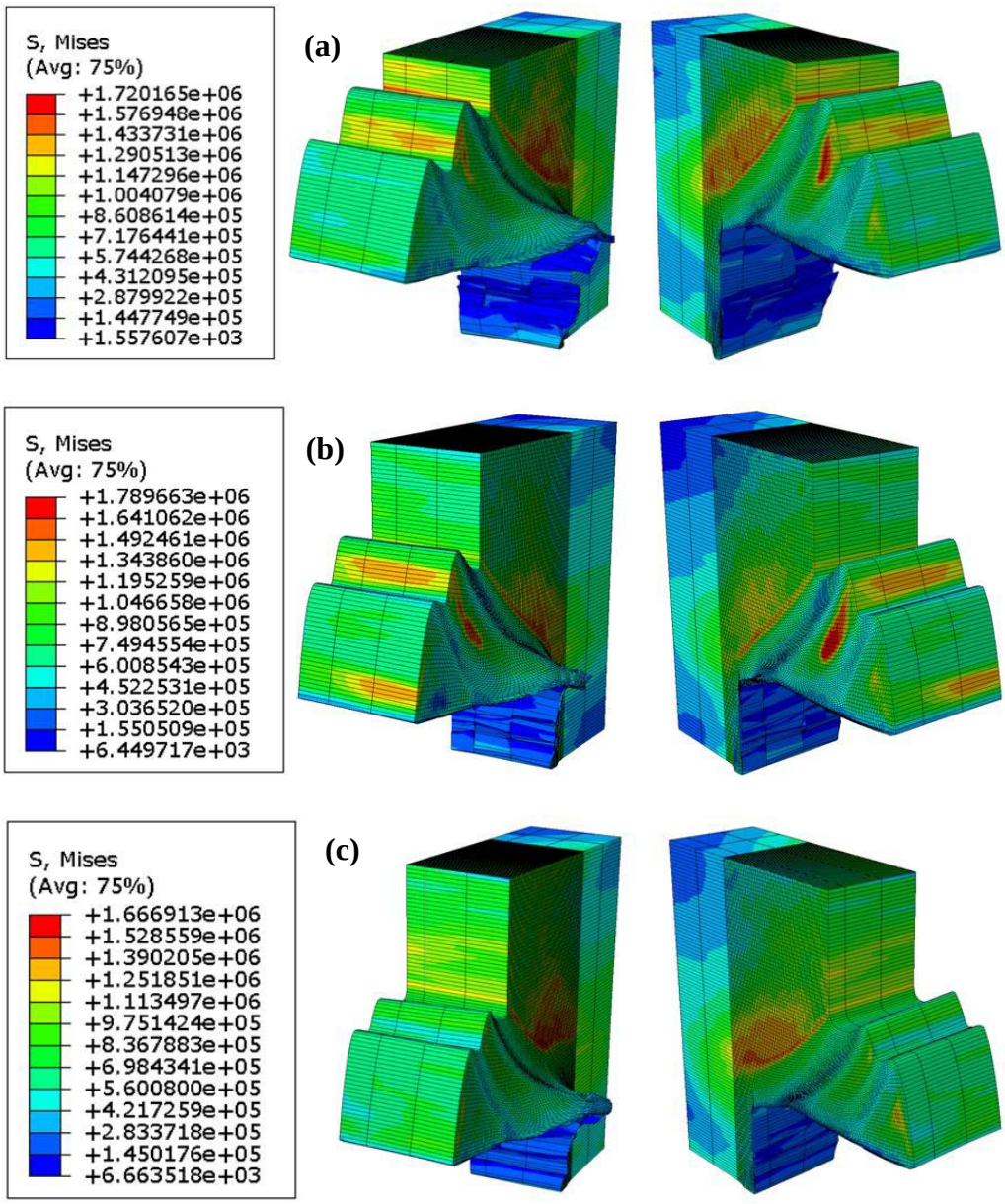

Figure 106. 3D view images of Von Mises stress distribution in workpiece (10^{-3}MPa) for a feed of 0.2mm/rev and a cutting speed of (a) 300m/min, (b) 250m/min, (c) 200m/min when simulating 3D machining of Ti-6Al-4V with the MTS and RWM models.

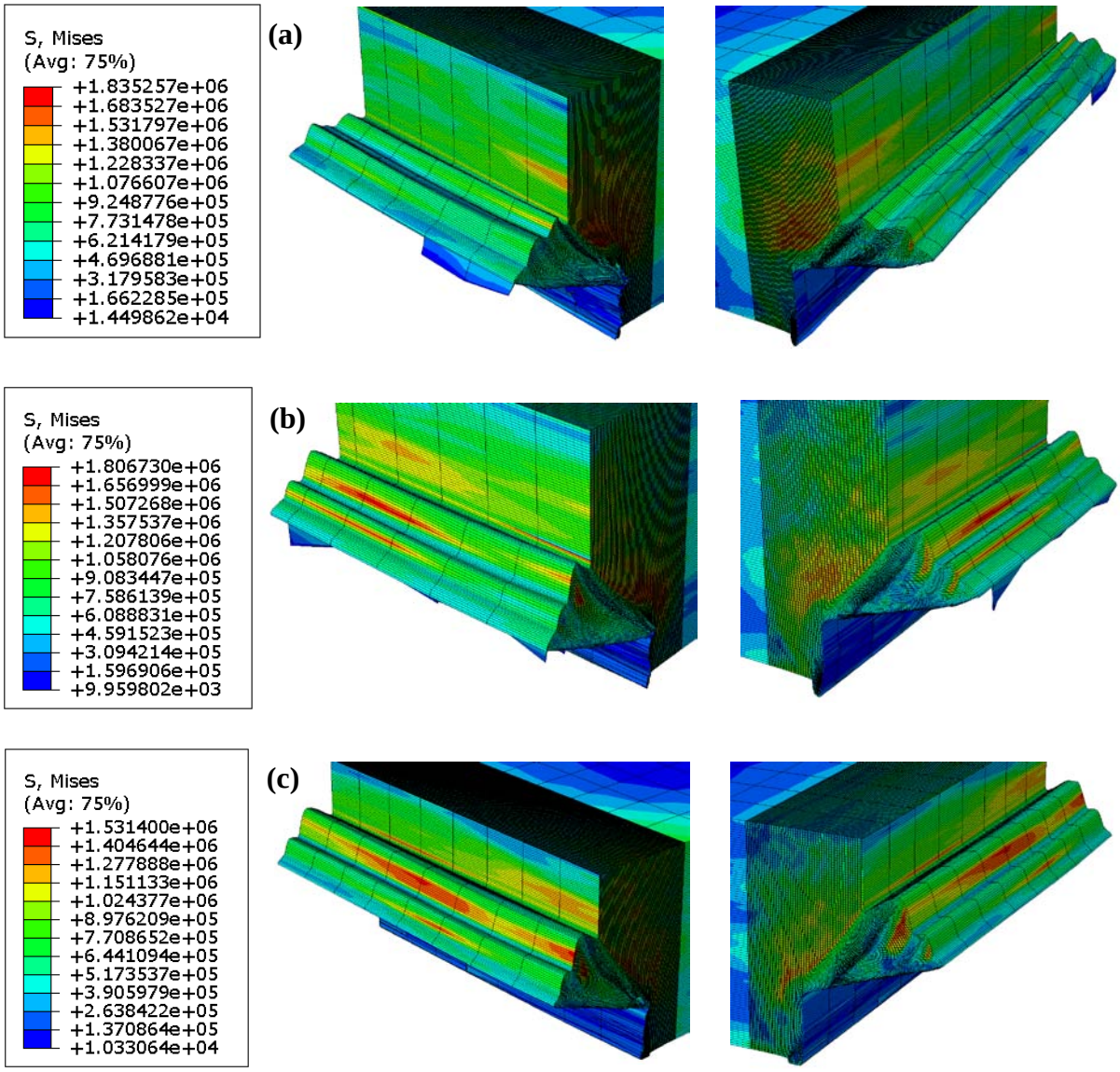

Figure 107. 3D view images of Von Mises stress distribution in workpiece (10^{-3}MPa) for a feed of 0.08mm/rev and a cutting speed of (a) 300m/min, (b) 250m/min, (c) 200m/min when simulating 3D machining of Ti-6Al-4V with the MTS and RWM models.

For all cutting speeds under analysis, predicted chips were moderately softened in regions that corresponded to the adiabatic shear bands formed while in their surrounding neighbourhoods, estimated stresses were found to reach their maximum values (~1,725MPa for both feeds). As before, the tool-chip interface was one of the areas in which the greatest level of softening was encountered (~4.9MPa and ~11.5MPa in average for feeds of 0.2 and 0.08mm/rev respectively), suggesting that not only damage mechanisms took place following the machining process in the region, but also elevated and highly localised temperatures that contributed to attain such end. Figures 108 and 109 present a 2D view of the predicted chip morphology and corresponding cross sectional micrographs of chips obtained from the cutting experiments for feed rates of 0.2 and 0.08mm/rev respectively whenever the JC relationship is used.

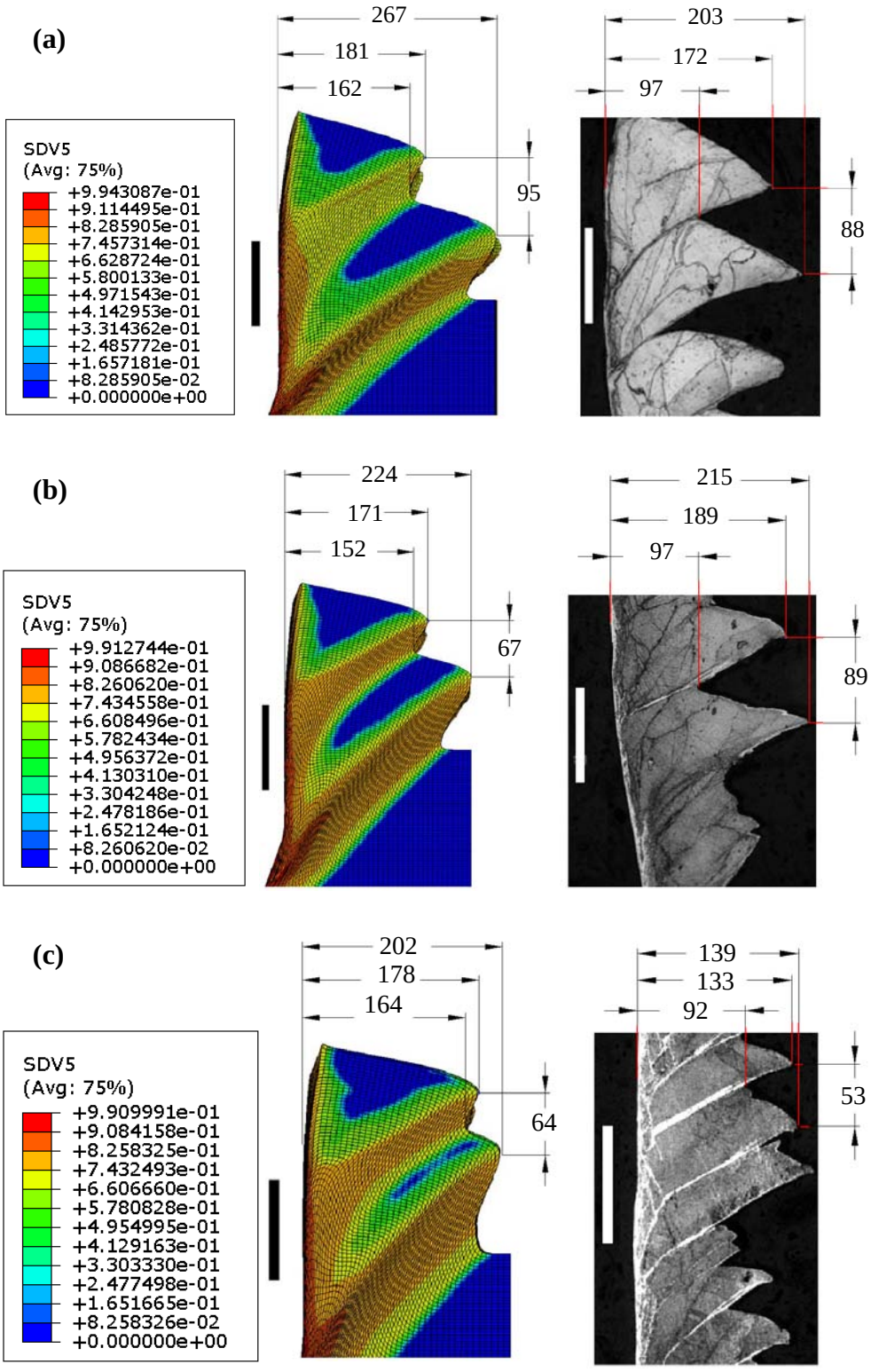

Figure 108. Comparison between experimental and predicted chip morphology (μm) for a feed of 0.2mm/rev and a cutting speed of (a) 300m/min, (b) 250m/min, (c) 200m/min when simulating 3D machining of Inconel 718 with the JC and RWM models. The scale bars correspond to 100μm while the variable SDV5 to D^{α} in Eq. (49).

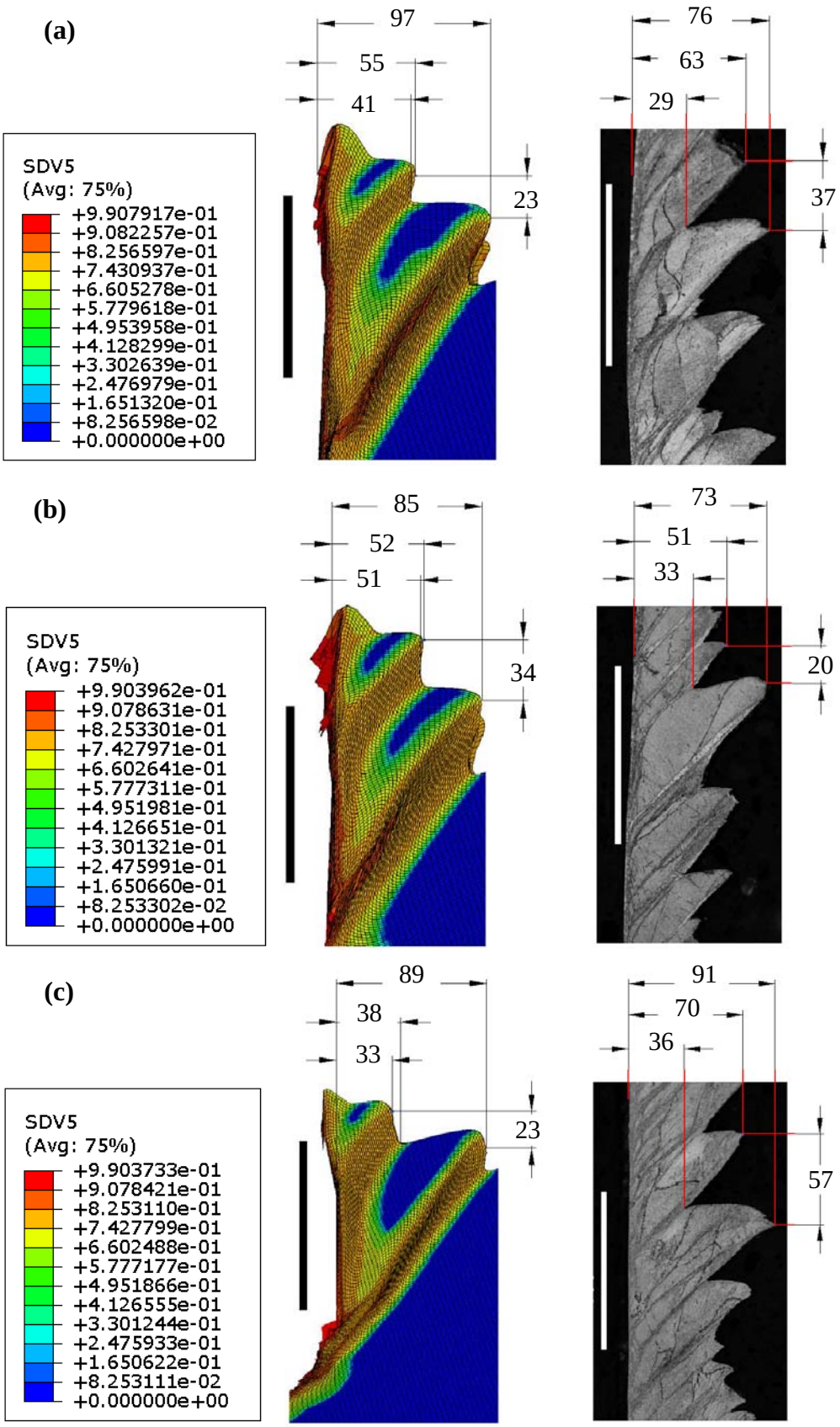

Figure 109. Comparison between experimental and predicted chip morphology (μm) for a feed of 0.08mm/rev and a cutting speed of (a) 300m/min, (b) 250m/min, (c) 200m/min when simulating 3D machining of Inconel 718 with the JC and RWM models. The scale bars correspond to 100μm while the variable SDV5 to D^a in Eq. (49).

The most accurate numerical estimations when dimensions of the chip are being considered at the higher feed, corresponded to a cutting speed of 250m/min. Both first and second predicted chip peaks together with the pitch concerned acceptable mean errors of ~7.5% and ~25% respectively, however chip valley (still) showed an overestimation of ~60% when compared to experimental results. An equivalent situation occurred when the feed was reduced to 0.08mm/rev, in which case the best FE predictions were attained. Shear bands, in all cases, were reasonably originated (with a higher degree of damage encountered at the tool tip and the tool-chip interface) though their thickness was not in complete accordance with findings obtained from cutting trials. This lack of damage/flow softening concourse does not seem to be motivated by the mesh size (which, for obvious reasons, was substantially fine for a feed of 0.08mm/rev), instead it is believed that more cogent workpiece material degradation mechanisms were necessitated.

A relevant prediction common to all FE simulations is that the length of the peak of the second saw-tooth was greater than the first one, which was in total agreement with its respective experimental analogue. The mismatch, however, presented an increasing value when the cutting speed increased for all feeds under study.

Similar results in terms of predicted chip morphology were retrieved when the MTS constitutive model was adopted instead. Chip pitch, valley and peak features were measured indirectly following the FE simulations and etching operations respectively for all cutting conditions, with the results plotted as it can be observed in Figures 110 and 111.

In this scenario therefore, serrated chip formation was simulated in all cases irrespective of cutting speed, which reflected the morphology of swarf detailed in the optical etched micrographs. A meticulous examination of both predicted and experimental chip dimensional characteristics was performed in order to evaluate quantitatively the forecasts given by both the MTS and RWM constitutive and damage models respectively.

For a feed of 0.2mm/rev, the predicted chip pitch found its best estimation when the cutting speed was 300m/min (~2% error), whereas the highest error in doing so was correlated with a cutting speed of 250m/min (~30% error). With regard to chip valley, experimental results suggest that its value remains approximately constant (~95μm in average) irrespective of the cutting speed employed, trend that was closely followed by the simulated findings (~145μm in average). However the accuracy when predicting this chip dimensional feature was low with an error ~30%, implying that the RWM damage model should have provoked a higher degree of softening in the shear bands in order to delay the appearance of the second saw-tooth. Concerning the size estimation of peaks that could be individualised from the

simulated chips, results show that in all cases the dimension of the first peak was lower than the second, which was in agreement with experimental findings.

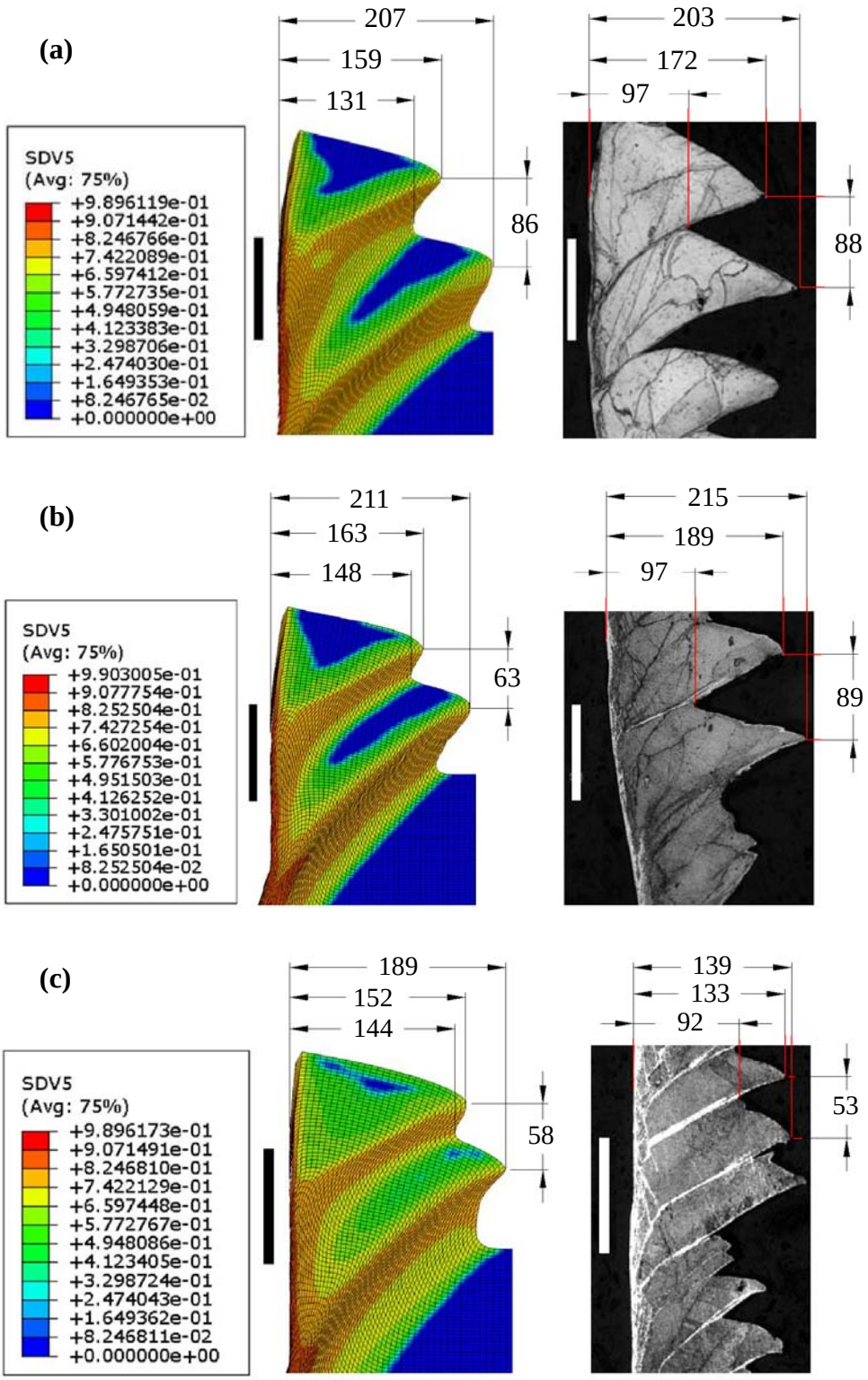

Figure 110. Comparison between experimental and predicted chip morphology (μm) for a feed of 0.2mm/rev and a cutting speed of (a) 300m/min, (b) 250m/min, (c) 200m/min when simulating 3D machining of Inconel 718 with the MTS and RWM models. The scale bars correspond to 100μm while the variable SDV5 to D^a in Eq. (49).

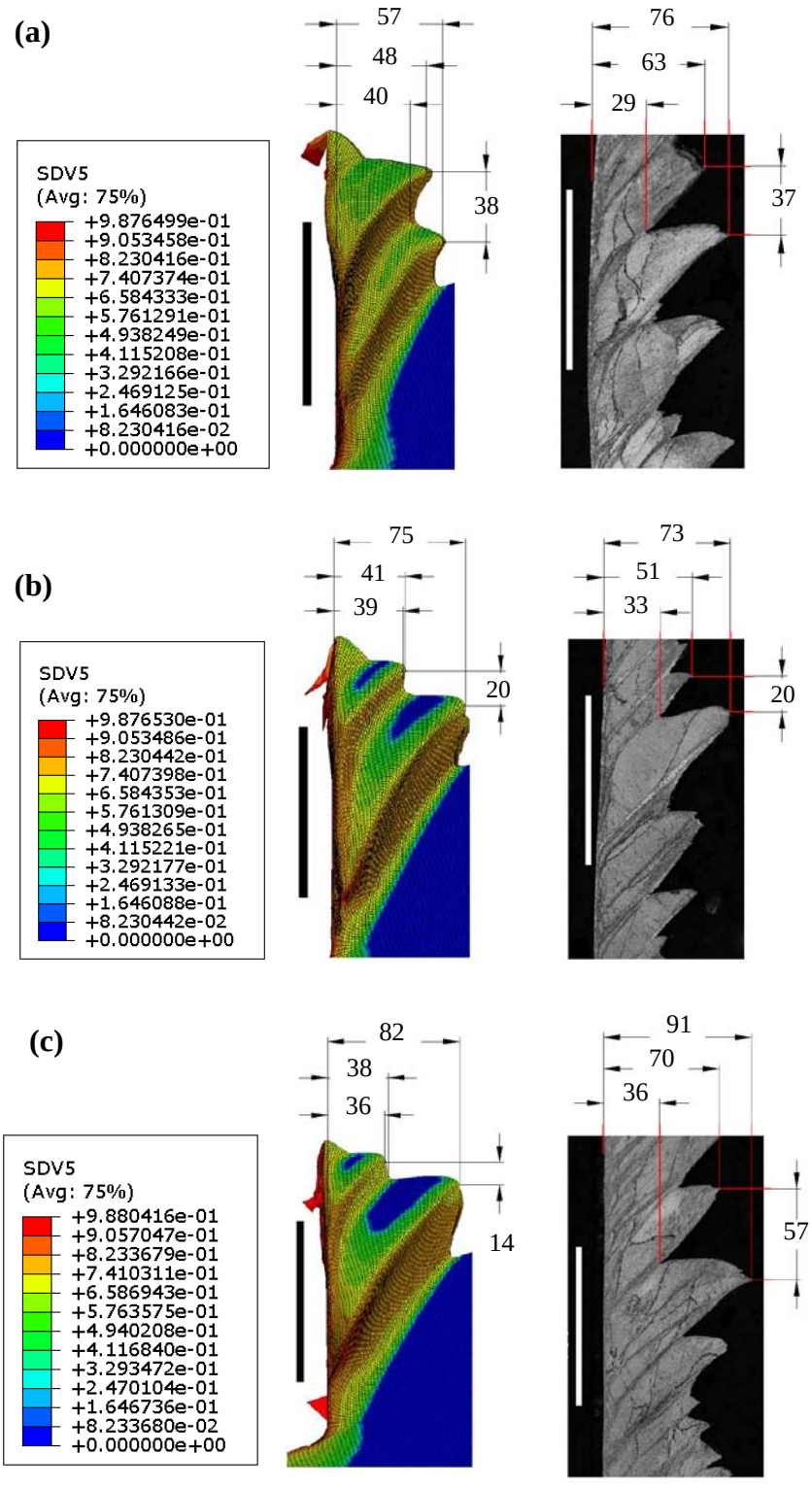

Figure 111. Comparison between experimental and predicted chip morphology (μm) for a feed of 0.08mm/rev and a cutting speed of (a) 300m/min, (b) 250m/min, (c) 200m/min when simulating 3D machining of Inconel 718 with the MTS and RWM models. The scale bars correspond to 100μm while the variable SDV5 to D^a in Eq. (49).

However the exactness of the predictions diminished from the first to the second saw-tooth, with average values of ~159μm (165μm experimental) and ~202μm (186μm experimental), that involved mean errors of ~4 and ~9% respectively.

When the feed decreased to 0.08mm/rev, alike conclusions can be withdrawn with regard to chip size in general. Qualitatively speaking, the fidelity of predictions appeared to be higher when the cutting speed was 300m/min than when it was reduced to 200m/min. When numbers were associated with chip features though, the best estimations were obtained when the orthogonal turning was conducted at 250m/min, which comprised accuracies of 80, 97 and 85% for the first and second chip saw-tooth and chip valley respectively (the comparison between predicted and experimental chip pitch was neglected as their values were, strikingly, equal).

Interestingly, in neither feed evaluated the predicted adiabatic shear bands were as narrow as those found experimentally, therefore it was expected a low correlation between simulated and etched swarf valleys. In summary, the estimations given by the RWM damage model gave the impression to be reliable not only for predicting adiabatic shear banding occurrence, but also for capturing with an acceptable level of accuracy the dimensional features of the bands. Nevertheless it is believed that narrower shear bands should have been simulated leading to a more defined chip serrated morphology which was observed in the etched micrographs.

5.3.4.2 Cutting forces

When characterising the material behaviour by making use of the JC model, Table 29 reports the experimental and predicted tangential and feed forces when the cutting velocity and feed increased from 200 to 300m/min and 0.08 to 0.2mm/rev respectively. When the MTS constitutive model is utilised instead, the results are summarised in Table 30.

Feed (mm/rev)	**0.2**			**0.08**		
Cutting speed (m/min)	**200**	**250**	**300**	**200**	**250**	**300**
Experimental tangential force (N)	370	390	405	200	260	195
ABAQUS prediction (N)	319.9 (15.6%)	329.6 (18.3%)	335.4 (20.8%)	133.4 (33.3%)	142.6 (45.1%)	148.8 (23.7%)
Experimental feed force (N)	140	150	170	100	125	110
ABAQUS prediction (N)	150.2 (7.1%)	155.2 (3.5%)	158.1 (7.5%)	78.8 (21.2%)	85.9 (31.3%)	88.8 (19.3%)

Table 29. Comparison between averaged experimental and predicted forces including error deviation when simulating 3D machining of Inconel 718 with the JC and RWM models.

Feed (mm/rev)	**0.2**			**0.08**		
Cutting speed (m/min)	**200**	**250**	**300**	**200**	**250**	**300**
Experimental tangential force (N)	370	390	405	200	260	195
ABAQUS prediction (N)	350.8 (5.2%)	361 (7.4%)	372.7 (8%)	151.2 (24.4%)	174.2 (33%)	170.4 (12.6%)
Experimental feed force (N)	140	150	170	100	125	110
ABAQUS prediction (N)	161.3 (15.2%)	169.9 (13.2%)	176.3 (3.7%)	97.8 (2.2%)	107.6 (13.9%)	100.4 (8.7%)

Table 30. Comparison between averaged experimental and predicted forces including error deviation when simulating 3D machining of Inconel 718 with the MTS and RWM models.

As it can be initially deduced from the results outlined in both tables when a feed of 0.2mm/rev is taken into account, the JC and MTS models gave cutting force values that could be considered reliable. While the feed component was well predicted with the former model involving a minimum error of 7.5%, the tangential part was as accurate as ~95% when the latter was employed. Although these errors may seem similar and state that both material models are comparable at a first glance, when a detailed analysis is undertaken the MTS constitutive model exhibited more credibility when compared to JC however. For instance, when the remaining cutting force components are considered, the higher deviation from the experimental feed force was 15.2% with the MTS model whereas this value reached 20.8% for the tangential force when JC was in use. Furthermore, if average percentage error values are taken as the basis for comparisons between the JC and MTS constitutive models, the main conclusion that the latter delivers better results than the former can be perfectly validated. In this regard therefore, while JC presented mean errors of ~18% and ~6% for predicted tangential and feed forces, the MTS model did so comprising values of ~7% and ~11% respectively.

A noticeable deviation is appreciated though, when both constitutive models are assessed considering predictions of forces for a feed of 0.08mm/rev. In such a situation, the JC relationship presented an average accuracy for tangential and feed forces of ~66% (error of ~34%) and ~76% (error of ~24%) respectively. On the other hand, the MTS model exhibited an augmented accuracy when compared to JC, as for the tangential component this was ~77% (error of ~23%) while for the feed component it took a value of ~92% (error of ~8%).

The riveting outcome common to both flow models nevertheless, was that for a feed of 0.2mm/rev, they predicted satisfactorily an increase in both together tangential and feed forces when the cutting speed increased, in conformity with experimental recordings.

However, the only constitutive model which was able to follow the variable trend in cutting forces for a feed of 0.08mm/rev was the MTS, therefore evidencing that in principle it would not only be more accurate than JC, but also much more effective when mimicking the erratic behaviour with regard to tangential and feed forces that may take place during the measuring procedure of the cutting operation.

5.3.4.3 Workpiece/tool temperature distribution

The estimated temperature configuration for cutting tool and workpiece/chip for all cutting speeds under study following the use of the JC model is shown in Figures 112 and 113, the former corresponding to a feed of 0.2mm/rev while the latter corresponds to a feed of 0.08mm/rev. As expected, the maximum predicted temperatures were found for those cutting speeds which were maximum, regardless of the feed under evaluation. Moreover, such values for a feed of 0.2mm/rev were higher than those for a feed of 0.08mm/rev, implicating that a direct relationship between cutting temperature and feed could be considered.

While for the highest feed under consideration the predicted peak values of temperature were mainly experienced by the workpiece in the particular region which involved the interaction with the tool rake face, a different pattern was observed when the feed was 0.08mm/rev. In this case consequently, the most drastic thermal effects were estimated to be concentrated on the domain which interplayed with the tool cutting edge, involving values that ranged from ~1,290K to ~900K when the cutting varied from 300 to 200m/min respectively.

As the feed decreased, the contact area between tool and chip did so, effect that was clearly confirmed by the FE predictions at all cutting speeds and potentiated by the geometry of the former body. The numerical results nevertheless, are believed not to have been altered significantly if the tool geometry had remained unchanged, by virtue of the inevitable curling of the chip that results when machining at any feed. Having said this, estimated temperatures in the tool following machining at 300m/min were as elevated as ~650K and ~525K for feeds of 0.2 and 0.08mm/rev respectively. These values, as envisioned, decreased to ~545K and ~520K for the exactly alike feeds at the moment that the cutting speed was reduced to 200m/min.

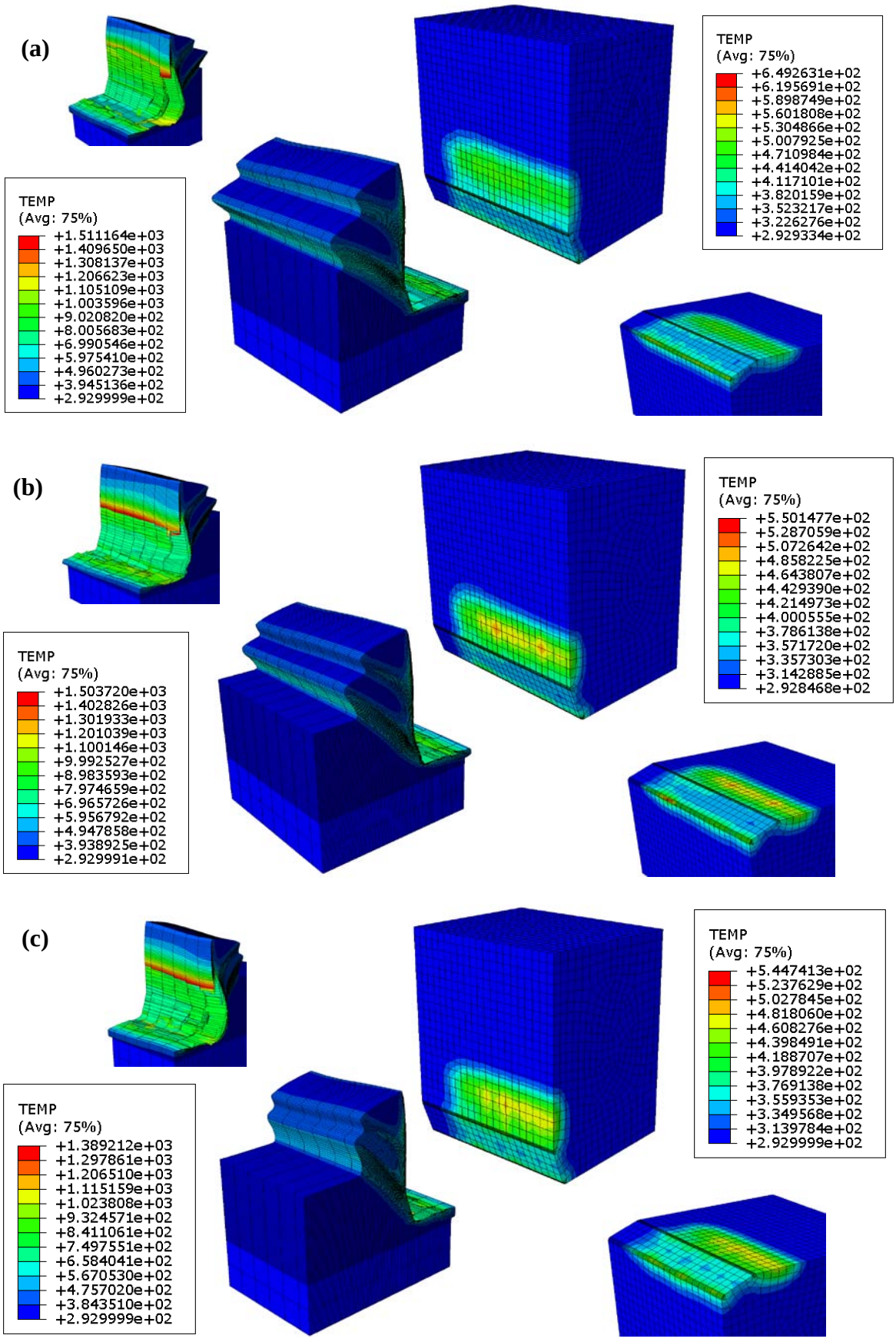

Figure 112. Predicted temperature distribution in tool and workpiece (K) for a feed of 0.2mm/rev and a cutting speed of (a) 300m/min, (b) 250m/min, (c) 200m/min when simulating 3D machining of Inconel 718 with the JC and RWM models.

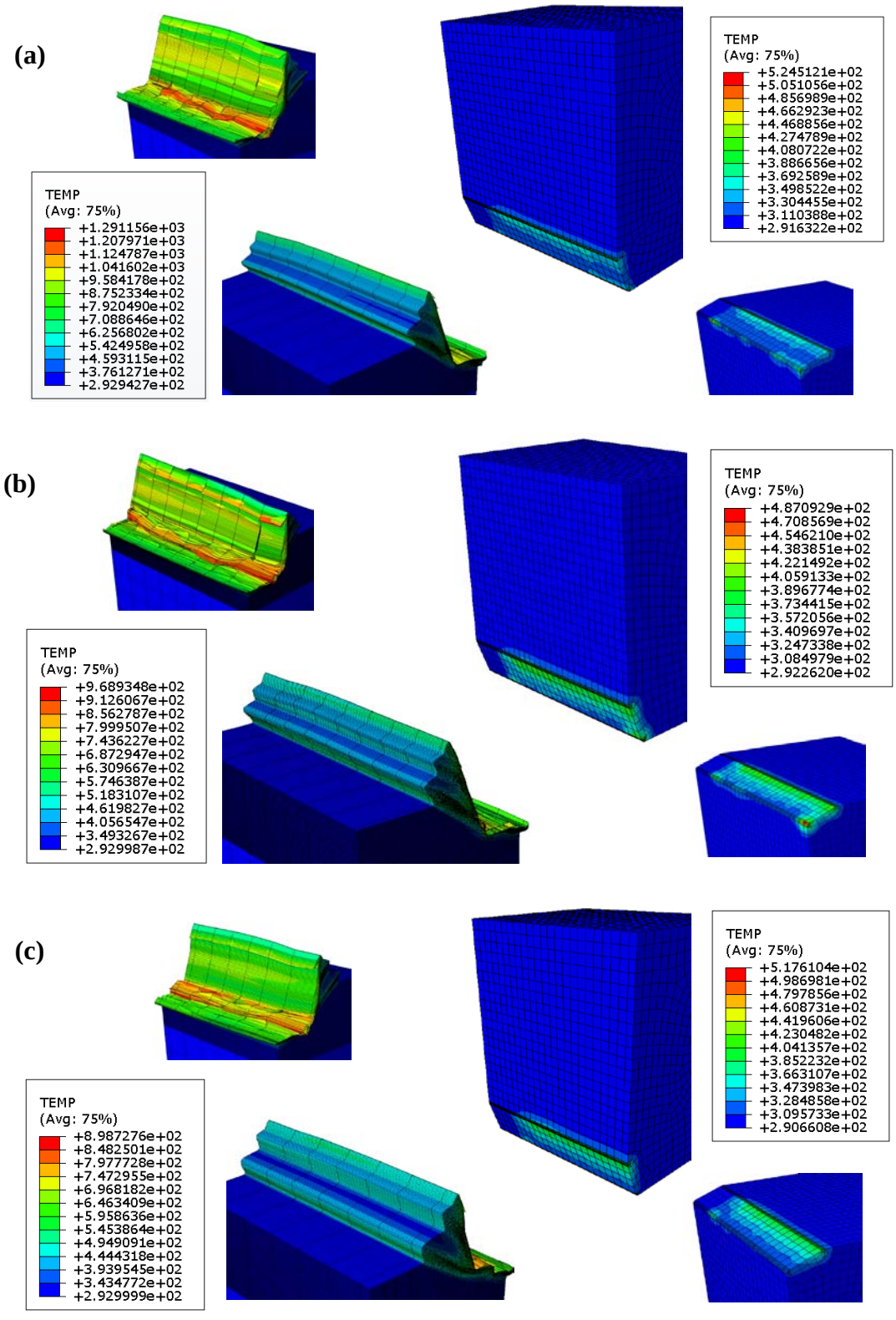

Figure 113. Predicted temperature distribution in tool and workpiece (K) for a feed of 0.08mm/rev and a cutting speed of (a) 300m/min, (b) 250m/min, (c) 200m/min when simulating 3D machining of Inconel 718 with the JC and RWM models.

Figures 114 and 115 on the other hand, display the tool and workpiece thermal distribution that succeeded the numerical computations when the MTS model was used, each one relative to a feed of 0.2 and 0.08mm/rev for the three cutting speeds specified.

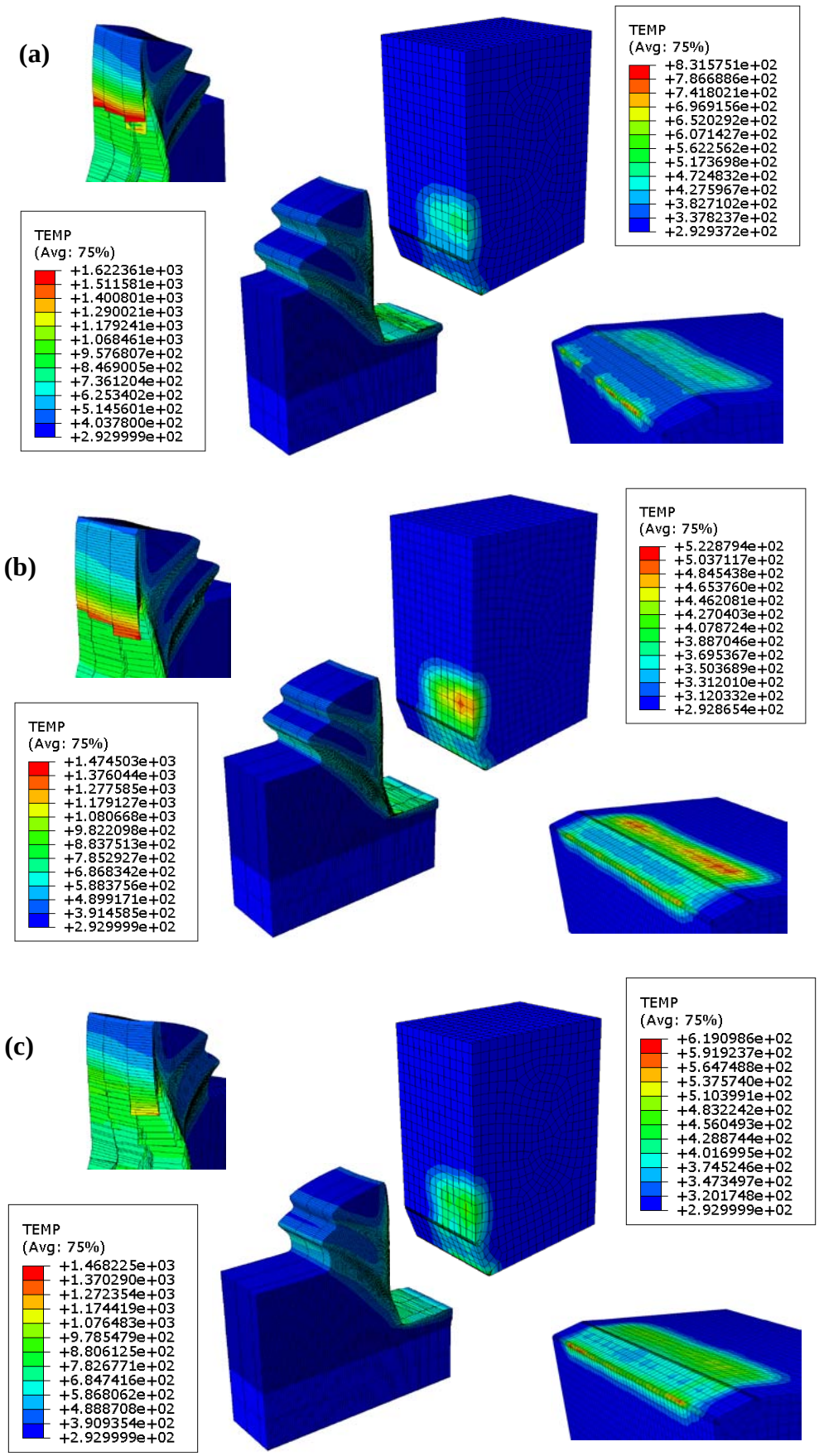

Figure 114. Predicted temperature distribution in tool and workpiece (K) for a feed of 0.2mm/rev and a cutting speed of (a) 300m/min, (b) 250m/min, (c) 200m/min when simulating 3D machining of Inconel 718 with the MTS and RWM models.

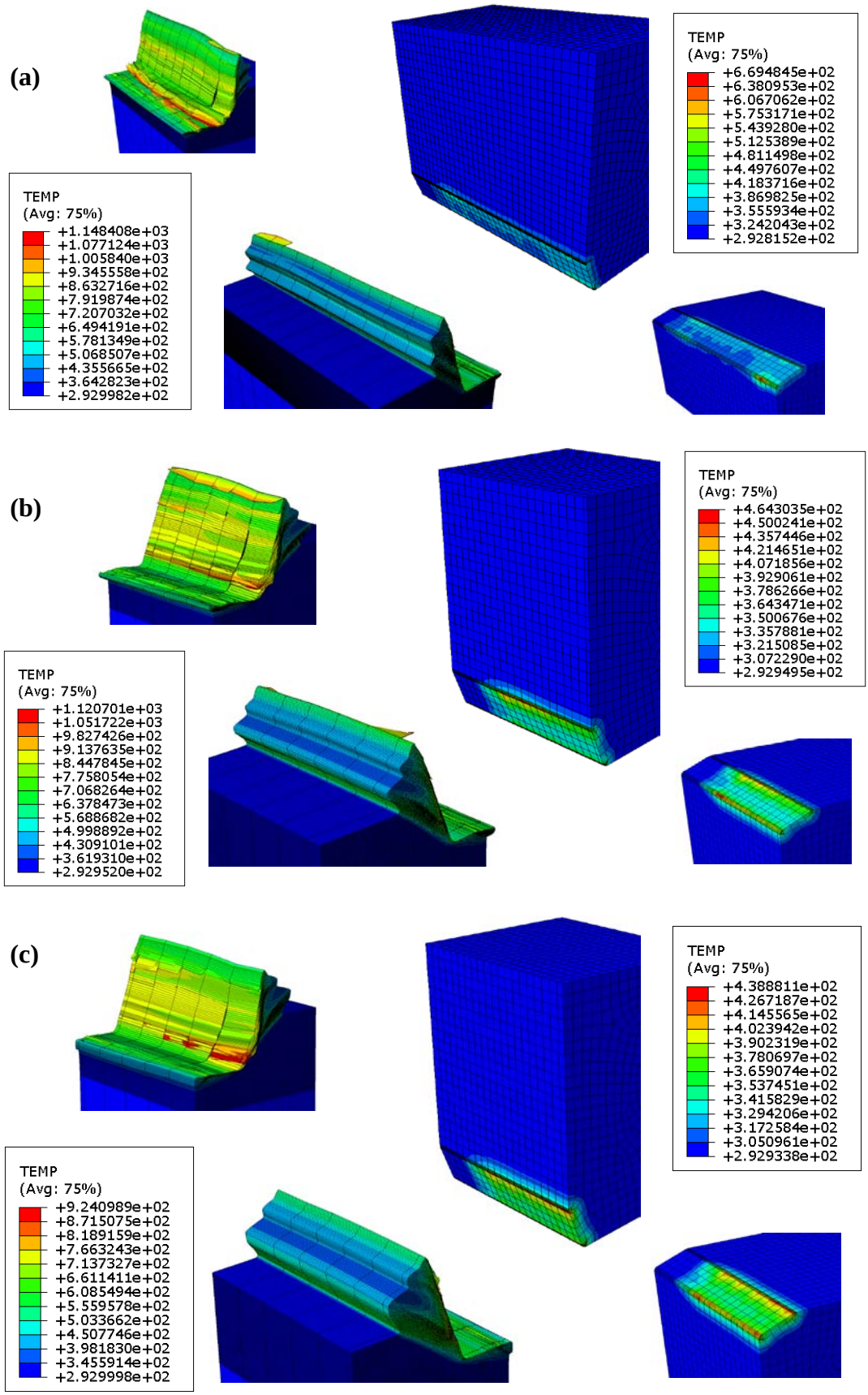

Figure 115. Predicted temperature distribution in tool and workpiece (K) for a feed of 0.08mm/rev and a cutting speed of (a) 300m/min, (b) 250m/min, (c) 200m/min when simulating 3D machining of Inconel 718 with the MTS and RWM models.

The most staggering finding that initially emanates from the FE simulations is that each and every maximum temperature was to a small extent higher than that obtained with the JC model, with the solely exception for a speed and feed of 300m/min and 0.08mm/rev apiece. For example, a rise in the predictions of ~110K was made when operating at 300m/min and a feed of 0.2mm/rev whilst this value was ~24K when the feed of 0.08mm/rev and a speed of 200m/min were adopted. In spite of the process temperatures not being able to be measured as explained before, it could be conjectured that the use of the MTS model gave, in general, more realistic predictions when compared to JC. As an example of this, it would be more logical to prophesied temperatures of the order of ~1,620K (or even higher) rather than ~1,510K when dry cutting Inconel 718 at the maximum speed and feed, trend that repeats itself in all cutting situations apart from the one mentioned above.

Thermal distribution in the tool was also concise with this observation regarding a rise in the estimations when applying the MTS model, though in this case they were much higher than those in the workpiece, with values of ~180K and ~145K that corresponded to a cutting speed of 300m/min and feeds of 0.2 and 0.08mm/rev respectively. It needs to be noticed however, that the situation was the opposite when the cutting decreased to 200m/min, in which case the discrepancies had values of ~75K and ~80K when machining at feeds of 0.2 and 0.08mm/rev respectively.

5.3.5 Prediction of DRX with MTS and RWM - Inconel 718

5.3.5.1 Chip formation/morphology

Based on the discoveries emphasised in all previous subsections, the FE modelling of grain refinement (dynamic recrystallisation) occurring in the machined layer was done by coupling the model described in subsection 4.5.1.3 to the MTS and RWM models, as the former seemed to be more representative of the flow behaviour featured by Inconel 718 than JC while the latter consummated more reliable predictions in terms of shear banding formation than CL. As such, Figures 116 and 117 display therefore different views of the Von Mises effective stress distribution of the workpiece involving cutting feeds of 0.2 and 0.08mm/rev respectively, for the three speeds under judgement.

Comparative comments than those made when analysing Figures 106 and 107 apply in this situation also, with the unique dissimilarity that when the DRX module is employed, the adiabatic shear bands tended to be more defined. This side effect is presupposed to be due to the additional softening the complementing DRX model generated

on the viscoplastic response of the superalloy, giving the preliminary idea that its implementation into the general VUMAT subroutine was appropriate.

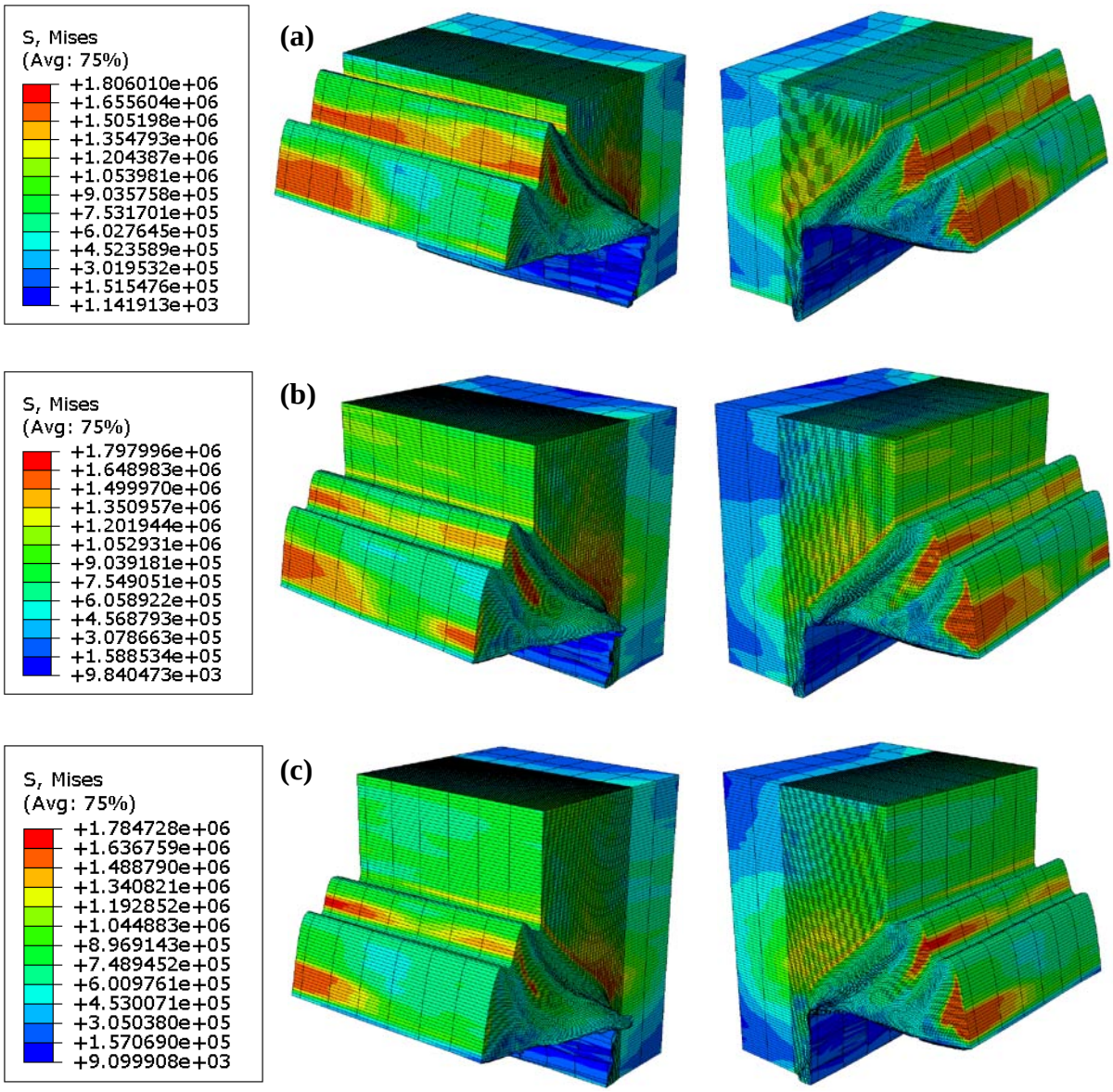

Figure 116. 3D view images of Von Mises stress distribution in workpiece (10^{-3}MPa) for a feed of 0.2mm/rev and a cutting speed of (a) 300m/min, (b) 250m/min, (c) 200m/min when simulating 3D machining of Inconel 718 with the MTS, DRX and RWM models.

A more comprehensive analysis to confirm this assumption is required obviously, as the predicted stresses in the workpiece did not show a tendency which could make one think that the incorporation of the DRX module provoked a noticeable flow softening, perhaps due to the perceptible rapidness of the machining process. Nevertheless, chip serration was produced in all cases and the formation of a burr in the inner and outer faces of the workpiece was the rule rather than the exception, confirming undoubtedly that the DRX model did not quantitatively alter previous FE results. Moreover, a significant degree of

softening can be witnessed in the machined surface for each and every cutting simulation, which not only allows one to arrive at the conclusion that this result was in agreement with preceding FE predictions, but also hypothesise that the extra flow softening effect included due to DRX played a part in achieving such end.

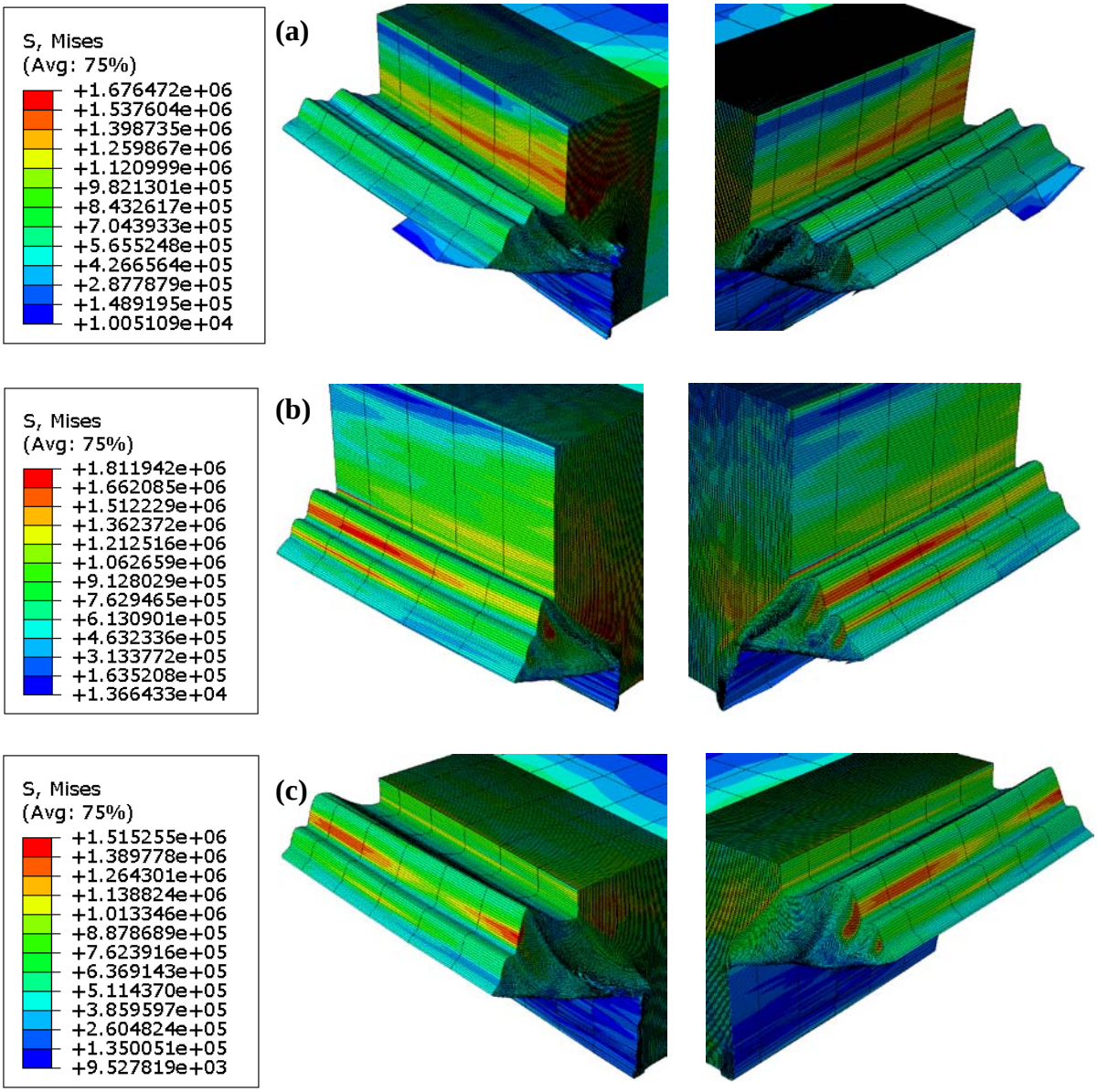

Figure 117. 3D view images of Von Mises stress distribution in workpiece (10^{-3}MPa) for a feed of 0.08mm/rev and a cutting speed of (a) 300m/min, (b) 250m/min, (c) 200m/min when simulating 3D machining of Inconel 718 with the MTS, DRX and RWM models.

Figures 118 and 119 depict cross sectional views of the 3D predicted chip morphology (including the distribution of the internal state variable D^a observed in Eq. (49) obtained from the FE models) in conjunction with those corresponding to the chips that were etched, all together for feeds of 0.2 and 0.08mm/rev and cutting speeds of 200, 250 and 300m/min. In situations where the maximum feed is brought into attention, it is recognised

that the first chip peak was underpredicted by a mean percentage of approximately 13% when machining at 300 and 250m/min whereas the contrary situation was evidenced for the other cutting speed, with a value which was close to 25%.

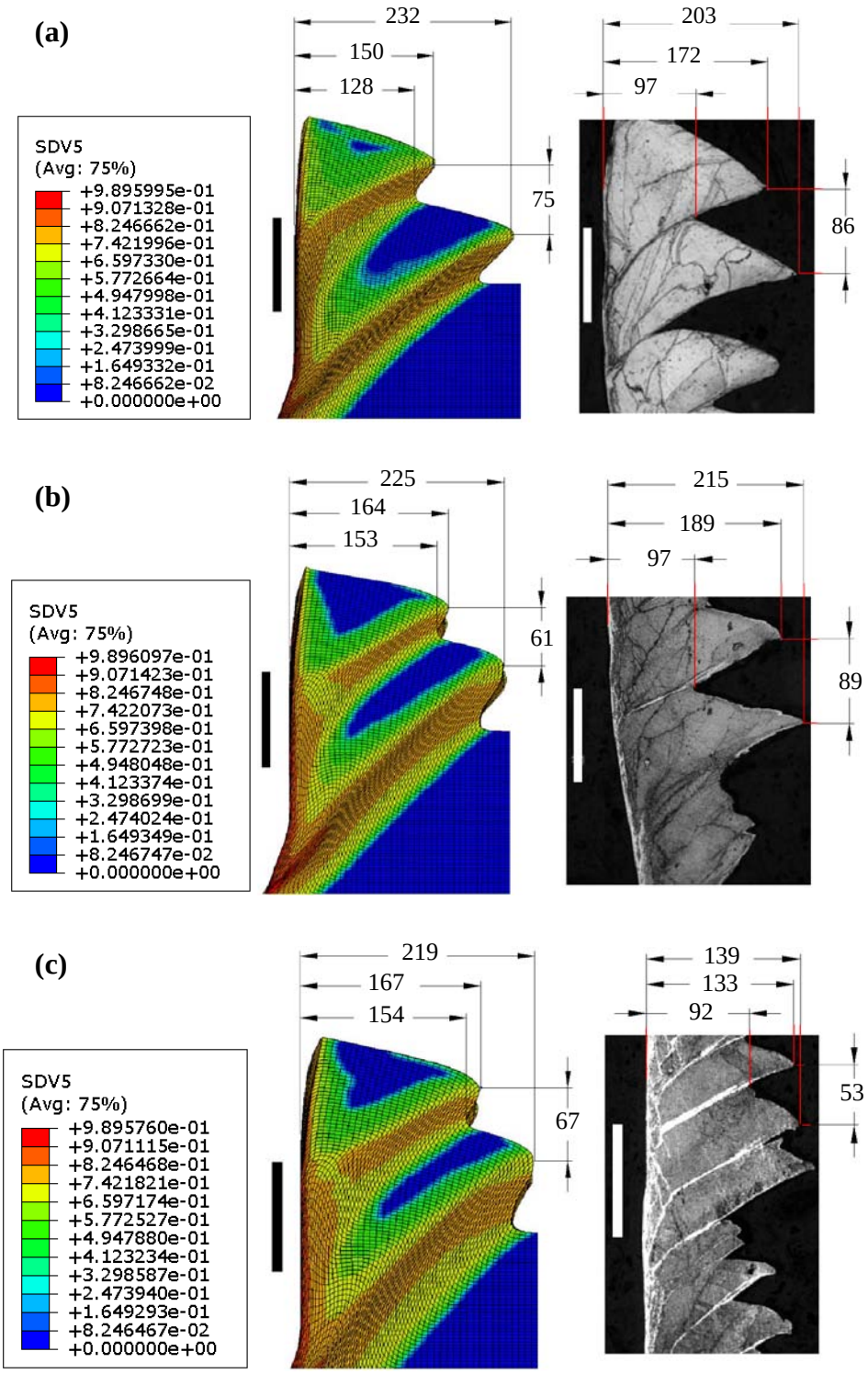

Figure 118. Comparison between experimental and predicted chip morphology (μm) for a feed of 0.2mm/rev and a cutting speed of (a) 300m/min, (b) 250m/min, (c) 200m/min when simulating 3D machining of Inconel 718 with the MTS, DRX and RWM models. The scale bars correspond to 100μm while the variable SDV5 to D^{α} in Eq. (49).

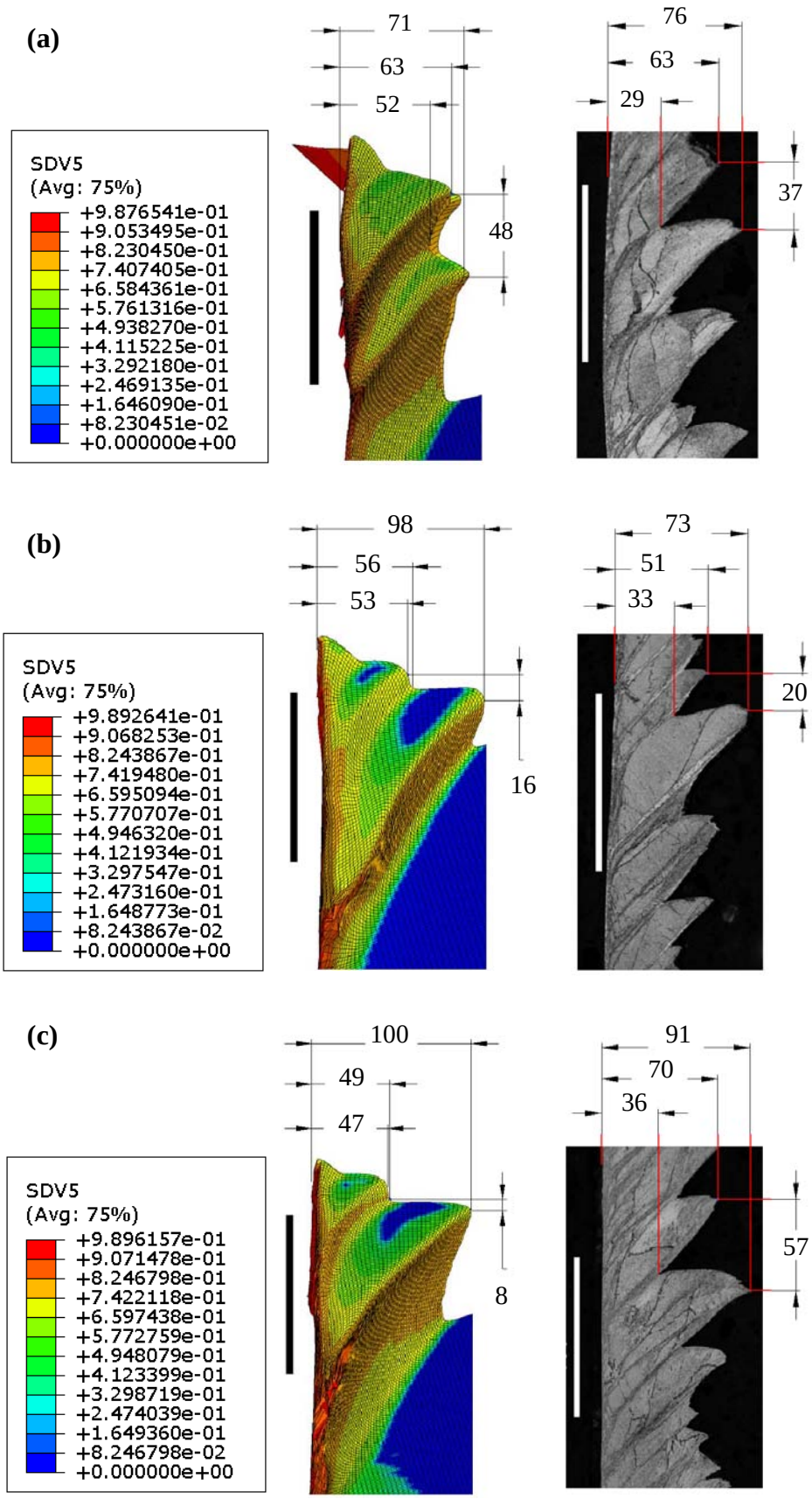

Figure 119. Comparison between experimental and predicted chip morphology (μm) for a feed of 0.08mm/rev and a cutting speed of (a) 300m/min, (b) 250m/min, (c) 200m/min when simulating 3D machining of Inconel 718 with the MTS, DRX and RWM models. The scale bars correspond to 100μm while the variable SDV5 to D^a in Eq. (49).

FE predictions concerned with the dimension of the second chip peak on the other hand, showed a recurrent behaviour of overestimation irrespective of the operating conditions, which was associated with values of ~14%, 5% and 58% for cutting speeds of 300, 250 and 200m/min respectively. Estimated chip peaks were not the exception in falling outside this pattern, as they encompassed mean deviations of ~32%, 58% and 67% for the corresponding just mentioned cutting speeds. Lastly, a blended affair involving over and underestimated chip pitches was encountered, which accused a shifting of ~26% (200m/min) from its experimental analogous for the former and errors of ~13% (300m/min) and ~31% (250m/min) for the latter.

Numerical computations indicated a less disperse response when the feed was diminished to 0.08mm/rev, however there was still not a well defined trend. For instance, when the cutting speed reached its minimum, the calculated chip first peak departed an approximate of 33% from that experimental (provided that the accuracy was 100% when the maximum cutting speed was implicated). Nevertheless, the predicted second chip peak displayed a completely opposite functioning, as for cutting speeds of 200 and 250m/min it was oversized by ~10% and 34% respectively, while it was underestimated by ~10% when operating at 300m/min. Ignoring the particular fact that the experimental chip pitch was qualitatively and quantitatively well reproduced at this speed, irregularities became more obvious when the machining conditions were more moderate. In this regard, the discrepancy the predicted chip pitch showed when removing material from 250 to 200m/min was enlarged from ~20% to ~86% for each case.

5.3.5.2 Cutting forces

The comparative analysis between experimental averaged forces and numerical predictions when orthogonally cutting Inconel 718 from 200 to 300m/min for feeds of 0.2 and 0.08mm/rev was based on results condensed in Table 31.

The first aspect to take into consideration in the study is that the addition of the DRX model into the constitutive response of Inconel 718 produced little to no variation when the issue of imitating the unsystematic force behaviour is brought forward, reinforcing what was reasoned in the previous subsection. With regard to tangential force FE estimations, increasing percentage inaccuracies (for a feed of 0.2mm/rev) were quantified when the cutting speed did so, which ranged from a minimum value of 3.8% to a maximum of 9.4%. This behaviour was different however in the judgement of the errors involved with respect to feed forces, as they showed a reduction from 18.7% to 5.5% when the cutting speed increased.

Feed (mm/rev)	**0.2**			**0.08**		
Cutting speed (m/min)	**200**	**250**	**300**	**200**	**250**	**300**
Experimental tangential force (N)	370	390	405	200	260	195
ABAQUS prediction (N)	356.6 (3.8%)	360.8 (8.1%)	370.2 (9.4%)	142.1 (28.9%)	173.4 (33.3%)	170.2 (12.7%)
Experimental feed force (N)	140	150	170	100	125	110
ABAQUS prediction (N)	166.2 (18.7%)	173.4 (15.6%)	179.3 (5.5%)	95.2 (4.8%)	105.1 (15.9%)	99.5 (9.5%)

Table 31. Comparison between averaged experimental and predicted forces including error deviation when simulating 3D machining of Inconel 718 with the MTS, DRX and RWM models.

When drawing parallels for a feed of 0.08mm/rev the highest disparities appeared, as it could be demonstrated when contrasting predicted to experimental tangential and feed forces. In this sense, the upper limits were 33.3% and 15.9% which corresponded to a cutting speed of 250m/min for both aforementioned forces respectively. In spite of these findings appearing to be of inferior quality, it needs to be highlighted that their variation from the corresponding ones seen in Table 30 was only ~1% and ~13% respectively, hence caution is required in this case when comparing the performance of the DRX model.

Although numerical results showed a reliable correlation with those summarised in Table 31, they were slightly less good than those already indicated in Table 30, manifesting that the influence of the grain size prediction module into the whole 3D FE model could be considered negligible in general terms and therefore, admitted to be stable as well as applicable to the flow response of the superalloy when further softening is required.

5.3.5.3 Workpiece/tool temperature distribution

Figures 120 and 121 display views of the numerically computed temperature distribution for both tool and workpiece when the removal of material was made at 300, 250 and 200m/min, each one corresponding to a feed of 0.2 and 0.08mm/rev.

As observed in Figure 120, the highest temperatures in the workpiece were recorded along the secondary shear zone (tool-chip interface) due to frictional interactions between the chip and cutting tool surface and forecasted to be within or even surpassing the melting temperature range of the superalloy (~1,550K-1,610K) when operating at 300m/min.

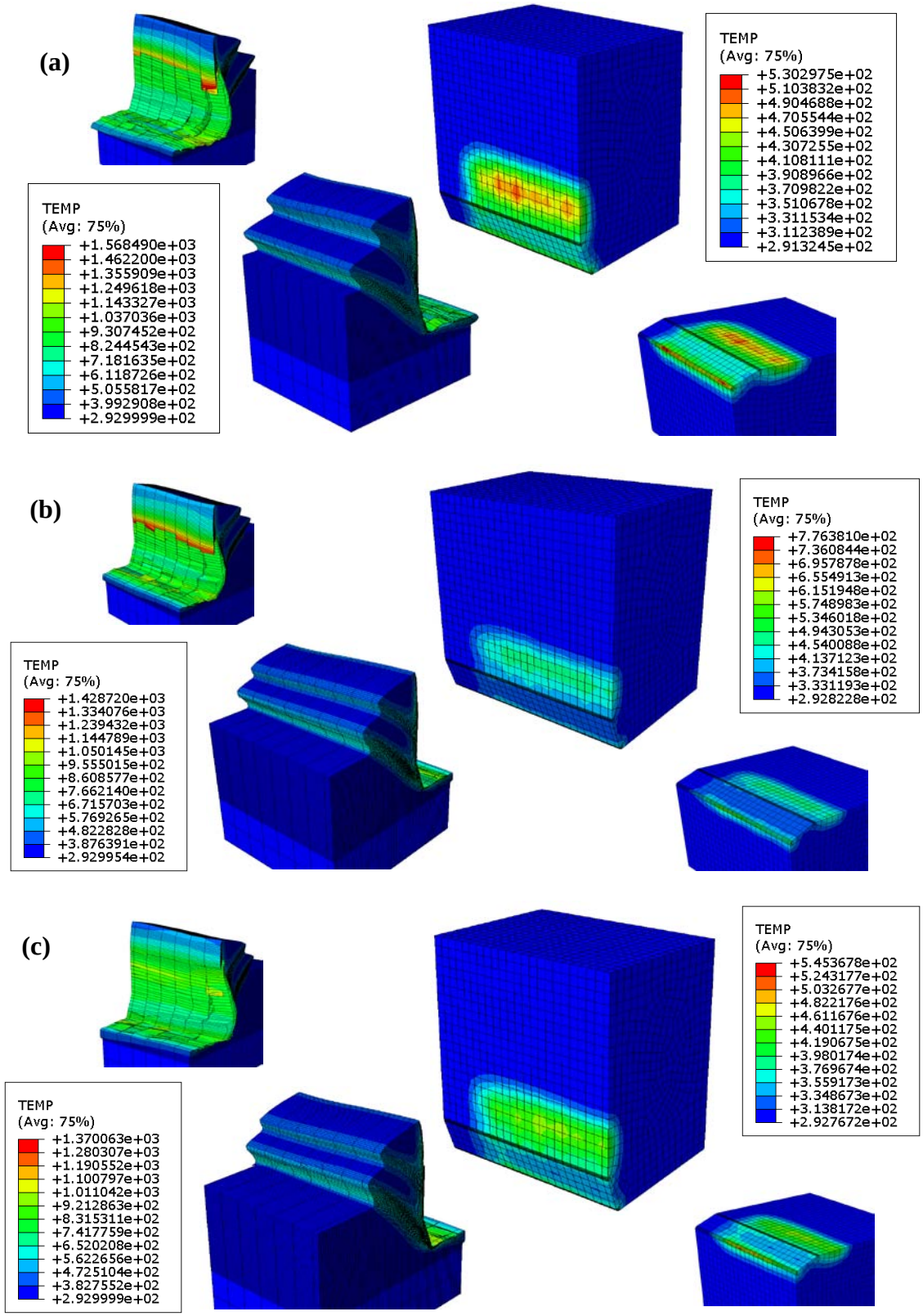

Figure 120. Predicted temperature distribution in tool and workpiece (K) for a feed of 0.2mm/rev and a cutting speed of (a) 300m/min, (b) 250m/min, (c) 200m/min when simulating 3D machining of Inconel 718 with the MTS, DRX and RWM models.

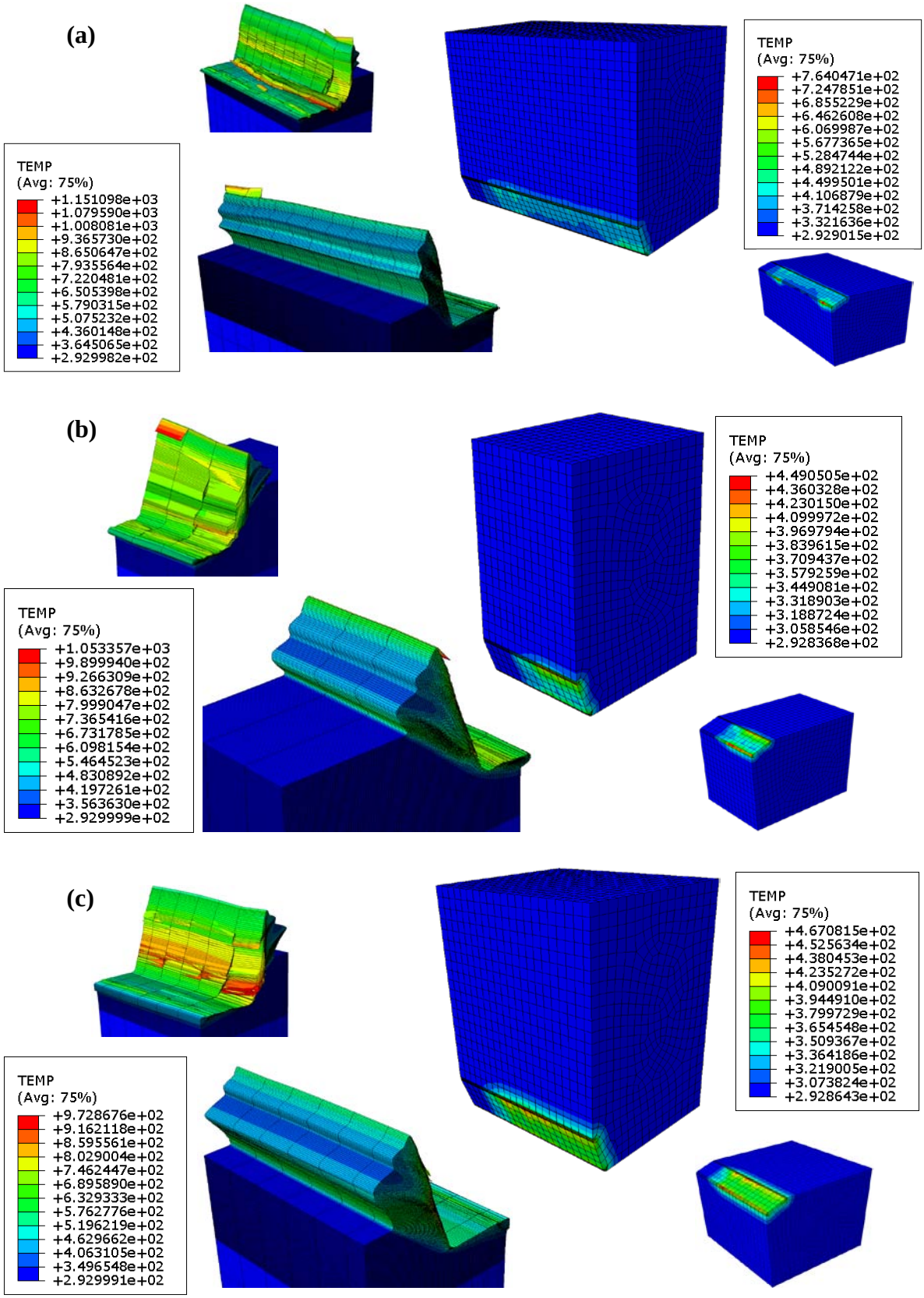

Figure 121. Predicted temperature distribution in tool and workpiece (K) for a feed of 0.08mm/rev and a cutting speed of (a) 300m/min, (b) 250m/min, (c) 200m/min when simulating 3D machining of Inconel 718 with the MTS, DRX and RWM models.

Estimated temperatures in the primary shear zone were generally found to vary from ~900K to 1,200K depending on the cutting speed and the interval of time evaluated, while those encountered in the shear bands reached and average value of 800K. These relatively high temperatures together with the softening produced by the RWM and DRX models, were expected to cause thermal and plastic flow softening of the Inconel 718 superalloy respectively on the grounds that the material strength typically deteriorates rapidly above temperatures of approximately ~920K, which would explain the observed formation of adiabatic shear bands leading to the serrated chip morphology.

Predicted temperatures in the cutting tool were as high as ~780K when machining at 250m/min (this probably corresponding to a peak rather than a operating condition), which were mostly localised in the tool tip due to the elevated friction interaction between both bodies that is found in such area. However in some cases the highest temperatures were found to be on the rake face of the tool (~530K and ~545K for cutting speeds of 300 and 200m/min apiece), suggesting that depending on the complex interaction between tool and workpiece together with the chip morphology that was predicted, the thermal distribution may fluctuate from the tip to different regions and vice versa.

When focusing on predictions made for a feed of 0.08mm/rev on the other hand, a noticeable diminution in both tool and workpiece temperatures could be seen. While the values decreased from ~765K to ~470K in correspondence to cutting speeds of 300 and 200m/min for the former, they oscillated from ~1150K to ~970K for the latter and the same cutting conditions.

Thermal concentration in the tool was principally detected in the chamfer with maximum values encountered along both the principal and secondary cutting edges regardless of the cutting speed employed. When referring the discussion to the workpiece nevertheless, such distribution was oppositely duplicated in the respective region of contact, with the exception seen when machining at 250m/min.

5.3.5.4 White layer formation/Grain size distribution

Exclusively due the aggressiveness of the dry orthogonal turning operation, a white layer was reasonably evidenced on the machined surface under microscopic examination in all cutting conditions, as shown in Table 32.

Although some micrographs presented insignificant defects following etching (this was associated with the difficulties faced when the procedure took place, frequently due to the

reduced area to be revealed), the layer was visible and therefore indicated that an alteration of the microstructure had occurred.

		Feed, f (mm/rev)	
		0.2	0.08
Cutting speed, v (m/min)	300	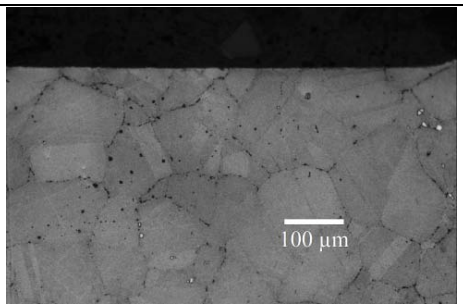	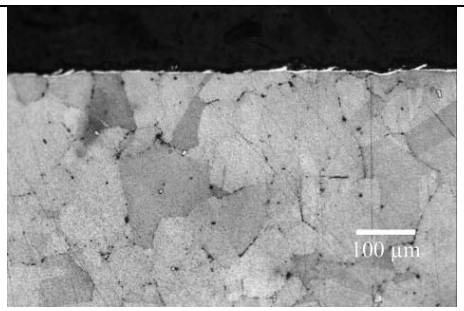
	250	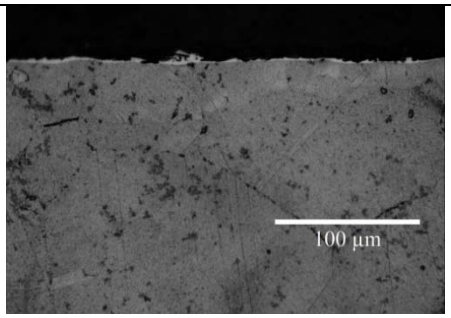	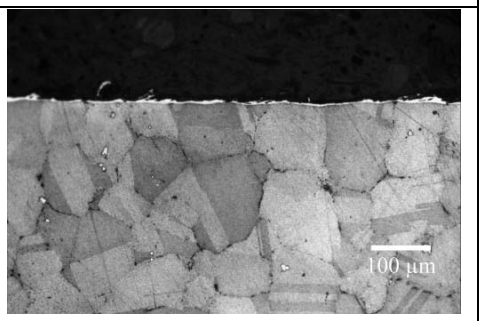
	200	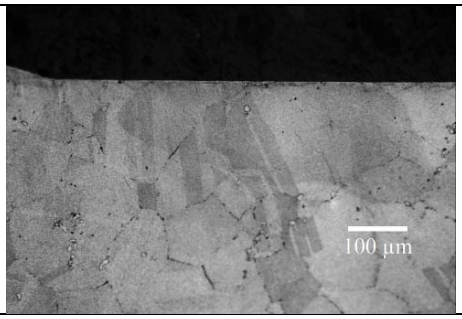	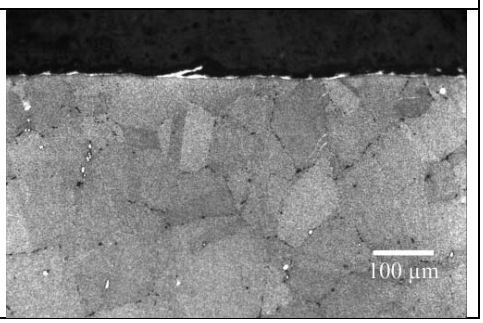

Table 32. Micrographs of the machined layer for feeds of 0.2 and 0.08mm/rev when cutting Inconel 718 at speeds of 300, 250 and 200m/min.

Contrary to what it could have been expected in the first place, the most evident transformations were observed for the lower feed, including at the same time an elevated degree of damage on the surface. This was believed to be occasioned by the different tool geometry used (negative rake angle), which is assumed in consequence, to have induced such tears and cracks.

In order to distinguish more precisely the characteristics of the white layer formed following the cutting trials, Tables 33 and 34 summarise low and high resolution SEM images that were captured from etched samples when feeds of 0.2 and 0.08mm/rev were utilised respectively.

Experimental outcomes accounting for a feed of 0.2mm/rev, attested not only the occurrence of white layer, but also the notably appearance of carbides together with a more irregular surface finishing than previously seen.

	Magnification	
	Low	High
(a)	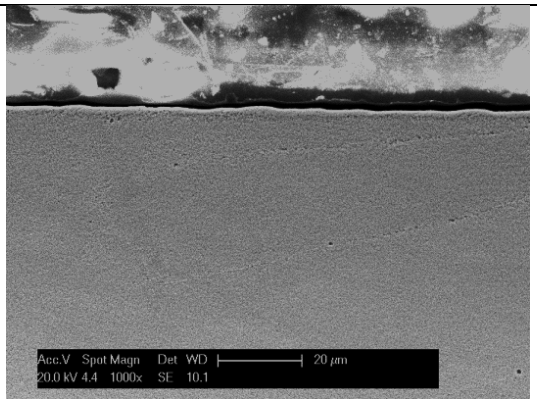	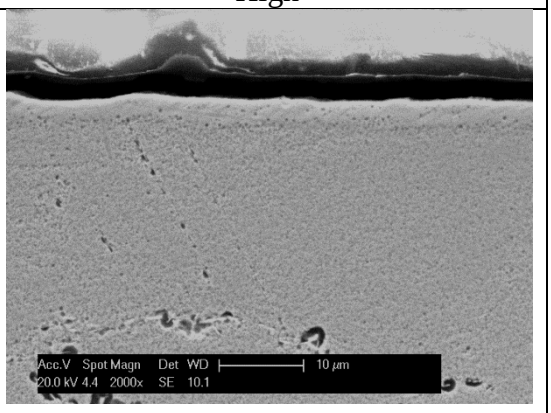
(b)	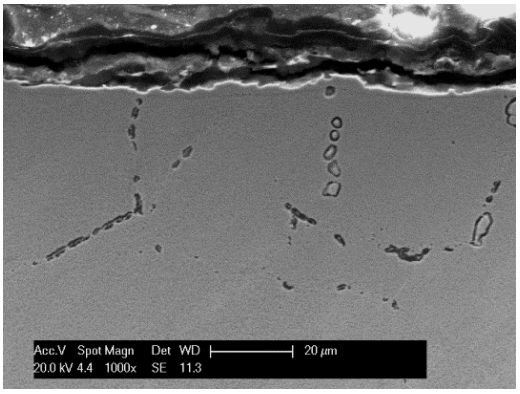	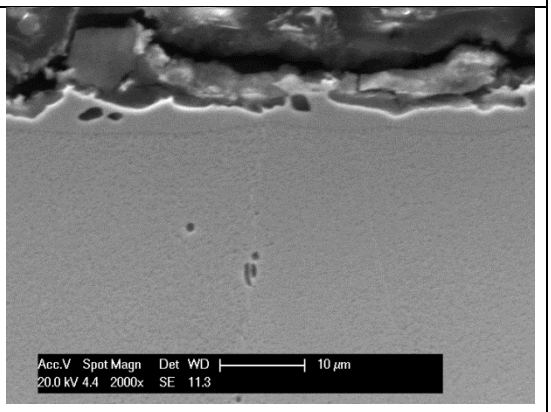
(c)	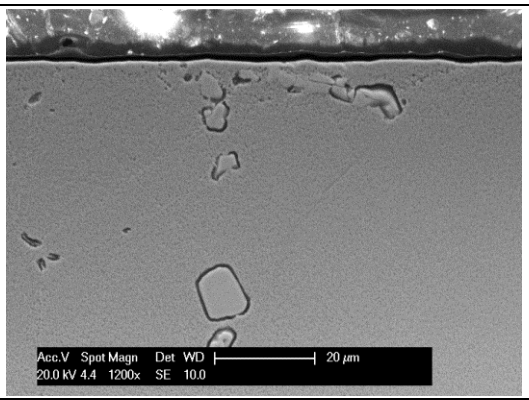	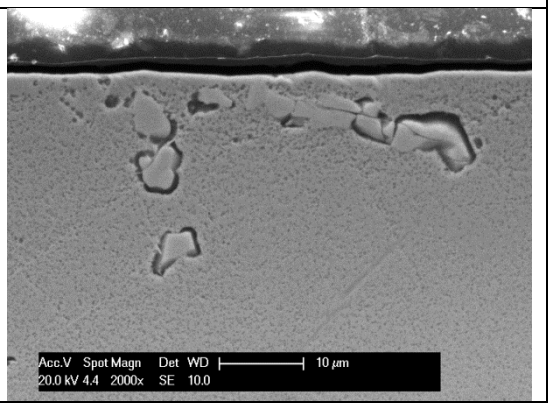

Table 33. SEM micrographs of the machined layer for a feed of 0.2mm/rev when cutting Inconel 718 at speeds of (a) 300m/min, (b) 250m/min and (c) 200m/min.

A clear example of this is conferred by low magnification micrographs obtained from tests conducted at 250 and 200m/min. Here, an uneven layer that varied from ~2 to ~6µm was clearly noticed in the former while the latter scenario featured cracked carbides as big as 10µm underneath the machined surface.

Comparatively, the surface aberration in terms of microstructure not only presented a more homogeneous thickness (~3µm) when cutting a 300m/min than when doing so at 250m/min (average of ~2.5µm), but also a better surface roughness generally speaking.

	Magnification	
	Low	High
(a)	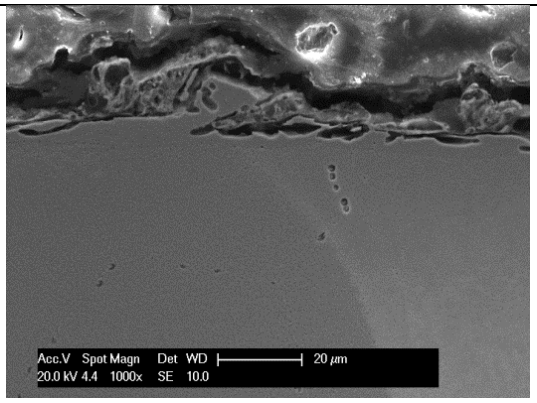	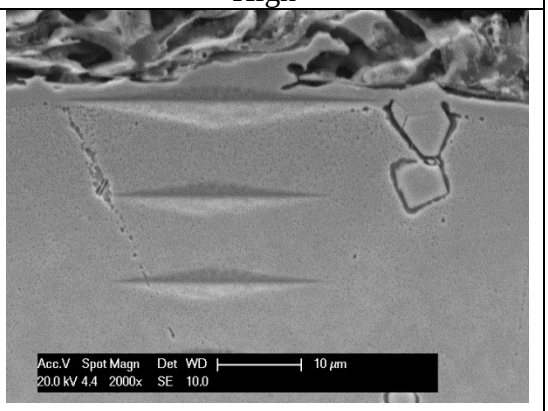
(b)	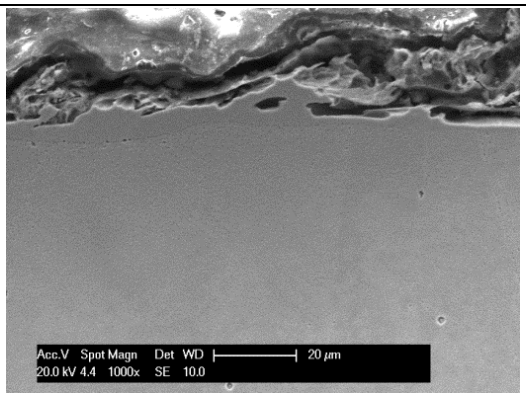	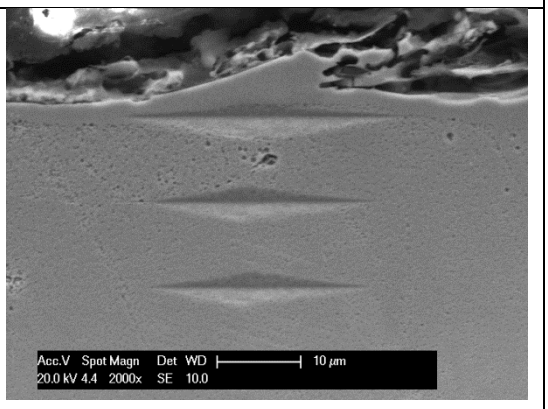
(c)	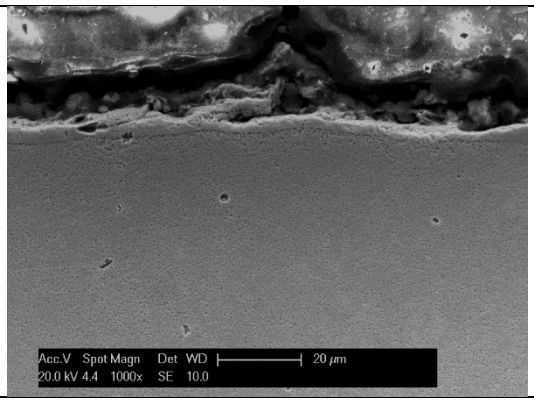	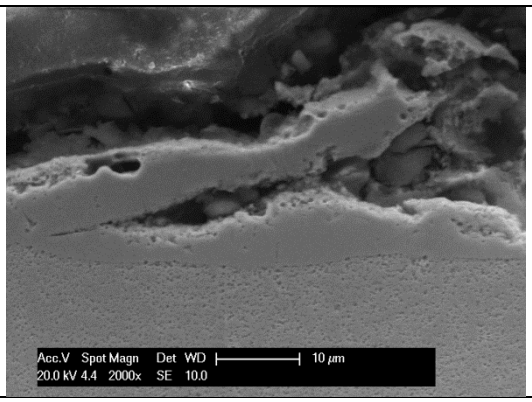

Table 34. SEM micrographs of the machined layer for a feed of 0.08mm/rev when cutting Inconel 718 at speeds of (a) 300m/min, (b) 250m/min and (c) 200m/min.

The white layer was much better delimitated when the feed was 0.08mm/rev and the magnification was intensified to 2,000x as perceived in Table 34. In spite of the regions being analysed with different resolutions were not the same when the cutting speeds were 300 and 250m/min, appreciable evidence of microstructural changes could be seen in either case.

A torn surface and fractured cracks in conjunction with a non uniform layer (that varied from ~1 to ~10μm) resulted from the most extreme turning circumstances, implying that a clear threshold for the material to avoid a catastrophic ending had been reached.

Figure 122 reveals the alteration suffered by the machined layer when the cutting conditions were 300m/min and 0.2mm/rev and leaves no doubt that it was composed of grains that were recrystallised, whose average size was <5μm. Furthermore, as a well established transition in size between the refined grains and those correlating with the bulk was not observed, it could be therefore confirmed that DRX took place.

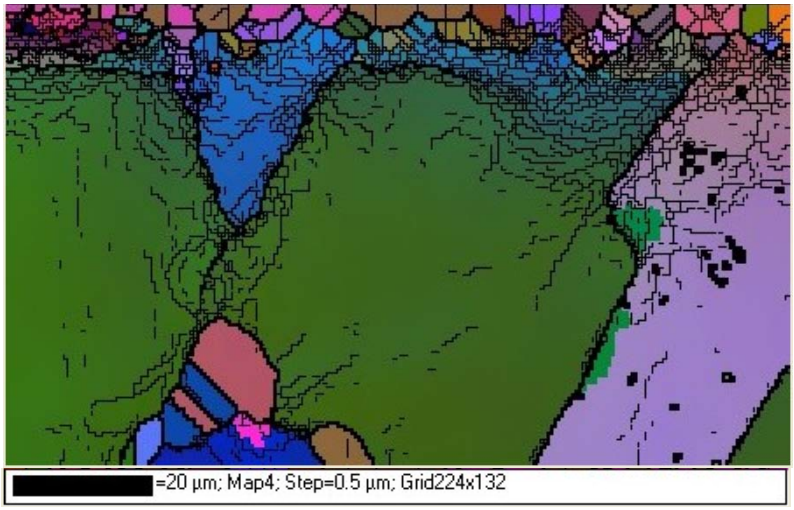

Figure 122. EBSD map obtained following orthogonal cutting of Inconel 718 at a cutting speed of 300m/min and a feed of 0.2mm/rev.

Results of the type in which grain refinement takes place when machining Inconel 718 have also been reported by Umbrello (2013). Although the author was able to identify near the machined surface grains as fine as ~9, 7.5 and 4μm when cutting at 50, 60 and 70m/min and a feed rate of 0.1mm/rev respectively, he highlighted that conventional microscopy analyses cannot indeed reveal the size of the (dynamic recrystallised) grains composing the actual altered layer, due to their featureless aspect; as also seen in this work (white colour). It is believed that a finer layer having much more smaller grains (<<1μm) should have been observed in the EBSD analysis, similarly as those found by Herbert et al. (2011) who twist drilled nickel based superalloy RR1000 at an abusive cutting speed of 35m/min and a feed of 0.12mm/rev. Instead of performing an EBSD analysis on selected samples, the authors studied a section of 0.3μm thickness (corresponding to the white layer) by TEM bright field imaging, which showed that grains of approximately 50nm had been produced on the surface due to the aggressive nature of the process. The refinement in grain size was thought to be caused by mechanical crushing due to thermal/mechanical effects

together with grain dissolution during the process followed by a re-precipitation mechanism upon cooling. Bushlya et al. (2011) also applied the TEM technique to investigate apparent surface modifications, though they did it after having turned aged Inconel 718 at cutting speeds and feed rates as high as 400m/min and 0.2mm/rev respectively, while keeping a 0.3mm depth of cut fixed. Results focused on the case when machining at 300m/min and 0.2mm/rev demonstrated not only that the white layer (up to 14μm in thickness) had been formed proportionally to tool wear and cutting speed, but also that it was composed of recrystallised grains, which in average varied between 50-150nm in size.

Techniques including SEM, TEM and EBSD among others to evaluate machined surfaces following turning and drilling of Inconel 718 were used by M'Saoubi et al. (2012) and M'Saoubi et al. (2014) respectively. Additional experimental trials replicating the cutting conditions employed by Herbert et al. (2011) were carried out by the latter (on RR1000 superalloy too). While EBSD maps corresponding to Inconel 718 obtained by M'Saoubi et al. (2012) for the near surface of the machined layers displayed recrystallised regions, a closer examination made by TEM estimated refined grains as small as 30nm, which were produced when operating with PCBN tooling at a cutting speed of 300m/min, feed of 0.15mm/rev and depth of cut of 0.25mm. As seen in the work of M'Saoubi et al. (2014), it is not always necessary to perform a TEM analysis, where grain size due to dynamic recrystallisation was able to be estimated by EBSD only and found to be ~105nm. These two microstructural crystallographic techniques therefore can be utilised to complement each other if desired, however EBSD was performed for the purposes of the present work.

Having demonstrated that the white layer that appeared following all machining trials was composed of recrystallised grains, the FE modelling work focused therefore on the attempt to reproduce as accurate as possible such microstructural occurrence. In this regard, Figures 123 and 124 showcase the numerical predictions in terms of grain size evolution for all previous cutting speeds mentioned and feeds of 0.2 and 0.08mm/rev respectively.

Regardless of the operating conditions under evaluation, it is initially observed that the resulting machined surface had an irregular aspect which (although not quantified) was in suitable agreement with findings acquired experimentally. In relation to the predicted white layer itself, it was evidenced that it was not only formed by refined grains, but also had a variable thickness, circumstances altogether that corroborated the DRX model as being suited to purpose and its applicability into the FE model.

With interest in computations made for a feed of 0.2mm/rev, the altered layer had a decreasing thickness when the cutting speed did so, which comprised average values of 11, 8.7 and 8μm in situations where the orthogonal operation was carried out at 300, 250 and

200m/min respectively. The minimum grain size that was forecasted in these three scenarios was in average 1.08μm, which was consistent with that viewed in the EBSD map (in spite of being representative only when the cutting was performed at 300m/min and 0.2mm/rev).

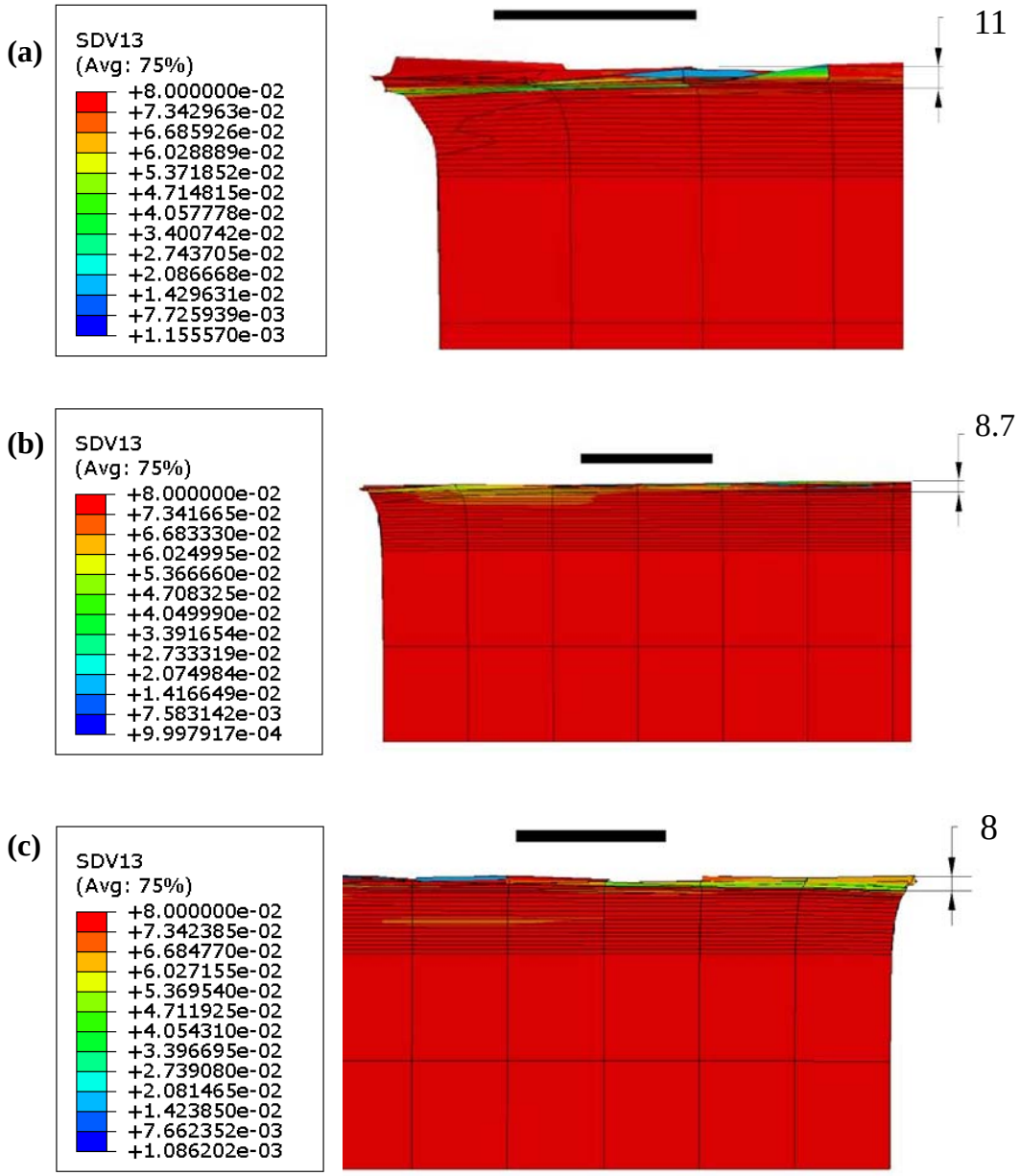

Figure 123. Predicted grain size distribution for a feed of 0.2mm/rev and a cutting speed of (a) 300m/min, (b) 250m/min, (c) 200m/min when simulating 3D machining of Inconel 718 with the MTS, DRX and RWM models. The scale bars correspond to 100μm while the variable SDV13 to grain size (mm).

Much more elevated oscillations in the layer's thickness were encountered when the feed decreased to 0.08mm/rev on the other hand. Even though the SEM micrographs displayed in Table 34 evidenced fluctuations in the depth of the modified subsurface, these were not as ample as those found in the FE predictions shown in Figure 124. For example

when orthogonally machining at 300m/min, it was estimated that the white layer could be as thick as 53μm and decrease to a stable value of ~23μm in average, which was roughly twice the size of its experimental counterpart. An improved situation was detected however when the cutting speed decreased to 200m/min, as the predicted thickness of the altered layer was in this case compatible with SEM results (~10μm).

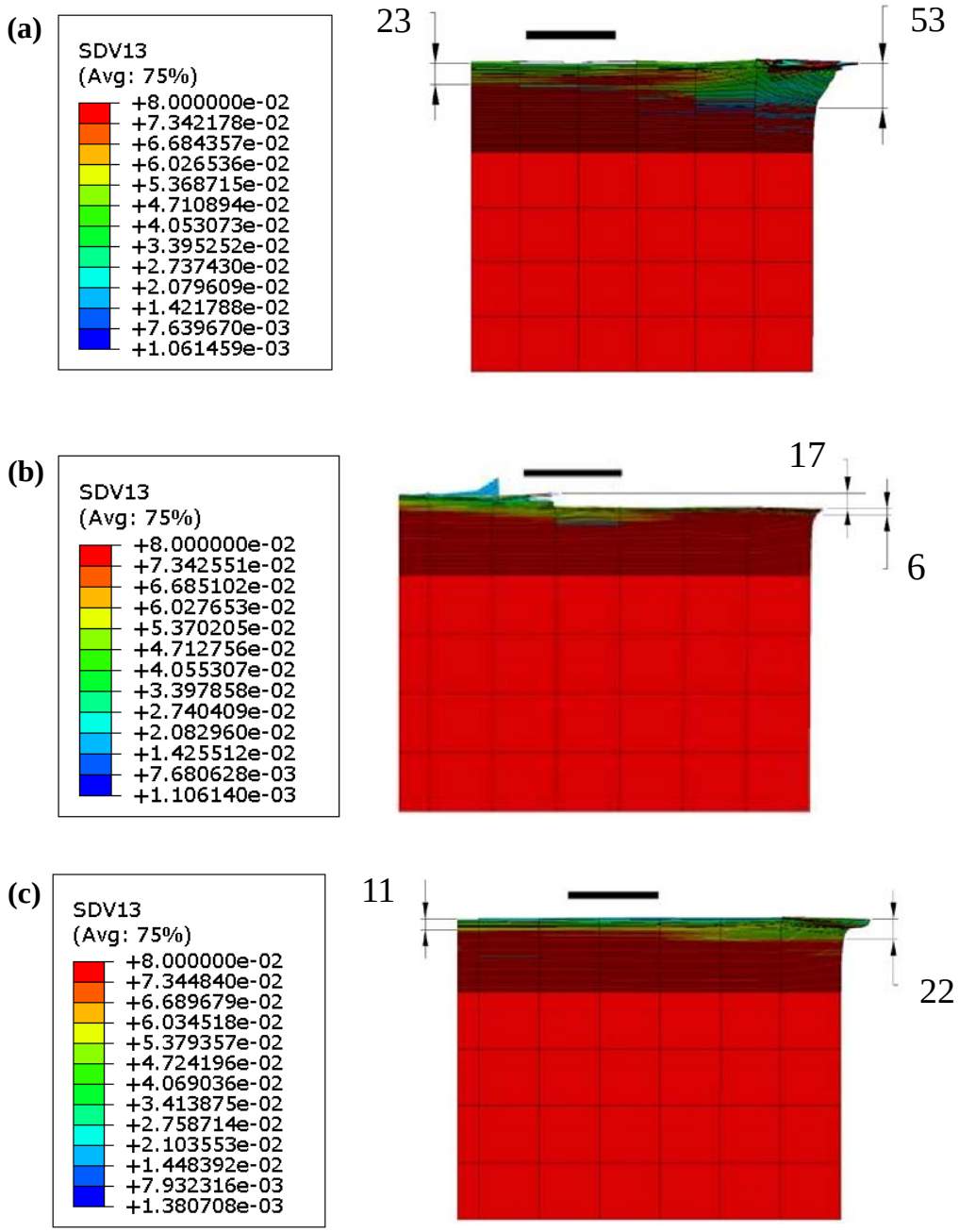

Figure 124. Predicted grain size distribution for a feed of 0.08mm/rev and a cutting speed of (a) 300m/min, (b) 250m/min, (c) 200m/min when simulating 3D machining of Inconel 718 with the MTS, DRX and RWM models. The scale bars correspond to 100μm while the variable SDV13 to grain size (mm).

An analogous result was recorded when removing material at an intermediate level, as the numerical calculations alleged a mean thickness for the white layer of ~6μm, which was in close relation to that easily determined from Table 34.

Grain size distribution was, as previously, well predicted in addition to present a defined trend, which related it to increasing cutting speeds in an inverse proportion. This state of affairs seemed to be motivated however, by pure chance instead of a robust connection between both magnitudes, principally due to the little variation in grain size that appeared when cutting from 300 to 200m/min (~0.32μm).

5.3.5.5 Assessment of the RWM damage model

It is noticed from Table 22 that energies which corresponded to the onset of adiabatic shear formation (W_{crit}) and the parameter a remained constant for all cutting speeds under analysis, while the only quantity that varied was the energy W_{frac}.

The variation of the latter followed the same trend found with cutting forces as discussed in subsection 5.3.4.2, suggesting that higher cutting speeds provoked not only higher tangential and feed forces (mostly due to tool wear), but also a rise in the quantities of energy needed to produce complete failure in the material. As forces are closely related to stresses, it can be deduced that in the workpiece material the latter effectively increased as the cutting speeds escalated. This is confirming that the value of energy calculated in a tensor fashion by Eq. (48) increased proportionally with cutting speeds. It could then be inferred that energies which lead to damage/fracture are likely to behave in a proportional fashion with recorded experimental forces.

Figures 125 and 126 show the predicted true stress and temperatures with respect to simulated machining time of two arbitrary nodes located on the adiabatic shear bands for all cutting speeds and feeds of 0.2 and 0.08mm/rev respectively, in order to analyse more in depth the performance of the RWM damage model. In addition, it is also displayed the equivalent plastic strain distribution (variable named as SDV1 in the VUMAT subroutine) that resulted from the numerical computations based on Eq. (124).

When operating at a feed of 0.2mm/rev and irrespective of the cutting speed under study, the predicted effective stress of Node 1 showed a significant degradation after reaching a peak of ~1,800MPa for cutting times that slightly decreased when the cutting speed did so.

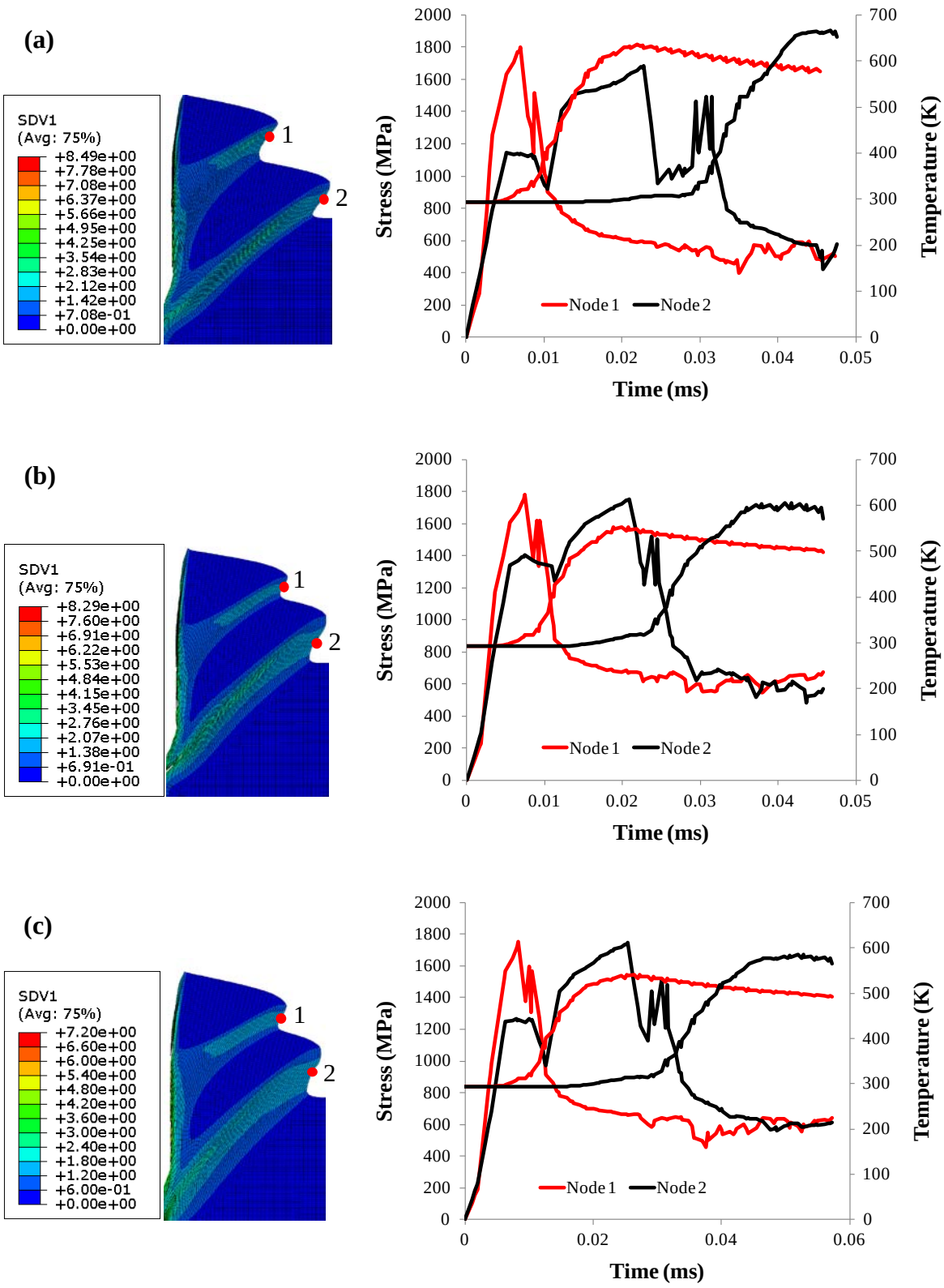

Figure 125. True equivalent stress (MPa) and temperature (K) graphs for arbitrary nodes 1 and 2 located on the shear bands for a feed of 0.2mm/rev and a cutting speed of (a) 300m/min, (b) 250m/min, (c) 200m/min when simulating 3D machining of Inconel 718 with the MTS, DRX and RWM models. The state dependent variable SDV1 corresponds to the predicted equivalent plastic strain (-) derived numerically from Eq. (124).

These results evidenced the fact that although the first saw-tooth was being formed in shorter time as the cutting speed increased, the equivalent stress corresponding to Node 1 remained constant in general terms.

The softening produced by the RWM and DRX models in the constitutive response of the superalloy was around ~70% in all cases, and although the latter model is believed to have played a part to achieve such end, the major effect in consequence could be attributed to the RWM damage model. This is because the diminution in stress provoked by the inclusion of the DRX model into the FE model was only about 15%, as stated in subsection 4.5.1.4. Nevertheless, the flow softening should have been more prominent as it was highlighted previously to generate much narrower shear bands and consequently match experimental findings.

Thermal effects were not believed to have a noticeable influence on the softening of the workpiece material as for example when operating at 300m/min, the highest predicted temperature was in average ~630K, which was recorded in a time in which a high level of softening had already taken place. The fact that thermal effects play a minor (though still considerable) role on adiabatic shear banding formation has been well documented by Rittel et al. (2008) and Rittel (2009), who concluded that the stored energy of cold work that led to the generation of dynamic recrystallisation, was the principal agent that provoked ulterior softening/damage by shear in metallic materials. In consequence, results from the FE simulations performed in this work for the machining of Inconel 718 appear to be reinforcing this experimental phenomenon. The same trend with regard to temperatures and stresses was found for Node 2 in all simulated cutting conditions, with the unique difference that their maximum predicted values were higher than those which were encountered for Node 1. Although estimated temperatures in Node 2 increased up to ~670K for a cutting speed of 300m/min, this happened in a time which was too late to be considered as the solely cause for adiabatic shear banding formation, hence mimicking to what occurred with Node 1.

In the event that the study is focused on results that were obtained following the machining operation at a feed of 0.08mm/rev, a more dramatic response in terms of effective stresses was found for Node 1 when cutting at 300m/min. In this scenario, a second peak of ~500MPa was noticed, which expeditiously decreased to ~200MPa in a time of approximately 0.06ms. This was most likely to be the result of an inefficient softening mechanism that took place in the interior/exterior of the shear band and one which could have been, in some sense, foretold, as its predicted thickness was considerably larger than that observed in the etched micrographs.

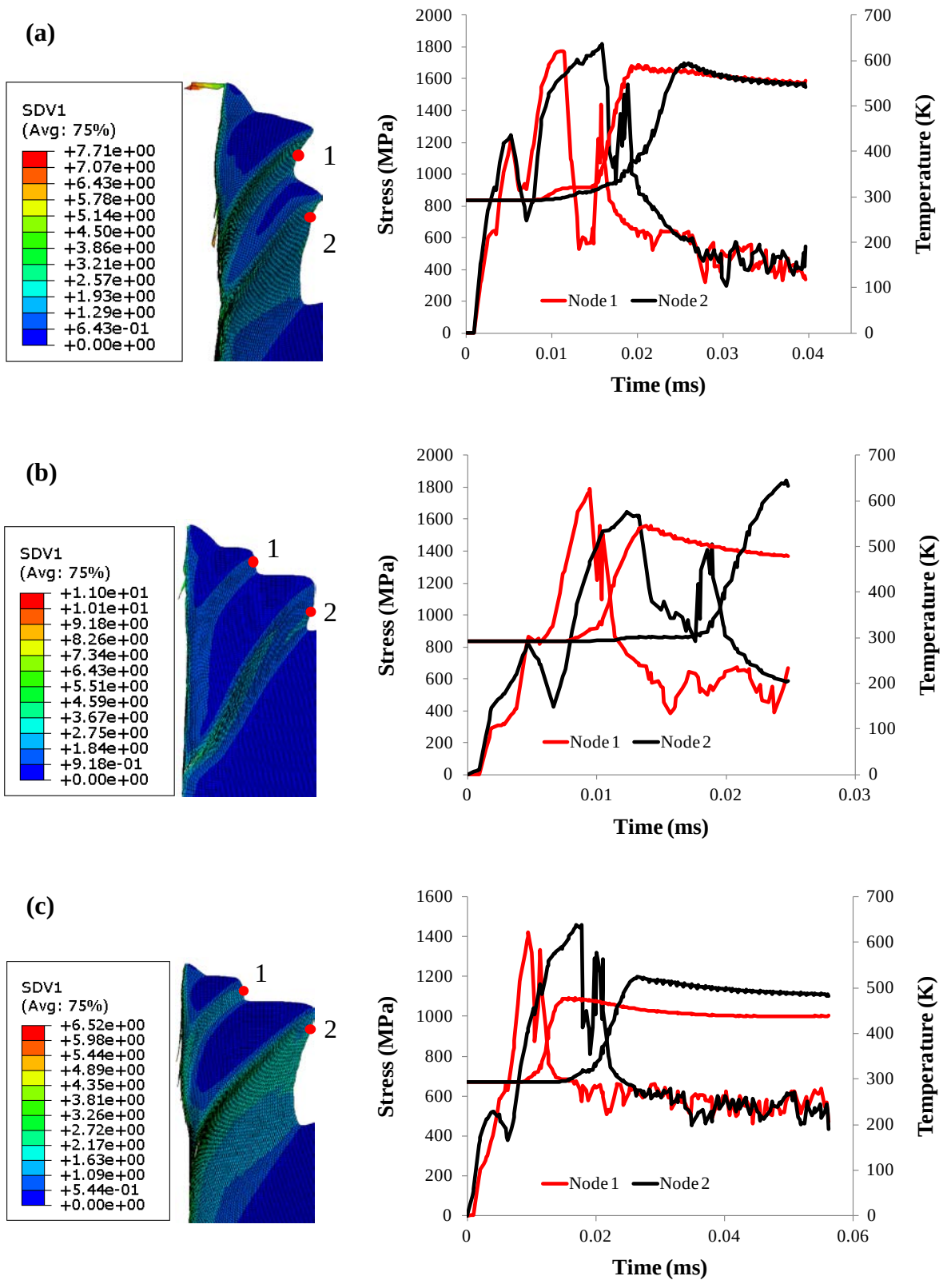

Figure 126. True equivalent stress (MPa) and temperature (K) graphs for arbitrary nodes 1 and 2 located on the shear bands for a feed of 0.08mm/rev and a cutting speed of (a) 300m/min, (b) 250m/min, (c) 200m/min when simulating 3D machining of Inconel 718 with the MTS, DRX and RWM models. The state dependent variable SDV1 corresponds to the predicted equivalent plastic strain (-) derived numerically from Eq. (124).

As the cutting speed continued to decrease, the pattern found with regard to stress arrangement for Node 1 was more comparable to that deduced from Figure 126, with the unique difference however that a peak value of ~1,400MPa was estimated when machining at 200m/min. The behaviour of Node 2 was more stable in all situations, and showed a tendency to exhibit lower effective stresses when the cutting speed decreased, with those reaching maximum values of ~1,800, 1,600 and 1,450MPa for 300, 250 and 200m/min respectively.

Predictions involving temperatures with respect to machined time for Node 1 were not the exception when following an inverse trend with increasing machining conditions, as they presented values as high as ~600, 550 and 480K, each of them corresponding to cutting speeds of 300, 250 and 200m/min. The same corollary cannot be reasoned when concentrating on Node 2, as an increase in the predicted temperature of ~50K was encountered when the orthogonal turning was performed from 300 to 250m/min.

It could therefore be concluded from the FE simulations carried out that although predicted shear bands were not as slender as they should have been, the major softening effect gave the impression to have come from sources of energy (which is put in a nutshell by the RWM damage model) and not from thermal causes, in line with experimental findings.

5.4 Recapitulation

Ti-6Al-4V: Initial 2D FE predictions when machining the alloy at 60m/min and using the JC and RWM models showed high agreement with experimental data. However the errors increased up to ~23% and 38% for the tangential and feed components respectively when cutting at 120m/min. This indicated that the JC model became inaccurate at high cutting speeds, because it was unable to represent the considerable strain/thermal softening the alloy is associated with in such circumstances. Predicted chip morphology in all situations was in line with experimental findings, which showed in principle the appropriateness of the RWM damage model to account for such event. Although overall machining temperatures were not measured, it seemed that the values numerically forecasted should have been higher.

When using the JC and CL models in 3D, results clearly evidenced that the strength deterioration the CL fracture model produced to further simulate the removal of material, was inappropriate not only in terms of cutting forces, but also chip morphology. In the former case, deviations (when orthogonally cutting at 120m/min) reached values of 350% while chip size was roughly twice that found experimentally. This explicitly exhibited that in addition to the employment of an unsuitable constitutive model, the use of an unreliable damage criterion

could make numerical estimations extremely erroneous. The application of the RWM damage model instead, improved all aspects of the FE simulations, though still some discrepancies in terms of cutting forces (as high as 138% for the feed component when operating at 120m/min) were encountered. Maximum predicted temperatures at the fastest cutting condition were not as elevated as those given by the CL model (~1,000K in comparison to ~1,800K), however they were more acceptable than the values seen in 2D FE simulations (~720K). Chip features such as peak, valley and pitch were much better represented in general terms with the favourable point that the formed adiabatic shear bands were continuous (which was in much better agreement with their experimental counterparts), unlike those predicted by the CL model. The RWM fracture model was unable to continuously generate ASB, contrary to what CL manifested, however the mismatches were drastically reduced to acceptable values, which confirmed that the RWM model performed better (despite its limitations) than CL.

Inconel 718: Preliminary 2D FE models generated to simulate machining of the superalloy at speeds of 300, 250 and 200m/min and feeds of 0.2 and 0.08mm/rev respectively, showed that the JC and RWM models provided good estimations with regard to chip morphology, including the formation of thin adiabatic shear bands that closely matched those that were etched. Predicted tangential and feed forces improved their accuracy when the feed was reduced from 0.2 to 0.08mm/rev, with minimum error values that were found to be 20% and 3.6% respectively and corresponded to the feed component. Nevertheless, discrepancies as nearly as ~40% were more likely to appear, which indicated that the FE model had inconsistencies in either its constitutive or damage formulations. Although a peak temperature of ~1,200K when operating at the highest cutting speed and feed was estimated, it did not seem to be high enough taking into account the severity at which the workpiece material was subject to, reinforcing the fact just mentioned. Thermal distribution in workpiece and tool on the other hand, presented a well defined pattern in general, which not only related predicted temperatures with cutting speeds in a direct fashion, but also did so when the feed varied.

The analysis of the orthogonal cutting problem in three-dimensional space with the JC and MTS viscoplastic models evidenced interesting and quantifiable results which allowed performing an individual/group assessment. In both situations, the dimensional characteristics of the chips were decorously reproduced by the FE simulations, though the problem related to the overestimation of the thickness of the shear bands as well as the quantity of them still persisted. This undoubtedly confirmed that the RWM model would need modifications in order to account for a higher degree of softening due to damage. Forecasted workpiece and tool temperatures were comparable to each other when utilising either constitutive model, and

these were more in agreement with values that could have been expected from experimental measurements. It is believed in consequence, that the JC and MTS models behaved similarly and provided suitable values of temperature.

The major difference encountered between both constitutive models was however, in the prediction of the cutting forces (as expected). While the tangential and feed force components when cutting at 0.08mm/rev were underestimated in each and every condition regardless of the viscoplastic model employed, the highest errors resulted from the direct application of JC (~34% and ~24% compared to ~23% and ~8% when focusing on tangential and feed forces respectively). The findings were mixed following the cutting of the superalloy at 0.2mm/rev, due to the clear fact that JC was more accurate in the estimation of feed forces (~6% average error for all cutting speeds) while the MTS model performed better with regard to tangential forces (mean error of ~7% for all machining conditions). Even though both models could be considered as appropriate in this case, the JC relationship was more disperse than the MTS model when estimating the remaining force component, because percentage deviations for the former were ~18% while for the latter ~11%. These numerical findings highlight what was previously found, that the MTS constitutive model approximated better the experimental plastic stress-strain curves, which provided in turn more reliable predictions when being employed in FE simulations of the machining operation.

When including the DRX module, numerical results in terms of chip morphology and workpiece/tool temperatures were much alike as those attained without it. A similar scenario was encountered when attention was paid to the prediction of cutting forces, in which case the differences with the MTS model (as the only one being used) were customarily less than 13% for both components under analysis. Grain size distribution in the microstructurally altered layer was satisfactorily predicted, with typical minimum dimensions that were neighbouring 1μm regardless of the process conditions, and were in consistency with the EBSD map generated. The average thickness of the predicted white layer decreased from 11 to 8μm when the cutting speed varied from 300 to 200m/min and the feed was 0.2mm/rev, which was in line with micrographs obtained from SEM analyses. A different situation was seen when decreasing the feed to 0.08mm/rev, as it was noticed that the modified layer was, in some regions, estimated to be as thick as ~50μm (for a cutting speed of 300/min) when it should have been closer to ~10μm generally speaking. In spite of these results, the custom-made DRX module developed showed good prediction capabilities as well as adequacy for its utilisation within the mathematical/phenomenological framework of the MTS model.

CHAPTER 6

CONCLUSIONS

6.1 Main contributions of the work

The following list summarises the main contributions/key aspects related to the FE modelling as well as experimental activities carried out in the present work:

- Design (NX7.5 software) and build of the SHPB apparatus,
- Generation of flow stress data for Inconel 718 superalloy using the SHBP at Technion – Israel Institute of Technology involving strain rates of ~1,000, 2,000, 3,000, 4,000, 5,000 and 6,000s^{-1} for temperatures of 20, 250 and 400°C respectively,
- Experimental validation trials involving orthogonal machining of Ti-6Al-4V and Inconel 718 aerospace alloys. Response measures included cutting force components, chip morphology, process temperature and workpiece microstructure alterations (in specific for the latter),
- Formulation and evaluation of 2D fully-coupled, thermo-mechanical Arbitrary Lagrangian Eulerian (ALE) based FE models with adaptive remeshing using ABAQUS,
- Development of 3D fully-coupled, thermo-mechanical Lagrangian based FE models of orthogonal machining incorporating element deletion techniques,
- Calculation of new constants for the Johnson-Cook material model to characterise the viscoplastic behaviour of Inconel 718 at various strain rates and temperatures based on flow stress data generated with the Gleeble and SHPB testing machines,

- Calculation of strain rate/temperature dependent parameters for the Mechanical Threshold Stress constitutive model when applied to the description of Inconel 718 (also based on flow stress data generated with the Gleeble and SHPB testing machines). Theoretical computation of yield strength values in the complete strain rate/temperature testing domain for numerical purposes,

- Development of 2D/3D thermo-mechanical VUMAT subroutines for the Johnson-Cook and Mechanical Threshold Stress constitutive models,

- Subsequent incorporation of the energy based Cockcroft-Latham and Rittel-Wang-Merzer damage models into VUMATs to simulate chip formation/morphology,

- Assessment of the Johnson-Cook and Mechanical Threshold Stress material models together with the Cockcroft-Latham and Rittel-Wang-Merzer fracture criteria when simulating 2D/3D orthogonal cutting of Ti-6Al-4V and Inconel 718 alloys in terms of cutting forces, chip shape and workpiece/tool temperatures.

- Development of a bespoke mathematical model (within the framework of the Mechanical Threshold Stress constitutive model and linked to the RWM damage criterion) to predict microstructural grain refinement following machining of Inconel 718. Validation of predicted grain size distribution/altered layer thickness against EBSD/SEM micrographs respectively.

CHAPTER 7

SUGGESTIONS FOR FUTURE WORK

7.1 Conclusive remarks

A considerable effort has been made to bring the research community forward in the FE modelling of machining operations, with particular engagement in the orthogonal turning of aerospace alloys such as Ti-6Al-4V and Inconel 718. Based on the work carried out here, the following areas have been identified as the most relevant in which useful suggestions for further work can be given:

2D FE simulations: Although the development of two-dimensional models of the cutting process can shed light in critical regions of the workpiece/tool where no measurements can be performed and therefore be valuable, care must be taken as it was demonstrated that 2D FE models lack of numerous features. In this regard, the customary assumption of plain strain conditions does not always apply and in consequence, only a handful of real machining cases can be simulated. In addition, modelling techniques utilised to simulate chip formation such as artificial separation layers, ALE/AR methods, etc. are not entirely representative of the process itself and therefore any conclusion withdrawn from their numerical results will be highly debated, irrespective of the level of accuracy said to be achieved. Furthermore, both methods for producing chips are applicable to 2D cases and for the orthogonal cutting process uniquely, hence a generalisation/upgrade to other processes or dimensions is impossible to make.

For these reasons, when developing 2D FE models of the machining operation, it is suggested to focus on standard modelling techniques that make use of damage models (which would assess all elements conforming the workpiece) to predict chip formation/morphology, in order to maintain unreal assumptions to a minimum and make estimations more reliable.

3D FE simulations: The ideal situation would be to model any machining operation in 3D so that no detail could be missed out. For obvious reasons, 3D FE modelling requires much more computation time than its two-dimensional counterpart; however the benefits of performing simulations at real scale are tremendous and according to this work, worth the effort. Firstly and as commented before, there is no limit to what cutting operation simulate, as for example turning, milling, grinding, twist drilling, broaching processes, etc., can all be modelled with the current software solutions available. Secondly, important characteristics of the workpiece material which are consequence when removing material can be forecasted, such as burr formation, general chip shape/size, surface irregularities, etc. Finally, there would be no necessity in creating beforehand any imaginary separation layer to account for chip formation/morphology as it would be too complicated, fact that would automatically lead to the utilisation of damage models which would be applied to all workpiece elements instead of a predetermined selected region.

Making a necessary balance between the advantages and disadvantages 3D FE modelling possess over 2D formulations, it is recommended to utilise the former in the first place (whenever possible) and leave the latter as a benchmark. Today, with the exceptional CAD software available to create complex parts together with the enormous power in computing systems, the development of 3D FE models should be the regular practice rather than the exception.

Chip formation/morphology prediction: With the aim of representing the machining process as much as possible in 3D, artificial techniques to simulate chip formation were discarded and instead, more realistic (from a physical point of view) energy-based models were employed. Consequently, the common CL and the less famous RWM damage models were assessed not only to predict material detachment, but also the saw-tooth aspect of the chip. The latter was more accurate than the former in all aspects (though it would need modifications according to the findings in order to improve the predictions), when estimating not only chip features such as peak, valley and pitch, but also tangential and feed forces. Nevertheless, the RWM model failed in the generation of several saw-teeth.

The corollary of this is that damage models based on energetical principles are a valid and the most recommendable option to simulate chip serration over alternative methods still in use by some researchers, due to their undeniable physical framework.

Constitutive modelling: In conjunction with representative FE models of the actual cutting operation, the development of constitutive relationships/models which could properly portray

the static and dynamic plastic behaviours of the workpiece material is essential if accuracy in the predictions in desired. The generation of high strain rate/temperature data comes in the first place in this sense, because these are highly likely to be found when machining, therefore any material model that attempts to be used in FE modelling and proclaims to be competent, must include these data in its inherent formulation.

Moreover, the utilisation of physical/phenomenological based viscoplastic models, such as the MTS, to describe the flow behaviour of Inconel 718 superalloy has assured to be more reliable than JC, as predicted stress-strain curves matched perfectly their experimental counterparts. Furthermore, it demonstrated better accuracy in the prediction of cutting forces and chip morphology.

In conclusion, it is deeply advised not only to generate high strain rate/temperature data for their subsequent use in constitutive models that could make proper estimations when representing the machining process by means of the FE method, but also to employ those that have stronger physical/mechanical backgrounds compared to the ones being purely empirical.

Surface integrity parameters prediction: In order to go further in the FE modelling exercise, a new model which accounted for grain refinement prediction was proposed, as it was found by experimental means following the orthogonal machining of Inconel 718 that this effect had taken place in the machined surface. The DRX module, which was linked to the MTS and RWM models, predicted adequately the final grain size as well as the (variable) thickness of the altered layer, in spite of not having been derived from physical principles. Nevertheless, it is clearly seen that these relationships/links/connections would have been impossible to make if the constitutive model had been of an empirical nature.

In this regard therefore, the most suitable way to deal with the prediction of surface integrity parameters following the machining operation seems to be by commencing with the development of a robust constitutive model, which could lead the way to more sophisticated and reliable models that could account for any surface modification of choice.

Even though the DRX model proposed in this work lacks of fundamental physical foundations, it would be expected (and suggested) to dedicate more efforts on this brand new developed path of investigation.

CHAPTER 8

REFERENCES

ABAQUS User Subroutines Reference Manual, 2010. Dassault Systemes Simulia Corp., Providence, RI, USA.

Abrao A.M., Aspinwall D.K., 1996. **The surface integrity of turned and ground hardened bearing steel**, Wear 196(1-2), 279-284.

Antolovich B.F., Evans M.D., 2000. **Predicting Grain Size Evolution of UDIMET® Alloy 718 During the 'Cogging' Process Through the Use of Numerical Analysis**, Superalloys, 9th International Symposium on Superalloys, 39-48.

Arrazola P.J., Ozel T., 2010. **Investigations on the effects of friction modeling in finite element simulation of machining**, International Journal of Mechanical Sciences 52(1), 31-42.

Arrazola P.J., Ugarte D., Domínguez X., 2008. **A new approach for the friction identification during machining through the use of finite element modeling**, International Journal of Machine Tools and Manufacture 48(2), 173-183.

ASME Brochure, 2006. **Split Hopkinson Pressure Bar Apparatus: An Historic Mechanical Engineering Landmark**, Southwest Research Institute, San Antonio, Texas, USA.

Bailey J.A., Jeelani S., Becker S.E., 1976. **Surface Integrity in Machining AISI 4340 Steel**, Transactions of the American Society of Mechanical Engineers, Journal of Engineering for Industry 98(3), 999-1006.

Banerjee B., 2007. **The Mechanical Threshold Stress model for various tempers of AISI 4340 steel**, International Journal of Solids and Structures 44(3-4), 834-859.

Barbacki A., Kawalec M., Hamrol A., 2003. **Turning and grinding as a source of microstructural changes in the surface layer of hardened steel**, Journal of Materials Processing Technology 133(1-2), 21-25.

Battaglia J.L., Cois O., Puigsegur L., Oustaloup A., 2001. **Solving an inverse heat conduction problem using a non-integer identified model**, International Journal of Heat and Mass Transfer 44(4), 2671-2680.

Boivineau M., Cagran C., Doytier D., Eyraud V., Nadal M.-H., Wilthan B., Pottlacher G., 2006. **Thermophysical Properties of Solid and Liquid Ti-6Al-4V (TA6V) Alloy**, International Journal of Thermophysics 27(2), 507-529.

Boothroyd G., 1961. **Photographic technique for the determination of metal cutting temperatures**, British Journal of Applied Physics 12, 238-242.

Boothroyd G., 1963. **Temperatures in Orthogonal Metal Cutting**, Proceedings of the Institution of Mechanical Engineers 177(1), 789-810.

Bower A.F., 2009. **Applied Mechanics of Solids**, CRC Press, Taylor & Francis Group, New York, USA. ISBN 10-1439802475.

Brand A.J., Karhausen K., Kopp R., 1996. **Microstructural simulation of nickel base alloy Inconel 718 in production of turbine discs**, Materials and Science Technology 12(11), 963-969.

Briks A.A., 1896. **Metal Cutting (in Russian)**, St. Petersburg, Dermakow Publishing House.

Brinksmeier E., Cammet J.T., Konig W., Leskovar P., Peters J., Tonshoff H.K., 1982. **Residual Stresses – Measurement and Causes in Machining Processes**, CIRP Annals – Manufacturing Technology 31(2), 491-510.

Brocail J., Watremez M., Dubar L., 2010. **Identification of a friction model for modelling orthogonal cutting**, International Journal of Machine Tools and Manufacture 50(9), 807-814.

Bushlya V., Zhou J.M., Lenrick F., Avdovic P., Stahl J-E., 2011. **Characterization of White Layer Generated when Turning Aged Inconel 718**, Procedia Engineering, 1st CIRP Conference on Surface Integrity (CSI) 19, 60-66.

Calamaz M., Coupard D., Girot F., 2008. **A new material model for 2D numerical simulation of serrated chip formation when machining titanium alloy Ti-6Al-4V**, International Journal of Machine Tools and Manufacture 48(3-4), 275-288.

Cappelini C., Attanasio A., Rotella G., Umbrello D., 2010. **Formation of white and dark layers in hard turning: influence of tool wear**, International Journal of Material Forming 3(1), 455-458.

Carroll III J.T., Strenkowski J.S., 1988. **Finite element models of orthogonal cutting with application to single point diamond turning**, International Journal of Mechanical Sciences 30(12), 899-920.

Caruso S., Outeiro J.C., Umbrello D., M'Saoubi R., 2010. **Modelling and Experimental Validation of the Surface Residual Stresses Induced by Hard Machining of AISI H13 Tool Steel**, International Journal of Material Forming 3(1), 515-518.

Ceretti E., Filice L., Umbrello D., Micari F., 2007. **ALE Simulation of orthogonal cutting: a new approach to model heat transfer phenomena at the tool-chip interface**, CIRP Annals – Manufacturing Technology 56(1), 97-72.

Ceretti E., Lucchi M., Altan T., 1999. **FEM simulation of orthogonal cutting: serrated chip formation**, Journal of Materials Processing Technology 95 (1-3), 17-26.

Chao B.T., Trigger K.J., 1955. **Temperature Distribution at Tool-Chip Interface in Metal Cutting**, Transactions of the American Society of Mechanical Engineers 77(2), 1107-1121.

Chao B.T., Trigger K.J., 1958. **Temperature Distribution at Tool-Chip and Tool-Work Interface in Metal Cutting**, Transactions of the American Society of Mechanical Engineers 80(1), 311-320.

Chaturvedi M.C., Han Y.F., 1983. **Strengthening mechanisms in Inconel 718 superalloy**, Metal Science 17(3), 145-149.

Che-Haron C.H., Ghani J.A., Ibrahim G.A., 2007. **Surface integrity of AISI D2 when turned using coated and uncoated carbide tools**, International Journal of Precision Tehcnology 1(1), 106-114.

Che-Haron C.H., Jawaid A., 2005. **The effect of machining on surface integrity of titanium alloy Ti-6% Al-4% V**, Journal of Materials Processing Technology 166(2), 188-192.

Chen G., Ren C., Yang X., Jin X., Guo T., 2011. **Finite element simulation of high-speed machining of titanium alloy (Ti-6Al-4V) based on ductile failure model**, The International Journal of Advanced Manufacturing Technology 56(9-12), 1027-1038.

Chen S.R., Gray III G.T., 1996. **Comparison Between the Mechanical Threshold Stress (Strength) Model and the New Zerilli-Armstrong Model**, Los Alamos National Laboratory. Los Alamos-Technical Report LA-UR-96-3534 (50 pp).

Cheng W.W., Song B., 2010. **Split Hopkinson (Kolsky) Bar: Design, Testing and Applications**, Springer. ISBN 978-1-4419-7981-0.

Childs T., Maekawa K., Obikawa T., Yamane Y., 2000. **Metal Machining: Theory and Applications**, Arnold, London, UK. ISBN 0-470-39245-2.

Choudhury I.A., El-Baradie M.A., 1998. **Machining nickel base superalloys: Inconel 718**, Proceedings of the Institution of Mechanical Engineers, Part B: Journal of Engineering Manufacture 212(3), 195-206.

Chuzhoy L., DeVor R.E., Kapoor S.G., Beaudoin A.J., Bammann D.J., 2003a. **Machining Simulation of Ductile Iron and its Constituents, Part 1: Estimation of Material Model Parameters and their Validation**, Journal of Manufacturing Science and Engineering 125(2), 181-191.

Chuzhoy L., DeVor R.E., Kapoor S.G., 2003b. **Machining Simulation of Ductile Iron and its Constituents, Part 2: Numerical Simulation and Experimental Validation of Machining**, Journal of Manufacturing Science and Engineering 125(2), 192-201.

Cockcroft M.G., Latham D.J., 1968. **Ductility and the workability of metals**, Journal of the Institute of Metals 96(2), 33-39.

Coelho R.T., Ng E., Elbestawi M.A., 2007. **Tool wear when turning hardened AISI 4340 with coated PBCN tools using finishing cutting conditions**, International Journal of Machine Tools and Manufacture 47(2), 263-272.

Cooper M.G., Mikic B.B., Yovanovich M.M., 1969. **Thermal contact conductance**, International Journal of Heat and Mass Transfer 12(3), 279-300.

Courbon C., Sajn V., Kramar D., Rech J., Kosel F., Kopac J., 2011. **Investigation of machining performance in high pressure jet assisted turning of Inconel 718: A numerical model**, Journal of Materials Processing Technology 211(11), 1834-1851.

Daridon L., Oussouadi O., Ahzi S., 2004. **Influence of the material constitutive models on the adiabatic shear band spacing: MTS, power law and Johnson-Cook models**, International Journal of Solids and Structures 41(11-12), 3109-3124.

da Silva M.G., Ramesh K.T., 1997. **The rate-dependent deformation and localization of fully dense and porous Ti-6Al-4V**, Materials Science and Engineering: A 232(1-2), 11-22.

Davies E.D.H., Hunter S.C., 1963. **The dynamic compression test of solids by the method of the split Hopkinson pressure bar**, Journal of the Mechanics and Physics of Solids 11(3), 155-179.

Davies R.M., 1948. **A critical study of the Hopkinson Pressure Bar**, Philosophical Transactions of the Royal Society A 240(821), 375-457.

Davim J.P. (Ed.), 2010. **Surface Integrity in Machining**, Springer, London, UK. ISBN 978-1-84882-873-5.

Davis J.W., 1997. ITER Materials Properties Handbook, ITER Document N° S74 RE1, 1-3.

DeMange J.J., Prakash V., Pereira J.M., 2009. **Effects of material microstructure on blunt projectile penetration of a nickel-based superalloy**, International Journal of Impact Engineering 36(8), 1027-1043.

Devillez A., Schneider F., Dominiak S., Dudzinski D., Larrouquere D., 2007. **Cutting forces and wear in dry machining Inconel 718 with coated carbide tools**, Wear 262(7-8), 931-942.

Ding H., Shin Y.C., 2011. **Dislocation density-based grain refinement modeling of orthogonal cutting of commercially pure Titanium**, Proceedings of the ASME 2011 International Manufacturing Science and Engineering Conference, MSEC2011-50220, American Society of Mechanical Engineers, Corvallis, Oregon, USA, 1-10.

Dirikolu M.H., Childs T.H.C., Maekawa K., 2001. **Finite element simulation of chip flow in metal machining**, International Journal of Mechanical Sciences 43(11), 2699-2713.

Doherty R.D., Hughes D.A., Humphreys F.J., Jonas J.J., Juul Jensen D., Kassner M.E., King W.E., McNelley T.R., McQueen H.J., Rollett A.D., 1997. **Current issues in recrystallization: a review**, Materials Science and Engineering: A 238(2), 219-274.

Donachie M.J., Donachie S.J., 2002. **Superalloys: A Technical guide**, ASM International, Ohio, USA. ISBN 0-87170-749-7.

Dutt R.P., Brewer R.C., 1965. **On the Theoretical Determination of the Temperature Field in Orthogonal Machining**, The International Journal of Production Research 4(2), 91-114.

Enahoro H.E., Oxley P.L.B., 1966. **Flow Along Tool-Chip Interface in Orthogonal Metal Cutting**, Journal of Mechanical Engineering Science 8(1), 36-41.

Ernst H., 1938. **Physics of Metal Cutting**, Machining of metals, ASM, 1-34.

Ernst H., Merchant M.E., 1940. Conference on Friction and Surface Finish, Massachusetts Institute of Technology, Cambridge, Massachusetts, 76.

Ernst H., Merchant M.E., 1941. **Chip Formation, Friction, and High-Quality Machined Surfaces**, Surface Treatment of Metals, ASM 29, 299.

Estrin Y., Mecking H., 1984. **A unified phenomenological description of work hardening and creep based on one-parameter models**, Acta Metallurgica 32(1), 57-70.

Ezugwu E.O., Wang Z.M., 1997. **Titanium alloys and their machinability – a review**, Journal of Materials Processing Technology 68(3), 262-274.

Fang N., Jawahir I.S., Oxley P.L.B., 2001. **A universal slip-line model with non-unique solutions for machining with curled chip formation and a restricted contact tool**, International Journal of Mechanical Sciences 43(2), 557-580.

Fenton R.G., Oxley P.L.B., 1969. **Mechanics of Orthogonal Machining: Allowing for the Effects of Strain Rate and Temperature on Tool-Chip Friction**, Proceedings of the Institution of Mechanical Engineers 183(1), 417-438.

Fenton R.G., Oxley P.L.B., 1970. **Mechanics of Orthogonal Machining: Predicting Chip Geometry and Cutting Forces from Work-Material Properties and Cutting Conditions**, Proceedings of the Institution of Mechanical Engineers 184(1), 927-942.

Field M., Khales J.F., 1964. **The surface integrity of machined and ground high strength steels**, DMIC Report 210, 54-77.

Field M., Khales J.F., 1971. **Review of surface integrity of machined components**, CIRP Annals – Manufacturing Technology 20(2), 153-162.

Field M., Khales J.F., Cammet J.T., 1972. **Review of measuring methods for surface integrity**, CIRP Annals – Manufacturing Technology 21, 219-238.

Filice L., Micari F., Rizzuti S., Umbrello D., 2007. **A critical analysis of the friction modelling in orthogonal machining**, International Journal of Machine Tools and Manufacture 47(3-4), 709-714.

Follansbee, P.S., Gray III, G.T., 1989. **An analysis of the low temperature low and high strain rate deformation of Ti-6Al-4V**, Metallurgical Transactions A 20(5), 863-874.

Follansbee, P.S., Huang J.C., Gray III, G.T., 1990. **Low-temperature and high-strain-rate deformation of nickel and nickel-carbon alloys and analysis of the constitutive behavior according to an internal state variable model**, Acta Metallurgica et Materialia 38(7), 1241-1254.

Follansbee P.S., Kocks U.F., 1988. **A Constitutive Description of the Deformation of Copper Based on the Use of the Mechanical Threshold Stress as an Internal State Variable**, Acta Metallurgica 36(1), 81-93.

Goto D.M., Garrett Jr. R.K., Bingert J.F., Chen S.R., Gray III G.T., 2000. **The Mechanical Threshold Stress Constitutive-Strength Model Description of HY-100 Steel**, Metallurgical and Materials Transactions A 31(8), 1985-1996.

Guo Y.B., Li W., Jawahir I.S., 2009. **Surface integrity characterization and prediction in machining of hardened and difficult-to-machine alloys: A state-of-art research review and analysis**, Machining Science and Technology: An International Journal 13(4), 437-470.

Hahn R.S., 1951. **On the Temperature Developed at the Shear Plane in the Metal Cutting Process**, Proceedings of the 1st United States National Congress of Applied Mechanics, 661-666.

Hauser F.E., Simmons J.A., Dorn J.E., 1961. **Strain rate effects in plastic wave propagation**, Conference Proceedings Colorado, Response of Metals to High Velocity Deformation, Ed. Shewmon P.G., Zackay V.F., Interscience, New York, 93-110.

Herbert C.R.J., Axinte D.A., Hardy M.C., Brown P.D., 2011. **Investigation into the characteristics of white layers produced in a nickel-based superalloy from drilling operations**, Procedia Engineering, 1st CIRP Conference on Surface Integrity (CSI) 19, 138-143.

Hill R., 1954. **On the limits set by plastic yielding to the intensity of singularities of stress**. Journal of the Mechanics and Physics of Solids 2, 278-285.

Hollander M.B., 1959. **An Infra-red, micro-radiation pyrometer technique investigation of the temperature distribution in the workpiece during metal cutting**, ASTE Research Report N°21.

Hopkinson B., 1914. **A Method for Measuring the Pressure Produced in the Detonation of High Explosives or by the Impact of Bullets**, Philosophical Transactions of the Royal Society of London A 213, 437-456.

Iqbal S.A., Mativenga P.T., Sheikh M.A., 2008. **An investigative study of the interface heat transfer coeeficient for finite element modelling of high-speed machining**, Proceedings of the Institution of Mechanical Engineers, Part B: Journal of Engineering Manufacture 222(11), 1405-1416.

Iqbal S.A., Mativenga P.T., Sheikh M.A., 2008. **A comparative study of the tool-chip contact length in turning of two engineering alloys for a wide range of cutting speeds**, International Journal of Advanced Manufacturing Technology 42(1-2), 30-40.

Iwata K., Osakada K., Terasaka Y., 1984. **Process Modeling of Orthogonal Cutting by the Rigid Plastic Finite Element Method**, Journal of Engineering Materials and Technology 106(2), 132-138.

Jam J.E., Fard V.N., 2011. **A novel method to determine tool-chip thermal contact conductance in machining**, International Journal of Engineering Science and Technology 3(12), 8491-8501.

Jaspers S.P.F.C., 1999. **Metal cutting mechanics and material behaviour**, Eindhoven, Technische Universiteit Eindhoven. ISBN 90-386-0950-7.

Jawahir I.S., Brinksmeir E., M'Saoubi R., Aspinwall D.K., Outeiro J.C., Meyer D., Umbrello D., Jayal A.D., 2011. **Surface integrity in material removal processes: Recent advances**, CIRP Annals – Manufacturing Technology 60(2), 603-626.

Johnson G.R., Cook W.H., 1983. **A constitutive model and data for metals subjected to large strains, high strain rates and high temperatures**, Proceedings of the 7th International Symposium on Ballistics, The Hague, The Netherlands, 1-7.

Johnson G.R., Cook, W.H., 1985. **Fracture Characteristics of Three Metals Subjected to Various Strains, Strain Rates, Temperatures and Pressures**, Engineering Fracture Mechanics 21(1), 31-48.

Karpat Y., 2011. **Temperature dependent flow softening of titanium alloy Ti6Al4V: An investigation using finite element simulation of machining**, Journal of Materials Processing Technology 211(4), 737-749.

Kececioglu D., 1958. **Shear-Zone Temperature in Metal Cutting and its Effects on Shear-Flow Stress**, Transactions of the American Society of Mechanical Engineers 80, 541-546.

Kitagawa T., Kubo A., Maekawa K., 1997. **Tempearture and wear of cutting tools in high-speed machining of Inconel 718 and Ti-6Al-6V-2Sn**, Wear 202(2), 142-148.

Kobayashi T., Simons J.W., Brown C.S., Shockey D.A., 2008. **Plastic flow behaviour of Inconel 718 under dynamic shear loads**, International Journal of Impact Engineering 35(5), 389-396.

Kolsky H., 1949. **An Investigation of the Mechanical Properties of Materials at very High Rates of Loading**, Proceedings of the Physical Society B 62(11), 676-700.

Komanduri R., Hou Z.B., 2001. **Thermal modeling of the metal cutting process - Part III: temperature rise distribution due to the combined effects of shear plane heat source and the tool-chip interface frictional heat source**, International Journal of Mechanical Sciences 43(1), 89-107.

Komvopoulos K., Erpenbeck S.A., 1991. **Finite element modeling of orthogonal cutting**, Transactions of the American Society of Mechanical Engineers, Journal of Engineering for Industry 113(1), 253-267.

Krafft J.M., Sullivan A.M., Tipper C.F., 1954. **The effect of static and dynamic loading and temperature on the yield stress of iron and mild steel in compression**, Proceedings of the Royal Society A 221(1144), 114-127.

Landon J.W., Quinney H., 1923. **Experiments with the Hopkinson Pressure Bar**, Proceedings of the Royal Society of London A 103(723), 622-643.

Lee E.H., Shaffer B.W., 1951. **The Theory of Plasticity Applied to a Problem of Machining**, Transactions of the American Society of Mechanical Engineers, Journal of Applied Mechanics 18, 405-413.

Lee W.S., Lin C.F., 1998. **Plastic deformation and fracture behaviour of Ti-6Al-4V alloy loaded with high strain rate under various temperatures**, Materials Science and Engineering: A 241(1-2), 48-59.

Lee W.S., Lin C.F., Chen T.H., Chen H.W., 2011. **Dynamic mechanical behaviour and dislocation substructure evolution of Inconel 718 over wide temperature range**, Materials Science and Engineering: A 528(19-20), 6279-6286.

Leone W.C., 1954. **Distribution of Shear-Zone Heat in Metal Cutting**, Transactions of the American Society of Mechanical Engineers 76, 121-125.

Lesuer D. R., 2000. **Experimental Investigations of Material Models for Ti-6Al-4V Titanium and 2024-T3 Aluminium**. U.S. Department of Transportation. Office of Aviation Research-Technical Report, 41 pp.

Li R., Shih A.J., 2005. **Finite element modeling of 3D turning of titanium**, The International Journal of Advanced Manufacturing Technology 29(3-4), 253-261.

Liang R., Khan A.S., 1999. **A critical review of experimental results and constitutive models for BCC and FCC metals over a wide range of strain rates and temperatures**, International Journal of Plasticity 15(9), 963-980.

Lin J., Liu Y., Farrugia D.C.J., Zhou M., 2005. **Development of dislocation-based unified material model for simulating microstructure evolution in multipass hot rolling**, Philosophical Magazine 85(18), 1967-1987.

Lin Y.P., Lin Y., Dean T.A., Brown P.D., 2007. **Modelling of Viscoplastic Behaviour of In718 Under Hot Forging Conditions**, AIP Conference Proceedings, 10th ESAFORM Conference on Material Forming 907(1), 1199-1204.

Lindholm U.S., 1964. **Some experiments with the split hopkinson pressure bar**, Journal of the Mechanics and Physics of Solids 12(5), 317-335.

Lindholm U.S., Yeakley L.M., 1968. **High Strain-rate Testing: Tension and Compression**, Experimental Mechanics 8(1), 1-9.

Liu Y., Lin J., 2003. **Modelling of microstructural evolution in multipass hot rolling**, Journal of Materials Processing Technology 143-144, 723-728.

Llanos I., Villar J.A., Urresti I., Arrazola P.J., 2009. **Finite element modeling of oblique machining using an arbitrary Lagrangian-Eulerian formulation**, Machining Science and Technology: An International Journal 13(3), 385-406.

Loewen E.G., Shaw M.C., 1954. **On the Analysis of Cutting-Tool Temperatures**, Transactions of the American Society of Mechanical Engineers 76, 217-231.

Lorentzon J., Jarvstrat N., Josefson B.L., 2009. **Modelling chip formation of alloy 718**, Journal of Materials Processing Technology 209(10), 4645-4653.

Lubliner J., 2008. **Plasticity Theory**, Dover Publications, New York, USA. ISBN-10:048642900.

Mackerle J., 1999. **Finite-element analysis and simulation of machining: a bibliography**, Journal of Materials Processing Technology 86(1-3), 17-44.

Mantle A.L., Aspinwall D.K., 1997. **Surface integrity and fatigue life of turned gamma titanium aluminide**, Journal of Materials Processing Technology 72(3), 413-420.

Matsumoto Y., Barash M.M., Liu C.R., 1986. **Effect of Hardness on the Surface Integrity of AISI 4340 Steel**, Transactions of the American Society of Mechanical Engineers, Journal of Engineering for Industry 108(3), 169-175.

Matsumoto Y., Hashimoto F., Lahoti G., 1999. **Surface Integrity Generated by Precision Hard Turning**, CIRP Annals – Manufacturing Technology 48(1), 59-62.

Mecking H., Kocks U.F., 1981. **Kinetics of flow and strain-hardening**, Acta Metallurgica 29(11), 1865-1875.

Medeiros S.C., Prasad Y.V.R.K., Frazier W.G., Srinivasan R., 2000. **Modeling grain size during hot deformation of In 718**, Scripta Materialia 42(1), 17-23.

Merchant M.E., 1944. **Basic Mechanics of the Metal Cutting Process**, Journal of Applied Mechanics 11, A168-A175.

Merchant M.E., 1945. **Mechanics of the Metal Cutting Process. II. Plasticity Conditions in Orthogonal Machining**. Journal of Applied Physics 16, 318-324.

Meyers M.A., Benson D.J., Vohringer O., Kad B.K., Xue Q., Fu H.H., 2002. **Constitutive description of dynamic deformation: physically-based mechanisms**, Materials Science and Engineering: A 322(1-2), 194-216.

Mikic B.B., 1974. **Thermal contact conductance; Theoretical considerations**, International Journal of Heat and Mass Transfer 17(2), 205-214.

Military Handbook, 1993. **Metallic Materials and Elements for Aerospace Vehicle Structures**, Department of Defense, USA.

Mitrofanov A.V., Babitsky V.I., Silberschmidt V.V., 2005. **Thermomechanical finite element simulations of ultrasonically assisted turning**, Computational Materials Science 32(3-4), 463-471.

Molinari A., Soldani X., Miguelez M.H., 2013. **Adiabatic shear banding and scaling laws in chip formation with application to cutting of Ti-6Al-4V**, Journal of the Mechanics and Physics of Solids 61(11), 2331-2359.

Movahhedy M., Gadala M.S., Altintas Y., 2000. **Simulation of the orthogonal metal cutting process using an arbitrary Lagrangian-Eulerian finite-element method**, Journal of Materials Processing Technology 103(2), 267-275.

M'Saoubi R., Axinte D., Herbert C., Hardy M., Salmon P., 2014. **Surface integrity of nickel-based superalloys subjected to severe plastic deformation by abusive drilling**, CIRP Annals – Manufacturing Technology 63(1), 61-64.

M'Saoubi R., Larsson T., Outeiro J., Guo Y., Suslov S., Saldana C., Chandrasekar S., 2012. **Surface integrity analysis of machined Inconel 718 over multiple length scales**, CIRP Annals – Manufacturing Technology 61(1), 99-102.

M'Saoubi R., Outeiro J.C., Chandrasekaran H., Dillon Jr. O.W., Jawahir I.S., 2008. **A review of surface integrity in machining and its impact on functional performance and life of machined products**, International Journal of Sustainable Manufacturing 1(1-2), 203-236.

Murr L.E., Pinaza C., 2007. **Dynamic Recrystallization: The Dynamic Deformation Regime**, Metallurgical and Materials Transactions A 38(11), 2611-2628.

Nakayama K., 1958. **Studies on the mechanism of metal cutting**, Bulletin of Faculty of Engineering, Yokohama National University 7, 1.

Ng E., Aspinwall D.K., 2002. **Modelling of hard part machining**, Journal of Materials Processing Technology 127(2), 222-229.

Outeiro J.C., Pina J.C., M'Saoubi R., Pusavec F., Jawahir I.S., 2008. **Analysis of residual stresses induced by dry turning of difficult-to-machine materials**, CIRP Annals – Manufacturing Technology 57(1), 77-80.

Outeiro J.C., Rossi F., Fromentin G., Poulachon G., Germain G., Batista A.C., 2013. **Process Mechanics and Surface Integrity Induced by Dry and Cryogenic Machining of AZ31B-O Magnesium Alloy**, Procedia CIRP, 14th CIRP Conference on Modeling of Machining Operations (CIRP CMMO) 8, 487-492.

Oxley P.L.B., 1961. **A Strain-Hardening Solution for the "Shear Angle" in Orthogonal Metal Cutting**, International Journal of Mechanical Sciences 3, 68-79.

Oxley P.L.B., Hatton A.P., 1963. **Shear Angle Solution Based on Experimental Shear Zone and Tool-Chip Interface Stress Distributions**, International Journal of Mechanical Sciences 5, 41-55.

Oxley P.L.B., Humphreys A.G., Larizadeh A., 1961. **The Influence of Rate of Strain-Hardening in Machining**, Proceedings of the Institution of Mechanical Engineers 175(1), 881-891.

Oxley P.L.B., Welsh M.J.M., 1961. **Calculating the Shear Angle in Orthogonal Metal Cutting from Fundamental Stress-Strain-Strain Rate properties of the Work Material**, Proceedings of the 4th International Machine Tool Design and Research Conference, 73-86.

Ozel T., 2006. **The influence of friction models on finite element simulations of machining**, International Journal of Machine Tools and Manufacture 46(5), 518-530.

Ozel T., Altan T., 2000. **Determination of workpiece flow stress and friction at the chip-tool contact for high-speed cutting**, International Journal of Machine Tools and Manufacture 40(1), 133-152.

Ozel T., Llanos I., Soriano J., Arrazola P.J., 2011. **3D Finite element modeling of chip formation process for machining Inconel 718: Comparison of FE software predictions**, Machining Science and Technoogy: An International Jounal 15(1), 21-46.

Ozel T., Sima M., Srivastava A.K., Kaftanoglu B., 2010. **Investigations on the effects of multi-layered coated inserts in machining Ti-6Al-4V alloy with experiments and finite element simulations**, CIRP Annals – Manufacturing Technology 59(1), 77-82.

Ozel T., Zeren E., 2007. **Finite element modeling the influence of edge roundness on the stress and temperature fields induced by high-speed machining**, The International Journal of Advanced Manufacturing Technology 35(3-4), 255-267.

Ozlu E., Molinari A., Budak E., 2010. **Two-zone analytical contact model applied to orthogonal cutting**, Machining Science and Technology: An International Journal 14(3), 323-343.

Palmer W.B., Oxley P.L.B., 1959. **Mechanics of Orthogonal Machining**, Proceedings of the Institution of Mechanical Engineers 173(1), 623-654.

Park N.K., Kim I.S., Na Y.S., Yeom J.T., 2001. **Hot forging of a nickel-base superalloy**, Journal of Materials Processing Technology 111(1-3), 98-102.

Pereira J.M., Lerch B.A., 2001. **Effects of heat treatment on the ballistic impact properties of Inconel 718 for jet engine fan containment applications**, International Journal of Impact Engineering 25(8), 715-733.

Piispanen V., 1937. **Lastunmuodostumisen Teoriaa (in Finnish)**, Teknillinen Aikakauslenti 27, 315-322.

Pollock T.M., Tin S., 2006. **Nickel-Based Superalloys for Advanced Turbine Engines: Chemistry, Microstructure, and Properties**, Journal of Propulsion and Power 22(2), 361-374.

Pu Z., Outeiro J.C., Batista A.C., Dillon Jr. O.W., Puleo D.A., Jawahir I.S., 2012. **Enhanced surface integrity of AZ31B Mg alloy by cryogenic machining towards improved functional performance of machined components**, International Journal of Machine Tools and Manufacture 56, 17-27.

Ranganath S., Guo C., Hedge P., 2009. **A finite element modeling approach to predicting white layer formation in nickel superalloys**, CIRP Annals – Manufacturing Technology 58(1), 77-80.

Rao B., Dandekar C.R., Shin Y.C., 2011. **An experimental study on the face milling of Ti-6Al-4V alloy: Tool performance and surface integrity**, Journal of Materials Processing Technology 211(2), 294-304.

Rapier A.C., 1954. **A theoretical investigation of the temperature distribution in the metal cutting process**, British Journal of Applied Physics 5, 400-405.

Rech J., Battaglia J.L., Moisan A., 2005. **Thermal influence of cutting tool coatings**, Journal of Materials Processing Technology 159(1), 119-124.

Reed R.C, 2006. **The Superalloys: Fundamentals and Applications**, Cambridge University Press, Cambridge, UK. ISBN-10: 0-521-85904-2.

Rice J.R., 1970. **On the structure of stress-strain relations for time dependent plastic deformation in metals**, Transactions of the American Society of Mechanical Engineers, Journal of Applied Mechanics 37(3), 728-737.

Rittel D., 2009. **A different viewpoint on adiabatic shear localization**, Journal of Physics D: Applied Physics 42(21), 214009 (6pp).

Rittel D., Landau P., Venkert A., 2008. **Dynamic Recrystallization as a Potential Cause for Adiabatic Shear Failure**, Physical Review Letters 101(16), 165501 (4pp).

Rittel D., Wang Z.G., Merzer M., 2006. **Adiabatic Shear Failure and Dynamic Stored Energy of Cold Work**, Physical Review Letters 96(7), 075502 (4pp).

Rotella G., Settineri L., Umbrello D., Dillon Jr. O.W., Jawahir I.S., 2012. **Finite Element Modeling of Microstructural Changes in Turning of AA7075-T651 Alloy and Validation**, Transactions of the North American Manufacturing Research Conference, Institution of SME 40, 481-490.

Roth R.N., Oxley P.L.B., 1971. **Slip-Line Field Analysis for Orthogonal Machining Based upon Experimental Flow Fields**, Journal of Mechanical Engineering Science 14(2), 85-97.

Sadat A.B., 1987. **Surface region damage of machined inconel-718 nickel-base superalloy using natural and controlled contact length tools**, Wear 119(2), 225-235.

Sadat A.B., Reddy M.Y., 1992. **Surface region damage of machined inconel-718 nickel-base superalloy using controlled and natural contact length tools. Part I: Lubricated**, Experimental Mechanics 32(3), 282-288.

Sadat A.B., Reddy M.Y., 1993. **Surface region damage of machined inconel-718 nickel-base superalloy using controlled and natural contact length tools. Part II: Unlubricated**, Experimental Mechanics 33(4), 343-348.

Salem J.A., Lerch B., Thesken J.C., Sutter J., Russel R., 2008. **Strength, Fatigue and Fracture Toughness of Ti-6Al-4V Liner From a Composite Over-Wrapped Pressure Vessel**. NASA/TM-2008-215147, USA.

Sandvik Coromant AB General Turning catalogue, 2011.

Sartkulvanich P., Koppka F., Altan T., 2004. **Determination of flow stress for metal cutting simulation – a progress report**, Journal of Materials Processing Technology 146(1), 61-71.

Sasahara H., Obikawa T., Shirakashi T., 1996. **FEM analysis of cutting sequence effect on mechanical characteristics in machined layer**, Journal of Materials Processing Technology 62(4), 448-453.

Sharman A.R.C., Hughes J.I., Ridgway K., 2006. **An analysis of the residual stresses generated in Inconel 718™ when turning**, Journal of Materials Processing Technology 173(3), 359-367.

Shaw M.C., Cook N.H., Finnie I., 1953. **The Shear-Angle Relationship in Metal Cutting**, Transactions of the American Society of Mechanical Engineers, Journal of Engineering for Industry 75, 273-288.

Sharpe Jr. W.N. (Ed.), 2008. **Springer Handbook of Experimental Solid Mechanics**, Springer. ISBN 978-0-387-26883-5.

Shekhar S., Abolghashem S., Basu S., Cai J., Ravi Shankar M., 2012. **Interactive effects of strain, strain-rate and temperatures on microstructure evolution in high rate severe plastic deformation**, Materials Science Forum 702-703, 139-142.

Shi B., Tounsi N., Attia H., 2010. **Identification of material constitutive laws for machining-Part II: Generation of the constitutive data and validation of the constitutive law**, Journal of Manufacturing Science and Engineering 132(5), 051009 (9pp).

Shi J., Liu C.R., 2004. **The Influence of Material Models on Finite Element Simulation of Machining**, Journal of Manufacturing Science and Engineering 126(4), 849-857.

Shih A.J., 1996. **Finite element analysis of the rake angle effects in orthogonal metal cutting**, International Journal of Mechanical Sciences 38(1), 1-17.

Sievert R., Noack H.D., Hamann A., Lowe P., Singh K.N., Kunecke G., Clos R., Schreppel U., Veit P., Uhlmann E., Zettier R., 2003. **Simulation der Spansegmentierung beim Hochgeschwindigkeits-Zerspanen unter Berücksichtigung duktiler Schädigung (in German)**, Technische Mechanik 23(2-4), 216-233.

Sima M., Ozel T., 2010. **Modified material constitutive models for serrated chip formation simulations and experimental validation in machining of titanium alloy Ti-6Al-4V**, International Journal of Machine Tools and Manufacture 50(11), 943-960.

Simoneau A., Ng E., Elbestawi M.A., 2006. **The Effect of Microstructure on Chip Formation and Surface Defects in Microscale, Mesoscale, and Macroscale Cutting of Steel**, CIRP Annals – Manufacturing Technology 55(1), 97-102.

Slama C., Abdellaoui M., 2000. **Structural characterization of the aged Inconel 718**, Journal of Alloys and Compounds 306(1-2), 277-284.

Song B., Connelly K., Korellis J., Lu W.Y., Antoun B.R., 2009. **Improved Kolsky-bar design for mechanical characterization of materials at high strain rates**, Measurement Science and Technology 20(11), 115701 (8pp).

Soo S.L., 2003. **3D modelling when high speed end milling Inconel 718 superalloy**, PhD thesis, University of Birmingham.

Special Metals Corporation Technical Bulletin, 2007. Publication number SMC-045.

Sweeney G., 1969. **The consistency of Experimental Observations with a Model for the Metal Cutting Process**, International Journal of Machine Tool Design and Research 9(3), 309-319.

Takeyama H., Usui E., 1958. **The Effect of Tool-Chip contact Area in Metal Machining**, Transactions of the American Society of Mechanical Engineers, Journal of Engineering for Industry 80(57-A-45), 1089-1096.

Tay A.O., Stevenson M.G., de Vahl Davis G., 1974. **Using the Finite Element Method to Determine Temperature Distributions in Orthogonal Machining**, Proceedings of the Institution of Mechanical Engineers 188(1), 627-638.

Thakur D.G., Ramamoorthy B., Vijayaraghavan L., 2009. **Study on the machinability characteristics of superalloy Inconel 718 during high speed turning**, Materials and Design 30(5), 1718-1725.

Thime I., 1870. **Soprotivlenie Mealov i Dereva Rezan'yu**, St. Petersburg, Russia.

Toropov A., Ko S-L., 2003. **Prediction of tool-chip contact length using a new slip-line solution for orthogonal cutting**, International Journal of Machine Tools and Manufacture 43(12), 1209-1215.

Torrano I., Barbero O., Kortabarria A., Arrazola P.J., 2011. **Prediction of Residual Stresses in Turning Inconel 718**, Advanced Materials Research 223, 421-430.

Uhlmann E., Graf Von der Schulenburg M., Zettier R., 2007. **Finite Element modeling and Cutting Simulation of Inconel 718**, CIRP Annals – Manufacturing Technology 56(1), 61-64.

Ulutan D., Ozel T., 2011. **Machining induced surface integrity in titanium and nickel alloys: A review**, International Journal of Machine Tools and Manufacture 51(3), 250-280.

Umbrello D., 2008. **Finite element simulation of conventional and high speed machining of Ti6Al4V alloy**, Journal of Materials Processing Technology 196(1-3), 79-87.

Umbrello D., 2013. **Investigation of surface integrity in dry machining of Inconel 718**, Journal of Advanced Manufacturing Technology 69(9-12), 2183-2190.

Umbrello D., Jawahir I.S., 2009. **Numerical modeling of the influence of process parameters and workpiece hardness on white layer formation in AISI 52100 steel**, The International Journal of Advanced Manufacturing Technology 44(9-10), 955-968.

Umbrello D., M'Saoubi R., Outeiro J.C., 2007. **The influence of Johnson-Cook material constants on finite element simulation of machining of AISI 316L steel**, International Journal of Machine Tools and Manufacture 47(3-4), 462-470.

Umbrello D., Outeiro J.C., M'Saoubi R., Jayal A.D., Jawahir I.S., 2010. **A numerical model incorporating the microstructure alteration for predicting residual stresses in hard machining of AISI 52100 steel**, CIRP Annals – Manufacturing Technology 59(1), 113-116.

Usui E., Shirakashi T., 1997. **Mechanics of machining – From descriptive to predictive theory**, ASME Publications, PED Sciences 39, 369-389.

Usui E., Takeyama H., 1960. **A Photoelastic analysis of machining stresses**, Transactions of the American Society of Mechanical Engineers, Journal of Engineering for Industry 82(4), 303-307.

Weiner J.H., 1955. **Shear-Plane Temperature Distribution in Orthogonal Cutting**, Transactions of the American Society of Mechanical Engineers 77(8), 1331-1341.

Welsch G., Boyer R., Collings E.W., 1994. **Materials Properties Handbook: Titanium Alloys**, ASM International, Ohio, USA. ISBN-10: 08717004811.

Wu H.C., 2004. **Continuum Mechanics and Plasticity**, CRC Press, Chapman & Hall/CRC, Florida, USA. ISBN 1-58488-363-4.

Zerilli F.J., Armstrong R.W., 1987. **Dislocation-mechanics-based constitutive relations for material dynamics calculations**, Journal of Applied Physics 61, 1816-1825.

Zhang S., Li J., Zhu X., Lv H., 2013. **Saw-tooth chip formation and its effects on cutting force fluctuation in turning Inconel 718**, International Journal of Precision Engineering and Manufaturing 14(6), 957-963.

Zhao X., Guest R.P., Tin S., Cole D., Brooks J.W., Peers M., 2004. **Modelling hot deformation of Inconel 718 using state variables**, Materials and Science Technology 20(11), 1414-1420.

Zhou J.M., Bushlya V., Peng R.L., Johansson S., Advovic P., Stahl J-E., 2011. **Effects of Tool Wear on Subsurface Deformation of Nickel-based Superalloy**, Procedia Engineering, 1st CIRP Conference on Surface Integrity (CSI) 19, 407-413.

Zhou L.X., Baker T.N., 1994. **Effects of strain rate and temperature on deformation behavior of IN 718 during high temperature deformation**, Materials Science and Engineering: A 177(1-2), 1-9.

Zorev N.N., 1963. **Results of the work in the field of the mechanics of metal cutting processes**, Proceedings of the Conference on Techniques of Engineering Manufacture, Institution of Mechanical Engineers, 255-270.

Zorev N.N., 1963. **Inter-relationship between shear processes occurring along the tool face and shear plane in metal cutting**, International Research in Production Engineering, ASME 42-49.

Zvorykin K.A., 1896. **On the force and energy necessary to separate the chip from the workpiece (in Russian)**, St. Petersburg, Vestnik Promuslenosty 123, 57-96.

APPENDIX I

SPLIT HOPKINSON PRESSURE BAR

AI.1 Fundamental principles and design best practices

There are three major sub-assemblies which are common to all SHPB testing machines (Chen and Song, 2010), irrespective of their final architecture. These are the striker launching system, the bars/cushion arrangement and the data acquisition system, as shown in Figure AI.1:

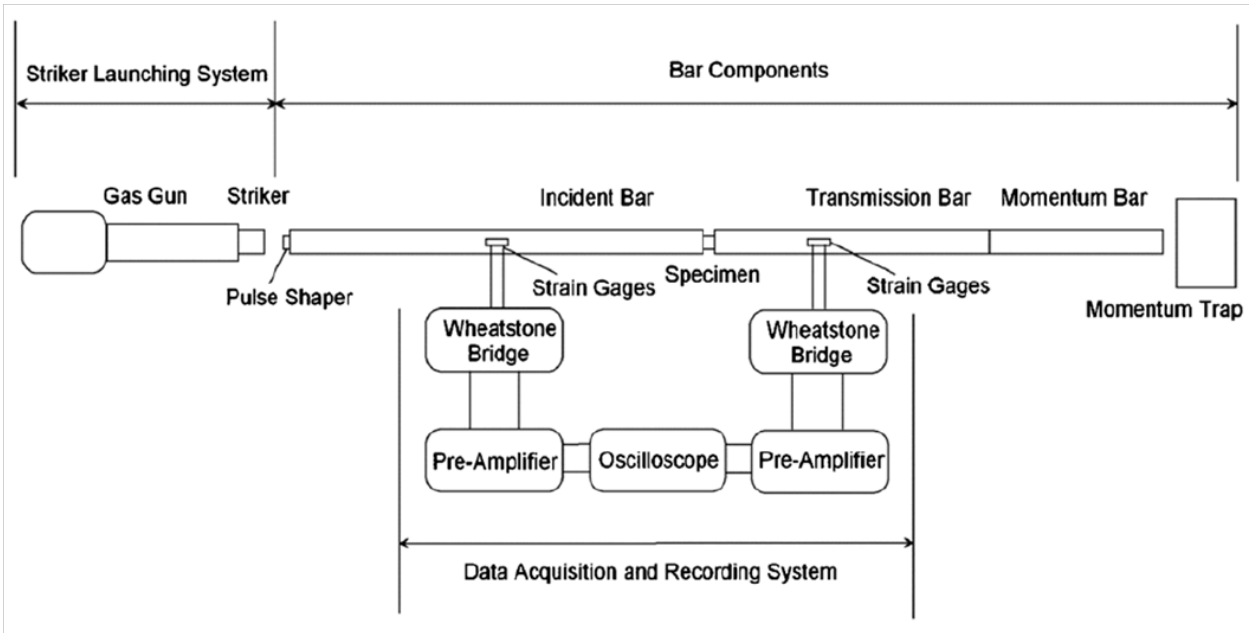

Figure AI.1. Split Hopkinson Pressure Bar testing apparatus sub-assemblies (Chen and Song, 2010).

The firing system consists in general of a pressurised gas reservoir (also known as the gas gun) which, when a (ball/solenoid type) valve is actuated, shoots the striker bar at high velocity that impacts the incident bar. The abrupt release of the fluid contained in the gas gun

(either compressed air or nitrogen sometimes to avoid condensation in the former) provokes the immediate acceleration of the striker bar which travels through a tube or gun barrel a certain distance and whose impact velocity can be increased by raising the pressure in the gas tank. In order to hit the incident bar at constant velocities with repeatable consistency, the gun barrel is drilled on its end to allow appropriate venting. Although not mandatory in most cases, the velocity at which the striker bar collides with the incident bar can be monitored if desired, e.g. by making use of laser technology.

The bars and cushion systems are designed to act as a medium to propagate the pressure waves and avoid the transmitter bar from travelling excessive distances and/or for safety reasons respectively. Unlike Figure AI.1, most practical SHPB machines do not incorporate a momentum bar to absorb the energy of the transmitter bar, but is instead achieved with a momentum trap. Striker, incident and transmitter bars typically have the same diameter and are made of the same material, which have elevated strength (not only on its surface, but also in its bulk) in order to remain elastic and enhance the measurement of the pressure waves throughout the duration of the trials.

The range of materials that is employed for fabricating the bars is fairly broad and includes tungsten, Maraging 250/300 steel and Inconel 718 superalloy to mention but a few, with the latter two generally used in their aged condition. The minimum length/diameter bar ratio recommended is 10 (Jaspers, 1999) in order to maintain the validity of the assumption that the pressure waves generated are one dimensional, however ratios can vary from 40 (Jaspers, 1999) to as high as 100 (Sharpe Jr., 2008) in some cases, depending on the requirements of each testing facility. The dimensions of the striker bar and its collision velocity are the principal factors that influence the size of the sample, which is usually constrained to verify a length/diameter ratio between 0.5-1 to minimise friction effects (Sharpe Jr., 2008).

The data acquisition scheme frequently consists of strain gauges located on both the incident and transmitter bars at a certain distance from their ends in order to capture with the maximum resolution possible, the incident (subscript I), reflected (subscript R) and transmitted (subscript T) pulses, as observed in the time-distance diagram plotted in Figure AI.2, where ε_I, ε_R and ε_T are the strains in each of the pulses that are actually measured by the strain gauges.

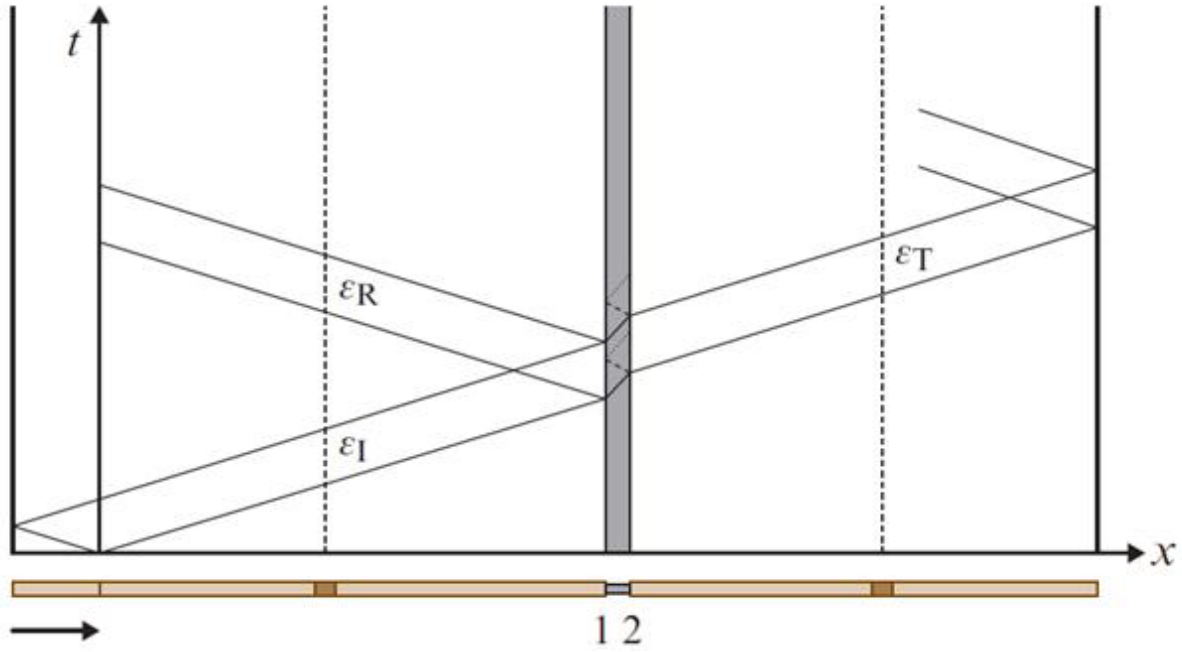

Figure AI.2. Time-distance diagram showing the incident, reflected and transmitted strains, according to Ramesh (2008) in Sharpe Jr. (2008).

Several vibrations of the initial pressure wave were also detected within the sample (between points 1-2), which instigates the material deformation. Therefore, the strain gauges must be situated in regions of the bars where no overlapping of the incident, reflected and transmitted pulses may occur, which are directed through a Wheatstone bridge, amplified and acquired on an oscilloscope. The recorded resolution of the pressure waves can be enhanced by increasing the frequency of the amplifiers and oscilloscope. A minimum value of 100kHz is suggested for all components of the acquisition and/or recording system in order to have an acceptable degree of confidence in the experimental results.

Further details regarding the mathematical theory of one dimensional wave propagation associated with the SHPB apparatus and proper treatment/translation of signals generated by the strain gauges to stress-strain curves as well as additional characteristics of the machine are given by Chen and Song (2010).

Figure AI.3 details a schematic illustration of a working SHPB apparatus (courtesy of the Southwest Research Institute) which clearly shows the general configuration of the gas tank, striker/incident/transmitter bars, the reverberating pulse acting on the sample as well as the customary shape of the pulses that are recorded by the strain gauges situated on the incident and transmitter bars and further displayed on the oscilloscope.

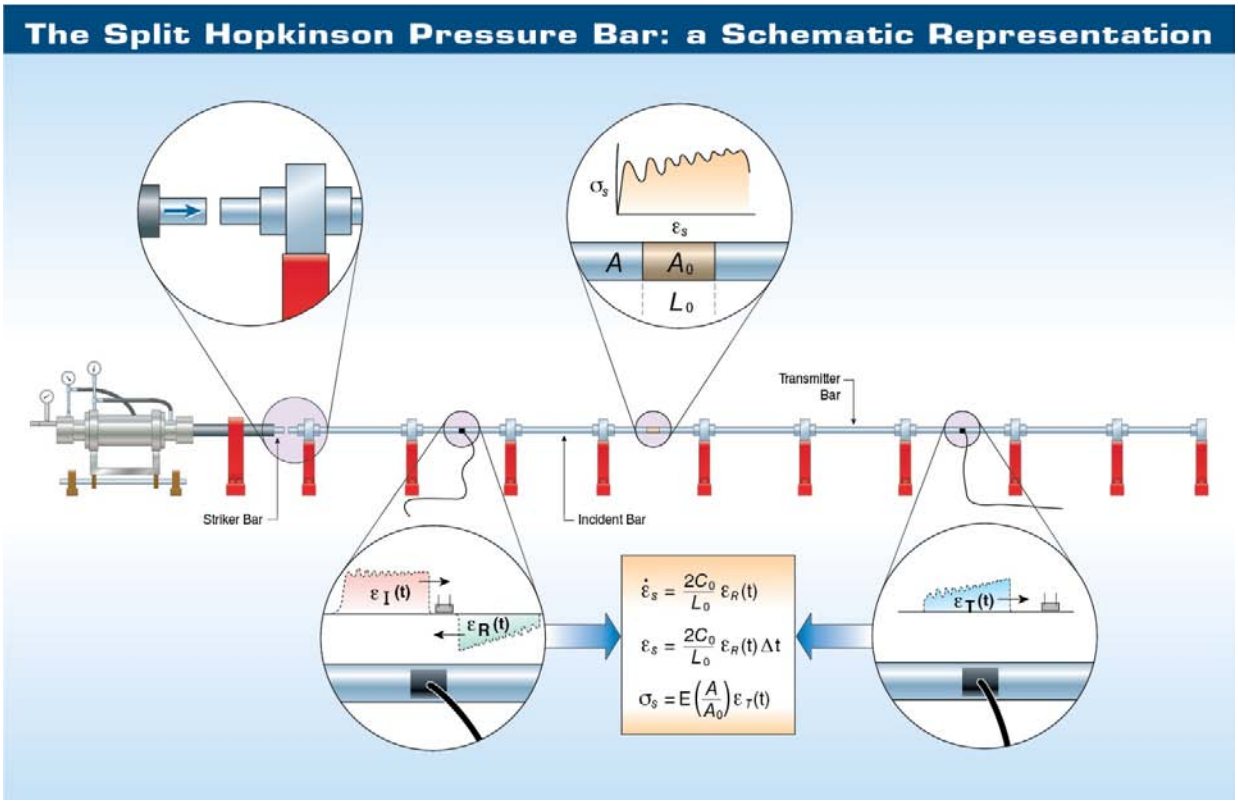

Figure AI.3. Split Hopkinson Pressure Bar testing apparatus schematic (image courtesy of Southwest Research Institute).

There is no design standard available for a SHPB system (Song et al., 2009), hence knowledge of related mechanical design/set-up/calibration is acquired through experience and by trial and error. Nonetheless, the following summary based on an extensive review of the literature, provides the fundamental principles to consider when designing a SHPB machine:

- The typical strain rates achieved can vary from 100 to 10,000s^{-1},
- Most SHPB units are designed with incident/transmitter bars that have diameters ranging from 10 to 25mm. However, smaller diameters from 7 to 13mm are also employed in order to achieve strain rates higher than 10,000s^{-1} (corresponding to a 'miniature' SHPB),
- The pulse (loading) duration is inversely proportional to the wave speed of the striker bar (material dependent) while it is proportional to the bar's length,
- Commonly, the length/diameter ratio of the incident and transmitter bars should vary from 40 to 100 to maintain the one-dimensionality of the pressure waves,
- The strain rate exerted to the specimen is inversely proportional to its thickness,
- The minimum suggested length/diameter ratio for the sample is 0.5 while a value of 1 is the generally recommended,
- The ratio between the incident (or the transmitter) bar diameter and the specimen diameter is recommended to be between 2 and 4.

AI.2 Design - University of Birmingham

At commencement of the doctoral study in October 2010, there was no in-house SHPB apparatus nor appropriate drawings to construct the testing machine, although an earlier initiative had amassed a number of relevant items of equipment. The task of designing a SHPB apparatus was therefore initiated using the parts/components bought previously. Table AI.1 summarises the parts available prior to the design of the SHPB.

Part	Qty.	Source	Model	Cost £ (each)	Total Cost £
Air Reservoir	1	Multi Pneumatics (Redditch) Ltd.	CRVZS-10 – Festo PN 160237 (10L)	209.55	209.55
Bearing	6	CBS Rotary Power Motion Ltd.	Linear Bearing LBE 25 AJ Split	10.70	64.20
Bearing House	6		Bearing Housing Support Block GW25	15.71	94.26
Induction Heater	1	Cheltenham Induction Heating Ltd.	Ambrell – EasyHeat 1.2Kw-2.4Kw/PN 801-9309	-	-
Pressure Bar	1	Maher Ltd.	C350 Round Black Bar Maraging Steel – Ø25mm x 2.40m	455.32	455.32
I-Beam	1	F.H. Warden Steel Ltd.	165x305x4.2mm	270.25	270.25
Legs	1		100x50x5mm – 7.5m	113.27	113.27
Steel	1		150x12mm BDMS – 3.0m	111.63	111.63

Table AI.1. Components available prior to the design of the SHPB machine, including individual and total cost (prices valid in 2010).

Preliminary assumptions were made with corresponding calculations to corroborate part dimensions and/or suggest probable machine specifications:

- At a strain rate of 10,000s^{-1} the SHPB must be able to produce a strain of 0.4 (max. 0.5) whereas at low strain rates (100s^{-1}), it must be able to produce a strain of 0.2 (min. 0.1),
- The maximum stress value exerted to the sample is adopted to be 1,500MPa (typical value for metallic samples),
- The striker, incident and transmitter bars have the same diameter (25mm) and material (Maraging steel) and both incident and transmitter bars have the same length,
- Sample dimensions are 5mm length (Le) x 10mm diameter (Di), Le/Di ratio 0.5,
- The barrel length to be set 2m,
- The air reservoir operating at pressure to range from 0.95bar to 16bar.

Following a series of trial and error iterations to achieve the optimum design for the SHPB instrument, the following conclusions were drawn:

- Using 25mm diameter striker, incident and transmitter bars and a sample of 5mm length x 10mm diameter, the pressure needed for high strain rates tests would exceed the maximum operating value of the air reservoir, hence this configuration was eliminated,
- Using 25mm diameter striker, incident and transmitter bars but with a smaller sample (3.125mm length x 6.25mm diameter) the pressure required decreased dramatically to a maximum value of 5.88bar for high strain rates conditions,
- Using 20mm diameter striker, incident and transmitter bars with samples of 4mm length x 8mm diameter, the pressure needed was found to be near the maximum operating value of the air reservoir which was not recommended for safety reasons,
- Using 20mm diameter striker, incident and transmitter bars but with a smaller sample (2.5mm length x 5mm diameter) the pressure needed decreased to a maximum value of 4.01bar for high strain rates conditions.

Therefore, based on these results the following recommendations were made:

- If possible, adopt incident, transmitter and striker bars of 20mm diameter each (this is in better accord with the values and proportions commonly used). Adopt a Le/Di bar ratio of 50 which means a length of 1m length for both incident and transmitter bars (better for low strain and strain rates). Adopt samples no smaller than 2.5mm length x 5mm diameter (Le/Di sample ratio is 0.5 and Di/di ratio is 4). The drawback of this proposal is that a new bar, bearings and pillow blocks would have to be bought,
- If samples are too small to machine and current bars (25mm diameter) are used, adopt a length of 1m for both incident and transmitter bars (although the Le/Di bar ratio is 40, it would be better to have higher bar ratios as previously explained). Adopt samples no smaller that 3.125mm length x 6.25mm diameter (Le/Di sample ratio is 0.5 and Di/di ratio is 4),
- Take into account the softening effect the temperature has on bars when testing materials at high temperatures,
- Specify a device to hold the sample while is being heated and see if this process can be done on the same I-beam in order to sandwich the sample as soon as possible once heated to avoid temperature drops.

Finally, after a discussion took place with all the personnel involved in the manufacturing process of the SHPB as well as those in charge of giving the green light for the project to start formally, it was decided to:

- Adopt a gun barrel of 0.80m in length (AISI 4340 steel),
- Adopt incident, transmitter and striker bars of 20mm diameter each,
- Adopt a Le/Di bar ratio of 57.5, which meant a length of 1.15m length for both incident and transmitter bars,
- Adopt samples no smaller than 2.5mm length x 5mm diameter,
- Design of a special device to hold the sample while is being heated so that it can be sandwiched between the incident and transmitter bars once it has reached the desired testing temperature,
- Adopt Nitrogen as a working fluid to fire the striker bar.

The full 3D mechanical design of all components in conjunction with the 2D individual/sub-assembly/assembly drawings were developed with the software NX7.5 Student Edition. Figure AI.4 shows a rendered image of the complete assembly in 3D including the description of each component.

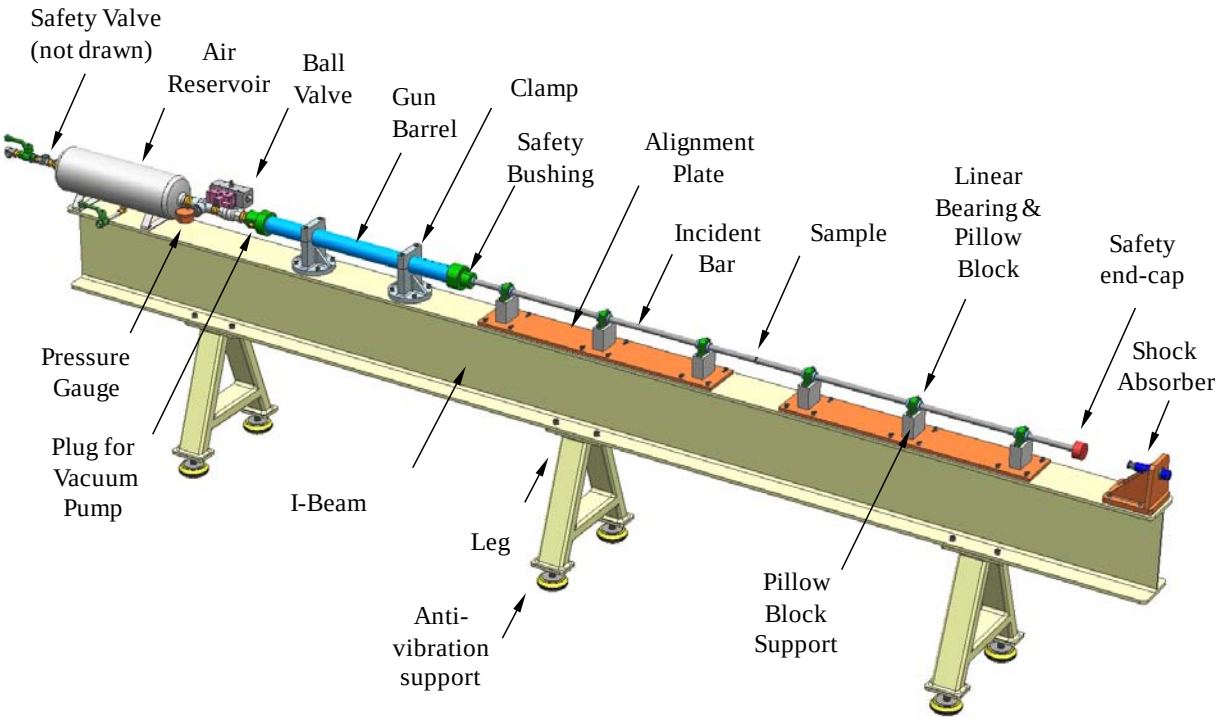

Figure AI.4. Image of the SHPB assembly including the description of each component.

Figure AI.5 details images and photographs of the various components.

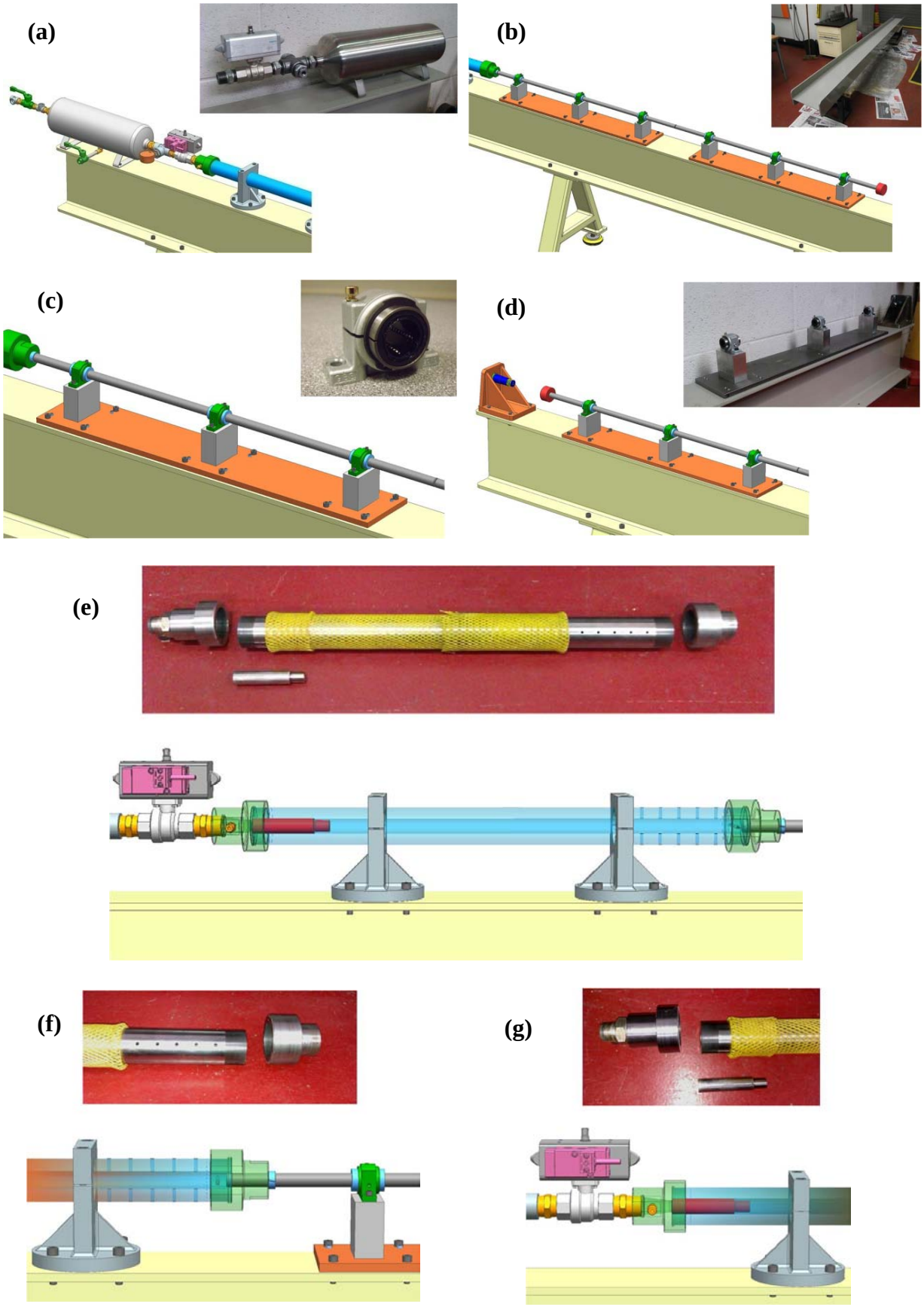

Figure AI.5. 3D images and photographs of (a) Air reservoir sub-assembly, (b) I-beam, (c) Linear bearing and pillow block, (d) Shock absorber and transmitter bar sub-assembly, (e) Gun barrel sub-assembly, (f) Gun barrel venting holes, (g) Striker bar and solenoid valve.

Furthermore, Figure AI.6 displays the sequence of manufacture for construction of the supporting legs.

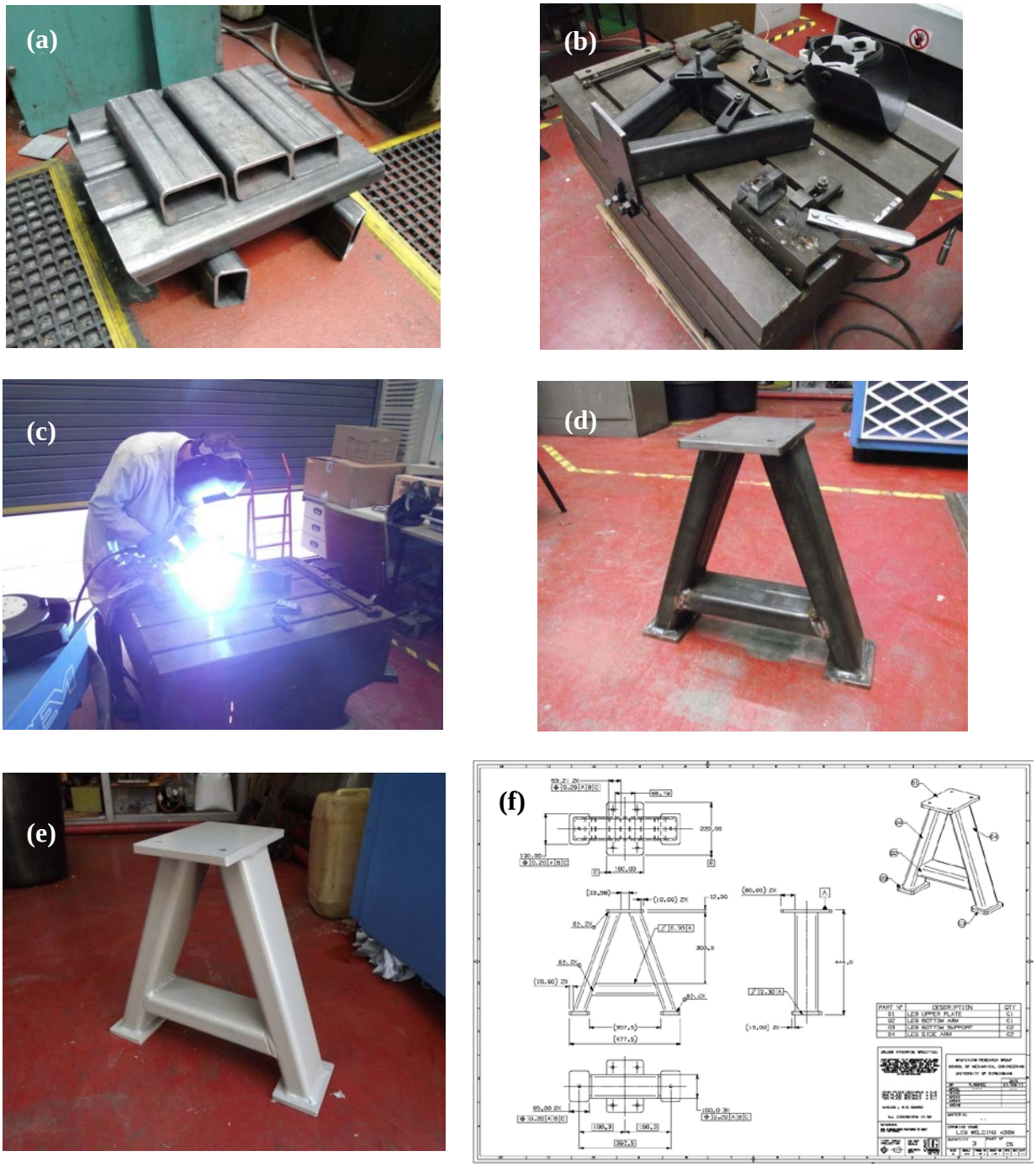

Figure AI.6. Sequence of work undertaken to fabricate one of the SHPB supporting legs. (a) Cutting of 100x50x5 section into smaller parts, (b) Setup made prior to the welding process, (c) Actual welding operation being carried out by former senior technician Mr. Richard Fasham, (d) Welded leg, (e) Painted leg, (f) 2D drawing of the assembled leg.

Figure AI.7 shows the current state of the apparatus at the School of Mechanical Engineering, University of Birmingham (2014).

Figure AI.7. SHPB apparatus assembly.

The following pages compile the 2D individual together with the assembly engineering drawings corresponding to the Split Hopkinson Pressure Bar testing apparatus (manufactured at the University of Birmingham) that were generated with the mechanical design software NX7.5 Student Edition.

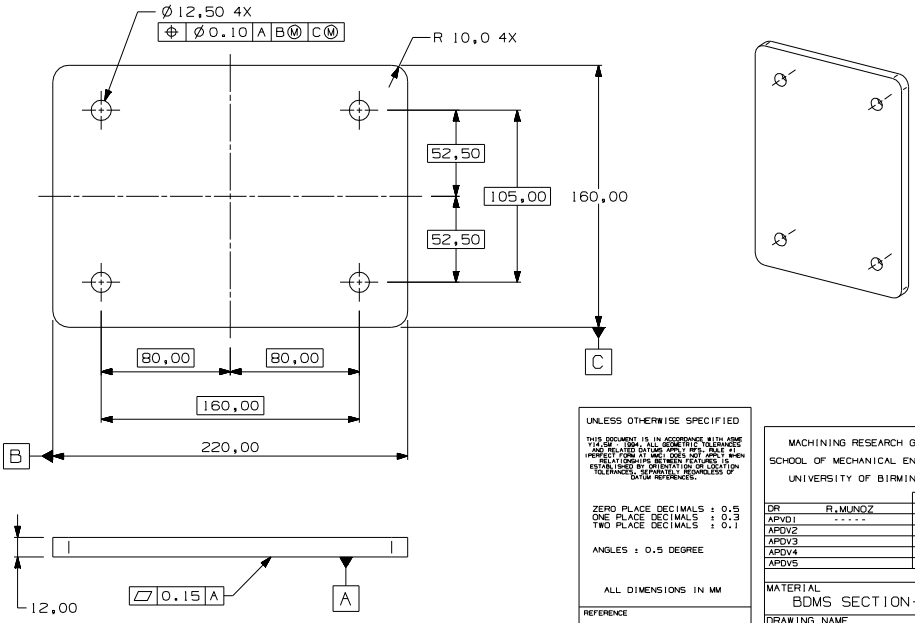

UNLESS OTHERWISE SPECIFIED

THIS DOCUMENT IS IN ACCORDANCE WITH ASME Y14.5M - 1994. ALL GEOMETRIC TOLERANCES AND RELATED DATUMS APPLY PER RULE #1. (PERFECT FORM AT MMC). DOES NOT APPLY WHEN A STATISTICAL TOLERANCE IS SPECIFIED. DATUMS ESTABLISHED BY ORIENTATION OR LOCATION TOLERANCES, SEPARATELY REGARDLESS OF DATUM REFERENCES.

ZERO PLACE DECIMALS : 0.5
ONE PLACE DECIMALS : 0.3
TWO PLACE DECIMALS : 0.1

ANGLES : 0.5 DEGREE

ALL DIMENSIONS IN MM

REFERENCE

NON DIMENSIONED FEATURES TO MEET DIN ISO 2768M

THIRD ANGLE PROJECTION

DO NOT SCALE

USE MATH DATA

CAD UG NX 7.5

MACHINING RESEARCH GROUP
SCHOOL OF MECHANICAL ENGINEERING
UNIVERSITY OF BIRMINGHAM

		DATE
DR	R.MUNOZ	01/03/11
APVD1	-----	----
APDV2		
APDV3		
APDV4		
APDV5		

MATERIAL
BDMS SECTION-STD

DRAWING NAME
LEG UPPER PLATE

QUANTITY	PART N°
3	01

SIZE	SCALE	FRAME NO	SHEET NO	STG	REV	N/P
A2	1/1	1 OF 1	1 OF 1	...	-	...

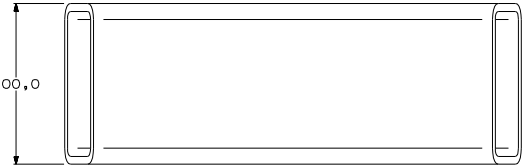

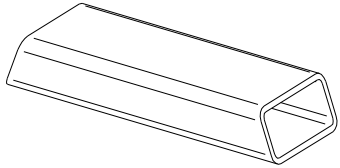

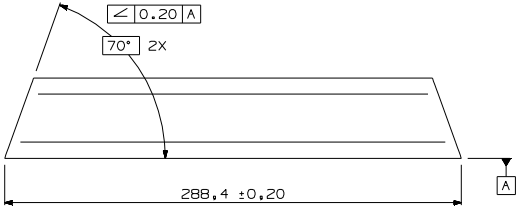

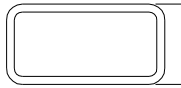

UNLESS OTHERWISE SPECIFIED

THIS DRAWING IS IN ACCORDANCE BSTH 8888 "TECHNICAL DRAWING" AND ALL DIMENSIONS ARE UNLESS OTHERWISE STATED IN MILLIMETRES AND TOLERANCED IN ACCORDANCE WITH ISO 2768-1 "GENERAL TOLERANCES". THIS DRAWING IS THE PROPERTY OF THE UNIVERSITY OF BIRMINGHAM AND MUST NOT BE COPIED OR REPRODUCED WITHOUT THE WRITTEN PERMISSION OF THE UNIVERSITY OF BIRMINGHAM.

ZERO PLACE DECIMALS : 0.5
ONE PLACE DECIMALS : 0.3
TWO PLACE DECIMALS : 0.1

ANGLES : 0.5 DEGREE

ALL DIMENSIONS IN MM

REFERENCE
NON SIMPLIFIED FEATURES TO MEET BTH 1567 (1988)

FIRST ANGLE PROJECTION

DO NOT SCALE

CAD UNITS MILLIMETRES

MACHINING RESEARCH GROUP
SCHOOL OF MECHANICAL ENGINEERING
UNIVERSITY OF BIRMINGHAM

		DATE
DR	R.MUNOZ	01/03/11
APVD1	-----	---
APDV2		
APDV3		
APDV4		
APDV5		

MATERIAL
100X50X5 THICK SECTION

DRAWING NAME
LEG BOTTOM ARM

QUANTITY 3

PART N° 02

SIZE	SCALE	TYPING NO	SHEET NO	STG	REV	APP
A3	1/1	1 OF 1	1 OF 1			

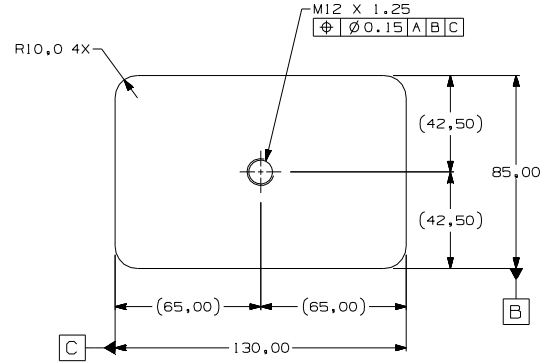

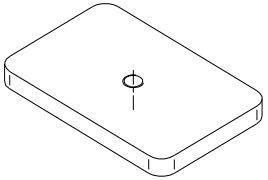

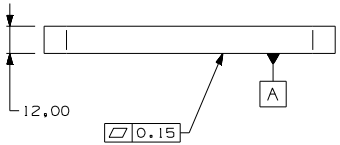

UNLESS OTHERWISE SPECIFIED

THIS DOCUMENT IS IN ACCORDANCE WITH ASME Y14.5M - 1994. ALL GEOMETRIC TOLERANCES AND RELATED DEFINITIONS MUST APPLY RULE #1 (PERFECT FORM AT MMC) UNLESS OTHERWISE NOTED. WHEN RELATIONSHIPS BETWEEN FEATURES IS ESTABLISHED BY ORIENTATION OR LOCATION TOLERANCES, SEPARATELY REGARDLESS OF DATUM REFERENCES.

ZERO PLACE DECIMALS : 0.5
ONE PLACE DECIMALS : 0.3
TWO PLACE DECIMALS : 0.1

ANGLES : 0.5 DEGREE

ALL DIMENSIONS IN MM

REFERENCE

NON DIMENSIONED FEATURES TO MEET DIN ISO 2768m

THIRD ANGLE PROJECTION

DO NOT SCALE

USE MATH DATA

CAD UG NX 7.5

MACHINING RESEARCH GROUP
SCHOOL OF MECHANICAL ENGINEERING
UNIVERSITY OF BIRMINGHAM

		DATE
DR	R.MUNOZ	01/03/11
APVD1	-----	----
APVD2		
APVD3		
APVD4		
APVD5		

MATERIAL
BDMS SECTION-STD

DRAWING NAME
LEG BOTTOM SUPPORT

QUANTITY	PART N°
6	03

SIZE	SCALE	FRAME NO	SHEET NO	STG	REV	N/P
A2	1:1	1 OF 1	1 OF 1	...	-	...

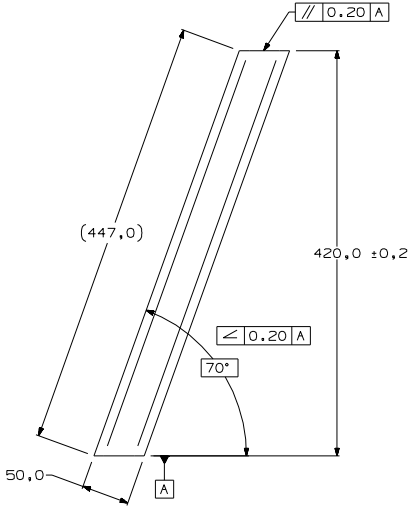

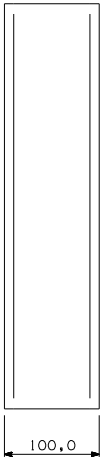

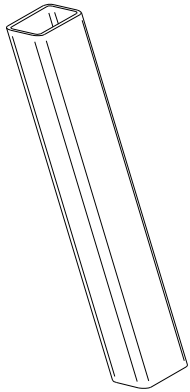

UNLESS OTHERWISE SPECIFIED

THIS DRAWING IS IN ACCORDANCE WITH BSPP 7:36 AND ISO 1101:1983. ALL MACHINED SURFACES ARE TO BE FINISHED TO THE VALUE GIVEN IN MICRONS UNLESS OTHERWISE STATED. ALL PARTS TO BE MANUFACTURED IN ACCORDANCE WITH BS 4500 TOLERANCES. NO PARTS TO BE MADE FROM DRAWINGS. ALL PARTS TO BE DIMENSIONED FROM DRAWINGS.

ZERO PLACE DECIMALS : 0.5
ONE PLACE DECIMALS : 0.1
TWO PLACE DECIMALS : 0.1

ANGLES : 0.5 DEGREE

ALL DIMENSIONS IN MM

REFERENCE
NON SIMPLIFIED FEATURES TO MEET BS 308 3135M

FIRST ANGLE PROJECTION

DO NOT SCALE

CAD/CAM

MACHINING RESEARCH GROUP
SCHOOL OF MECHANICAL ENGINEERING
UNIVERSITY OF BIRMINGHAM

		DATE
DR	R.MUNOZ	01/03/11
APVD1		
APDV2		
APDV3		
APDV4		
APDV5		

MATERIAL
100X50X5 THICK SECTION

DRAWING NAME
LEG SIDE ARM

QUANTITY 6 PART N° 04

SIZE	SCALE	FRAME NO	SHEET NO	STG	REV	MAT
A3	1/1	1 OF 1	1 OF 1			

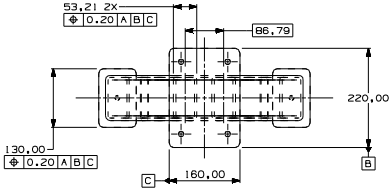

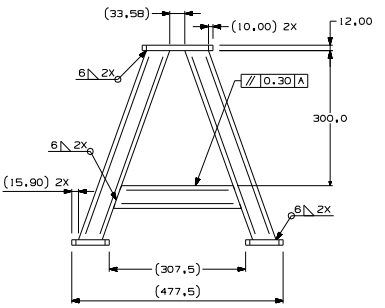

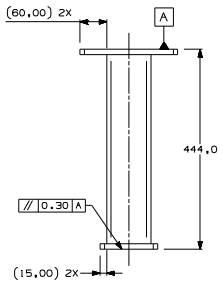

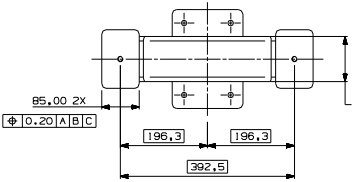

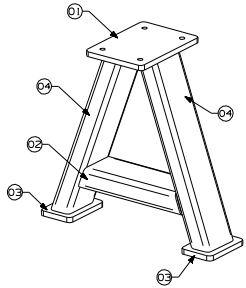

PART N°	DESCRIPTION	QTY
01	LEG UPPER PLATE	01
02	LEG BOTTOM ARM	01
03	LEG BOTTOM SUPPORT	02
04	LEG SIDE ARM	02

UNLESS OTHERWISE SPECIFIED

THIS DRAWING IS IN ACCORDANCE WITH BSPP 7:2007. IT IS THE RESPONSIBILITY OF THE MANUFACTURER TO ENSURE THAT THEIR PARTS COMPLY WITH THE LAW IN THE COUNTRY OF USE. THE INFORMATION CONTAINED IN THIS DRAWING IS THE COPYRIGHT OF UNLESS A LICENCE HAS BEEN EXPRESSLY GRANTED THE USE OR REPRODUCTION OF THIS DRAWING IN ANY FORM OR BY ANY MEANS IS PROHIBITED. IT MUST NOT BE LENT, COPIED OR DISCLOSED TO A THIRD PARTY WITHOUT PRIOR PERMISSION.

ZERO PLACE DECIMALS : 0.5
ONE PLACE DECIMALS : 0.3
TWO PLACE DECIMALS : 0.1

ANGLES : 0.5 DEGREE

ALL DIMENSIONS IN MM

REFERENCE
NON TOLERANCED FEATURES TO MEET BS 750 STAND.

FIRST ANGLE PROJECTION

DO NOT SCALE

DRAWING NO 1 0

MACHINING RESEARCH GROUP
SCHOOL OF MECHANICAL ENGINEERING
UNIVERSITY OF BIRMINGHAM

		DATE
DR	R.MUNOZ	01/03/11
APVD1	- - - -	- - -
APDV2		
APDV3		
APDV4		
APDV5		

MATERIAL
- -

DRAWING NAME
LEG WELDING ASSM

QUANTITY 3

PART N° 05

SIZE	SCALE	FRAME NO	SHEET NO	STD	REV
A3	1/2	1 OF 1	1 OF 1	- -	- -

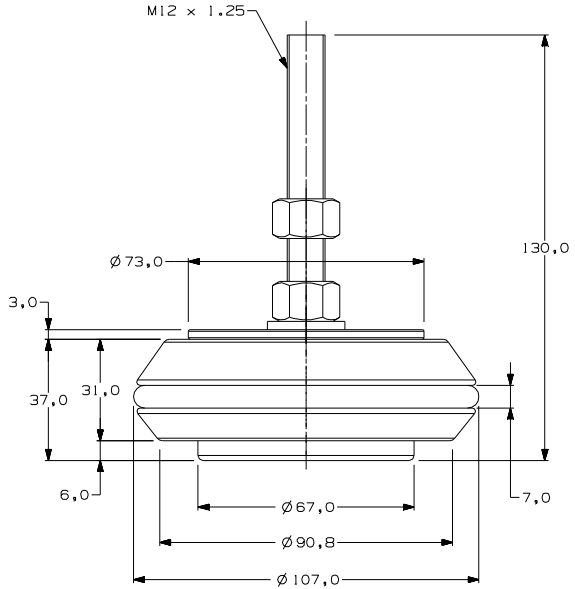

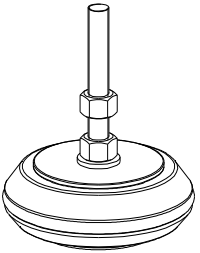

UNLESS OTHERWISE SPECIFIED

THIS DOCUMENT IS IN ACCORDANCE WITH ASME Y14.5M - 1994. ALL GEOMETRIC TOLERANCES AND RELATED DIMENSIONS MUST APPLY RULE #1 (PERFECT FORM AT MMC) UNLESS OTHERWISE NOTED. WHEN RELATIONSHIPS BETWEEN FEATURES IS ESTABLISHED BY ORIENTATION OR LOCATION TOLERANCES, SEPARATELY REGARDLESS OF DATUM REFERENCES.

ZERO PLACE DECIMALS : 0.5
ONE PLACE DECIMALS : 0.3
TWO PLACE DECIMALS : 0.1

ANGLES : 0.5 DEGREE

ALL DIMENSIONS IN MM

REFERENCE

NON DIMENSIONED FEATURES TO MEET DIN ISO 2768m

THIRD ANGLE PROJECTION

DO NOT SCALE

USE MATH DATA

CAD UG NX 7.5

MACHINING RESEARCH GROUP
SCHOOL OF MECHANICAL ENGINEERING
UNIVERSITY OF BIRMINGHAM

		DATE
DR	R.MUNOZ	01/03/11
APVD1	-----	----
APVD2		
APVD3		
APVD4		
APVD5		

MATERIAL

DRAWING NAME
MACHINE SHOE

QUANTITY
6

PART N°
06

SIZE	SCALE	FRAME NO	SHEET NO	STG	REV	N/P
A2	2/1	1 OF 1	1 OF 1	-	-	-

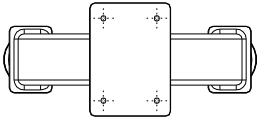

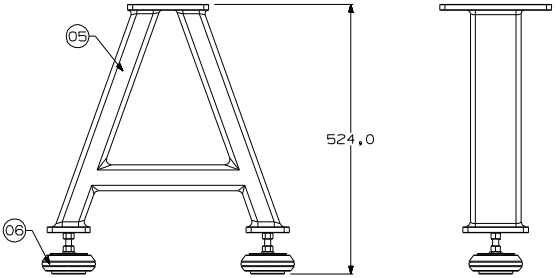

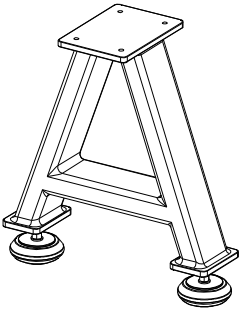

PART N°	DESCRIPTION	QTY
05	LEG WELDING ASSM	01
06	MACHINE SHOE	02

UNLESS OTHERWISE SPECIFIED

THIS DOCUMENT IS IN ACCORDANCE WITH ABNT NBR 10126 - TIPO 1 - ALL DIMENSIONS IN MILLIMETERS UNDER PLANE STATE. SHALL NOT BE USED FOR PURPOSES OTHER THAN THOSE FOR WHICH IT WAS SPECIFICALLY SUPPLIED. NEITHER IT NOR THE INFORMATION IT CONTAINS SHALL BE COPIED, LOANED, DISCLOSED OR DISPOSED OF TO OTHER PARTY(IES) WITHOUT

ZERO PLACE DECIMALS ± 0.5
ONE PLACE DECIMALS ± 0.3
TWO PLACE DECIMALS ± 0.1

ANGLES ± 0.5 DEGREE

ALL DIMENSIONS IN MM

REFERENCE
NON STANDARDIZED FEATURES TO MEET DIN 150 2768-f

THIRD ANGLE PROJECTION

DO NOT SCALE

USE METRIC

MACHINING RESEARCH GROUP
SCHOOL OF MECHANICAL ENGINEERING
UNIVERSITY OF BIRMINGHAM

		DATE
DR	R.MUNOZ	01/03/11
APVD1	- - -	- - -
APDV2		
APDV3		
APDV4		
APDV5		

MATERIAL
- - -

DRAWING NAME
LEG ASSM

QUANTITY 3

PART N° 07

SIZE	SCALE	FRAME NO	SHEET NO	STG	REV	SUF
A1	1/2	1 OF 1	1 OF 1	-	-	-

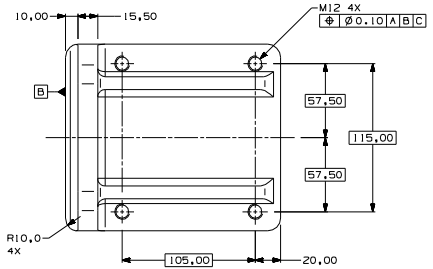

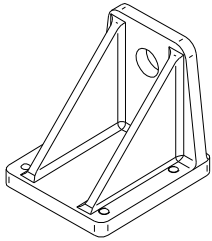

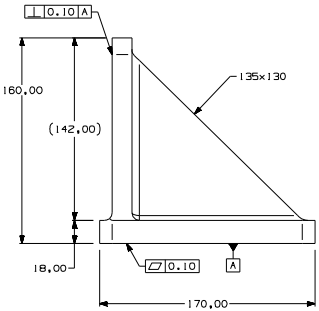

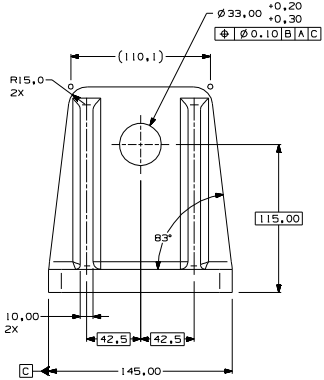

UNLESS OTHERWISE SPECIFIED

THIS DOCUMENT IS IN ACCORDANCE WITH ISO 1101:2004. THIS DOCUMENT IS CONFIDENTIAL AND MUST NOT BE USED FOR ANY PURPOSE OTHER THAN THAT FOR WHICH IT IS SUPPLIED, NOR MUST IT BE COPIED OR REPRODUCED IN ANY WAY WHATSOEVER WITHOUT THE PRIOR WRITTEN PERMISSION OF THE COMPANY. ALL RIGHTS RESERVED UNDER COPYRIGHT LAWS.

ZERO PLACE DECIMALS ± 0.5
ONE PLACE DECIMALS ± 0.3
TWO PLACE DECIMALS ± 0.1

ANGLES ± 0.5 DEGREE

ALL DIMENSIONS IN MM

REFERENCE

NON TOLERANCED FEATURES TO MEET BS 7192:1989

THIRD ANGLE PROJECTION

DO NOT SCALE

USE WITH

CAD/CAM

MACHINING RESEARCH GROUP
SCHOOL OF MECHANICAL ENGINEERING
UNIVERSITY OF BIRMINGHAM

		DATE
DR	R.MUNOZ	15/04/11
APVD1		
APVD2		
APVD3		
APVD4		
APVD5		

MATERIAL
BOMS SECTION-STD

DRAWING NAME
SHOCK ABSORBER SUPPORT

QUANTITY 1 | PART N° 08

SIZE	SCALE	TYPING NO	SHEET NO	STA	REV	SUP
A4	1/1	1 OF 1	1 OF ...	...	...	...

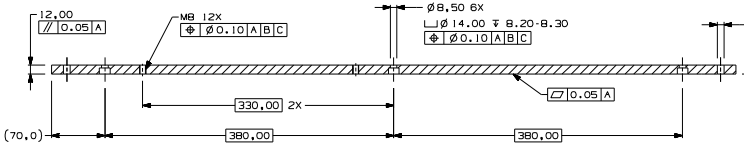

SECTION A - A

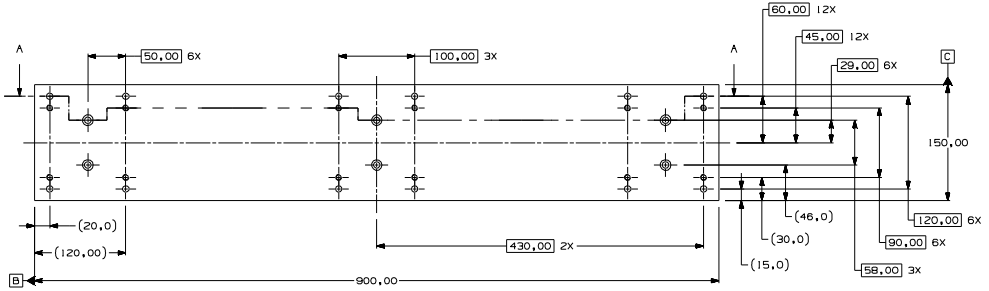

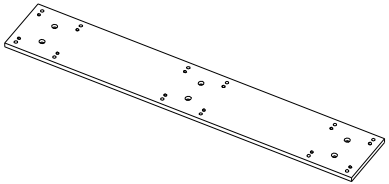

UNLESS OTHERWISE SPECIFIED

THIS DRAWING IS IN ACCORDANCE WITH BSPP THE APPLICABLE BRITISH STANDARD PRACTICE AND RELATED BRITISH STANDARDS AND IS TO BE INTERPRETED ACCORDINGLY. ALL DIMENSIONS ARE IN MILLIMETRES UNLESS OTHERWISE STATED. DIMENSIONS AND TOLERANCES APPLY IN THE FREE STATE. NON RIGID PARTS MUST BE RESTRAINED TO ACHIEVE DRAWING REQUIREMENTS. DO NOT SCALE FROM THIS DRAWING.

ZERO PLACE DECIMALS ± 0.5
ONE PLACE DECIMALS ± 0.2
TWO PLACE DECIMALS ± 0.1

ANGLES ± 0.5 DEGREE

ALL DIMENSIONS IN MM

REFERENCE
NON SUPERSEDED FEATURES TO MEET BTA 180 FINISH

THIRD ANGLE PROJECTION

DO NOT SCALE

DATE 15/04/11

MACHINING RESEARCH GROUP
SCHOOL OF MECHANICAL ENGINEERING
UNIVERSITY OF BIRMINGHAM

	DR R.MUNOZ	DATE 15/04/11
APVD1		
APDV2		
APDV3		
APDV4		
APDV5		

MATERIAL
BDMS SECTION-STD

DRAWING NAME
BAR ALIGNMENT PLATE

QUANTITY 2 PART N° 09

SIZE A1 | SCALE 1/2 | FRAME NO 1 OF 1 | SHEET NO 1 OF 1 | STD | REV | W/P

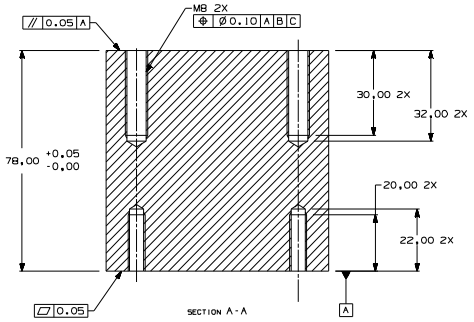

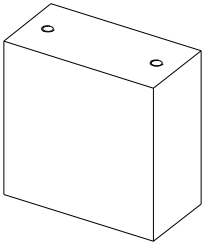

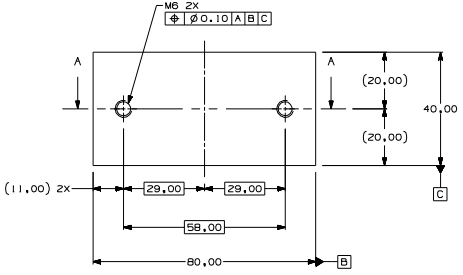

UNLESS OTHERWISE SPECIFIED

THIS DOCUMENT IS IN ACCORDANCE WITH ASME Y14.5M - 1994. ALL DIMENSIONS, TOLERANCES AND PROCESSES STATED SHALL BE MET. UNLESS OTHERWISE SPECIFIED ALL DIMENSIONS ARE IN MILLIMETRES AND ALL TOLERANCES ARE AS PER ISO 2768-mK. REMOVAL OF ALL SHARP EDGES, BURRS AND SWARF. INTERPRETATION OF GEOMETRIC TOLERANCING, PROJECTION AND DATUM REFERENCE.

ZERO PLACE DECIMALS ± 0.5
ONE PLACE DECIMALS ± 0.3
TWO PLACE DECIMALS ± 0.1

ANGLES ± 0.5 DEGREE

ALL DIMENSIONS IN MM

REFERENCE
SEE TOPOLOGIZED FEATURES TO MEET ISO 1101:2004

THIRD ANGLE PROJECTION

DO NOT SCALE

USE UNITS: MM

CAD SYSTEM: UG NX 7.5

MACHINING RESEARCH GROUP
SCHOOL OF MECHANICAL ENGINEERING
UNIVERSITY OF BIRMINGHAM

		DATE
DR	R.MUNOZ	15/04/11
APVD1		
APDV2		
APDV3		
APDV4		
APDV5		

MATERIAL: ALCOA 380

DRAWING NAME: BEARING UNIT SUPPORT

QUANTITY: 6

PART N°: 10

SIZE	SCALE	FRAME NO	SHEET NO	STK	REV	IMP
A1	2/1	1 OF 1	1 OF -	...	...	...

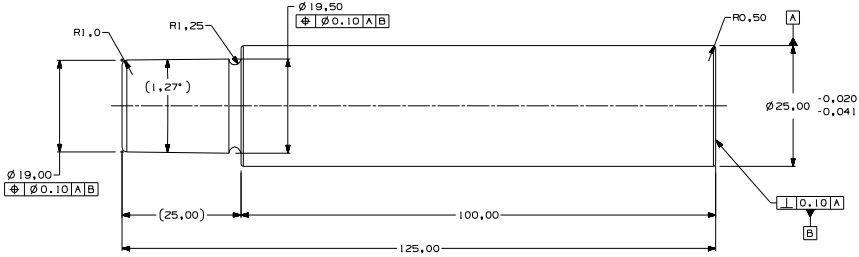

PRELIMINARY

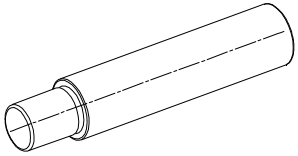

UNLESS OTHERWISE SPECIFIED

THIS DRAWING IS IN ACCORDANCE WITH ANSI Y14.5M-1982 AND ISO 1101:1983 GEOMETRIC TOLERANCING. ALL DIMENSIONS AND TOLERANCES ARE TO BE MET IN THE FREE STATE. ALL DIMENSIONS ARE IN MILLIMETRES UNLESS OTHERWISE SPECIFIED. ALL DIMENSIONS AND TOLERANCES APPLY AT 20°C. ALL MACHINED SURFACES TO BE FREE FROM BURRS AND SHARP EDGES. ANY INTERPRETATION OR DEVIATION FROM THIS DRAWING MUST BE APPROVED BY THE DESIGNER.

ZERO PLACE DECIMALS : 0.5
ONE PLACE DECIMALS : 0.1
TWO PLACE DECIMALS : 0.1

ANGLES : 0.5 DEGREE

ALL DIMENSIONS IN MM

REFERENCE
NON TURNROUNDED FEATURES TO MEET BTS 192 STAGE

THIRD ANGLE PROJECTION | DO NOT SCALE | UNLESS WITH NO TOL

MACHINING RESEARCH GROUP
SCHOOL OF MECHANICAL ENGINEERING
UNIVERSITY OF BIRMINGHAM

		DATE
DR	R.MUNOZ	15/04/11
APVD1		
APVD2		
APVD3		
APVD4		
APVD5		

MATERIAL
C350 MARAGING STEEL

DRAWING NAME
STRIKER BAR

QUANTITY 1 | PART N° 11

SIZE	SCALE	FRAME NO	SHEET NO	STD	REV	N/R
A1	2/1	1 OF 1	1 OF 1	---	---	---

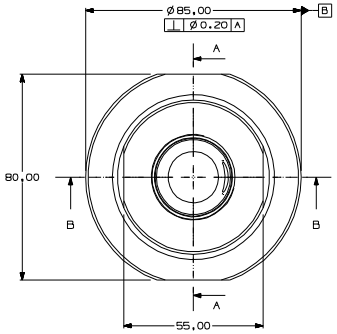

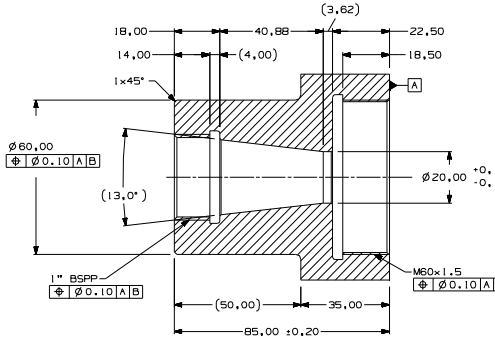

SECTION A - A

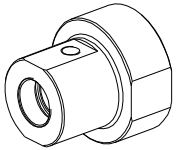

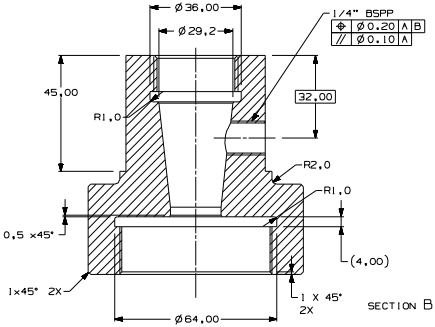

SECTION B-B

UNLESS OTHERWISE SPECIFIED

THIS DOCUMENT IS IN ACCORDANCE WITH ISO 1101:2004 - GEOMETRICAL TOLERANCING - TOLERANCES OF FORM, ORIENTATION, LOCATION AND RUNOUT. ISO 2692:2006 - GEOMETRICAL TOLERANCING - MAXIMUM MATERIAL REQUIREMENT (MMR), LEAST MATERIAL REQUIREMENT (LMR) AND REVERSIBLE REQUIREMENT (RPR). ISO 5459:2011 - GEOMETRICAL TOLERANCING - DATUMS AND DATUM SYSTEMS FOR GEOMETRICAL TOLERANCES. ISO 8015:2011 - GEOMETRICAL PRODUCT SPECIFICATIONS (GPS) - FUNDAMENTALS - CONCEPTS, PRINCIPLES AND RULES. ISO 14405-1:2010 - GEOMETRICAL PRODUCT SPECIFICATIONS (GPS) - DIMENSIONAL TOLERANCING - PART 1: LINEAR SIZES. ISO 16792:2006 - TECHNICAL PRODUCT DOCUMENTATION - DIGITAL DATA DEFINITION PRACTICES. ISO 129-1:2004 - TECHNICAL DRAWINGS - DIMENSIONING AND TOLERANCING - PART 1: GENERAL PRINCIPLES. ISO 1302:2002 - GEOMETRICAL PRODUCT SPECIFICATIONS (GPS) - INDICATION OF SURFACE TEXTURE IN TECHNICAL PRODUCT DOCUMENTATION. ISO 286-1:2010 - GEOMETRICAL PRODUCT SPECIFICATIONS (GPS) - ISO CODE SYSTEM FOR TOLERANCES ON LINEAR SIZES - PART 1: BASIS OF TOLERANCES, DEVIATIONS AND FITS. ISO 286-2:2010 - GEOMETRICAL PRODUCT SPECIFICATIONS (GPS) - ISO CODE SYSTEM FOR TOLERANCES ON LINEAR SIZES - PART 2: TABLES OF STANDARD TOLERANCE GRADES AND LIMIT DEVIATIONS FOR HOLES AND SHAFTS. ISO 406:1987 - TECHNICAL DRAWINGS - TOLERANCING OF LINEAR AND ANGULAR DIMENSIONS. ISO 5458:1998 - GEOMETRICAL PRODUCT SPECIFICATIONS (GPS) - GEOMETRICAL TOLERANCING - POSITIONAL TOLERANCING. ISO 5459:2011 - GEOMETRICAL TOLERANCING - DATUMS AND DATUM SYSTEMS FOR GEOMETRICAL TOLERANCES.

ZERO PLACE DECIMALS ± 0.5
ONE PLACE DECIMALS ± 0.3
TWO PLACE DECIMALS ± 0.1

ANGLES ± 0.5 DEGREE

ALL DIMENSIONS IN MM

REFERENCE
SIN THREADED FIXTURES TO MEET BS 7510:1990

THIRD ANGLE PROJECTION

DO NOT SCALE

USE units

CAD UG NX 7.5

MACHINING RESEARCH GROUP
SCHOOL OF MECHANICAL ENGINEERING
UNIVERSITY OF BIRMINGHAM

		DATE
DR	R.MUNOZ	15/04/11
APVD1		
APDV2		
APDV3		
APDV4		
APDV5		

MATERIAL
AISI 4340

DRAWING NAME
GUN BARREL BUSHING

QUANTITY 1 | PART N° 12

SIZE	SCALE	FRAME NO	SHEET NO	STK	REV	MAT
A1	2/1	1 OF 1	1 OF -	...	...	...

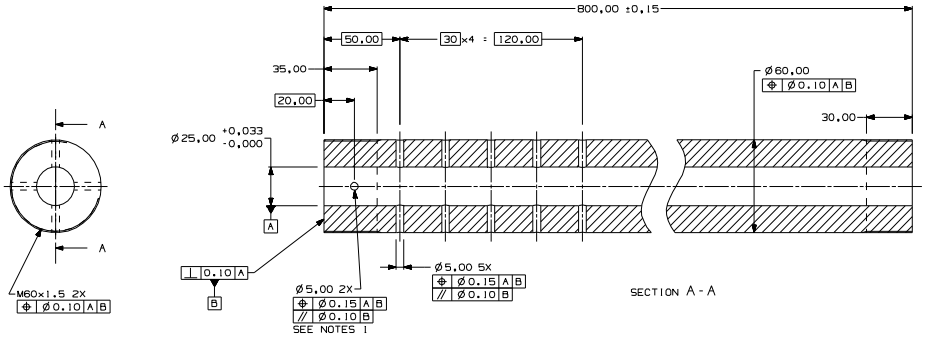

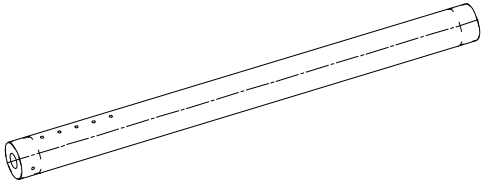

NOTES:

1. MAKE THE HOLE ONCE THE SAFETY BUSHING IS MOUNTED

UNLESS OTHERWISE SPECIFIED

THIS DOCUMENT IS IN ACCORDANCE WITH ASME Y14.5M - 1994. ALL DIMENSIONS ARE IN MILLIMETRES UNLESS OTHERWISE STATED. DO NOT SCALE FROM THIS DRAWING. ALL DIMENSIONS AND TOLERANCES ARE AS PER ASME Y14.5M - 1994 UNLESS OTHERWISE STATED. ALL TOLERANCES, INCLUDING GEOMETRICAL TOLERANCES, APPLY AT 20°C UNLESS OTHERWISE STATED.

ZERO PLACE DECIMALS ± 0.5
ONE PLACE DECIMALS ± 0.3
TWO PLACE DECIMALS ± 0.1

ANGLES ± 0.5 DEGREE

ALL DIMENSIONS IN MM

REFERENCE

FOR TOLERANCED FEATURES TO MEET THIS TEST PIECE

THIRD ANGLE PROJECTION

DO NOT SCALE

USE units

CAD UNITS: mm

MACHINING RESEARCH GROUP
SCHOOL OF MECHANICAL ENGINEERING
UNIVERSITY OF BIRMINGHAM

		DATE
DR	R.MUNOZ	15/04/11
APVD1		
APDV2		
APDV3		
APDV4		
APDV5		

MATERIAL: AISI 4340

DRAWING NAME: GUN BARREL

QUANTITY: 1 | PART N°: 13

SIZE	SCALE	FRAME NO	SHEET NO	STK	REV	IMP
A1	2/1	1 OF 1	1 OF -	...	-	...

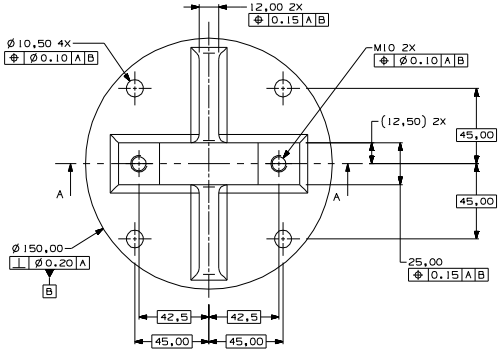

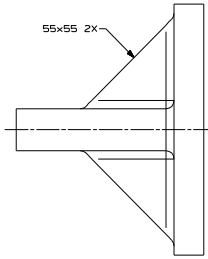

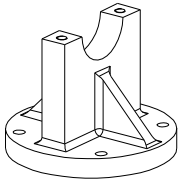

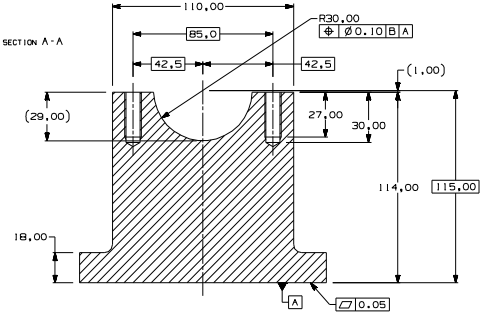

UNLESS OTHERWISE SPECIFIED

THIS DOCUMENT IS IN ACCORDANCE WITH ISO 1101:2004. ALL ASSEMBLY CLEARANCES AND TOLERANCES SHOWN ARE ONLY TO BE USED FOR THE PURPOSE OF THIS ASSEMBLY AND NOT FOR ANY OTHER PURPOSE. REMOVAL OF ANY CLEARANCES, TOLERANCES, REPRODUCTION OR OTHER REFERENCES.

ZERO PLACE DECIMALS ± 0.5
ONE PLACE DECIMALS ± 0.3
TWO PLACE DECIMALS ± 0.1

ANGLES ± 0.5 DEGREE

ALL DIMENSIONS IN MM

REFERENCE

NON STANDARDISED FEATURES TO MEET DIN ISO 7089

THIRD ANGLE PROJECTION

DO NOT SCALE

USE WITH GD&T

CAD UNIGRAPHICS NX 7.0

MACHINING RESEARCH GROUP
SCHOOL OF MECHANICAL ENGINEERING
UNIVERSITY OF BIRMINGHAM

		DATE
DR	R.MUNOZ	15/04/11
APVD1		
APDV2		
APDV3		
APDV4		
APDV5		

MATERIAL
BOMS SECTION-STD

DRAWING NAME
LOWER GUN BARREL CLAMP

QUANTITY 2

PART N° 14

SIZE	SCALE	TYPE NO	SHEET NO	STK	REV	SUP
A1	1:2	1 OF 1	1 OF ...	...	...	...

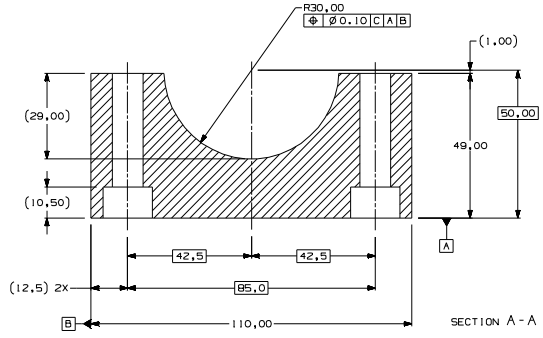

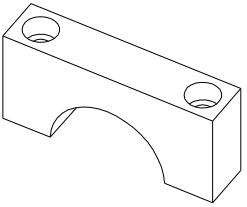

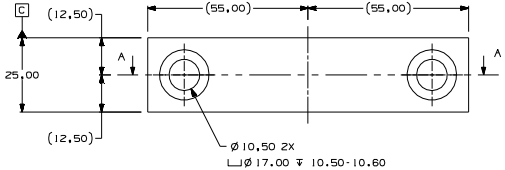

UNLESS OTHERWISE SPECIFIED

THIS DOCUMENT IS IN ACCORDANCE WITH ISO TC/SC / BSI / BS PUBLICATIONS / ALTERNATIVELY AS STATED BY THE USER. ALL DIMENSIONS ARE IN MILLIMETRES UNLESS OTHERWISE STATED. DO NOT SCALE FROM THIS DRAWING. ALL DIMENSIONS AND TOLERANCES ARE AFTER ANY PROCESSING. REMOVAL OF SHARP EDGES AND BURRS. INTERPRETATION OF GEOMETRICAL TOLERANCING, DATUMS & DATUM REFERENCES

ZERO PLACE DECIMALS ± 0.5
ONE PLACE DECIMALS ± 0.3
TWO PLACE DECIMALS ± 0.1

ANGLES ± 0.5 DEGREE

ALL DIMENSIONS IN MM

REFERENCE
NON TOLERANCED FEATURES TO MEET BS 7192 (MED)

THIRD ANGLE PROJECTION

DO NOT SCALE

USE METRIC

CAD UG NX 7.5

MACHINING RESEARCH GROUP
SCHOOL OF MECHANICAL ENGINEERING
UNIVERSITY OF BIRMINGHAM

		DATE
DR	R.MUNOZ	15/04/11
APVD1		
APDV2		
APDV3		
APDV4		
APDV5		

MATERIAL
BDMS SECTION-STD

DRAWING NAME
UPPER GUN BARREL CLAMP

QUANTITY 2

PART Nº 15

SIZE	SCALE	PROJ	SHEET NO	STG	REV	MAT
A1	2/1		1 OF 1	-	-	-

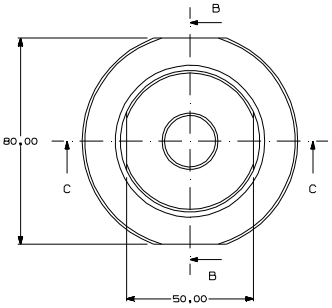

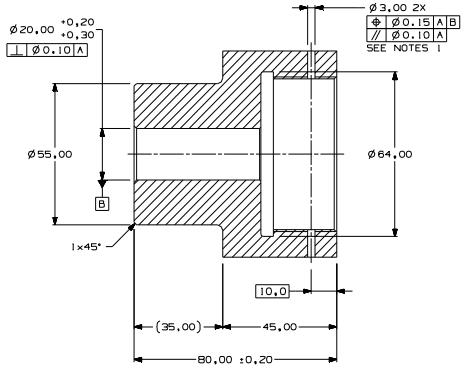

SECTION B-B

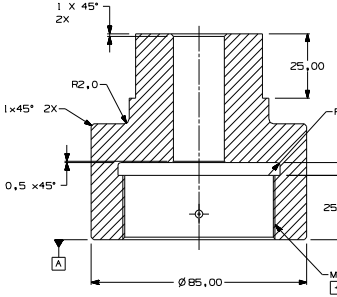

SECTION C-C

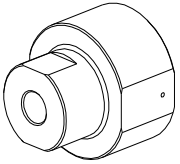

NOTES:

1. MAKE THE HOLE ONCE THE BUSHING FULLY THREADED TO THE GUN BARREL

UNLESS OTHERWISE SPECIFIED

THIS DOCUMENT IS IN ACCORDANCE WITH ASME Y14.5M - 1994. ALL DIMENSIONS, TOLERANCES AND PRACTICES USED SHALL BE AS SET FORTH HEREIN UNLESS OTHERWISE SPECIFIED. ALL DIMENSIONS AND TOLERANCES ARE APPLICABLE AT 20°C. ALL DIMENSIONS AND TOLERANCES ARE APPLICABLE AT 20°C. ALL DIMENSIONS AND TOLERANCES, INCLUDING ALL APPLICATION OF DATUM REFERENCES.

ZERO PLACE DECIMALS ± 0.5
ONE PLACE DECIMALS ± 0.3
TWO PLACE DECIMALS ± 0.1

ANGLES ± 0.5 DEGREE

ALL DIMENSIONS IN MM

REFERENCE
NON TOOLING HOLES FEATURES TO MEET BS 7192 FINISH

THIRD ANGLE PROJECTION

DO NOT SCALE

USE MATRIX

CAD UG NX 7.5

MACHINING RESEARCH GROUP
SCHOOL OF MECHANICAL ENGINEERING
UNIVERSITY OF BIRMINGHAM

		DATE
DR	R.MUNOZ	15/04/11
APVD1		
APDV2		
APDV3		
APDV4		
APDV5		

MATERIAL
AISI 4340

DRAWING NAME
GUN BARREL SAFETY BUSHING

QUANTITY 1 | PART N° 16

SIZE	SCALE	FRAME NO	SHEET NO	STK	REV	MAT
A1	2/1	1 OF 1	1 OF 1	...	...	...

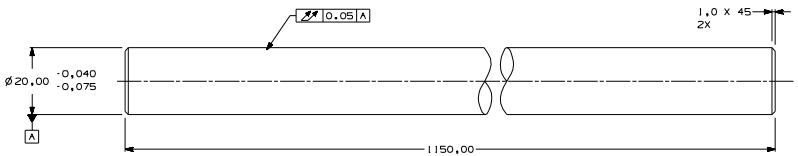

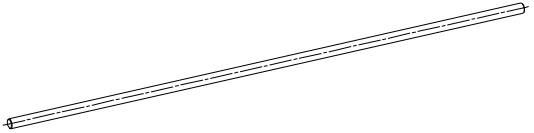

UNLESS OTHERWISE SPECIFIED

THIS DOCUMENT IS IN ACCORDANCE WITH ISO TO THE 1994 BASIC DIMENSIONAL TOLERANCES AND PRINCIPLES OF ISO 8015. ISO 2692 (ICM) AND ISO 1101 FOR GEOMETRICAL TOLERANCING. ISO 14405 FOR DIMENSIONAL TOLERANCING. NO FURTHER INTERPRETATION SHALL BE MADE. ALL TOLERANCES, MATERIALS, REVISIONS OF DATUM REFERENCES.

ZERO PLACE DECIMALS ± 0.5
ONE PLACE DECIMALS ± 0.3
TWO PLACE DECIMALS ± 0.1

ANGLES ± 0.5 DEGREE

ALL DIMENSIONS IN MM

REFERENCE
NON TOLERANCED FEATURES TO MEET BS 7192:1989

THIRD ANGLE PROJECTION

DO NOT SCALE

USE METRIC

CAD UNIGRAPHICS NX 7.0

MACHINING RESEARCH GROUP
SCHOOL OF MECHANICAL ENGINEERING
UNIVERSITY OF BIRMINGHAM

		DATE
DR	R.MUNOZ	15/04/11
APVD1		
APDV2		
APDV3		
APDV4		
APDV5		

MATERIAL
C350 MARAGING STEEL

DRAWING NAME
INCIDENT BAR

QUANTITY 1 | PART N° 17

SIZE	SCALE	FRAME NO	SHEET NO	STG	REV	SUP
A1	2/1	1 OF 1	1 OF 1	-	-	-

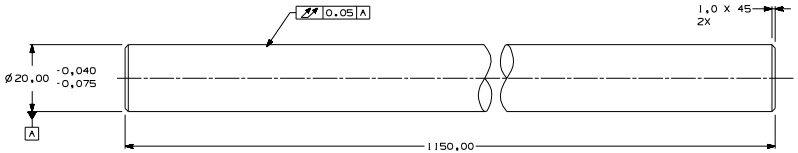

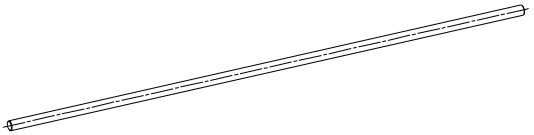

UNLESS OTHERWISE SPECIFIED

THIS DOCUMENT IS IN ACCORDANCE WITH ISO/PAS 12166:1998 "TOLERANCING AND DIMENSIONING". ALL DIMENSIONS AND TOLERANCES ARE TO BE APPLIED AT 20°C (68°F) UNLESS OTHERWISE STATED. DO NOT SCALE FROM DRAWING. ALL DIMENSIONS AND TOLERANCES ARE APPLICABLE AT THE FREE STATE CONDITION. ALL DIMENSIONS AND TOLERANCES, INCLUDING ALL APPLICATION OF DATUM REFERENCES.

ZERO PLACE DECIMALS ± 0.5
ONE PLACE DECIMALS ± 0.3
TWO PLACE DECIMALS ± 0.1

ANGLES ± 0.5 DEGREE

ALL DIMENSIONS IN MM

REFERENCE
SEE TOOLBUILDER FIXTURES TO MEET BS 797:1984

THIRD ANGLE PROJECTION

DO NOT SCALE

USE METRIC

CAD UG NX 7.5

MACHINING RESEARCH GROUP
SCHOOL OF MECHANICAL ENGINEERING
UNIVERSITY OF BIRMINGHAM

		DATE
DR	R.MUNOZ	15/04/11
APVD1		
APDV2		
APDV3		
APDV4		
APDV5		

MATERIAL
C350 MARAGING STEEL

DRAWING NAME
TRANSMITTED BAR

QUANTITY 1

PART Nº 18

SIZE	SCALE	FRAME NO	SHEET NO	STK	REV	MAT
A1	2/1	1 OF 1	1 OF 1	...	...	...

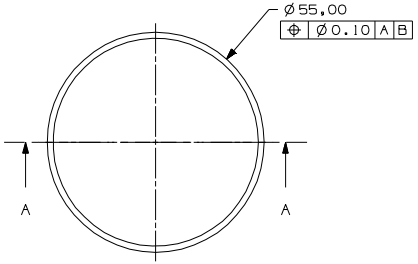

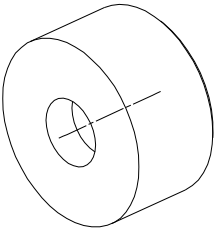

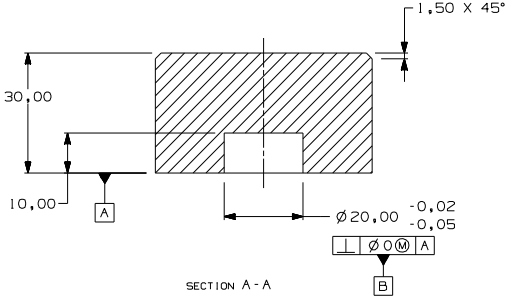

SECTION A-A

UNLESS OTHERWISE SPECIFIED

THIS DOCUMENT IS IN ACCORDANCE WITH ASME Y14.5M-1994. ALL GEOMETRIC TOLERANCES ARE IN RELATION TO DATUMS. WHERE PERFECT FORM AT MMC DOES NOT APPLY, WHEN RELATIONSHIPS BETWEEN FEATURES IS ESTABLISHED BY ORIENTATION OR LOCATION TOLERANCES, SEPARATELY REGARDLESS OF DATUM REFERENCES.

ZERO PLACE DECIMALS : 0.5
ONE PLACE DECIMALS : 0.3
TWO PLACE DECIMALS : 0.1

ANGLES : 0.5 DEGREE

ALL DIMENSIONS IN MM

REFERENCE

NON DIMENSIONED FEATURES TO MEET DIN ISO 2768m

THIRD ANGLE PROJECTION

DO NOT SCALE

USE MATH DATA

CAD UG NX 7.5

MACHINING RESEARCH GROUP
SCHOOL OF MECHANICAL ENGINEERING
UNIVERSITY OF BIRMINGHAM

		DATE
DR	R.MUNOZ	15/04/11
APVD1	-----	----
APVD2		
APVD3		
APVD4		
APVD5		

MATERIAL
NYLON

DRAWING NAME
BAR SAFETY END-CAP

QUANTITY
1

PART N°
19

SIZE	SCALE	FRAME NO	SHEET NO	STG	REV	N/P
A2	2/1	1 OF 1	1 OF 1	...	-	...

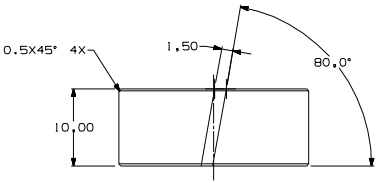

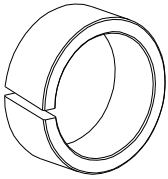

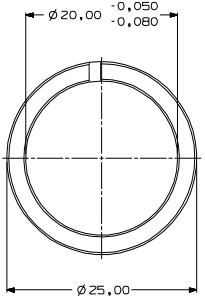

UNLESS OTHERWISE SPECIFIED

THIS DOCUMENT IS IN ACCORDANCE WITH ISO 128. THE DRAWING IS CLEAR AND SUFFICIENTLY DETAILED TO ENABLE ONE UNIT, OR ANY NUMBER OF UNITS, TO BE MANUFACTURED WITHOUT ANY FURTHER INFORMATION BEING REQUIRED. IF ANY ADDITIONAL INFORMATION IS REQUIRED, IT SHOULD BE CLEARLY STATED ON THE DRAWING.

ZERO PLACE DECIMALS ± 0.5
ONE PLACE DECIMALS ± 0.3
TWO PLACE DECIMALS ± 0.1

ANGLES ± 0.5 DEGREE

ALL DIMENSIONS IN MM

REFERENCE

NON DIMENSIONED FEATURES TO MEET BS 7192 (1989)

THIRD ANGLE PROJECTION

DO NOT SCALE

USE WITH BSI

MACHINING RESEARCH GROUP
SCHOOL OF MECHANICAL ENGINEERING
UNIVERSITY OF BIRMINGHAM

		DATE
DR	R.MUNOZ	15/04/11
APVD1	----	----
APVD2		
APVD3		
APVD4		
APVD5		

MATERIAL
AISI 4340

DRAWING NAME
BAR POSITIONING RING

QUANTITY 1

PART N° 20

SIZE	SCALE	FRAME NO	SHEET NO	STK	REV	SUP
A4	5/1	1 OF 1	1 OF ---	---	---	---

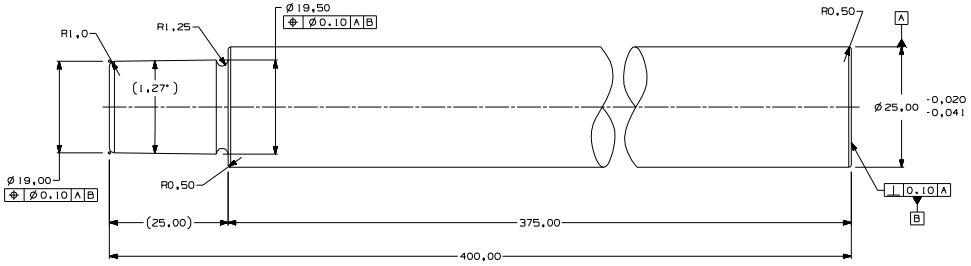

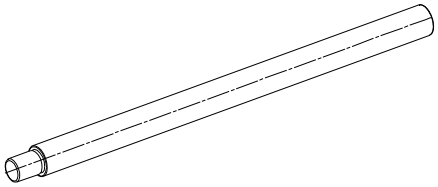

UNLESS OTHERWISE SPECIFIED

THIS DOCUMENT IS IN ACCORDANCE WITH ASME Y14.5M - 1994. ALL DIMENSIONS, TOLERANCES AND PROCESSES STATED SHALL BE MET EXCEPT WHERE SPECIFICALLY OVERRIDDEN BY A HIGHER DRAWING REVISION OR ENGINEERING CHANGE NOTE. ALL TOLERANCES, INCLUDING GEOMETRICAL TOLERANCES, APPLY AT 20°C UNLESS OTHERWISE STATED.

ZERO PLACE DECIMALS ± 0.5
ONE PLACE DECIMALS ± 0.3
TWO PLACE DECIMALS ± 0.1

ANGLES ± 0.5 DEGREE

ALL DIMENSIONS IN MM

REFERENCE
NON TOOLING HOLES TO MEET BS 7192 2:1989

THIRD ANGLE PROJECTION

DO NOT SCALE

USE METRIC

CAD UNIGRAPHICS NX 7.0

MACHINING RESEARCH GROUP
SCHOOL OF MECHANICAL ENGINEERING
UNIVERSITY OF BIRMINGHAM

		DATE
DR	R.MUNOZ	15/04/11
APVD1		
APDV2		
APDV3		
APDV4		
APDV5		

MATERIAL
C350 MARAGING STEEL

DRAWING NAME
LONG STRIKER BAR

QUANTITY 1 | PART N° 21

SIZE	SCALE	FRAME NO	SHEET NO	ITEM	REV	IMP
A1	2/1	1 OF 1	1 OF 1	-	-	-

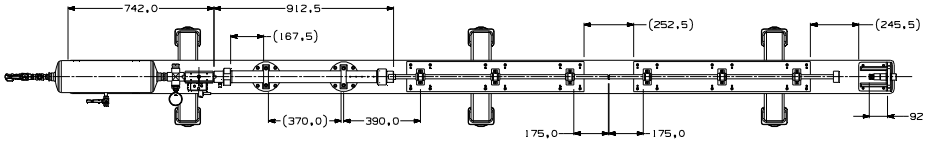

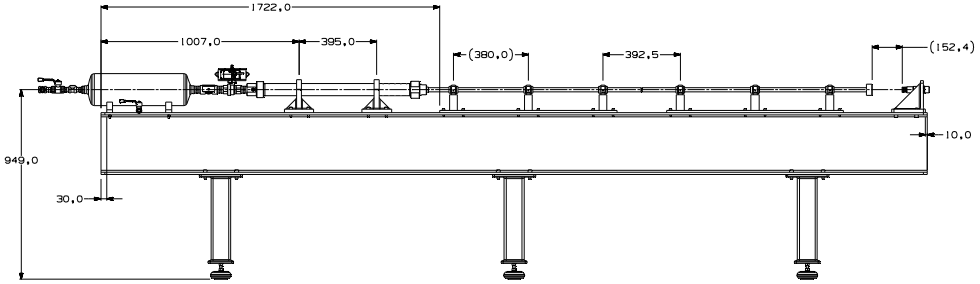

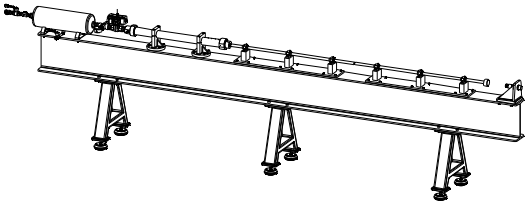

UNLESS OTHER WISE SPECIFIED

THE ABSOLUTE CLEARANCE CALLED FOR ON THIS DRAWING IS THE MINIMUM CLEARANCE AT MAXIMUM MATERIAL CONDITION AND IS THE ONLY DIMENSION TO BE USED FOR ACCEPTANCE OR REJECTION OF THE PART.

BORE PLACE DECIMALS	0.0
TOL PLACE DECIMALS	0.00
TOL PLACE DECIMALS	0.7

ANGLES ± 0.5 DEGREE

ALL DIMENSIONS IN MM

MATERIAL
TO BE MADE TO PRINTS 10 HS1

FINISH
ALL OVER

MACHINING RESEARCH GROUP
SCHOOL OF MECHANICAL ENGINEERING
UNIVERSITY OF BIRMINGHAM

	DATE
AP	15/09/11
APP01	
APP02	
APP03	
APP04	
APP05	

MATERIAL
...

DRAWING
KOLSKY BAR ASSM

QUANTITY
...

PART Nº
...

SIZE	SCALE	DRAWING NO	REV	SHT
A0	1:5	1 OF 1		

APPENDIX II

VUMAT user subroutine for the Johnson-Cook model – Examples

In order to validate the thermo-mechanical VUMAT subroutine developed for the Johnson-Cook relationship, a comparison to the built-in model ABAQUS offers was made. The FE model was a 1x1x1mm cube of Inconel 718 (see Table 17 for the mechanical/physical properties in conjunction with the JC constants used) which was meshed with 1,000 C3D8T type elements. The step time was defined as 0.1s while a compressive load of 0.002N was applied to the superior face of the cube (provided that the opposite face was constrained in all degrees of freedom). Figures 132 and 133 show the predicted Von Mises effective stress, plastic strain and temperature distributions when the built-in JC and VUMAT JC constitutive models were utilised respectively.

As clearly evidenced from the results given by both 3D fully coupled thermo-mechanical FE simulations, it can be concluded that the VUMAT subroutine developed for the Johnson-cook relationship was correctly coded, as the deviations observed from numerical values provided by the built-in JC model can be totally neglected.

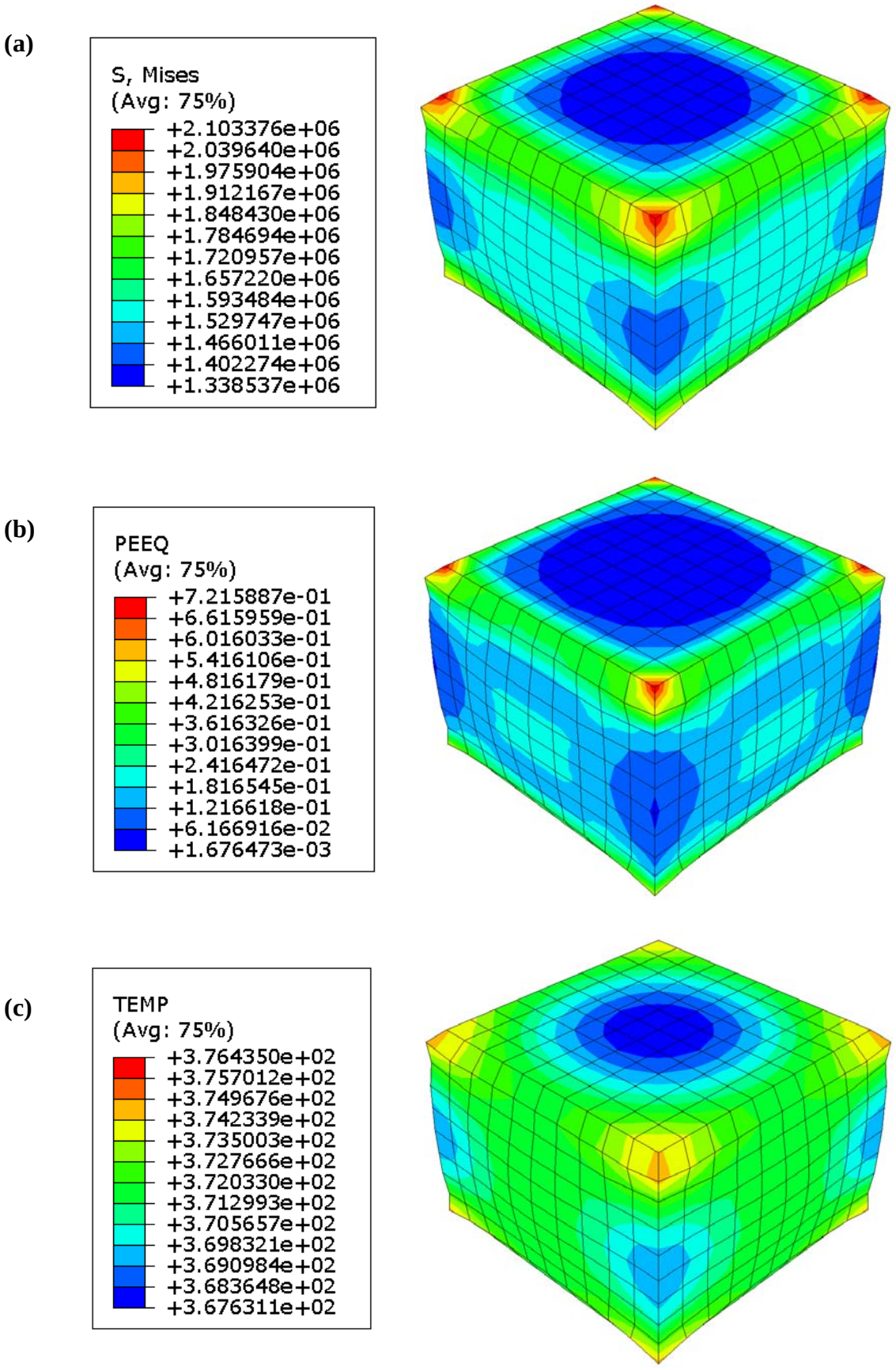

Figure 132. Predicted (a) Von Mises stress (MPa), (b) Plastic equivalent strain (-) and (c) Temperature (K) distributions when employing the built-in JC model ABAQUS offers following the unidirectional deformation of a 1x1x1mm cube of Inconel 718.

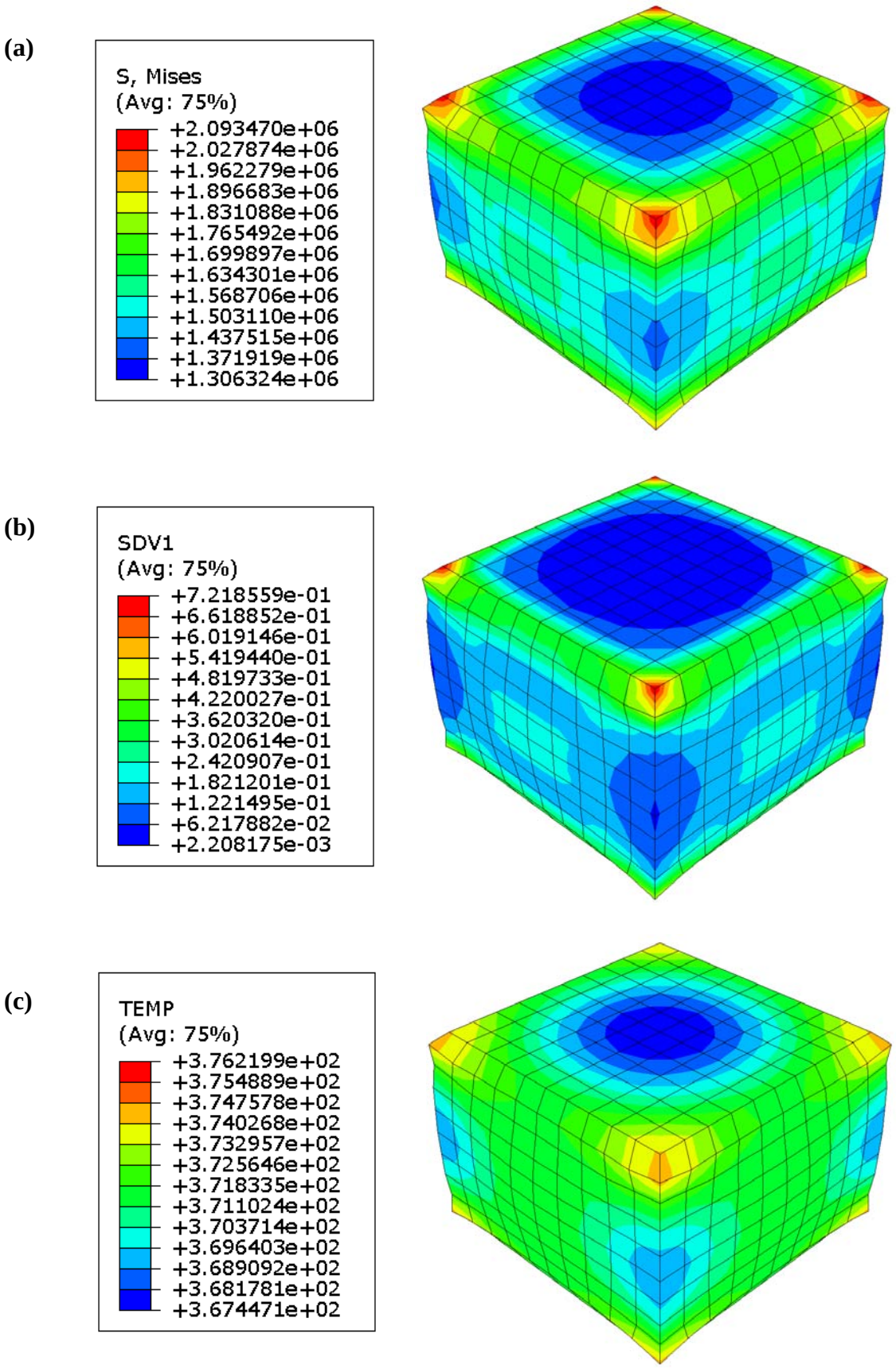

Figure 133. Predicted (a) Von Mises stress (MPa), (b) Plastic equivalent strain SDV1 (-) derived numerically from Eq. (124) and (c) Temperature (K) distributions when employing the VUMAT JC model following the unidirectional deformation of a 1x1x1mm cube of Inconel 718.

APPENDIX III

VUMAT user subroutine for the Mechanical Threshold Stress model – Examples

This appendix intends to show that the numerical predictions given by the VUMAT subroutine developed for the Mechanical Threshold Stress model were reasonable compared to those obtained from the VUMAT JC model. The 3D FE model geometry as well as the boundary conditions and loads were the same as those used in Appendix II. In this regard therefore, Figure 134 displays the predicted Von Mises effective stress, plastic strain and temperature distributions following the application of the 0.002N load on the superior face of the workpiece material.

Predicted maximum effective stresses were ~15% lower than those given by the VUMAT JC model, fact that evidenced the moderate hardening characteristics the MTS constitutive model possesses. When studying the numerical predictions related to the effective plastic strains together with temperatures, the peak values in both cases showed a remarkable similarity to those predicted by the VUMAT JC model, which suggested in consequence that the subroutine developed for the MTS model was appropriate.

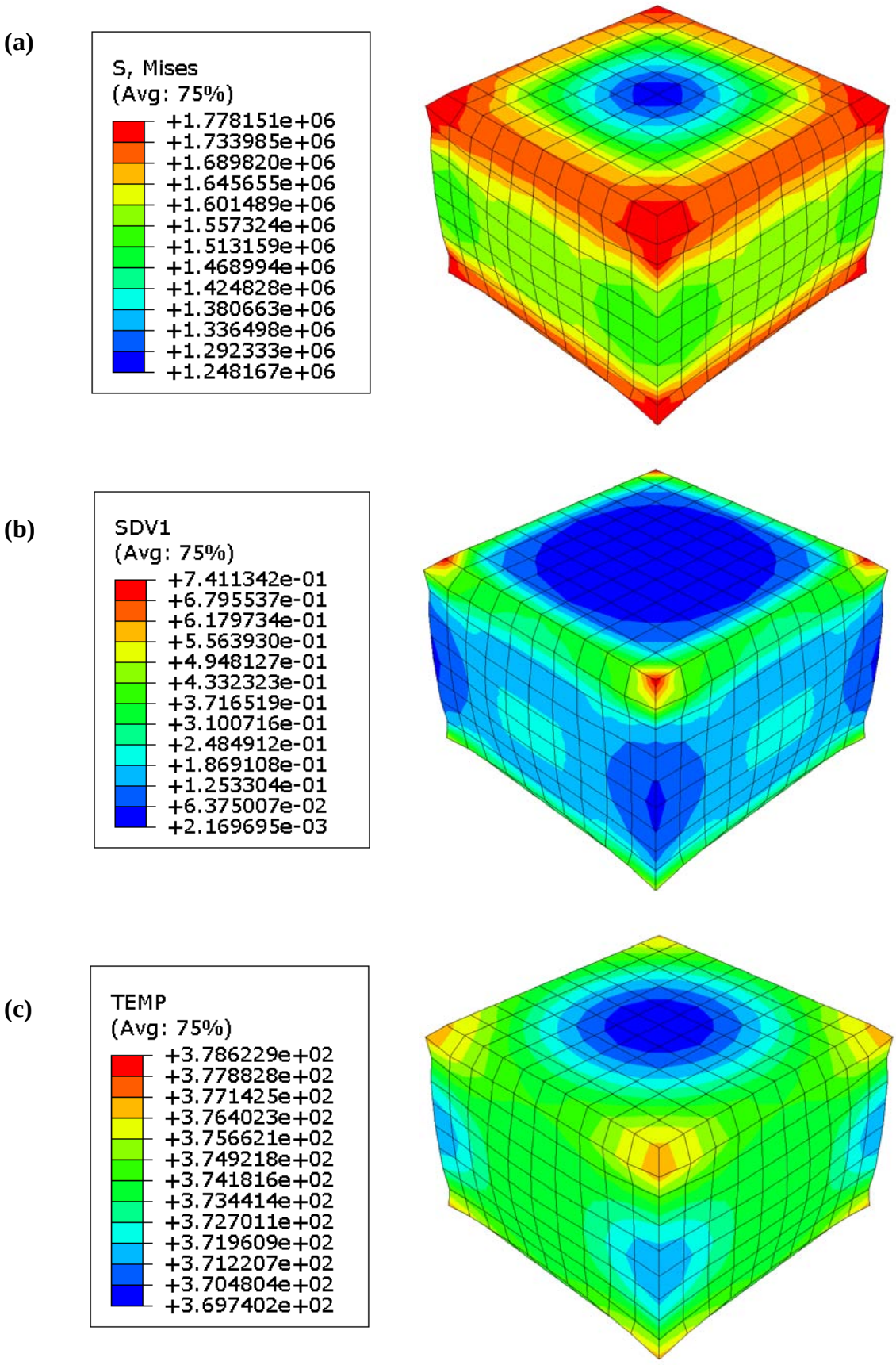

Figure 134. Predicted (a) Von Mises stress (MPa), (b) Plastic equivalent strain SDV1 (-) derived numerically from Eq. (124) and (c) Temperature (K) distributions when employing the VUMAT MTS model following the unidirectional deformation of a 1x1x1mm cube of Inconel 718.

APPENDIX IV

VUMAT user subroutine for the Mechanical Threshold Stress model including the Rittel-Wang-Merzer damage criterion – Examples

In this appendix, the incorporation of the RWM damage criterion to the MTS model in the VUMAT subroutine was made in order to visualise the degeneration in flow stress it produces. Neither the geometry of the FE model nor the boundary conditions were modified. The terms W_{crit}, W_{frac} and a corresponding to the RWM damage model were (arbitrarily) stipulated to be 300J/m^3, 500J/m^3 and 2 respectively. Figure 135 shows the Von Mises effective stress, plastic strain and temperature values corresponding to the deformed cube of Inconel 718 that were predicted once the 0.002N load was completely applied.

Even though the predicted maximum effective stresses were ~4% higher than those obtained solely when the MTS constitutive model was employed, it can be observed that in the four superior nodes of the cube a significant degree of softening took place. As the plastic strains in such particular regions were predicted to the highest (~7.6), this visibly implies that the degradation in flow stress that occurred was in direct relation to those areas in which the maximum deformations were expected to appear, fact which is somewhat in agreement with common sense and more importantly, with experimental stress-strain curves. Predicted temperatures were much alike those seen in Figure 134c, presumably because the flow softening at the maximum strains was abrupt, which in turn made the plastic energy (responsible for giving a rise in temperature) to remain relatively constant.

In summary, it can be reasoned that the RWM model was properly included in the VUMAT MTS subroutine to provide, according to the circumstances, the necessary flow softening.

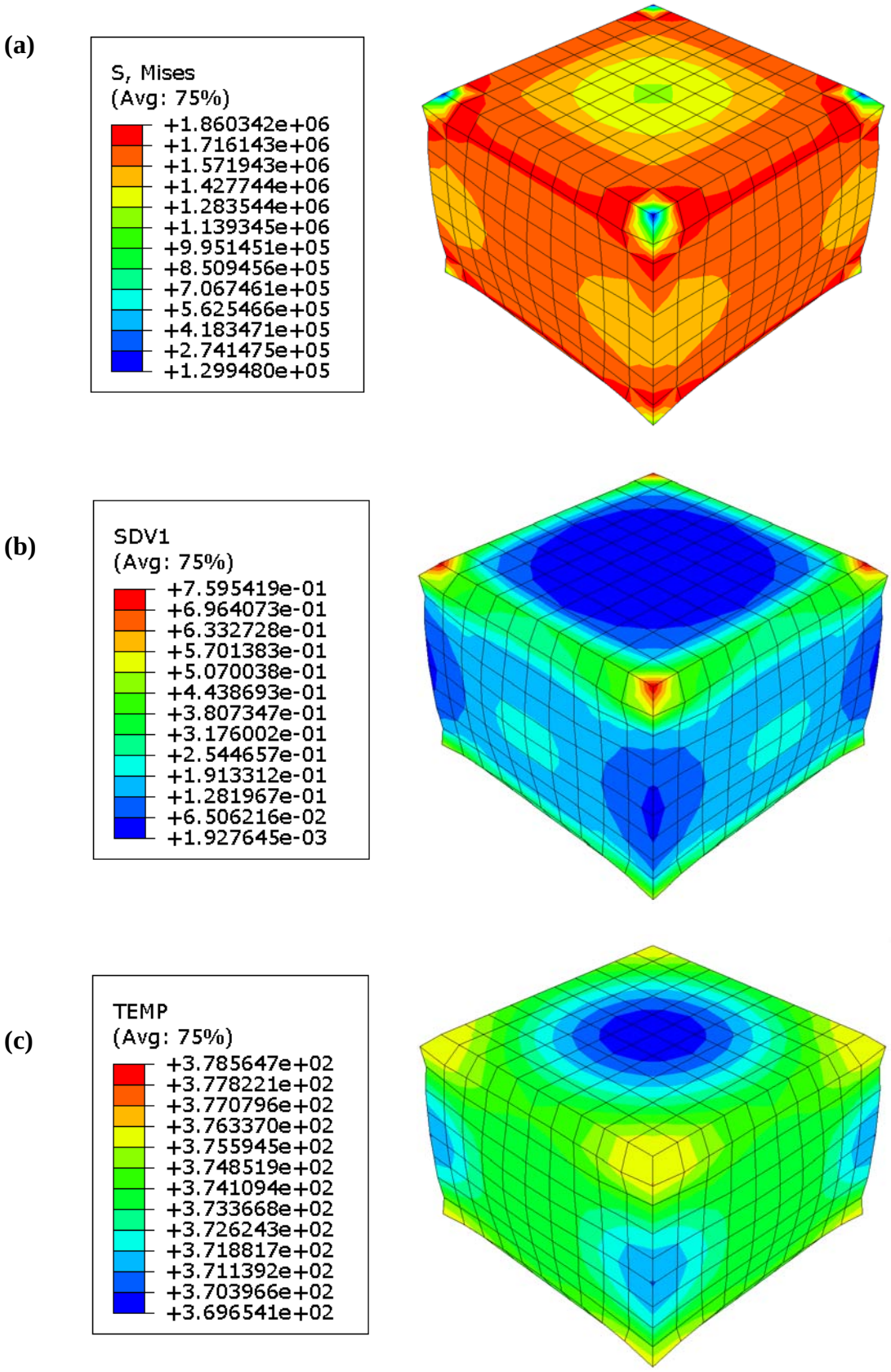

Figure 135. Predicted (a) Von Mises stress (MPa), (b) Plastic equivalent strain SDV1 (-) derived numerically from Eq. (124) and (c) Temperature (K) distributions when employing the VUMAT MTS and RWM models following the unidirectional deformation of a 1x1x1mm cube of Inconel 718.

APPENDIX V

VUMAT user subroutine for the Mechanical Threshold Stress model including the Rittel-Wang-Merzer damage criterion and the Dynamic Recrystallisation module – Examples

In this situation, the incorporation of the DRX module to both the RWM and MTS models was made in order to visualise the further degeneration in flow stress it produces. The geometry of the 3D FE model and the boundary conditions remained invariable. The terms W_{crit}, W_{frac} and a corresponding to the RWM damage model were (arbitrarily) stipulated to be 300J/m^3, 500J/m^3 and 2 respectively. For the purposes of this example only, it was in addition specified that flow softening due to DRX effects commenced when the accumulated energy reached a value $W = 0.25 * W_{crit}$. In this case therefore, Figure 136 shows the Von Mises effective stress, plastic strain and temperature values corresponding to the deformed cube of Inconel 718 that were predicted once the 0.002N load was completely applied.

It can clearly be observed that the maximum predicted stresses were ~4% lower than those in which the DRX module was not including, reinforcing the fact that further flow softening has taken place. While estimated maximum effective plastic strains together with temperatures did not suffered notable variations compared to those seen in Figures 135b and 135c respectively, their distribution in the entire workpiece material was symmetrically found, fact which undoubtedly proved that the incorporation of the DRX module into the VUMAT subroutine provoked not only the further material softening desired, but also an homogenous dispersal of variables, in agreement with previous findings.

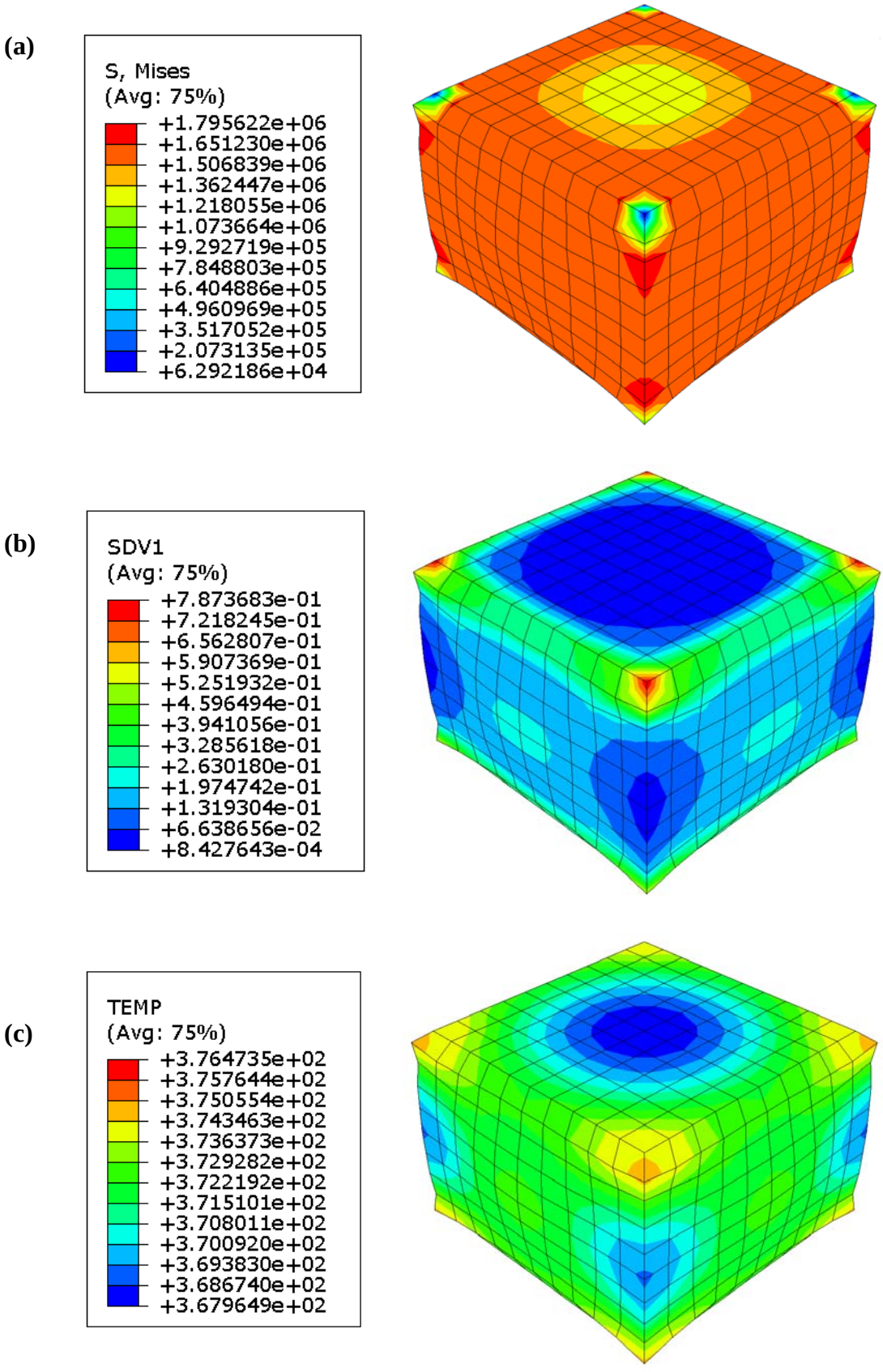

Figure 136. Predicted (a) Von Mises stress (MPa), (b) Plastic equivalent strain SDV1 (-) derived numerically from Eq. (124) and (c) Temperature (K) distributions when employing the VUMAT MTS, RWM and DRX models following the unidirectional deformation of a 1x1x1mm cube of Inconel 718.

APPENDIX VI

PUBLICATIONS

The following list specifies the publications directly emanated from the research investigation:

Munoz R.E., Soo S.L, Aspinwall D.K., 2013. **Formulation of a 3D fully coupled thermo-mechanical finite element model for simulating orthogonal cutting of Ti-6Al-4V.** Proceedings of the 30th International Manufacturing Conference (IMC30), Dublin, Ireland.